

# Computational Models of Cardiovascular Response to Orthostatic Stress

by

Thomas Heldt

Master of Science, Physics  
Yale University, 1997

Master of Philosophy, Physics  
Yale University, 1998

Submitted to the  
Harvard – MIT Division of Health Sciences and Technology  
in partial fulfillment of the requirements for the degree of

Doctor of Philosophy in Medical Physics


at the

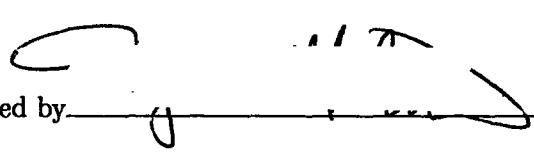
MASSACHUSETTS INSTITUTE OF TECHNOLOGY

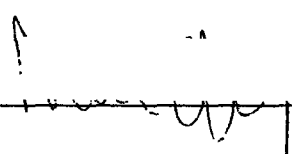
September 2004

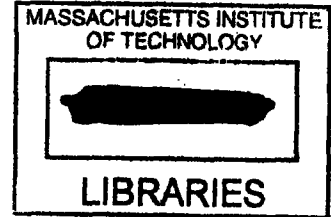
© Thomas Heldt, MMIV. All rights reserved.

The author hereby grants to MIT permission to reproduce and distribute publicly paper  
and electronic copies of this thesis document in whole or in part.

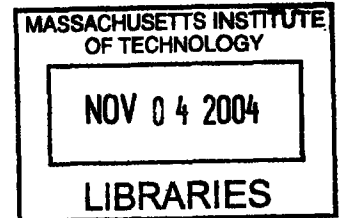
Author   
Harvard – MIT Division of Health Sciences and Technology  
September 3, 2004

Certified by   
Roger G. Mark  
Distinguished Professor of Health Sciences and Technology  
Professor of Electrical Engineering  
Thesis Supervisor

Accepted by   
Martha L. Gray  
Edward Hood Taplin Professor of Medical and Electrical Engineering  
Co-Director, Harvard – MIT Division of Health Sciences and Technology



ARCHIVES



ARCHIVES

SECRET

[REDACTED]

SECRET

# Computational Models of Cardiovascular Response to Orthostatic Stress

by  
Thomas Heldt

Submitted to the  
Harvard – MIT Division of Health Sciences and Technology  
on September 3, 2004, in partial fulfillment of the  
requirements for the degree of  
Doctor of Philosophy in Medical Physics

## Abstract

The cardiovascular response to changes in posture has been the focus of numerous investigations in the past. Yet despite considerable, targeted experimental effort, the mechanisms underlying orthostatic intolerance (OI) following spaceflight remain elusive. The number of hypotheses still under consideration and the lack of a single unifying theory of the pathophysiology of spaceflight-induced OI testify to the difficulty of the problem.

In this investigation, we developed and validated a comprehensive lumped-parameter model of the cardiovascular system and its short-term homeostatic control mechanisms with the particular aim of simulating the short-term, transient hemodynamic response to gravitational stress. Our effort to combine model building with model analysis led us to conduct extensive sensitivity analyses and investigate inverse modeling methods to estimate physiological parameters from transient hemodynamic data. Based on current hypotheses, we simulated the system-level hemodynamic effects of changes in parameters that have been implicated in the orthostatic intolerance phenomenon.

Our simulations indicate that changes in total blood volume have the biggest detrimental impact on blood pressure homeostasis in the head-up posture. If the baseline volume status is borderline hypovolemic, changes in other parameters can significantly impact the cardiovascular system's ability to maintain mean arterial pressure constant. In particular, any deleterious changes in the venous tone feedback impairs blood pressure homeostasis significantly. This result has important implications as it suggests that  $\alpha_1$ -adrenergic agonists might help alleviate the orthostatic syndrome seen post-spaceflight.

Thesis Supervisor: Roger G. Mark  
Title: Distinguished Professor of Health Sciences and Technology  
Professor of Electrical Engineering



## Acknowledgments

As I close this chapter of my life, I want to pause and acknowledge appreciatively the help and support that sustained me over the years and therefore made this work possible.

First and foremost, I would like to thank my thesis advisor, Professor Roger G. Mark, for his friendship and for seven years of support and thoughtful guidance. Your dedication to your students, Roger, your honesty, and your integrity are truly inspiring. The scientific and personal examples you set will continue to guide me as I now embark on my own scientific career. Your ability to assemble an outstanding group of people, whose extraordinary abilities and intellects are only matched by their remarkable personal qualities, has provided me with a great home for the past several years. I count myself fortunate to have been given the opportunity to work in such a stimulating environment.

I am grateful to Professor Roger D. Kamm for his advice over the years and for serving as the chair of my thesis committee. Roger gave me a home in the fluids lab when I first started graduate school and remained involved in my research ever since. I enjoy your wit, Roger, and your keen scientific insight. I admire your ability to doze off during presentations yet to ask the most insightful questions at the end. I also enjoy our early-morning or late-afternoon runs around the Charles river, and I admire your ability to step up the pace (both literally and figuratively) just when I thought that I finally caught up.

I am grateful to Professors Cecil (Pete) H. Coggins, Steve G. Massaquoi, and George C. Verghese for their support and their service on my thesis committee. I met Pete when I took his class on renal pathophysiology at Harvard Medical School. I stand in awe at his clarity of thought and his enviable physiological insight. I first met Steve in 1999 when I attended his thesis defense. I appreciate his unwavering enthusiasm for my work and the conversations we had in the hallways with topics ranging from the absolute trivial to the deep philosophical. George introduced me to the topic of subset selection. He provided a much-needed mathematical foundation when my approach to parameter estimation was quite heuristic. He has also revised my manuscript with seemingly infinite care. Thank you, George, and I am looking forward to starting my post-doctoral training under your guidance.

I thank Professor Richard J. Cohen, MIT, Janice V. Meck, NASA Johnson Space Center, and Karin Toska, University of Oslo, for making their experimental data available to us and for providing feedback on our work along the way.

This work got jump-started when Professor Eun Bo Shim from Kwangwon National University, Republic of Korea, joined Roger Kamm's laboratory for a sabbatical year in 1998. I appreciate your friendship, Eun Bo, and fondly remember your wonderful hospitality during my visit to South Korea.

I owe much gratitude to my officemates in the Laboratory of Computational Physiology. It has been a wonderful experience to share an office with such dependable and thoroughly able people. I thank Wei Zong, my officemate of six years, for the many ways in which he contributed to my work and my life. He never tired of answering my seemingly endless programming questions, and he never hesitated to first assist and then lead when my car needed repair. I was fortunate to have moved into an office next to George Moody's. George's computer skills are legendary and irreplaceable. He is a beacon of calm and tranquility, and when the pressure mounted, to have George at my side, was to me the greatest joy. Mohammed Saeed is single-handedly responsible for the most memorable moments in the lab. Hardly have I met someone more convinced of his own work and more willing to defend it. His quick wit and his ability to view the big picture helped to keep things in proper perspective, for which I owe him much gratitude. Ramakrishna Mukkamala's tenure in our laboratory had many lasting effects, not the least of which is free food during our lab meetings. Rama influenced the way I think about physiological systems. Appreciatively, I continue to seek his advice on technical and non-technical matters alike. Matthew Oefinger came to our laboratory two years ago. We could have not asked for a better match, both in terms of skills and personality, to join our office. I want to thank Kenneth Pierce for administrative support over the years and, in particular, for his support in rendering and manipulating images (some of which are contained in this document). Finally, I would like to give a single round of applause to the more recent members of our laboratory.

I want to thank Raymond Chan for his boundless support and enthusiasm. Ray's cheerful disposition is contagious; it never ceased to lighten up even the darkest moments of my graduate school career.

Graduate school would have been a lot harder had it not been for the support and help from exceptional friends. I would like to thank Volker Bromm, Jeff Cooper, John Gould, Chris Hartemink, Vitaly Napadow, Patrick Purdon, Bruce Roscherr, Sham Sokka, Thanh-Ngá Tran, Neil Weisenfeld, and Sanith Wijesinghe for their support and their camaraderie.

In Nina Menezes, I met my alter ego when I came to MIT seven years ago. Nina has been a wonderful friend and a strong influence on my life ever since. The sharpness of her wit is only matched by the warmth of her character. Your friendship, Nina, has been the most rewarding aspect of my tenure at MIT.

At this point, I come to those for whom acknowledgment is most overdue. I would like to express my deep gratitude and love for my sisters, Silvia and Carolin, my mother, Karin, and my father, Ulrich, whose love and support have carried me over the years.

I want to dedicate this thesis to my parents for having instilled in me a desire to learn. I fully attribute my achievements to their support and to the self-confidence their up-bringing has fostered.

I gratefully acknowledge financial support for my graduate studies from the Studienstiftung des deutschen Volkes, the Gottlieb Daimler- und Karl Benz-Stiftung, the Lee and Harris Thompson fellowship fund in Health Sciences and Technology, the Hugh Hampton Young Fellowship from the Massachusetts Institute of Technology, and last — but certainly not least — my parents. This work was made possible through the National Aeronautics and Space Administration Cooperative Agreement NCC 9-58 with the National Space Biomedical Research Institute.





# Contents

<b>1</b>	<b>Introduction</b>	<b>17</b>
1.1	Motivation . . . . .	17
1.2	Specific Aims . . . . .	21
1.3	Thesis Organization . . . . .	21
<b>I</b>	<b>Cardiovascular Model of Orthostatic Stress</b>	<b>23</b>
<b>2</b>	<b>Hemodynamic Model</b>	<b>25</b>
2.1	Systemic Circulation . . . . .	25
2.1.1	Architecture . . . . .	25
2.1.2	Parameter Assignments . . . . .	28
2.2	Cardiac Model . . . . .	36
2.2.1	Architecture . . . . .	37
2.2.2	Parameter Assignments . . . . .	38
2.2.3	Limitations . . . . .	41
2.3	Pulmonary Circulation . . . . .	43
2.4	Orthostatic Stress Simulations . . . . .	47
2.4.1	Tilt Table Simulation . . . . .	47
2.4.2	Stand Tests . . . . .	53
2.4.3	Lower Body Negative Pressure . . . . .	54
2.5	Model Implementation . . . . .	55
<b>3</b>	<b>Cardiovascular Control System</b>	<b>57</b>
3.1	Arterial Baroreflex . . . . .	57
3.1.1	Architecture of the Model . . . . .	59
3.1.2	Parameter Assignments . . . . .	61
3.2	Cardiopulmonary Reflex . . . . .	65
3.3	Cardiac Pacemaker . . . . .	67
<b>4</b>	<b>Model Validation</b>	<b>69</b>
4.1	Baseline Simulation . . . . .	69
4.2	Population Simulations . . . . .	73
4.3	Gravitational Stress Simulations . . . . .	76
4.4	Lower Body Negative Pressure . . . . .	80

4.5	Modeling Exercise . . . . .	82
4.6	Summary Remarks . . . . .	86
<b>II Sensitivity Analyses and Parameter Estimation</b>		<b>87</b>
<b>5</b>	<b>Sensitivity Analysis</b>	<b>89</b>
5.1	Local Sensitivity Analysis . . . . .	90
5.2	Results and Discussion . . . . .	92
5.3	Summary and Conclusions . . . . .	99
<b>6</b>	<b>Parameter Estimation</b>	<b>103</b>
6.1	Non-linear Least Squares and Subset Selection . . . . .	104
6.1.1	Non-linear Least Squares Estimation . . . . .	104
6.1.2	Subset Selection . . . . .	106
6.1.3	Numerical Implementation . . . . .	108
6.1.4	Formulation of the Estimation Problem . . . . .	108
6.2	Results . . . . .	109
6.3	Summary and Conclusions . . . . .	113
<b>III Clinical Study and Model-based Data Analysis</b>		<b>117</b>
<b>7</b>	<b>Clinical Study</b>	<b>119</b>
7.1	Methods . . . . .	120
7.2	Results . . . . .	122
7.2.1	Steady-state Results . . . . .	122
7.2.2	Transient Responses . . . . .	122
7.3	Pilot Study . . . . .	126
7.4	Discussion . . . . .	127
<b>8</b>	<b>Post-spaceflight Orthostatic Intolerance</b>	<b>129</b>
8.1	Historical Perspective . . . . .	130
8.2	Mechanistic Studies . . . . .	133
8.3	Testing Hypotheses . . . . .	138
8.4	Model-based Data Analysis . . . . .	144
8.5	Summary and Conclusions . . . . .	146
<b>9</b>	<b>Conclusions and Further Research</b>	<b>147</b>
9.1	Summary and Contributions . . . . .	147
9.2	Suggestions for Further Research . . . . .	150
<b>A</b>	<b>Parameters of the Cardiovascular Model</b>	<b>153</b>
<b>B</b>	<b>Allometry of the Cardiovascular System</b>	<b>159</b>

# List of Figures

2-1	Single-compartment circuit representation. . . . .	26
2-2	Circuit representation of the hemodynamic system. . . . .	27
2-3	Aortic pressure-volume relation. . . . .	32
2-4	Aortic volume per unit length of vessel. . . . .	32
2-5	Pressure-volume relation of the legs. . . . .	33
2-6	Pressure-volume relation of a common iliac vein. . . . .	33
2-7	Circuit model of atrial and ventricular compartments. . . . .	37
2-8	Normalized left ventricular time-varying elastance. . . . .	38
2-9	Simulated left ventricular pressure-volume loops. . . . .	39
2-10	Left ventricular end-diastolic pressure-volume relation. . . . .	39
2-11	Left atrial and left ventricular time-varying elastances. . . . .	42
2-12	Right atrial and right ventricular time-varying elastances. . . . .	42
2-13	Circuit model of the pulmonary vasculature. . . . .	44
2-14	Schematic of a Starling resistor set-up. . . . .	45
2-15	Schematic lateral view of the lung. . . . .	45
2-16	Tilt angle profile during a rapid tilt. . . . .	48
2-17	Percent change in plasma volume during 85° HUT. . . . .	50
2-18	Absolute change in plasma volume on return to supine posture. . . . .	50
2-19	RC model of the interstitial fluid compartment. . . . .	51
2-20	Simplified hydrostatic pressure profile. . . . .	51
2-21	Simulated changes in plasma volume; dependence on tilt angle. . . . .	52
2-22	Simulated changes in plasma volume; dependence on tilt angle and tilt time. . . . .	52
2-23	Pleural and esophageal pressure traces during change in posture. . . . .	53
2-24	Profiles of extra-luminal pressures during simulated stand test. . . . .	53
2-25	Numerical volume error time series. . . . .	56
3-1	Diagrammatic representation of the cardiovascular control model. . . . .	58
3-2	Arterial baroreflex model: functional representation of afferent and central nervous pathways. . . . .	59
3-3	Arterial baroreflex model: functional representation of central nervous and efferent pathways. . . . .	60
3-4	Autonomic impulse response functions. . . . .	61
3-5	Intracellular recording of cardiac pacemaker activity. . . . .	67
3-6	Neural influence on cardiac depolarization. . . . .	67

4-1	Simulated pressure waveforms. . . . .	72
4-2	Cardiovascular response to Valsalva maneuver. . . . .	72
4-3	Normalized cardiac output as a function of body weight. . . . .	75
4-4	Effect of heart rate on stroke volume. . . . .	76
4-5	Effect of heart rate on cardiac output. . . . .	76
4-6	Changes in steady-state hemodynamic variables in response to head-up tilt. . . . .	77
4-7	Transient changes in mean arterial pressure and heart rate during changes in posture. . . . .	79
4-8	Steady-state hemodynamic response to lower body negative pressure. . . . .	81
4-9	Cardiovascular response to sudden-onset exercise. Comparison of simulations to experimental data. . . . .	85
5-1	First-order relative parametric sensitivities of the uncontrolled hemodynamic model. . . . .	93
5-2	Second-order relative parametric sensitivities of the uncontrolled hemodynamic model. . . . .	94
5-3	First-order relative parametric sensitivities of the controlled model. . . . .	95
5-4	Second-order relative parametric sensitivities of the controlled model. . . . .	96
5-5	First-order relative parametric sensitivities at the conclusion of head-up tilt. . . . .	98
5-6	Second-order relative parametric sensitivities at the conclusion of gravitational stress. . . . .	99
5-7	First-order relative parametric sensitivities during gravitational stress. . . . .	100
6-1	Eigenvalue spectrum of the Hessian matrix. . . . .	110
6-2	Gaps $\lambda_i/\lambda_{i+1}$ of the eigenvalue spectrum. . . . .	110
6-3	Estimation results for reduced-order, well-conditioned problem. Ill-conditioned parameters kept at their "true" values. . . . .	112
6-4	Estimation results of reduced-order, ill-conditioned problem. Ill-conditioned parameters kept at their "true" values. . . . .	113
6-5	Estimation results of reduced-order, well-conditioned problem. Ill-conditioned parameters perturbed randomly. . . . .	114
6-6	Estimation results of reduced-order, ill-conditioned problem. Ill-conditioned parameters not kept at their "true" values. . . . .	115
7-1	Derivation of instantaneous heart rate signal from ECG. . . . .	121
7-2	Derivation of systolic, mean, and diastolic arterial pressure time series from arterial pressure waveform. . . . .	121
7-3	Transient hemodynamic responses to changes in posture. . . . .	123
7-4	Changes in mean arterial pressure and heart rate during changes in posture. . . . .	124
7-5	Comparison of transient mean arterial pressure responses. . . . .	126
7-6	Comparison of transient heart rate responses. . . . .	126
7-7	Comparison of transient mean arterial pressure responses. Pilot study. . . . .	127

7-8	Comparison of transient heart rate responses. Pilot study. . . . .	127
8-1	Dependence of changes in mean arterial pressure and heart rate on volume status. . . . .	139
8-2	Mean arterial pressure and heart rate changes in response to head-up tilt under varying parametric conditions. Euvolemic case. . . . .	141
8-3	Mean arterial pressure and heart rate changes in response to head-up tilt under varying parametric conditions. Hypovolemic case. . . . .	142
8-4	Dependence of mean arterial pressure and heart rate changes on $\alpha$ -sympathetically mediated reflex mechanisms. . . . .	143
8-5	Dependence of supine stroke volume on volume status. . . . .	143
8-6	Dependence of supine stroke volume under varying parametric conditions. Hypovolemic case. . . . .	144
8-7	Hemodynamic response to standing pre- and post-spaceflight. . . . .	145
8-8	Simulated hemodynamic response to stand tests pre- and post-flight. . . . .	145
B-1	Correlation of body height and body weight. . . . .	160
B-2	Correlation of total blood volume and body weight. . . . .	160



# List of Tables

2.1	Anthropometric and cardiovascular variables. . . . .	29
2.2	Anatomical lengths of arterial vascular segments. . . . .	30
2.3	Anatomical lengths of venous vascular segments. . . . .	31
2.4	Systemic microvascular resistance values. . . . .	35
2.5	Parameter assignments for systemic arterial compartments. . . . .	35
2.6	Parameter assignments for systemic venous compartments. . . . .	36
2.7	Parameters of the cardiac model. . . . .	40
2.8	Cardiac Timing Parameters. . . . .	41
2.9	Nominal parameters for the pulmonary circulation. . . . .	47
3.1	Parameterization of the reflex impulse response functions. . . . .	63
3.2	Arterial baroreflex static gain values. . . . .	64
3.3	Cardiopulmonary static gain values. . . . .	66
4.1	Steady-state hemodynamic variables of normal recumbent adults; comparison to simulations. . . . .	70
4.2	Anthropometric profile of simulated population. . . . .	73
4.3	Comparison of population simulations to steady-state hemodynamic variables of recumbent adults. . . . .	74
4.4	Parameter assignments for exercise simulations. . . . .	84
6.1	Mean relative errors of estimated parameters with respect to their true values. . . . .	111
7.1	Subject information. . . . .	120
7.2	Comparison of steady-state values of hemodynamic variables before and after changes in posture. . . . .	125
8.1	Hypothesized mechanisms of post-spaceflight orthostatic intolerance. . . . .	134
A.1	Parameters of the cardiovascular model. . . . .	153
B.1	Allometric exponents of the human cardiovascular system. . . . .	161





# Chapter 1

## Introduction

### 1.1 Motivation

Like morphological features or behavioral patterns, organ systems in higher organisms have adapted over time in response to local ecological challenges and global environmental influences. The spectacular heterogeneity in size, shape, and way of life among different species is testimony to their adaptive capabilities and their need to function optimally in particular environmental niches.

One relentless and enduring influence common to the development of all life as we know it has been earth's gravitational force. Its direct impact is probably most striking on the cardiovascular system as gravitational pressure heads influence dramatically the distribution of blood volume and blood flow within the cardiovascular system. Without proper adaptation, the mere raising of the head above the level of the heart could potentially lead to a serious and quite possibly life-threatening reduction in cerebral blood flow and oxygenation. This holds true in particular for long-necked animals such as the giraffe or, in the distant past, members of the sauropod family of dinosaurs, whose head towered 8–12 m above heart level in the neck-erect posture.

Not surprisingly, terrestrial-dwelling animals have all developed special physiological mechanisms to counteract the strong influence gravity imposes upon the cardiovascular system. These mechanisms include functional anatomical features, such as venous valves and tight connective tissue surrounding the veins of the dependent limbs to prevent retrograde blood flow and excessive venous pooling, respectively. They also include an array of potent cardiovascular reflex mechanisms that dynamically and adaptively regulate key cardiovascular variables, such as heart rate and peripheral resistance, to maintain blood pressure constant near the base of the head. The integrity and combined action of these mechanisms allow the giraffe to raise its head quickly after drinking from a pool of water, for example, or humans to change posture quickly and continuously, normally without even noticing the profound changes that the cardiovascular system is undergoing. It is only when some of these mechanisms fail to function properly that we become painfully aware of the important function they normally serve.

Conditions such as varicose veins or pure autonomic failure are examples in which

failure of these mechanisms often leads to clinically overt symptoms of orthostatic hypotension, namely an excessive drop in arterial pressure upon assumption of the upright posture. On observing the clinical symptoms of orthostatic hypotension, one is frequently left wondering as to the mechanisms underlying the observed symptoms. In such cases, clinicians usually perform a limited number of typically non-invasive diagnostic studies to elucidate the underlying mechanisms and to devise treatment strategies.

The physiological interpretation of limited experimental data can benefit substantially from the concomitant use of a reasonably complete mathematical model. Mathematical models reflect our current level of understanding of the functional interactions that determine the overall behavior of the system under consideration. They allow us to probe the system, often in much greater detail than is possible in experimental studies, and can therefore help design and test physiological hypotheses and help establish the cause of a particular observation.

The focus of this work is to establish a computational model of the cardiovascular system that represents the normal human response to gravitational stress, and to use this model in the analysis of experimental observations derived from a particular group of individuals who suffer from transient maladaptation following transition to the upright posture. The group we focus on comprises astronauts upon return to the normal gravitational environment.

**Representing the cardiovascular system** Like other physiological systems, the cardiovascular system is remarkable for its intricate, distributed anatomical structure, its spatially distributed physical characteristics, and its temporal range of dynamic behavior. To design a computational model that represents the entire range of cardiovascular behavior is neither technically feasible nor scientifically desirable, as the architecture of any model is indissolubly linked to the particular research questions to be addressed. For these models to be meaningful, they require a choice of the temporal and spatial representation of the system under study that is appropriate for the research question, with refined rendering of some aspects and aggregation or even neglect of others.

Models of both the hemodynamic and control elements of the cardiovascular system have been available for decades and have been progressively improved. Furthermore, even fairly elaborate models are well within the power of inexpensive modern computer hardware and software. The models vary in complexity and purpose, some focusing on arterial hemodynamics [1–5], others on cardiovascular control [6–10]. Some models are based on lumped-parameter representations of the arterial and venous networks [11–14], while others model one or more of the vascular beds using the fluid dynamic equations that govern flow through a distributed, compliant network [2, 3]. Finally, very elaborate models of the circulation and the various short- and long-term control mechanisms have been devised [15].

In the context of cardiovascular adaptation to orthostatic stress, numerous computational models have been developed over the past forty years [1, 3, 4, 6, 7, 10, 16–28]. Their foci range from simulating the physiological response to experiments such as

head-up tilt or lower body negative pressure [4, 6, 7, 14, 16–22, 24, 27], to explaining observations seen during spaceflight [3, 18, 26–28]. The spatial and temporal resolutions with which the cardiovascular system has been represented are correspondingly broad. Several studies have been concerned with changes in steady-state values of certain cardiovascular variables [3, 4, 25, 28], others have investigated the system’s dynamic behavior over seconds [17, 19, 20], minutes [6, 7, 16], hours [18, 26, 27], days [18, 23, 26], weeks [18], or even months [24]. The spatial resolutions range from simple two- to four-compartment representations of the hemodynamic system [6, 17, 21, 22, 28] to quasi-distributed or fully-distributed models of the arterial or venous system [3, 4, 19, 25].

In choosing the time and length scales of our model, we are guided by the clinical practice of diagnosing orthostatic hypotension, which is usually based on average values of hemodynamic variables, such as arterial pressure or heart rate, a few minutes after the onset of gravitational stress [29]. In the research setting, continuous recordings of heart rate and blood pressures during changes in posture might be made for slightly longer periods of time [30]. Since the purpose of the model developed in subsequent chapters is to represent such responses, we aim at simulating the short-term ( $\lesssim 5$  minutes), transient, beat-to-beat cardiovascular response to orthostatic stress. As such, we are not interested in the detailed intra-cycle variations of pressure, flow, and volume waveforms but in the faithful, beat-by-beat representation of average pressures, average flows, and average volumes. A lumped-parameter modeling of the hemodynamic system therefore seems superior to modeling the distributed nature of the arterial and venous circulations, as lumped models reduce the computational cost significantly and produce average variables at similar degrees of fidelity.

Much like previously reported models [10, 31], our model will be based on a closed loop lumped-parameter hemodynamic system with regional blood flow to major circulatory beds. The pumping action of the cardiac chambers will be implemented by time-varying elastances<sup>1</sup>. We will represent the cardiovascular reflex mechanisms for the short-term blood pressure homeostasis, namely the arterial and the cardio-pulmonary baroreflex control loops, while neglecting other control mechanisms that act at longer time scales [36].

In contrast to previously reported models, we will represent not only the steady-state response of the cardiovascular system to orthostatic stress. We will also validate its transient response to changes in posture, and perform sensitivity studies to identify which parameters contribute significantly to a particular model response. Furthermore, we will use the model to estimate parameters from synthetic and experimental data, and will employ the model to test the relative importance of several parameters in the genesis of post-spaceflight orthostatic intolerance. Such a wide spectrum of model applications calls for particular care in model development.

---

<sup>1</sup>One could argue that such a time-varying elastance model with its focus on intra-cycle dynamic behavior is unnecessarily detailed and computationally burdensome for the purpose of our investigation. Some nascent work in our group is aimed at developing dynamic cycle-averaged models [32–35]. However, this work is in too early a stage to be included in this document.

**Orthostatic intolerance in astronauts** As mentioned above, the cardiovascular system is superb at adapting to short-term stresses. Other stresses could be mentioned, such as changes in metabolic requirements during exercise and acute disease states, for instance hemorrhage or myocardial infarction. The cardiovascular system is also effective at compensating for long-term stresses such as environmental changes (high altitude or bed-rest) or chronic disease (aortic stenosis, anemia). However, compensation and adaptation under one set of boundary conditions may result in decompensation and failure to perform when the environmental conditions are suddenly changed.

Human space flight, for example, has demonstrated that the microgravity environment is managed surprisingly well by the cardiovascular system. There is an initial transient period during which astronauts are uncomfortably aware of cephalad shifts of intravascular volume, but within a couple of days these symptoms resolve and astronauts are able to perform well in microgravity, with essentially normal hemodynamics and neurohumoral status.

Extended exposure to microgravity causes adaptive changes in the cardiovascular system that presumably optimize its function in space, but seriously impair its function upon return to the normal gravitational environment. Indeed, the disability produced by a microgravity-adapted cardiovascular system re-entering a gravitational field may be severe enough to seriously impair the ability of astronauts to complete their mission. As summarized in NASA's Critical Path Roadmap, "following exposure to microgravity, upright posture results in the inability to maintain adequate arterial pressure and cerebral perfusion. This may result in syncope (loss of consciousness) during re-entry or egress." [37]

Although considerable experimental effort has been focused on the problem of post-flight orthostatic intolerance (OI), there remains a lack of consensus about its physiological causes. Based on evidence gathered from astronauts during flight and from numerous bed-rest studies, a number of hypotheses have been considered to explain microgravity-induced orthostatic intolerance. Mechanisms that have been proposed as contributors to post-flight OI include: impaired venous return due to hypovolemia [38, 39], hypovolemia and changes in venous capacitance [40], decreased left ventricular distensibility [41–43], changes in cardiac function consequent to reduced cardiac mass [44], alterations in the venous compliance of the leg [45], changes in alpha-adrenoreceptor responsiveness [46], changes in baroreflex gain [38], alterations in vestibular influences on cardiovascular control [47], deficiencies in skeletal muscle function and reduced fitness [48, 49], and reduced systemic vasoconstrictor response [49–54].

Hypovolemia is one of the best documented, unequivocally accepted adaptations to the weightless environment, and is certainly one of the principal contributors to the clinical presentation of post-flight OI. Increasing credence, however, is given to the possibility that, in addition, a critical combination of some of the other mechanisms mentioned above results in the astronauts' inability to tolerate gravitational stress upon return [12, 30, 49]. Furthermore, it is quite likely that the relative importance of the various contributing mechanisms is subject-specific and changes the longer the astronaut is exposed to the microgravity environment [30, 44].

## 1.2 Specific Aims

There are four specific aims to the research presented in this thesis:

1. To build a model of the cardiovascular system that is capable of simulating the short-term hemodynamic response to gravitational stress such as head-up tilt and lower body negative pressure.
2. To perform extensive sensitivity analyses on the model so developed in order to identify sets of parameters that significantly influence the hemodynamic response to gravitational stress.
3. To perform a clinical study to elucidate the transient and steady-state hemodynamic responses to rapid head-up tilt, slow head-up tilt, and standing up in normal healthy volunteers.
4. To use the model to test hypotheses regarding the maladaptation of astronauts to earth's gravitational environment upon their return from space.
5. To investigate which parameters of the cardiovascular system can be estimated from the transient hemodynamic response to changes in posture.

## 1.3 Thesis Organization

This thesis is organized in three major parts. The first part, on *Computational Cardiovascular Model*, comprises Chapters 2 through 4. Here we develop the hemodynamic and the reflex model and present the validation of the composite model through comparison of its predictions to experimental results taken from the medical literature. The second part, *Sensitivity Analyses and Parameter Estimation*, consists of Chapters 5 and 6 and introduces the analysis of the model assembled in the first part: we discuss global and local sensitivity analyses and introduce methods to estimate parameters of the cardiovascular system from hemodynamic data streams. Chapters 7 and 8 constitute the third part of the thesis, *Clinical Study and Model-based Data Analysis*. Here we present the results of the clinical study and use the model to aid our understanding of post-spaceflight orthostatic intolerance.

In Chapter 2, we present the architecture of and the parameter assignments for the hemodynamic model. First, we present the topology of the systemic circulation deemed appropriate to represent blood volume redistribution between different vascular compartments. Next, we describe the representation of the cardiac chambers in terms of time-varying elastance models before turning our attention to the model of the pulmonary circulation. Subsequently, we describe the implementation in the model of commonly used orthostatic stress routines: head-up tilt, stand tests, and lower body negative pressure. We conclude the chapter with a description of the model implementation.

Chapter 3 focuses on the architecture and the parameter assignments of the neurally-mediated cardiovascular control mechanisms. In particular we describe the

arterial baroreflex and the cardio-pulmonary reflex loop. Throughout Chapters 2 and 3, we try as much as possible to provide the reader with a detailed rationale as to the assignment of baseline numerical values to the parameters of the model.

In Chapter 4, we validate the model by comparing its predictions to experimental results reported in the medical literature for normal healthy subjects. First, we compare the steady-state values of certain hemodynamic variables that are commonly used clinically to assess the cardiovascular state of patients. Next, we introduce the simulation of a population of normal subjects and compare the population-averaged values, their standard deviations, and ranges to the same set of hemodynamic variables. It will be shown that the mean values, the standard deviations, and the ranges of the population simulation match their experimental analogs quite well. Subsequently, we introduce the simulations of the orthostatic stress tests and compare the steady-state responses at different stress levels to reported experimental data. We also present the transient simulations for each orthostatic stress test. We conclude Chapter 4 with a simulation of the effects of exercise and concluding remarks on the forward modeling effort.

In Chapter 5, we begin to analyze the model with a series of sensitivity studies aimed at identifying which parameters of the model contribute most to a given simulation output of choice. We will address this problem exclusively from a local perspective.

In Chapter 6, we turn our attention to the problem of estimating parameters of the model from synthetic, noise-corrupted data. We will employ a non-linear least squares optimization algorithm along with a subset selection approach for overcoming the problem of *ill-conditioning*. We will show that this approach yields reliable parameter estimates for a small number of model parameters. Fixing the remaining parameters to *a priori* values has little effect on the quality of the parameter estimates.

Chapter 7 summarizes the results of the clinical study designed to elucidate the transient hemodynamic response to rapid tilt, slow tilt, and standing up. We show that each stress test leads to a somewhat different hemodynamic response. We also demonstrate that despite marked differences in the transient amplitude response of standing up and rapid tilting, the timing of the initial hemodynamic response is well preserved. We also demonstrate that the difference in the amplitude response can be explained on the basis of muscle contraction preceding the changes in posture.

In Chapter 8, we turn our attention to the problem of post-spaceflight orthostatic intolerance and how our model can help elucidate which changes in cardiovascular performance have the greatest detrimental impact on orthostatic stress test post-flight. We will briefly review the evolution of post-flight orthostatic intolerance from a historical perspective before summarizing mechanistic studies of its etiology. We will use the model to assess the system-level impact that some of the proposed mechanisms have on cardiovascular performance.

We summarize the contributions of this work and suggest further directions of research in Chapter 9.

Appendix A summarizes the numerical values of the hemodynamic and the control models. In Appendix B, we describe the scaling laws and sampling algorithm employed to generate the population simulations introduced in Chapter 2.

## **Part I**

# **Cardiovascular Model of Orthostatic Stress**





# Chapter 2

## Hemodynamic Model

In this chapter, we describe the architecture of the hemodynamic system and discuss in detail the numerical value assigned to each of the model parameters. We start in Section 2.1 by discussing the representation of the systemic vasculature. In Section 2.2, we focus on the cardiac model whose pump-function is described in terms of time-varying atrial and ventricular elastance waveforms. The pulmonary vascular model will be the topic of Section 2.3, where we will describe a non-linear, gravity-dependent model of the pulmonary microvascular resistance. In Section 2.4, we describe the implementation of various orthostatic stress tests. Section 2.5 comments on the numerical implementation of the hemodynamic model.

### 2.1 Systemic Circulation

The systemic circulation can be conceptualized as comprising three distinct functional units: the arterial system (representing the aorta, large arteries, and the main and terminal arterial branches); the micro-circulation (consisting of the arterioles and the capillary network); and the venous system (consisting of the venules, terminal and main venous branches, the large veins, and the venae cavae). Substantial differences in their respective physical properties require separate representation of these three units at a resolution commensurate with our goal of simulating regional blood flow during gravitational stress.

In this section, we will introduce the general architecture and topology of the systemic circulatory model and discuss in detail the choice of nominal parameter values.

#### 2.1.1 Architecture

The central building block of the systemic circulation is the circuit analog representation of a vascular segment shown in Figure 2-1. The lumped physical properties of each segment are characterized by an inflow resistance,  $R_n$ , an outflow resistance,  $R_{n+1}$ , and a capacitive element that represents the volume-pressure relation,  $V_n(P_n - P_e)$ , of the segment. The latter relates the volume,  $V_n$ , stored in the seg-

ment under consideration to transmural pressure,  $\Delta P = P_n - P_e$ . In addition, the pressure source  $P_h$  represents the hydrostatic pressure associated with the segment under consideration;  $P_e$  represents the pressure acting external to these vessels, such as intra-thoracic pressure, intra-abdominal pressure, or lower body negative pressure. The flows can be expressed using the constitutive relations for the resistors and the capacitor:

$$\begin{aligned} q_n &= \frac{P_{n-1} - P_n + P_h}{R_n} \\ q_{n+1} &= \frac{P_n - P_{n+1}}{R_{n+1}} \\ q_c &= \frac{d}{dt} V_n = \frac{dV_n}{d(P_n - P_e)} \cdot \frac{d}{dt} (P_n - P_e) \end{aligned}$$

Combining these expressions for the flow rates yields an expression for the rate of change of the luminal pressure,  $P_n$ :

$$\frac{d}{dt} P_n = \frac{P_{n-1} - P_n + P_h}{C_n R_n} - \frac{P_n - P_{n+1}}{C_n R_{n+1}} + \frac{d}{dt} P_e \quad (2.1)$$

where we have introduced the short-hand notation for the (incremental) vascular capacitance  $C_n = dV_n/d(P_n - P_e)$ . The entire hemodynamic model is thus described by a set of coupled first-order differential equations.

Since we are chiefly interested in cycle-to-cycle changes of pressures and regional blood flows, we have neglected all inertial effects. Their contribution to pressures and flows is greatest in the presence of large changes in flow rates, which commonly occur within a beat, rather than from beat to beat. Even during sudden orthostatic stress, cycle-by-cycle changes in blood flow are relatively small compared to changes in blood flow within the cardiac cycle. Defares estimated inertial effects to account for less than 1% of stroke volume and mean arterial pressure [55]. Inclusion of inertial effects would therefore only serve as cosmetic refinement of the arterial waveform

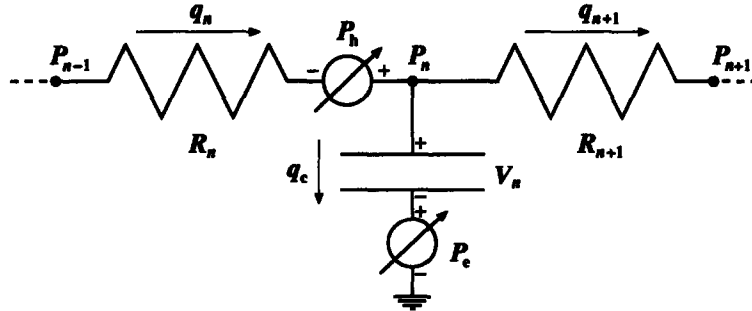


Figure 2-1: Single-compartment circuit representation.  $P_{n-1}$ ,  $P_n$ ,  $P_{n+1}$ : compartment pressures;  $P_h$ ,  $P_e$ : hydrostatic and external pressures;  $q_n$ ,  $q_{n+1}$ ,  $q_c$ : flow rates;  $V_n$ : compartment volume;  $R_n, R_{n+1}$ : flow resistance.

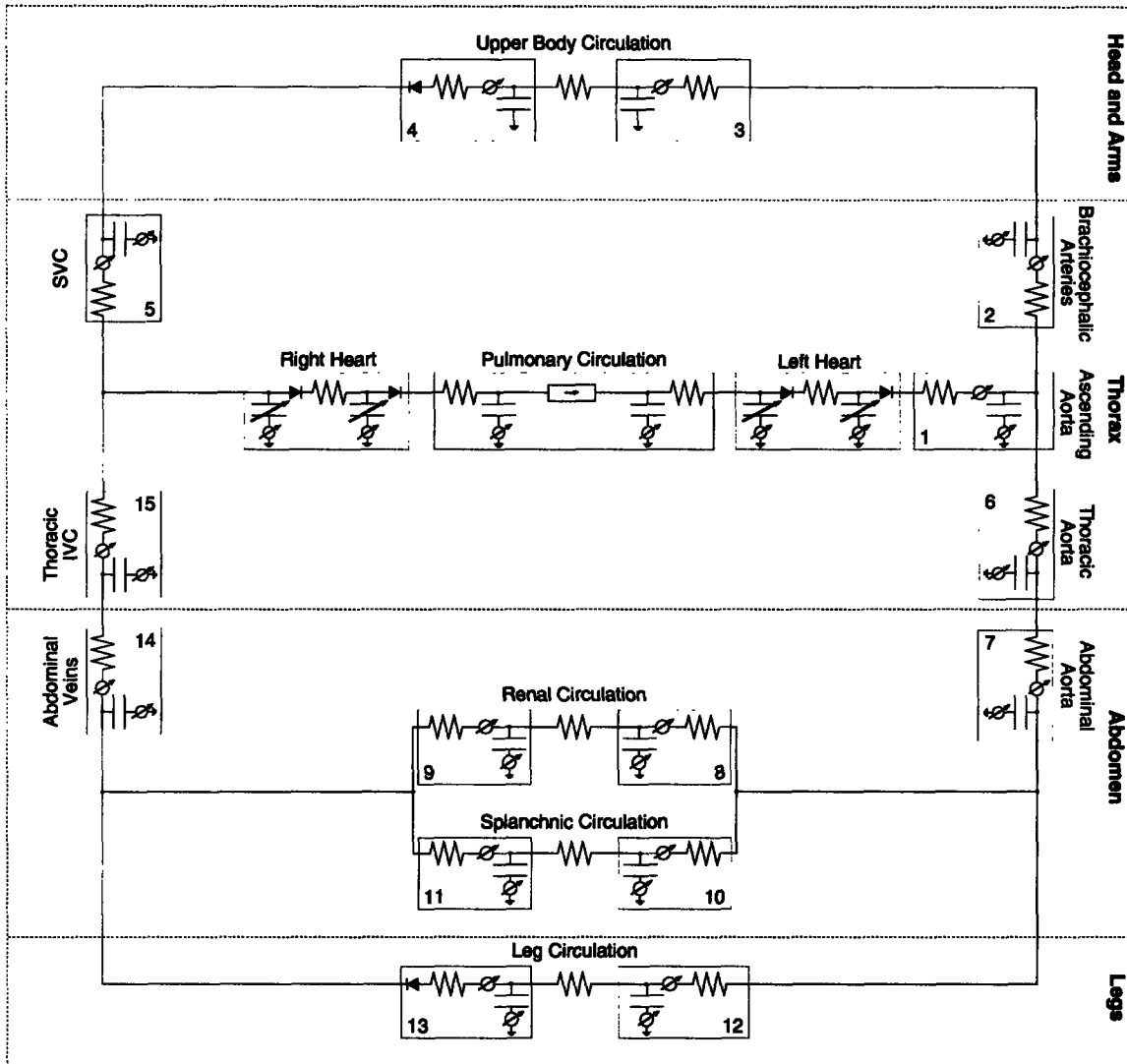


Figure 2-2: Circuit representation of the hemodynamic system. IVC: inferior vena cava; SVC: superior vena cava. Numbers indicate compartment index.

morphology and would come at an increased computational cost.

The topology of the entire hemodynamic system is modeled in Figure 2-2. The peripheral circulation is divided into upper body, renal, splanchnic, and lower body sections on the basis that they receive similar fractions of cardiac output [56]. The superior vena cava and the intra-thoracic and abdominal portions of the inferior vena cava are separately identified, as are the ascending aorta, the brachiocephalic arteries, and the thoracic and abdominal portions of the aorta. The arterio-venous resistances of the four peripheral vascular beds have not been assigned to particular arterial or venous compartments as their properties are representative of the respective micro-circulations. The latter are described primarily by their resistive properties and are assumed to exhibit negligible capacitive characteristics. The systemic circulation thus consists of fifteen compartments, each of which requires specification of a resistance, a pressure-volume relation, and an effective anatomical length. The latter will be used to determine the compartments' hydrostatic pressure components in the erect posture. Since we will neglect gravitational gradients in the anterior-to-posterior direction, the effective anatomical lengths are the projections of the vessel lengths onto the major body axis.

Since the entire peripheral vasculature is represented by only four vascular beds, it is important for our later discussion of blood volume and blood flow distribution to be clear about which anatomical structures are assigned to which vascular bed. We assume the upper body compartment to represent the circulation of the head, the neck, and the upper extremities. The latter are assumed to account for 10 % of total skeletal muscle mass. Furthermore, we assume that one third of the blood supply to the skin and one half of the blood supply to the skeleton occurs in the upper body compartment. The renal compartment represents the kidneys and the adrenal glands. The splanchnic compartment comprises the entire gastro-intestinal tract, one half of the adipose tissue, and one third of the skin. Finally, the leg compartment represents the lower extremities and the pelvic circulation. As such, it contains 90 % of the skeletal muscle, one half of the skeleton, one third of the skin, one half of the adipose tissue, and the pelvic organs.

### 2.1.2 Parameter Assignments

Below and in sections to follow, we discuss in detail the rationale for the numerical values assigned to the various physical parameters of the hemodynamic system. In reviewing the medical literature, we strive to characterize each parameter by giving estimates for its population mean, its standard error, and, where possible, provide a reasonable physiological range. Since the choice of parameter values will define the nominal cardiovascular state of the model, we first comment on what we intend this nominal state to represent and which *a priori* assumptions this representation necessitates.

The main focus of this work is to understand the physiological response to orthostatic stress in normal, healthy subjects, of whom we consider astronauts to constitute a subset. The cardiovascular state of the model must therefore be representative of a normal, healthy subject population. However, it is well established that particu-

larly blood volume scales with the size of the subject under consideration [57]. In Table 2.1, we summarize anthropometric and cardiovascular variables for the subject population we aim to represent. The data are based on sizable clinical studies of normal male subjects who are assumed free of cardiovascular pathology [57–62]. In the following, we therefore assume a 169 cm, 70 kg subject with a total blood volume of 5150 ml and cardiac output of 4813 ml/min.

**Vascular Lengths** To determine the hydrostatic pressure component to be assigned to each compartment, we need to supply an estimate of the superior-to-inferior extension of the vascular segments each compartment represents. For most compartments, such as, for example, the thoracic aorta, this estimate is identical with their anatomical length, as their primary orientation is parallel to the major body axis. For the upper body, renal, and splanchnic compartments, however, this does not hold true and we estimate the vascular lengths of these compartments by their average inferior-to-superior extension measured from the point of origin of their arterial blood supply.

Obtaining detailed measurements of vascular segment lengths from the literature proved to be surprisingly difficult, so we had to rely on anthropometric studies [61] and standard anatomy textbooks [63, 64] to assign most nominal values.

We represent the hydrostatic contribution of the blood column in the left ventricular outflow tract, the ascending aorta, and parts of the aortic arch by a single, lumped hydrostatic pressure component. Assigning to the outflow tract half the base-to-apex length of the heart, which is about 10 cm [65], and using Gray’s estimate of 5 cm [63, p. 1504] for the length of the ascending aorta, we can assign an anatomical length of approximately 10 cm to the aortic root compartment. Similarly, using Gray’s estimate of 4 to 5 cm [63, p. 1513] for the brachiocephalic artery, we can assign a nominal value of approximately 4.5 cm to the compartment representing the ascending thoracic arteries. The corresponding compartment on the venous side represents parts of the right atrium, the superior vena cava, and the brachiocephalic veins. Since they cover the same vertical height as the corresponding segments on the arterial side, their hydrostatic contributions have to be equal. Assigning 7 cm [63, p. 1592] to the superior vena cava and 2.5 cm to the right brachiocephalic vein [63, p. 1591] leaves

Table 2.1: Population characteristics of anthropometric and cardiovascular variables. BSA: body surface area; TBV: total blood volume; CO: cardiac output; MAP: mean arterial pressure; CVP: central venous pressure.

Height cm	Weight kg	BSA m <sup>2</sup>	TBV ml	CO ml/min	MAP mm Hg	CVP mm Hg
(169.3 ± 1.5)	(70.3 ± 2.1)	(1.83 ± 0.02)	(5150 ± 124)	(4813 ± 103)	(91 ± 2)	(6 ± 2)
(161.5–186.8)	(59.8–98.5)	(1.51–2.10)	(3750–6890)	(4344–7602)	(84–103)	(2.2–9.6)

Data represent mean ± standard error and (0.05 – 0.95) interquantile range.

the remaining 5 cm to be assigned to the right atrium, which is about one half of the height of the heart. The remainder of the right atrium and the thoracic inferior vena cava account for a height of approximately 6 cm. Finally, at the level of the diaphragm the hydrostatic contribution in the descending aorta must be equal to the hydrostatic contribution in the thoracic inferior vena cava, which implies the descending aorta to have a nominal length of 16 cm.

Using ultrasonography in 180 adult healthy volunteers, Macchi and Catini [66] report the lengths of the infra-renal portions of the abdominal aorta and inferior vena cava to be  $(8.31 \pm 0.22)$  cm with a range of (5.9 – 10.5) cm and  $(9.52 \pm 0.27)$  cm with a range of (5.8 – 13.6) cm, respectively. The latter value agrees with the work by Bonnichon and co-workers [67] who used cavography to measure the length of the infra-renal inferior vena cava in 100 subjects, and report an average length of 9.6 cm with a range of (8.0 – 14.2) cm. Martini [64] suggests that the renal arteries are located about 2.5 cm distal to the superior mesenteric artery, which in turn branches off the abdominal aorta approximately 2.5 cm distal to the coeliac trunk. The combined data therefore suggest a length of the inferior vena cava and abdominal aorta of approximately 14 to 15 cm.

The lower extremity compartment of our model represents the vasculature of the legs and pelvis. Its anatomical height is approximated by the waist height, which is the vertical distance from the floor to the top of the iliac crest and has been measured in 24,469 US Army men [68] to be  $(105.6 \pm 5.0)$  cm with a range of (94.2 – 117.6) cm. This estimate is justified as the aortic bifurcation occurs at the base of the fourth lumbar vertebra which in turn is level with the iliac crest [63, p. 426]. The vasculature of the neck, the head, and the arms is lumped into a single upper body compartment to which we assigned a lumped vertical distance of 20 cm. This value corresponds to the length of the common carotid arteries [63, p. 1514]. The kidneys are approximately symmetrical in shape about the transverse plane defined by the renal arteries and veins. As such, their superior-to-inferior extension does not contribute further to blood pooling and their effective hydrostatic length is assumed to be zero. Lastly, the splanchnic compartment comprises the circulation of the liver, the spleen, the pancreas, and the gastrointestinal tract which anatomically span the entire abdominal cavity. We assume most of the compliance of the splanchnic circulation to reside in the small and large intestines and assume their effective hydrostatic length

Table 2.2: Anatomical lengths of arterial vascular segments. Values given in cm. Compartment indices are from Figure 2-2.

	Compartment Index							
	1	2	3	6	7	8	10	12
Mean	10	4.5	20	16	14.5	0	10	106
Range	(9-11)	(4-5)	(18-22)	(14-18)	(11-19)	(0.0-0.1)	(9-11)	(94-118)

to be zero as well.

In closing the discussion on the lengths of the individual vascular segments, it should be pointed out that the data for the arterial components described above are all in good agreement with the estimates presented by Avolio [69] and Noordergraaf and co-workers [70]. Since it is unclear whether their estimates are based on actual anatomic investigations, we chose to justify the parameter assignments independently of their work. Our estimates of the anatomic lengths of the vascular compartments are summarized in Tables 2.2 and 2.3 where we have assigned the upper and lower limits in the general population to be  $\pm 10\%$  of the nominal value for variables where experimental ranges could not be found.

**Pressure-Volume Relations** Blood vessels behave like distensible tubes in that they require a certain amount of volume (the unstressed or zero-pressure filling volume) in order to be distended at zero transmural pressure; their vascular volume rises in an approximately linear fashion at low enough transmural pressures, and they exhibit an elastic limit at high transmural pressures. Figure 2-3 illustrates these characteristics for a human aorta and its major subdivisions [71]. It also demonstrates that the compliance of the human aorta changes not only as a function of transmural pressure but also along the length of the vessel. While the elastic properties of vascular segments are fully specified by their (non-linear) pressure-volume relationships, under baseline physiological conditions most vessels operate in a range of transmural pressures over which their pressure-volume relations can be presumed linear. Under the assumption of a linear pressure-volume relation over the range of 60 – 140 mm Hg, the data in Figure 2-3 suggest compliances per unit vessel length of 0.008 ml/mm Hg/cm, 0.017 ml/mm Hg/cm, and 0.028 ml/mm Hg/cm for the abdominal aorta, the thoracic aorta, and the ascending aorta, respectively. When analogously normalized by the lengths of the vessel segments, the unstressed volumes are 0.7 ml/cm, 1.0 ml/cm, and 2.1 ml/cm. The values of 1.0 ml/cm and 0.017 ml/mm Hg/cm for the thoracic aorta compare very favorably with the values  $(1.20 \pm 0.15)$  ml/cm and  $(0.013 \pm 0.002)$  ml/mm Hg/cm that can be estimated from the data reported by Hallock and Benson [72] and reproduced in Figure 2-4. Assuming the same percentage errors, we assign  $(0.7 \pm 0.09)$  ml/cm and  $(0.007 \pm 0.001)$  ml/mm Hg/cm to the abdominal

Table 2.3: Anatomical lengths of venous vascular segments. Values given in cm. Compartment indices are from Figure 2-2.

	Compartment Index						
	4	5	9	11	13	14	15
Mean	20	14.5	0	0	106	14.5	6
Range	(18-22)	(13-16)	(0-1)	(0-2)	(94-118)	(11-19)	(5-7)

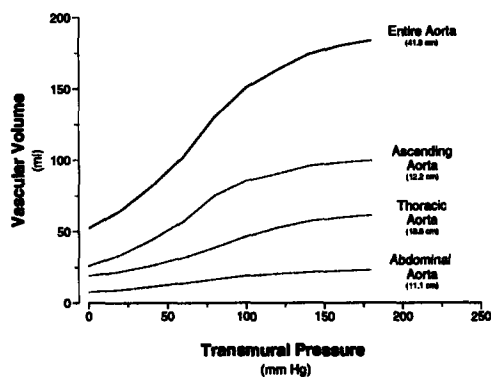


Figure 2-3: Pressure-volume relation of a human aorta. Segment lengths indicated in parentheses. Data adapted from [71].

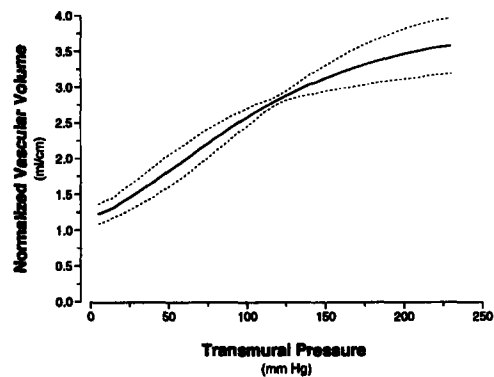


Figure 2-4: Volume per unit length of thoracic aorta. Solid line: population mean; dashed lines:  $\pm$  standard deviation. Data adapted from [72].

aorta,  $(1.0 \pm 0.13)$  ml/cm and  $(0.013 \pm 0.002)$  ml/mm Hg/cm to the thoracic aorta, and  $(2.1 \pm 0.3)$  ml/cm and  $(0.028 \pm 0.004)$  ml/mm Hg/cm to the ascending aorta, respectively. Furthermore, we assume negligible difference between the histological structure of the ascending aorta and the brachiocephalic arteries and assign the same per-length values of unstressed volume and vascular compliance to that compartment.

Reliable experimental values for the lumped arterial compliances of the peripheral vascular beds could not be obtained from the literature. In estimating these values, we assume that the compliance per unit length of the leg arteries is  $(0.004 \pm 0.001)$  ml/mm Hg/cm, or approximately half the value of the abdominal aorta. Furthermore, we assign the same value, namely  $(0.42 \pm 0.1)$  ml/mm Hg, to the upper body and splanchnic compartments and half that value to the renal arterial compartment. The total compliance of the systemic arterial system thus equates to  $(2.19 \pm 0.27)$  ml/mm Hg.

During orthostatic stress, the venous transmural pressures in parts of the dependent vasculature can reach levels at which the non-linear nature of their pressure-volume relations become important [73, 74]. This phenomenon was investigated by Henry [75], who used water-displacement plethysmography to measure changes in the volume of both legs as a function of increments in venous distending pressure. His data for one subject are reproduced in Figure 2-5. It should be recalled that the leg compartment in our model represents the dependent limbs and the pelvic circulation. Figure 2-6 shows the pressure-volume relation of a common iliac vein [76]. Under the assumption that the right and left common, internal, and external iliac veins have the same physical characteristics, the pelvic venous vasculature accommodates roughly one tenth of the venous volume of the legs at physiological transmural pressures, and has about 4% of their vascular compliance. A non-linear model of the venous pressure-volume relation has been implemented assuming a functional relationship



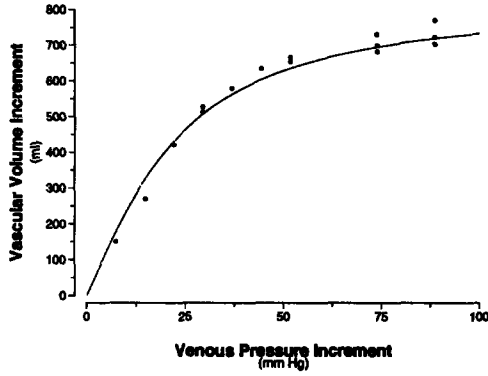


Figure 2-5: Pressure-volume relation of both legs. Data (filled circles) adapted from [75].

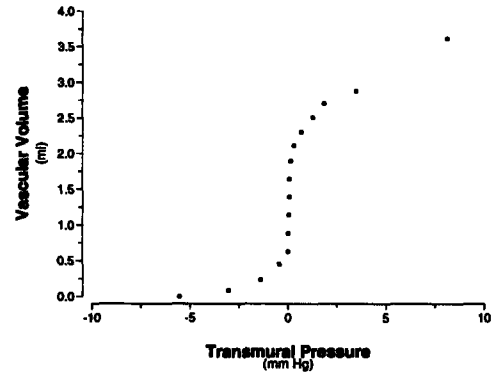


Figure 2-6: Pressure-volume relation of a common iliac vein. Data (filled circles) adapted from [76].

between total vascular volume,  $V_t$ , and transmural pressure,  $\Delta P$ , of the form

$$V_t(\Delta P) = V_0 + \frac{2V_{\max}}{\pi} \cdot \arctan\left(\frac{\pi C_0}{2V_{\max}} \cdot \Delta P\right) \quad \text{for } \Delta P > 0$$

where  $V_{\max}$  denotes the distending volume limit of the lower body compartment,  $C_0$  is the vascular compliance at zero transmural pressure, and  $V_0$  is the venous unstressed volume. Synthesizing the information from Figures 2-5 and 2-6, we assign  $(1200 \pm 100)$  ml to  $V_{\max}$  and  $(20 \pm 3)$  ml/mm Hg to  $C_0$ . The data reviewed by Leggett and Williams [77] suggest a total blood volume of the legs, pelvis, and buttocks of approximately 1112 ml in the supine posture if one assumes that the leg and gluteal muscles make up the majority of skeletal muscle in the human body. Accounting for 160 ml and 36 ml of distending volume for the venous and the arterial vessels, respectively, suggests an unstressed volume of 916 ml of which we assign  $(200 \pm 20)$  ml to the arterial compartment and the remaining  $(716 \pm 50)$  ml to the venous side.

Figure 2-6 can also be used to obtain an estimate of the compliance of the inferior vena cava which is formed by the confluence of the right and the left common iliac veins. Assuming that the physical properties of the inferior vena cava are not significantly different from the ones of the common iliac veins, and combining the data in Figure 2-6 with the morphometric analyses by Macchi and Catini [66], one can estimate the caval compliance per unit length to be  $(0.09 \pm 0.01)$  ml/mm Hg/cm. Combining this value with the length estimates from Table 2.3 yields  $(1.3 \pm 0.1)$  ml/mm Hg,  $(0.5 \pm 0.1)$  ml/mm Hg, and  $(1.3 \pm 0.1)$  ml/mm Hg for the compliances of the abdominal, the thoracic inferior, and the thoracic superior vena cava, respectively. Assuming a central venous pressure of  $(6 \pm 2)$  mm Hg in combination with the compliance of  $(1.8 \pm 0.1)$  ml/mm Hg for the entire inferior vena cava suggests a distending volume of  $(10.8 \pm 3.6)$  ml. The data by Macchi and Catini cited above suggest a total volume of the inferior vena cava of  $(116 \pm 12)$  ml which, in turn, suggests an unstressed volume of  $(53 \pm 13)$  ml or  $(5.5 \pm 0.6)$  ml/cm.

The splanchnic circulation is the most capacious vascular bed and the principal reservoir of blood volume in the entire circulation. Under normal physiological conditions, it is estimated to contain about (20-26)% of total blood volume [77] and to receive about 25% of cardiac output [56]. Animal experiments in dogs suggest a specific splanchnic vascular compliance of  $(1.0 \pm 0.4)$  ml/mm Hg/kg body weight [78]. While it would be fallacious to extrapolate from this value to the human body as the spleen of the dog in particular is a much bigger relative blood reservoir than it is in the human [79], the specific vascular compliance of the dog does provide an upper bound on the venous vascular compliance of the human splanchnic vascular bed. Rowell [80, p. 207] cites a specific vascular compliance of 2.5 ml/mm Hg/kg of tissue weight for the intestines and suggests ten times this value for the liver. Combining these estimates with the dry tissue masses for humans tabulated by Leggett and Williams [77] suggests an average human splanchnic venous compliance of approximately 50 ml/mm Hg. We shall assume a value of  $(50 \pm 7.5)$  ml/mm Hg where the relatively large uncertainty is reflective of the lack of more accurate experiments to refine the estimate. The data compiled by Leggett and Williams [77] also suggest total splanchnic blood volume to be 1880 ml. Assuming an arterial unstressed volume of  $(300 \pm 50)$  ml and a splanchnic venous pressure of 8 mm Hg suggests an unstressed volume of  $(1142 \pm 100)$  ml for the splanchnic venous circulation.

The kidneys are thought to contain  $(2.0 \pm 0.7)$  % of total blood volume or  $(120 \pm 40)$  ml [77]. Assuming arterial renal unstressed volume to be  $(20 \pm 5)$  ml and accounting for another  $(20 \pm 5)$  ml of arterial stressed volume leaves approximately 80 ml of renal venous volume. Assuming a venous vascular compliance of  $(5 \pm 1)$  ml/mm Hg suggests a venous unstressed volume of  $(30 \pm 10)$  ml.

Finally, the circulation of the head, the neck, and the upper limbs constitute the upper body compartment to which we assign  $(18.2 \pm 2.9)$  % of total blood volume, or  $(937 \pm 90)$  ml, based on the percentage estimates tabulated in [77]. The arterial distending volume is approximately  $(38 \pm 8)$  ml. When assuming an arterial unstressed volume of  $(200 \pm 40)$  ml we are left with a total venous volume of approximately  $(700 \pm 50)$  ml. Bleeker and co-workers [81] used occlusion plethysmography to estimate the compliance of the arm veins. Their data suggest a lumped venous compliance of both arms of  $(1.2 \pm 0.2)$  ml/mm Hg and is probably a conservative estimate of the true venous compliance as their measurement of volume is made at single location. We assign a lumped venous compliance of  $(7 \pm 2)$  ml/mm Hg to the upper body compartment which reflects our belief that the large veins in the neck contribute significantly to the capacitance of this compartment. The venous unstressed volume is therefore assigned the value of  $(643 \pm 50)$  ml.

**Resistances** The largest resistance to blood flow occurs at the level of the pre-capillary arterioles within the systemic micro-circulation. We represent these resistive properties by a lumped resistance for each of the four micro-circulatory beds. Minor resistance to blood flow occurs along the systemic arterial and venous circulations.

Based on the data reviewed by Leggett and Williams [56] we assume 22 % (15 % - 29 %) of resting cardiac output to supply the upper body compartment, 21 % (18 % -

Table 2.4: Parameter assignments for systemic microvascular resistances.

		Microcirculation			
		upper body	kidneys	splanchnic	legs
$R$	PRU	$(4.9 \pm 1.7)$	$(5.2 \pm 1.0)$	$(3.3 \pm 1.0)$	$(4.5 \pm 1.8)$

24 %) to perfuse the kidneys, 33 % (24 % – 48 %) to flow through the splanchnic compartment, and 24 % (14 % – 33 %) to represent pelvic and leg blood flow. Assuming a perfusion pressure of  $(87 \pm 10)$  mm Hg and cardiac output of  $(4813 \pm 103)$  ml/min, the respective micro-vascular resistances, where we chose to represent the numerical values in terms of peripheral resistance units,  $\text{PRU} = \text{mm Hg} \cdot \text{s/ml}$ , are  $(4.9 \pm 1.7)$  PRU,  $(5.2 \pm 1.0)$  PRU,  $(3.3 \pm 1.0)$  PRU, and  $(4.5 \pm 1.8)$  PRU for the upper body, renal, splanchnic, and leg compartments, respectively.

The resistances on the venous side can be estimated from the respective flows and observed pressure drops along the venous system. Barratt-Boyes and Wood [60] measured the pressure drop between the inferior vena cava and the right atrium to be  $(0.5 \pm 0.2)$  mm Hg, suggesting a venous flow resistance of  $(0.008 \pm 0.003)$  PRU for the thoracic inferior vena cava compartment and  $(0.019 \pm 0.007)$  PRU for the abdominal vena cava compartment, respectively. The authors report the same pressure drop of  $(0.5 \pm 0.2)$  mm Hg between the superior vena cava and the right atrium, which suggests a value of  $(0.028 \pm 0.014)$  PRU for the flow resistance of the superior vena cava compartment. Arnoldi and Linderholm [82] report venous pressure to drop by  $(2.8 \pm 1.1)$  mm Hg between various locations in the deep veins of the legs and and the right atrium. This suggests a venous resistance of  $(0.05 \pm 0.06)$  PRU for the outflow resistance of the leg compartment. This resistance value is rather small and quite likely a low estimate of the venous outflow resistance. We will assume a slightly

Table 2.5: Parameter assignments for the systemic arterial compartments. Compartment indices are from Figure 2-2.

		Compartment Index							
		1	2	3	6	7	8	10	12
$C$	$\frac{\text{ml}}{\text{mmHg}}$	0.28 $\pm 0.04$	0.13 $\pm 0.02$	0.42 $\pm 0.10$	0.21 $\pm 0.03$	0.10 $\pm 0.01$	0.21 $\pm 0.05$	0.42 $\pm 0.05$	0.42 $\pm 0.10$
$V_0$	ml	21 $\pm 3$	5 $\pm 1$	200 $\pm 40$	16 $\pm 2$	10 $\pm 1$	20 $\pm 5$	300 $\pm 50$	200 $\pm 20$
$R$	PRU	0.007 $\pm 0.002$	0.003 $\pm 0.001$	0.014 $\pm 0.004$	0.011 $\pm 0.003$	0.010 $\pm 0.003$	0.10 $\pm 0.05$	0.07 $\pm 0.04$	0.09 $\pm 0.05$
$h$	cm	10.0	4.5	20.0	16.0	14.5	0.0	10.0	106

Table 2.6: Parameter assignments for the systemic venous compartments. Compartment indices are from Figure 2-2.

		Compartment Index						
		4	5	9	11	13	14	15
$C$	$\frac{\text{ml}}{\text{mmHg}}$	7 $\pm 2$	1.3 $\pm 0.1$	5 $\pm 1$	50 $\pm 7.5$	27 $\pm 3$	1.3 $\pm 0.1$	0.5 $\pm 0.1$
$V_0$	ml	645 $\pm 40$	16 $\pm 4$	30 $\pm 10$	1146 $\pm 100$	716 $\pm 50$	79 $\pm 10$	33 $\pm 4$
$R$	PRU	0.11 $\pm 0.05$	0.028 $\pm 0.014$	0.11 $\pm 0.05$	0.07 $\pm 0.04$	0.10 $\pm 0.05$	0.019 $\pm 0.007$	0.008 $\pm 0.003$
$h$	cm	20.0	14.5	0.0	10.0	106	14.5	6.0

higher value of  $(0.10 \pm 0.06)$  PRU for the outflow resistance of the leg compartment. Similarly, we will assume venous resistances of  $(0.07 \pm 0.04)$  PRU,  $(0.11 \pm 0.06)$  PRU, and  $(0.11 \pm 0.05)$  PRU for the splanchnic, the renal, and the upper body compartment, respectively.

Similarly, the pressure drop in the systemic arterial system does not exceed 2–3 mm Hg between the ascending aorta and the brachial or abdominal arteries [83]. Assuming a reduction in mean arterial pressure of  $(2 \pm 1)$  mm Hg between the ascending aorta and the abdominal aorta suggests an aortic resistance per unit length of  $(7.0 \pm 2.0) \cdot 10^{-4}$  PRU/cm or lumped aortic resistances of  $(0.007 \pm 0.002)$  PRU,  $(0.011 \pm 0.003)$  PRU, and  $(0.010 \pm 0.003)$  PRU for the ascending, the thoracic, and the abdominal aorta compartments, respectively. Similarly, we assign  $(0.003 \pm 0.001)$  PRU and  $(0.014 \pm 0.004)$  PRU for the arterial segments of the brachiocephalic and the upper body compartments. Finally, we assume another pressure drop of  $(2 \pm 1)$  mm Hg to occur between the abdominal aorta and the arterial beds of the kidneys, the splanchnic, and the leg compartments. The remaining three arterial resistances are therefore  $(0.10 \pm 0.05)$  PRU,  $(0.07 \pm 0.04)$  PRU, and  $(0.09 \pm 0.05)$  PRU, respectively. The parameters of the systemic circulation are summarized in Tables 2.4, 2.5, and 2.6.

## 2.2 Cardiac Model

Macroscopically, cyclic changes in the heart’s myocardial elastic properties account for its ability to pump blood from the low pressure systems (pulmonary and systemic veins) to the high pressure systems (systemic and pulmonary arteries). In a series of seminal publications [84–87], Suga measured the time course of the canine instantaneous ventricular pressure-volume ratio and demonstrated that the resultant time-varying elastance waveforms, when properly scaled, reduce to a single, universal curve. The analogy of a time-varying mechanical elastance (or its reciprocal, a time-varying compliance) to a time-varying electric capacitor and the fact that the scaled

waveform assumes a universal shape makes this description of cardiac contraction particularly attractive, and forms the basis of the cardiac model described below.

## 2.2.1 Architecture

Suga's work suggests the cardiac representation shown in Figure 2-7, in which an atrial compartment is coupled to a ventricular compartment. The diodes represent the respective cardiac valves and ensure unidirectional flow. The time-varying pressure source,  $P_{th}$ , represents intrathoracic pressure. To complete the description of cardiac contraction, we have to specify the time course of the atrial and ventricular elastances,  $E^a(t)$  and  $E^v(t)$ , respectively.

Suga normalized the amplitudes of the canine time-varying elastance waveforms by their respective maxima, or end-systolic values,  $E_{es}$ , and scaled the time axis by the time to maximal amplitude,  $T_s$ . Once scaled, the shape of the resultant normalized waveform turned out to be quite independent of heart rate, inotropic state, and the chamber's loading conditions (both preload and afterload) [87]. The same approach has subsequently been used to characterize the elastic properties of the human cardiac chambers. Figure 2-8 shows recent data of the normalized time-varying elastance waveform for human left ventricles [88] along with a functional representation thereof (blue line). The latter is described by Equation 2.2, where we represent the systolic and early diastolic portions of the elastance waveform in terms of appropriately scaled trigonometric functions, though a representation in terms of piecewise linear segments is similarly justified [33, 34]. We assume the time for early diastolic relaxation,  $T_d^r$ , to be one half of the systolic time interval  $T_s$ . This assumption seems well justified by the data presented.

$$\frac{E(t)}{E_{es}} = \begin{cases} \frac{E_d}{E_{es}} + \frac{E_{es}-E_d}{2E_{es}} \cdot \left\{ 1 - \cos\left(\pi \cdot \frac{t}{T_s}\right) \right\} & 0 \leq t \leq T_s \\ \frac{E_d}{E_{es}} + \frac{E_{es}-E_d}{2E_{es}} \cdot \left\{ 1 + \cos\left(2\pi \cdot \frac{t-T_s}{T_s}\right) \right\} & T_s < t \leq \frac{3}{2}T_s \\ \frac{E_d}{E_{es}} & \frac{3}{2}T_s < t \end{cases} \quad (2.2)$$

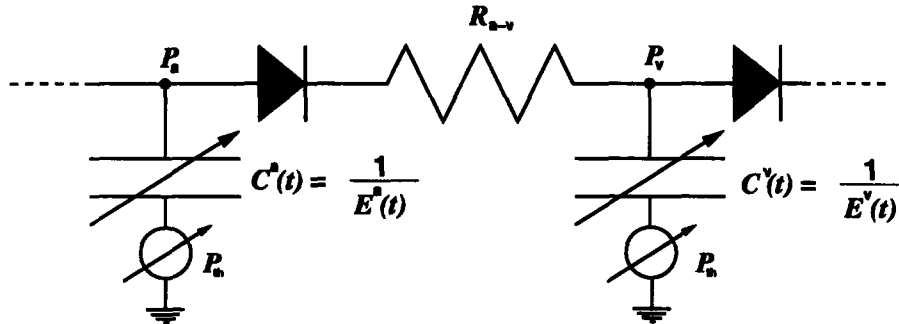


Figure 2-7: Circuit model of atrial and ventricular compartments.  $P_a$  and  $P_v$ : atrial and ventricular pressures;  $P_{th}$ : intrathoracic pressure;  $C^a(t)$  and  $C^v(t)$ : atrial and ventricular capacitances;  $E^a(t)$  and  $E^v(t)$ : atrial and ventricular elastances.  $R_{a-v}$ : atrio-ventricular flow resistance.

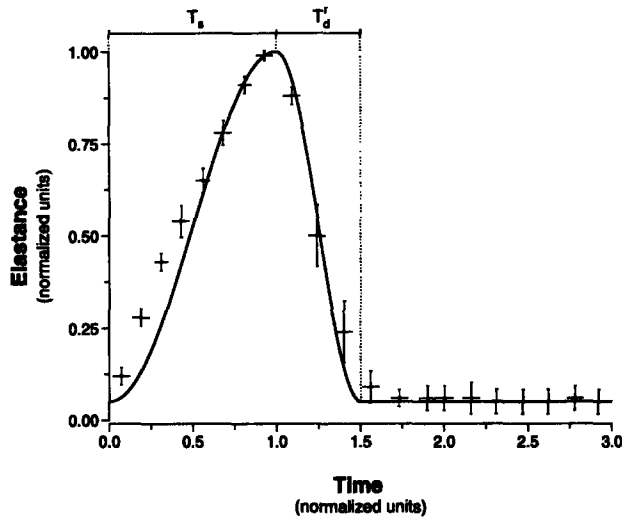


Figure 2-8: Normalized time-varying elastance of the human left ventricle.  $T_s$ : systolic time interval;  $T_d'$ : time interval of diastolic relaxation. Data adapted from [88].

We assumed the shape of the normalized time-varying elastance waveforms to be identical for all four cardiac chambers. The assignment of the respective parameters for each chamber is discussed in detail in the following section.

## 2.2.2 Parameter Assignments

The time-varying elastance model described above requires that end-systolic elastance,  $E_{es}$ , and diastolic elastance,  $E_d$ , be assigned for each cardiac chamber, along with rules that specify the fraction of the cardiac cycle spent in atrial and ventricular systole. As indicated in Figure 2-9, the determination of the end-systolic elastance necessitates simultaneous beat-by-beat measurements of chamber pressures and volumes under various loading conditions, and subsequent regression analysis of the resulting diastolic and end-systolic pressure-volume relations. While pressure measurements can be made routinely with high fidelity, the methods currently in use for assessing chamber volumes throughout the cardiac cycle are frequently based on simplifying geometric assumptions and continue to be a source of significant uncertainties.

The most extensively studied chamber is the left ventricle. Using a conductance catheter approach for volume determination and transient inferior vena caval balloon obstruction to alter preload, Senzaki and co-workers [88] reported left ventricular end-systolic elastance in fifteen subjects to be  $E_{es}^{lv} = (2.0 \pm 0.7)$  mmHg/ml. Assuming a mean body surface area of  $1.9 \text{ m}^2$ , Senzaki's results seem congruent with earlier estimates by McKay [89] ( $E_{es}^{lv} = (2.5 \pm 0.6)$  mmHg/ml) and Grossman [90] ( $E_{es}^{lv} = (2.8 \pm 0.8)$  mmHg/ml) who used gated blood pool radionuclide ventriculography and biplane contrast cineangiography, respectively, to determine ventricular volume, and who chose to reference their respective results to the body size of their patient populations. In contrast, using biplane contrast cineangiography Starling [91]

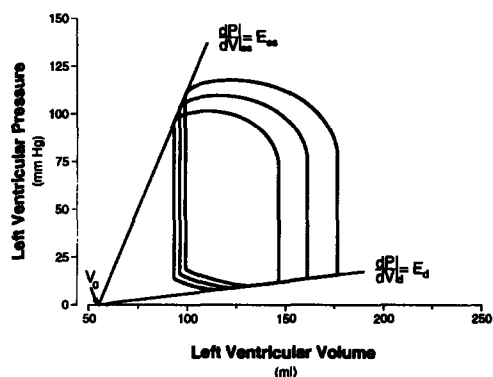


Figure 2-9: Simulated left ventricular pressure-volume loops.  $E_{es}$ : end-systolic elastance;  $E_d$ : diastolic elastance;  $V_0$ : unstressed volume.

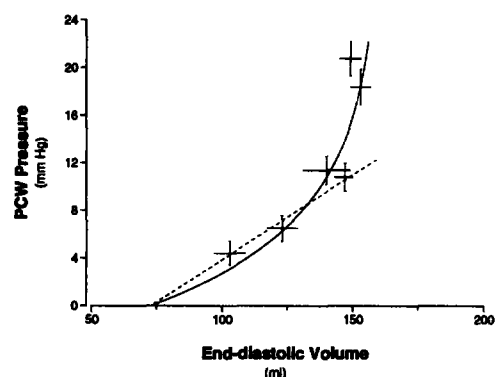


Figure 2-10: Left ventricular end-diastolic pressure-volume relation. PCW pressure: pulmonary capillary wedge pressure. Data adopted from Perhonen et al. [43]

reported a significantly higher value ( $E_{es}^{lv} = (5.5 \pm 1.2) \text{ mm Hg/ml}$ ) in ten subjects. We chose to adopt McKay's results for  $E_{es}^{lv}$ .

Although the diastolic elastic properties of the ventricles are fairly linear over the range of normal filling pressures, they do exhibit a marked non-linearity when filled to capacity, as illustrated in Figure 2-10. Since filling pressures decrease with increasing gravitational stress, it is admissible to represent the diastolic pressure-volume relations of the various cardiac chambers by linear relations as indicated by the dashed line in the same figure. Information provided by Senzaki [88] and Starling [91] allows for computation of left ventricular diastolic elastance values of  $E_d^{lv} \approx (0.13 \pm 0.05) \text{ mm Hg/ml}$  and  $E_d^{lv} \approx (0.10 \pm 0.06) \text{ mm Hg/ml}$ , respectively. Similarly, the data presented by Perhonen and co-workers [43] suggest  $E_d^{lv} \approx (0.13 \pm 0.02) \text{ mm Hg/ml}$ . We chose to adopt this latter value for our simulations.

The right ventricle has been studied less extensively, mostly because of its more complex geometry. Using biplanar contrast cineangiography, Dell'Italia and co-workers [92] report right ventricular end-systolic elastance to be  $E_{es}^{rv} = (1.3 \pm 0.8) \text{ mm Hg/ml}$  with a range of  $(0.62 - 2.87) \text{ mm Hg/ml}$ . Using their estimate of right ventricular unstressed volume ( $V_0^{rv} = (46 \pm 21) \text{ ml}$ ) and their reported values for end-diastolic pressures and volumes, the diastolic right ventricular elastance equates to  $E_d^{rv} \approx (0.07 \pm 0.03) \text{ mm Hg/ml}$  with a range of  $(0.02 - 0.09) \text{ mm Hg/ml}$ .

Even less quantitative information is available for the atria. Dernellis and co-workers [93] performed echocardiographic and hemodynamic studies on the human left atrium. They report an end-systolic elastance of  $E_{es}^{la} = (0.61 \pm 0.07) \text{ mm Hg/ml}$ , a diastolic elastance of  $E_d^{la} = (0.50 \pm 0.10) \text{ mm Hg/ml}$ , and a left atrial unstressed volume of  $V_0 = (3.15 \pm 0.42) \text{ ml}$ . While a relatively small ratio of end-systolic to diastolic elastance has been a consistent finding in canine experiments [94], the ratio suggested by Dernellis' data is quite low. Furthermore, it seems that the value he derived for the unstressed volume is particularly low as well. In the absence of further experiments

Table 2.7: Cardiac Model Parameters.

		Right Heart		Left Heart	
		Atrium	Ventricle	Atrium	Ventricle
$E_{es}$	$\frac{\text{mmHg}}{\text{ml}}$	$(0.74 \pm 0.1)$	$(1.3 \pm 0.8)$	$(0.61 \pm 0.07)$	$(2.5 \pm 0.6)$
$E_d$	$\frac{\text{mmHg}}{\text{ml}}$	$(0.30 \pm 0.05)$	$(0.07 \pm 0.03)$	$(0.50 \pm 0.10)$	$(0.13 \pm 0.02)$
$V_0$	ml	$(14 \pm 1)$	$(46 \pm 21)$	$(24 \pm 13)$	$(55 \pm 10)$
$R_{a-v}$	PRU	$(0.005 \pm 0.001)$		$(0.010 \pm 0.001)$	

on humans, one is forced to direct one's attention to detailed animal experiments. Mindful of the difficulties involved and the uncertainties introduced by such an approach, one can derive scaling factors that extrapolate results obtained in different animal models to human physiology. If one compares the right ventricular data presented by Dell'Italia in humans with the ones presented by Schwiep and colleagues [95] for mongrel dogs, one can introduce a scaling factor of 3.5 that relates the respective end-systolic and end-diastolic volumes. When scaled by this factor, Schwiep's canine end-systolic ventricular elastance translates to 1.2 mm Hg/ml which compares favorably with Dell'Italia's  $E_d^{rv} \approx (1.3 \pm 0.8)$  mm Hg/ml. Applying the same scaling factor to the left atrial data presented by Alexander [94] yields an end-systolic elastance of  $(0.52 \pm 0.11)$  mm Hg/ml, a diastolic elastance of 0.4 mm Hg/ml, and an unstressed volume of  $(24 \pm 13)$  ml. The elastance values so derived are in approximate agreement with the results reported by Dernellis. The extrapolated unstressed volume seems more appropriate for a human and will therefore be used in our model. When the same scaling factor is applied to the right atrial data reported by Lau and colleagues [96] one derives an end-systolic elastance of  $E_{es}^{ra} = (0.74 \pm 0.1)$  mm Hg/ml, a diastolic elastance of  $E_d^{ra} = (0.30 \pm 0.05)$  mm Hg/ml, and an unstressed volume of  $V_0^{ra} = (14 \pm 1)$  ml.

Barratt-Boyes and Wood [60] used right-heart catheter withdrawal maneuvers to investigate the pressure drop across the tricuspid valve during right ventricular filling. The investigators found no significant difference between maximal atrial systolic pressure (atrial a-wave) and right ventricular end-diastolic pressure. There was also no statistically significant difference between minimal right atrial pressure and initial diastolic right ventricular pressure. We attribute these findings to a very small tricuspid flow resistance and assign the value of  $(0.005 \pm 0.001)$  PRU to the atrio-ventricular resistance of the right heart. The data presented by Firstenberg and colleagues [97] suggest an average trans-mitral pressure gradient during diastole of approximately 1 mm Hg. Combining this estimate with their data of heart rate and cardiac output, we can estimate the mitral flow resistance to be  $(0.010 \pm 0.001)$  PRU. The physical parameters of the cardiac model are summarized in Table 2.7.

To finalize the time-varying elastance description of the cardiac cycle, we need to specify the delay between the onsets of atrial and ventricular contraction,  $T_{a-v}$ .



Table 2.8: Mean values and ranges of cardiac timing parameters  $K$ .

		$T_S^a$	$T_S^v$	$T_{a-v}$
mean	s	0.25	0.37	0.19
range	s	0.2 – 0.3	0.34 – 0.39	0.18 – 0.20

Furthermore, we need to assign rules that specify the duration of atrial,  $T_S^a$ , and ventricular,  $T_S^v$ , systole relative to the length of the cardiac cycle. In a strict sense, this timing information can only be derived from the relative timing of mechanical events visualized in the pressure-volume loop, such as the onsets of isovolumic contraction or relaxation. Unfortunately, these mechanical events do not correspond to precise or readily identifiable points on conventionally recorded signals, such as pressure tracings or the electrocardiogram (ECG). However, if one neglects differences in relative timing between electrophysiological and mechanical events due to the mechanisms of excitation-contraction coupling, one can approximate the desired timing information with the help of the surface ECG.

The delay between the onsets of atrial and ventricular contraction can be readily approximated by the P-R-interval, the time interval between the onsets of atrial and ventricular depolarization. At resting heart rates the P-R-interval is normally on the order of 180 – 200 ms. The ventricular systolic time interval can be approximated by the Q-T-interval, the interval between the onset of ventricular depolarization and the end of ventricular repolarization. In 1920, Bazett [98] reported an empirical formula for the Q-T-interval that today bears his name. He established that the Q-T-interval scales with R-R-interval length,  $T_{RR}$ , according to  $K \cdot \sqrt{T_{RR}}$  where the constant  $K$  ranges from (342 – 392) ms. Atrial repolarization occurs during ventricular depolarization and is therefore masked by the QRS complex in the surface ECG. The atrial systolic time interval can, however, be approximated by a value slightly larger than the P-R-interval. We will assume that the P-R-interval and the atrial systolic time interval also scale with the square root of the R-R-interval. Finally, we assign a value (895±125) ms and the range of (667–1300) ms to the R-R-interval [62]. Table 2.8 summarizes the timing information.

### 2.2.3 Limitations

The cardiac contraction model described so far is based on several simplifying assumptions that should not go unmentioned. We have already alluded to the non-linearity of the diastolic pressure-volume relation and justified its linearization for the scope of this work. Similarly, at very high transmural pressures the end-systolic pressure volume relation will also begin to show a significant deviation from its assumed linearity. Again, the simulation of pathologically high pressures is beyond the scope of the work presented here. However, two assumptions do pertain to our work. First, as suggested by Figure 2-9, we assume unstressed volume to be static throughout the cardiac cy-

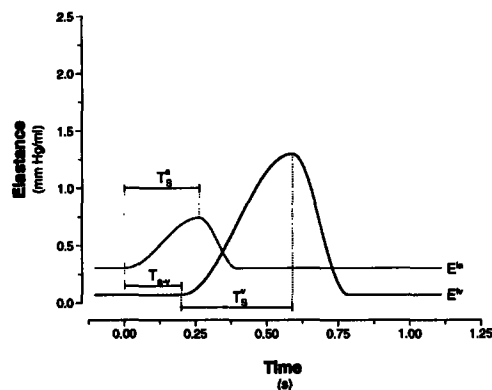
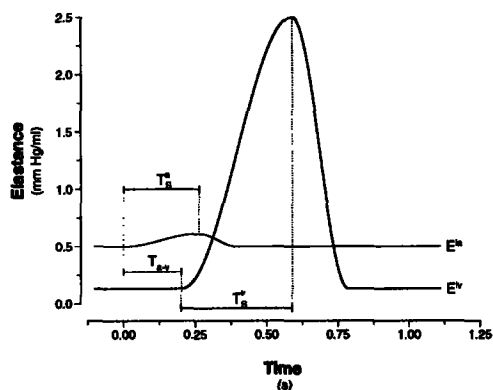


Figure 2-11: Left ventricular,  $E^{lv}$  (blue) , and left atrial,  $E^{la}$  (red), elastances.

Figure 2-12: Right ventricular,  $E^{lv}$  (blue), and right atrial,  $E^{la}$  (red), elastances.

cle, that is, the volume intercept as determined by the end-systolic pressure-volume relation is the same as the one derived from the diastolic pressure-volume relation. Animal experiments have shown consistently that the unstressed volume at the end of systole is 25% – 40% lower than the diastolic unstressed volume [94, 96] indicating a small but potentially significant contribution to stroke volume. We can account for this effect quantitatively by slightly decreasing the diastolic elastances of the various chambers so that end-diastolic volumes, and thus stroke volumes, are slightly higher for given end-diastolic pressures. Second, the time-varying elastance model described so far assumes that the progression from the diastolic pressure-volume relation to the end-systolic pressure-volume relation is independent of the details of the intervening ejection phase and of the chamber’s loading conditions. Sagawa [99] reviews experimental evidence against this assumption and proposes modifications to the simple time-varying elastance model. The modified “elastance-resistance” model mostly affects the detailed shape of the time-varying elastance and is therefore of importance for correct reproduction of the cardiac and arterial pressure waveform morphologies [100]. Given the relative insensitivity of the end-systolic pressure-volume relation<sup>1</sup> [99], we assume this modification to be of higher (and therefore negligible) order for determination of beat-to-beat stroke volume which is most crucial to our analysis here.

As previously mentioned, simultaneous measurements of cardiac pressures and volumes are needed to determine cardiac elastance parameters. In concluding this section, it is worthwhile to comment on the experimental difficulty involved and possible bias introduced in conducting such studies in humans. Advances in catheter technology enabled cardiac chamber pressures to be measured with a remarkable degree of accuracy. The highly invasive nature of these measurements, however, usually allows for their employment in the left heart only when medically necessary. Having to restrict the study population to those patients in whom cardiac catheterization

<sup>1</sup>It is important to point out that the ventricular end-systolic pressure-volume relations change significantly under inotropic stimulation. Reflex control is the topic of the next chapter.

is medically indicated introduces significant selection bias, not least in terms of age and gender, such that the results derived are not necessarily reflective of the population at large. The same holds true for volume measurements that are based on catheterization, such as cineangiography or conductance catheter approaches, or the administration of radionuclides, such as radioisotope imaging. In contrast to pressure measurements, volumetric assessment of the various cardiac chambers can at best be described as approximate. Several techniques currently in use, such as cineangiography and biplanar echocardiography, rely on simplifying geometric assumptions that might hold true to some degree for the left ventricle. The other cardiac chambers have significantly more complex geometries which render simple approximations more questionable. Most methods to determine cardiac chamber volumes have been demonstrated to correlate favorably with each other. In the absence of an overall gold standard, however, these correlations do not reveal systematic errors that are bound to be present. Magnetic resonance imaging (MRI) and, more recently, four-dimensional (space and time) phased-array ultrasound imaging are modalities free of geometric assumptions having the potential of becoming the much-needed gold standards. At this point, however, volume measurement by MRI is still limited by relatively long acquisition times ( $\approx 10$  minutes for one average cardiac cycle) and 4-d ultrasound imaging is an emerging technology that still seems in its validation phase [101].

## 2.3 Pulmonary Circulation

The pulmonary circulation is characterized by low resistance and high compliance in order to accommodate, at low pressures, the same flow per unit time as the entire systemic circulation. Local pulmonary blood flow and volume are therefore exquisitely sensitive to even small variations in perfusion or transmural pressures that naturally occur with changes in hydrostatic pressure components. The pulmonary capillary vasculature, in particular, can exhibit interesting nonlinear flow phenomena, such as flow limitation and complete cessation of flow during vascular collapse, as a result of changes in luminal or extra-luminal pressures.

Below, we describe the architecture and parameter assignments for the pulmonary vascular model with specific emphasis on representing a gravity-dependent nonlinear pulmonary pressure-flow relation.

As indicated in Figure 2-13, we represent the pulmonary circulation by passive pulmonary arterial and venous capacitances,  $C_{pa}$  and  $C_{pv}$ , and a nonlinear pulmonary microvascular resistance,  $R_p$ . Central to the model of the flow-dependent resistance to be developed below is the understanding of the behavior of a Starling resistor [102] shown in Figure 2-14, modeling the flow-characteristics of a pulmonary capillary. The experimental set-up involves a pressurizable chamber with rigid inlets and outlets between which a thin-walled, collapsible tube is fastened. Brower and Noordergraaf [103] noted that the steady-state behavior of the Starling resistor can be described by one dependent and two independent variables. The former is usually taken to be the

volumetric flow rate,  $q$ . The latter are expressed in terms of two of the three possible pressure differences ( $P_1 - P_e$ ,  $P_2 - P_e$ , and  $P_1 - P_2$ ) involving the inlet pressure,  $P_1$ , the outlet pressure,  $P_2$ , and the external pressure  $P_e$ . In the following, we assume an idealized Starling resistor model in which the tube is assumed in one of two states: either completely collapsed, presenting infinite flow resistance and therefore denying flow; or conducting with flow resistance  $R$ . The behavior of the steady-state flow separates into three domains, depending on the values of the independent variables:

$$q(P_1 - P_e, P_2 - P_e) = \begin{cases} 0 & \text{if } P_1 - P_e < 0 \text{ and } P_2 - P_e < 0 \text{ (Zone I)} \\ \frac{P_1 - P_e}{R} & \text{if } P_1 - P_e > 0 \text{ and } P_2 - P_e < 0 \text{ (Zone II)} \\ \frac{P_1 - P_2}{R} & \text{if } P_1 - P_e > 0 \text{ and } P_2 - P_e > 0 \text{ (Zone III)} \end{cases}$$

where we have borrowed the designation of zones from the physiology literature [104]. In Zone I, flow ceases as the external pressure exceeds both the inlet and outlet pressures and the tube is in a state of collapse. Flow in Zone III is purely driven by the pressure difference between inlet and outlet pressures; changes in external pressure are inconsequential. Finally, flow in Zone II has been termed “vascular waterfall” [105] as changes in the outlet pressure  $P_2$  fail to influence flow rate. A detailed analysis of flow in Zone II is quite intricate and involves models of the structural mechanics of the tube itself [105–107].

The single Starling resistor just described models the behavior of a pulmonary capillary whose external pressure is alveolar pressure  $P_{alv}$  and whose inlet and outlet pressures depend on its location in the gravitational field. To derive the macroscopic pressure-flow relation for the entire lung under the influence of gravity at different tilt angles, we extended a previously proposed model for pulmonary blood flow in the upright posture [108].

We model the pulmonary microvasculature as a series of parallel Starling resistors that are homogeneously distributed over the length  $L$  of the entire lung. The differential vascular conductance of a section of lung tissue of thickness  $dl$  is therefore given by  $dl/(L \cdot R_p)$  where  $R_p$  is the macroscopic pulmonary resistance assuming every capillary behaves like a Zone III-Starling resistor. The differential flow rate,  $dq(l)$ , a

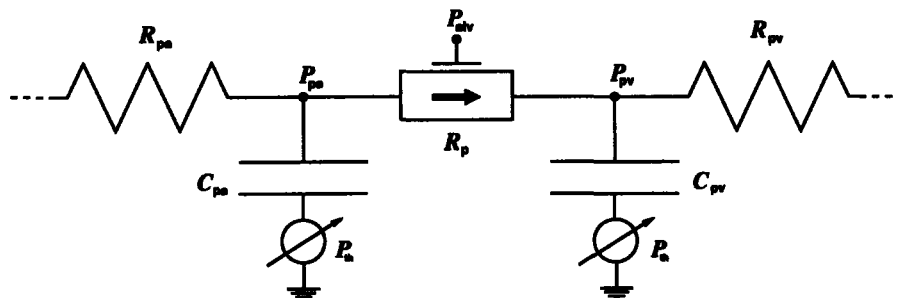


Figure 2-13: Circuit model of the pulmonary vasculature.  $P_{pa}$ : pulmonary artery pressure;  $P_{pv}$ : pulmonary venous pressure;  $P_{th}$ : intra-thoracic pressure;  $P_{alv}$ : alveolar pressure;  $C_{pa}$ : pulmonary arterial compliance;  $C_{pv}$ : pulmonary venous compliance;  $R_p$ : pulmonary microvascular resistance.

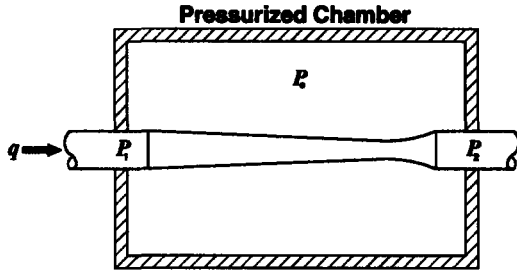


Figure 2-14: Starling resistor.  $P_1$ : inlet pressure;  $P_2$ : outlet pressure;  $P_e$ : external pressure;  $q$ : flow rate. Figure adapted from [107].

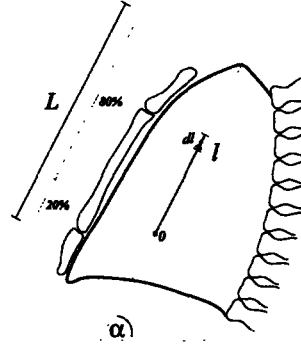


Figure 2-15: Schematic lateral view of the lung.  $L$ : apex-to-base length of the lung;  $l$ : distance from left atrium;  $dl$ : differential length element;  $\alpha$ : tilt angle.

distance  $l$  from the level of the main pulmonary artery and vein, is given by:

$$dq(l) = \begin{cases} 0 & \text{if } P_{pa} - \rho g l \sin(\alpha) - P_{alv} < 0 \\ & \text{and } P_{pv} - \rho g l \sin(\alpha) - P_{alv} < 0 \\ \frac{P_{pa} - \rho g l \sin(\alpha) - P_{alv}}{LR_p} dl & \text{if } P_{pa} - \rho g l \sin(\alpha) - P_{alv} > 0 \\ & \text{and } P_{pv} - \rho g l \sin(\alpha) - P_{alv} < 0 \\ \frac{P_{pa} - P_{pv}}{LR_p} dl & \text{if } P_{pa} - \rho g l \sin(\alpha) - P_{alv} > 0 \\ & \text{and } P_{pv} - \rho g l \sin(\alpha) - P_{alv} > 0 \end{cases}$$

Lewis and Christianson [109] estimated the basal-to-apical length of the lung in fifteen subjects and determined a mean value of  $L = 23.6$  cm with 19.3 cm residing above the level of the left atrium (see Figure 2-15). Assuming, therefore, that 20 % of the lung parenchyma is located below the level of the main pulmonary artery and vein, we can integrate the differential flow to obtain the macroscopic pulmonary pressure-flow relation:

$$\begin{aligned} q &= \int_{-L/5}^{4L/5} dq(l) = \int_{-L/5}^{l_1} \frac{P_{pa} - P_{pv}}{LR_p} dl + \int_{l_1}^{l_2} \frac{P_{pa} - \rho g l \sin(\alpha) - P_{alv}}{LR_p} dl \\ &= \frac{P_{pa} - P_{pv}}{LR_p} \cdot \left( l_1 + \frac{L}{5} \right) + \frac{P_{pa} - P_{alv}}{LR_p} \cdot (l_2 - l_1) - \frac{\rho g}{2LR_p} \cdot \sin(\alpha) \cdot (l_2^2 - l_1^2) \end{aligned}$$

$l_1$  and  $l_2$  specify the boundaries between Zones II and III and Zones I and II, respectively, and are implicitly defined through:

$$\rho g l_1 \sin(\alpha) = P_{pv} - P_{alv} \quad \text{and} \quad \rho g l_2 \sin(\alpha) = P_{pa} - P_{alv},$$

subject to the constraint  $-L/5 \leq l_1, l_2 \leq 4L/5$ . To determine the nominal value of

the macroscopic pulmonary vascular resistance  $R_p$ , we pooled data from four studies [110–113] to arrive at a reasonable sample size (27 subjects) for control subjects without cardiovascular or pulmonary pathologies. The resultant value is  $(0.07 \pm 0.04)$  mm Hg · s/ml with a range of  $(0.01–0.16)$  mm Hg · s/ml. Since we currently do not model respiratory variation in intra-thoracic or alveolar pressure, we assume mean alveolar pressure to equal atmospheric pressure [114, p. 433].

To finalize the description of the pulmonary model, we have to supply nominal values for the pulmonary arterial and venous compliances and unstressed volumes. Using a Windkessel model to represent the pulmonary arterial compartment, Reuben [113] and Milnor and co-workers [112] have estimated the lumped pulmonary arterial compliance from the diastolic decay of pulmonary arterial waveforms. When one's attention is restricted to the pulmonary normotensive group in Reuben's study population, his data suggest a pulmonary arterial compliance of  $(3.0 \pm 0.6)$  ml/mm Hg. Milnor's estimate of  $(3.4 \pm 1.8)$  ml/mm Hg is based on a group of eight patients with normal pulmonary vascular resistance but elevated mean pulmonary artery pressures. These two estimates are compatible with the widely-used value of 4.3 ml/mm Hg quoted by Beneken and DeWitt [115, p. 19] but certainly too low if one were to believe Guyton [114, p. 445] who suggests a pulmonary arterial capacitance of 7 ml/mm Hg. Guyton's suggestion that the latter value is similar to the compliance of the entire systemic arterial tree seems a gross overestimation based on the data presented in Section 2.1.

The determination of pulmonary venous compliance in vivo is quite difficult and usually laden with assumptions that render experimental results rough estimates of the truth. In two publications, Hirakawa [116, 117] developed an empirical formula to relate the rise in pulmonary capillary wedge pressure during ventricular systole to a change in the combined pulmonary venous and left atrial volume. His estimates from two studies, when scaled to a 75-kg male subject, equate to  $(9.8 \pm 4.0)$  ml/mm Hg [117] and  $(9.0 \pm 3.7)$  ml/mm Hg [118]. When accounting for the diastolic compliance of the left atrium, these values are compatible with 8.5 ml/mm Hg quoted by Beneken and DeWitt [115] for the pulmonary venous compliance.

Historically, estimates of pulmonary blood volume have ranged from 9% [114, p. 445] to over 20% [119] of total blood volume. Leggett and Williams [77] reviewed 23 studies of pulmonary blood volume and suggest a reference value of  $(12.5 \pm 2.5)$ %. Burton [120, p. 64] determined, in a single subject, pulmonary arterial blood volume to account for 30% of total pulmonary blood volume. This value agrees with data tabulated by Milnor [121]. With these numbers and assuming a mean pulmonary artery pressure of 16 mm Hg, we can estimate the zero pressure filling volume of the pulmonary artery to be approximately  $(160 \pm 20)$  ml for a 75-kg male subject. Analogously, the venous zero pressure filling volume equates to  $(430 \pm 50)$  ml, assuming a mean pulmonary venous pressure of 9 mm Hg.

Barratt-Boyes and Wood [60] measured the pressure gradient across the pulmonic valve during catheter withdrawal in 21 healthy subjects to be  $(2.0 \pm 0.3)$  mm Hg. One can arrive at an upper bound for the inflow resistance,  $R_{pa}$ , to the pulmonary arterial compartment by assuming that the entire stroke volume is ejected over the systolic

Table 2.9: Nominal parameter values for the pulmonary circulation.

		Pulmonary	
		Arteries	Veins
$C$	$\frac{\text{ml}}{\text{mmHg}}$	$(3.4 \pm 1.8)$	$(9.0 \pm 3.7)$
$V_0$	ml	$(160 \pm 20)$	$(430 \pm 50)$
$R$	PRU	$(0.006 \pm 0.003)$	$(0.006 \pm 0.003)$

time interval  $T_s$ , which leads to a value of  $R_{pa} \lesssim (0.006 \pm 0.003)$  PRU. This value is an upper estimate since the ejection period is smaller than the systolic time interval. Similar data is not available for the pulmonary venous outflow resistance,  $R_{pv}$ . We will simply assume a similarly low value.

Finally, we adopt Daly and Bondurant’s estimate of  $(-3.0 \pm 0.5)$  mm Hg for intra-thoracic pressure [122].

## 2.4 Orthostatic Stress Simulations

The transition from the supine to the upright posture constitutes a significant challenge to the cardiovascular system, as gravity induces a primary, rapid intravascular fluid shift from the thoracic to the dependent vasculature and a consequent secondary, slow fluid shift from the intravascular to the interstitial fluid compartment. Both fluid shifts act in concert to provoke a state of central hypovolemia that elicits a sequence of reflex responses to counteract a reduction in arterial pressure and central blood volume. Artificial orthostatic stress tests such as lower body negative pressure interventions or short radius centrifugation are designed to induce similar perturbations in cardiovascular homeostasis.

In the following sections, we introduce three commonly used orthostatic stress tests and outline how the primary and secondary fluid shifts have been represented for each.

### 2.4.1 Tilt Table Simulation

Tolerance to gravitational stress is commonly assessed clinically by passively tilting subjects to the head-up position while heart rate and arterial blood pressure are being monitored. As opposed to standing up, passive tilts aim to minimize hemodynamic effects associated with muscle contraction of the lower extremities and the abdominal wall. As described in the remainder of this section, the effects of tilting will be represented by changes in hydrostatic pressure components, changes in intra-thoracic pressure, and changes in total blood volume.

During the transition to the head-up posture, the major vascular segments gradually become aligned with the direction of the gravitational field and, therefore, hydro-

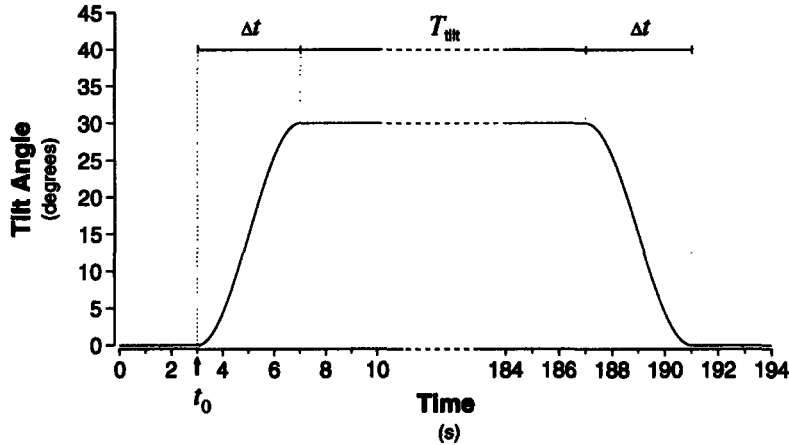


Figure 2-16: Tilt angle  $\alpha(t)$  during a rapid tilt to (left) and from (right) 30° head-up.  $t_0$ : time of tilt onset;  $\Delta t$ : tilt time;  $T_{\text{tilt}}$ : time in head-up position.

static pressure components become significant determinants of blood flow and blood volume distribution. As alluded to in Section 2.1, each vascular segment modeled has the provision for specifying a hydrostatic pressure component,  $P_h$ , which is given by

$$P_h = \rho g h \cdot \sin(\alpha(t)) \quad (2.3)$$

where  $\rho$  is the density of blood, and, in the context of gravitational stress on earth,  $g$  is earth's gravitational acceleration;  $h$  is the effective length of the vascular compartment under consideration and the angle  $\alpha(t)$  represents the orientation of the particular vessel segment with respect to the horizontal plane. It is the changes in  $P_h$  that are responsible for the rapid intravascular volume redistribution at the beginning of gravitational stress.

For a passive head-up tilt to a maximal angle  $\alpha_{\text{max}}$  over a time interval of length  $\Delta t$ , we assume the time course of  $\alpha(t)$  to be

$$\alpha(t) = \begin{cases} 0 & \text{for } t < t_0 \\ \alpha_{\text{max}} \cdot \frac{1}{2} \cdot \left(1 - \cos\left(\pi \frac{t-t_0}{\Delta t}\right)\right) & \text{for } t_0 \leq t \leq t_0 + \Delta t \\ \alpha_{\text{max}} & \text{for } t > t_0 + \Delta t \end{cases} \quad (2.4)$$

where it is implicitly assumed that all vessels are aligned in the horizontal plane in the supine position and that the change in posture is initiated at some arbitrary time point  $t_0$ . The transition from the head-up to the supine posture can be modeled in analogy to the approach outlined above as illustrated in Figure 2-16. We termed  $h$  the *effective* length of the vascular compartment under consideration to distinguish it from the anatomical length of the vascular segments each compartment represents. The latter have been discussed in Section 2.1 and tabulated in Tables 2.2 and 2.3.



The distinction is important as each compartment is a lumped representation of the aggregate function of various anatomical structures, and in order to simulate representative pressures, volumes and flows,  $h$  has to represent the effective hydrostatic height of each lumped compartment. We assume  $h$  to be one half of the superior-to-inferior extension of the anatomical structures comprised in each compartment.

In addition to changes in the luminal pressures described by  $P_h$ , Mead and Gaensler [123] and Ferris and co-workers [124] showed that intra-thoracic pressure,  $P_{th}$ , changed over similarly short periods of time in response to gravitational stress. Mead and Gaensler reported intra-thoracic pressure to drop by  $(3.1 \pm 1.0)$  mm Hg in response to sitting up from the supine position. Ferris demonstrated a drop of  $(3.5 \pm 0.7)$  mm Hg in response to head-up tilts to  $90^\circ$ . We implemented these changes in intra-thoracic pressure by assuming a time course similar to the one described by Equation 2.4.

Changes in the hydrostatic pressure components in the circulation affect the balance between hydrostatic and oncotic pressure gradients across capillary walls that govern transcapillary fluid exchange. During orthostatic stress, transcapillary hydrostatic pressure gradients change, depending on the nature of the stress and the location of the capillary bed. However, the net effect of orthostatic stress is an increase in transcapillary fluid flow and a resultant decrease in intravascular volume. Several studies have been devoted to identifying the magnitude and the time course of plasma volume reduction upon assumption of the upright posture, or plasma volume restitution upon resumption of the supine position (see, e.g., [125] and the references therein). While Tarazi and co-workers [126] report a modest decline in plasma volume of only  $(4.1 \pm 0.8)\%$  over a 20-minute period of  $50^\circ$  head-up tilt, Hinghofer-Szalkay and Moser [127] report plasma volume to drop by as much as  $16.8\%$  in response to a  $70^\circ$  head-up tilt. This difference cannot be explained solely on the basis of the difference in gravitational stress. During quiet standing, the data presented by Jacob et al. [36] suggest a reduction in plasma volume by  $12.8\%$  whereas Hagan and co-workers [128] demonstrate a reduction by  $16.2\%$ . A similar discrepancy emerges when looking at the time constants of plasma volume reduction. Tarazi's data suggest a time constant of  $(12.2 \pm 0.3)$  min whereas Hagan reports a time constant of 7.8 min. The data presented by Jacob suggest much faster dynamics with a time constant of 4.0 min. Despite these substantial differences in the rate and magnitude of volume reduction, it is a consistent finding that the data within each study are described well by mono-exponential models. While some of the discrepancies described above might be attributable to the relatively small number of subjects ( $n \lesssim 10$ ) enrolled in each study, Lundvall and Bjerkhoel [129] have identified the location of blood sampling as a major source of systematic error. In a series of publications, these authors presented a careful analysis of the effects of venous and arterial sampling in the upright posture and devised a novel method to estimate more accurately plasma volume changes during standing [125, 129–132]. The authors report a substantial degree of plasma volume reduction,  $(17.7 \pm 0.8)\%$  or  $(707 \pm 41)$  ml, over a relatively short period of time,  $\tau = (4.6 \pm 0.4)$  min, in response to an  $85^\circ$  head-up tilt [125] as shown in Figure 2-17. In a subsequent publication from the same laboratory, the authors compare commonly used indices of plasma volume changes and surmise that their own previ-

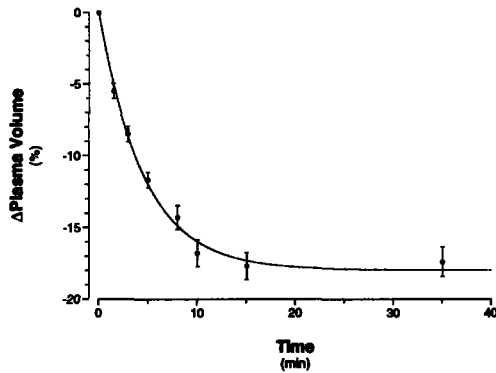


Figure 2-17: Percent change in plasma volume during 85° HUT. Data adapted from [125]; solid line represents best-fit exponential model.

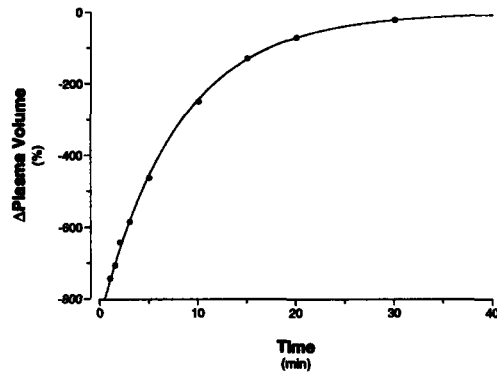


Figure 2-18: Absolute change in plasma volume upon return to supine posture. Data adapted from [132]; solid line represents best-fit exponential model.

ously reported results might have been subject to systematic underestimation of the true changes in plasma volume [133]. Their claim that prolonged ( $\approx 15$  min) standing can lead to a reduction in plasma volume of as much as 25% is a conjecture they have yet to prove. For lack of population averaged data of plasma volume restitution upon resumption of the supine position, Figure 2-18 shows the restitution dynamics in one subject as reported by the same group of investigators.

The literature reviewed above indicates that the reduction in plasma volume is significant even over short periods of orthostatic stress and has to be taken into account when modeling cardiovascular adaptation to gravitational challenge. The mono-exponential nature of plasma volume reduction and restitution suggests a phenomenological description of transcapillary fluid flow in terms of a single RC compartment, as shown in Figure 2-19. While one could easily incorporate an interstitial fluid space into the mathematical description of the hemodynamic model, such an approach would add two parameters per compartment and would unnecessarily increase computational complexity. The approach taken here is to obtain analytical solutions for the transcapillary flow and the interstitial volume, assuming the model in Figure 2-19 and a simplified hydrostatic pressure profile, such as the one shown in Figure 2-20. Once known, one can subtract transcapillary flow from venous return at designated, dependent circulatory compartments, which basically amounts to reducing overall blood volume as a function of time during gravitational stress. Conversely, once gravitational stress is released, transcapillary flow reverses direction and can be added to venous return to account for plasma and blood volume restitution.

Below, we give the analytical solutions for the transcapillary flow  $q$  and the interstitial fluid volume  $V = P_i C$  for the four regions indicated in Figure 2-20. The solutions depend on two parameters, the time constant  $\tau = RC$  and the maximal volume  $V_{\max} = P_h C$ . The numerical values of both depend on the nature of the stress to be modeled.

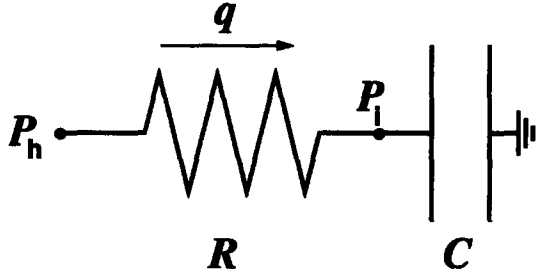


Figure 2-19: RC model of interstitial compartment.

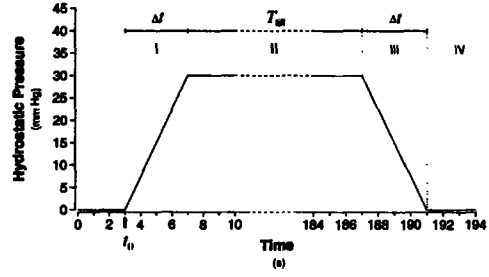


Figure 2-20: Simplified hydrostatic pressure profile. See text for details.

Region I: Gradual increase in orthostatic stress a over period of length  $\Delta t$ .

$$q(t) = \frac{V_{\max}}{\Delta t} \cdot \left(1 - e^{-\frac{t}{\tau}}\right)$$

$$V(t) = V_{\max} \cdot \left(\frac{t}{\Delta t} - \frac{\tau}{\Delta t}(1 - e^{-\frac{t}{\tau}})\right)$$

Region II: Full orthostatic stress during period of duration  $T_{\text{tilt}}$ .

$$q(t) = \frac{V_{\max}}{\Delta t} \cdot \left(1 - e^{-\frac{\Delta t}{\tau}}\right) \cdot e^{-\frac{t-\Delta t}{\tau}}$$

$$V(t) = V_{\max} \cdot \left(1 - \frac{\tau}{\Delta t}(1 - e^{-\frac{\Delta t}{\tau}})e^{-\frac{t-\Delta t}{\tau}}\right)$$

Region III: Gradual decline in orthostatic stress over a period of length  $\Delta t$ .

$$q(t) = \frac{V_{\max}}{\Delta t} \cdot \left(1 + (1 - e^{-\frac{\Delta t}{\tau}})e^{-\frac{T_{\text{tilt}}}{\tau}}\right) \cdot e^{-\frac{t-(\Delta t+T_{\text{tilt}})}{\tau}} - \frac{V_{\max}}{\Delta t}$$

$$V(t) = V_{\max} \cdot \left(1 - \frac{t - (\Delta t + T_{\text{tilt}})}{\Delta t}\right) - V_{\max} \cdot \frac{\tau}{\Delta t} \cdot \left(1 - e^{-\frac{\Delta t}{\tau}}\right) \cdot e^{-\frac{T_{\text{tilt}}}{\tau}} +$$

$$+ V_{\max} \cdot \frac{\tau}{\Delta t} \cdot \left(1 + (1 - e^{-\frac{\Delta t}{\tau}})e^{-\frac{T_{\text{tilt}}}{\tau}}\right) \cdot \left(1 - e^{-\frac{t-(\Delta t+T_{\text{tilt}})}{\tau}}\right) -$$

Region IV: Post-orthostatic stress recovery of unspecified length.

$$q(t) = -\frac{V_{\max}}{\Delta t} \cdot \left(1 - e^{-\frac{\Delta t}{\tau}}\right) \cdot \left(1 - e^{-\frac{T_{\text{tilt}}+\Delta t}{\tau}}\right) \cdot e^{-\frac{t-(2\Delta t+T_{\text{tilt}})}{\tau}}$$

$$V(t) = V_{\max} \cdot \frac{\tau}{\Delta t} \cdot \left(1 - e^{-\frac{\Delta t}{\tau}}\right) \cdot \left(1 - e^{-\frac{T_{\text{tilt}}+\Delta t}{\tau}}\right) \cdot e^{-\frac{t-(2\Delta t+T_{\text{tilt}})}{\tau}}$$

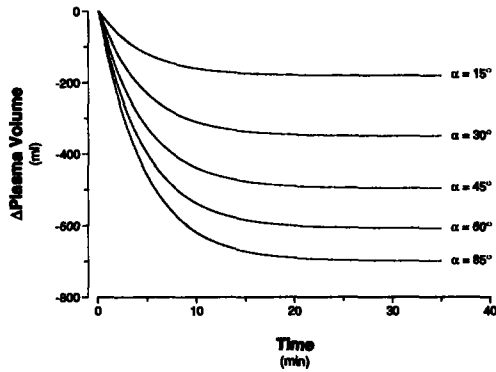


Figure 2-21: Absolute changes in plasma volume during simulated tilts.

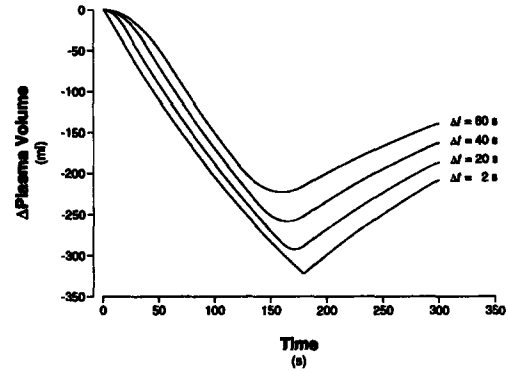


Figure 2-22: Absolute change in plasma volume during three minutes of simulated tilts.

The model outlined above specifies the net intra-vascular volume loss and the net trans-capillary leakage current as functions of time. To allow for spatially distributed leakage to occur, we assign fractions of the total volume loss and leakage current according to the distribution of hydrostatic pressure heads in the various dependent vascular compartments. The volume loss and leakage current assigned to the splanchnic compartment, for example, is given by:

$$V^{sp}(t) = \frac{P_h^{sp}}{\sum_n P_h^n} \cdot V(t) \quad \text{and} \quad q^{sp}(t) = \frac{P_h^{sp}}{\sum_n P_h^n} \cdot q(t)$$

where the summations extend over all dependent vascular compartments. Having thus established the form of the analytical solutions, we have to supply empirical values for the time constant  $\tau$  and the maximal interstitial volume change  $V_{max}$  for the various gravitational stresses we intend to model.

For tilt and stand tests, we will assign these parameters according to the data reported by Lundvall [125] as discussed in the previous section. To allow for tilts to different angles  $\alpha$ , we hypothesize that the maximal plasma volume loss is a linear function of the magnitude of the gravitational stress and therefore scales according to:

$$V_{max} = (700 \pm 41) \text{ ml} \cdot \frac{\sin(\alpha_{max})}{\sin(85^\circ)}$$

The nominal value for the time constant is  $\tau = (4.6 \pm 0.4) \text{ min}$  and is assumed independent of the tilt angle. Furthermore, as suggested by Figures 2-17 and 2-18, we assume plasma volume loss and restitution to have the same temporal dynamics. Figure 2-21 shows simulated changes in plasma volume to various angles of tilt. Figure 2-22 shows the time course of simulated plasma volume loss and restitution as a function of the transition time  $\Delta t$ .

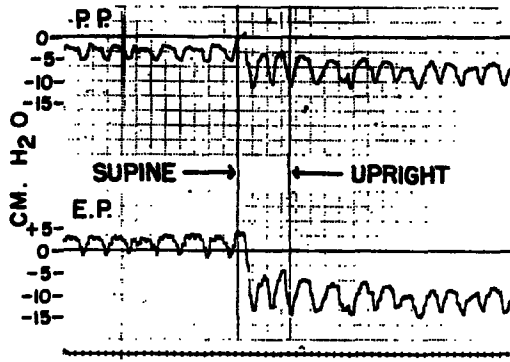


Figure 2-23: Pleural pressure, PP, and esophageal pressure, EP, during changes in posture. Figure taken from [123].

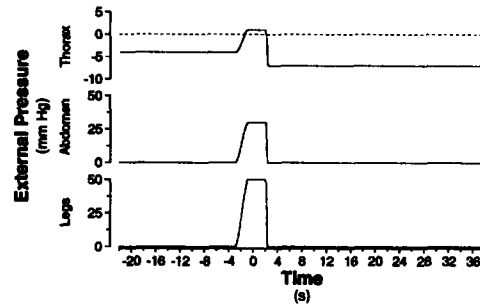


Figure 2-24: External pressures to the thoracic, abdominal, and leg vasculature during standing up.

## 2.4.2 Stand Tests

In a second, commonly used test to assess gravitational tolerance, subjects are asked to stand up actively from the lying position, and, once upright, maintain the posture with minimal muscular contraction while heart rate and blood pressure are being monitored. During the transition to the head-up posture, significant abdominal and leg muscular activity occurs which affects hemodynamics by influencing the extraluminal pressures of the abdominal and leg vasculature.

The venous circulation of the legs is richly endowed with valves which prevent blood flow from reversing direction in the upright position and thus ensure venous return from the dependent extremities. When calf and thigh muscles are contracted, they exert significant external pressure on leg veins which tend to collapse these vessels and propel their blood contents toward the heart — a phenomenon termed muscle pumping. Arnoldi [134] showed that the venous pressure in the Vena tibialis posterior increases transiently by (53 – 158) mm Hg with a mean of 75 mm Hg in response to a single forceful contraction of the flexor muscles of the lower leg. Slightly lower values were measured in the Vena saphena magna (mean increase of 34 mm Hg with a range of (21 – 66) mm Hg) and the Vena poplitea (mean increase of 29 mm Hg with a range of (15 – 45) mm Hg).

In the process of standing up, the muscular walls around the abdominal cavity contract to stabilize the trunk and allow for controlled flexion in the hip and therefore raising of the torso. Abdominal contraction significantly increases intra-abdominal pressure as demonstrated by Tanaka and co-workers [135], who measured rectal pressure as a surrogate for intra-abdominal pressure. Their study shows intra-abdominal pressure to increase precipitously and transiently by  $(43 \pm 22)$  mm Hg over the the first five seconds of active standing, while no appreciable changes were seen during passive tilts. Once the upright posture is assumed, the abdominal musculature relaxes and intra-abdominal pressure returns to baseline.

Surprisingly little information is available on the time course of intra-thoracic

pressure during standing-up from the supine position. It is conceivable that just as the muscular walls of the abdominal cavity contract upon standing up, so do the muscles of the chest wall, leading to a brief Valsalva-type maneuver that would increase intra-thoracic pressure transiently. The latter argument seems to be supported by the work of Mead and Gaensler [123] who show a pleural pressure tracing in one subject upon sitting up. Their tracing is reproduced in Figure 2-23 and indicates a brief increase in mean intra-thoracic pressure (indicated as pleural pressure, PP) by about 4.5 mm Hg. Interestingly, this increase in pleural pressure is not reflected in the tracing of its surrogate, esophageal pressure (EP). Similarly, a transient increase was not seen by Sprangers and co-workers, who investigated changes in esophageal pressure in two subjects during active changes in posture [136].

To simulate a stand test, we specify the time course and magnitudes of external vascular pressures in the legs, the abdomen, and the thorax, as indicated in Figure 2-24, and superimpose these changes on the tilt simulation described in the previous section.

### 2.4.3 Lower Body Negative Pressure

Lower body negative pressure (LBNP) interventions have been used extensively in spaceflight-related life science research. In LBNP experiments, subjects rest in the supine position with their lower bodies enclosed in an air-tight chamber whose internal air pressure can be controlled tightly. During the experiment, the chamber pressure is reduced significantly below ambient atmospheric pressure, which leads to blood volume redistribution from the thoracic region to the lower body, thus challenging cardiovascular reflex mechanisms.

In analogy to the changes in external vascular pressures described in the previous section, a step reduction in chamber pressure is simulated by specifying the time course of the pressure sources external to the leg vasculature according to:

$$P_{\text{ext}}(t) = \begin{cases} 0 & \text{for } t < t_0 \\ P_{\text{max}} \cdot \frac{1}{2} \cdot (1 - \cos(\pi \frac{t-t_0}{\Delta t})) & \text{for } t_0 \leq t \leq t_0 + \Delta t \\ P_{\text{max}} & \text{for } t > t_0 + \Delta t \end{cases} \quad (2.5)$$

where  $P_{\text{max}}$  is the maximal external negative pressure applied during the experiment.  $\Delta t$  and  $t_0$  are defined as in Equation 2.4 and Figure 2-16.

Changes in plasma volume during LBNP interventions have been studied less rigorously and less intensively than those during tilt or stand tests. Lundvall and co-workers investigated leg volume changes with a set of strain gauges during 10 minutes of high level (70 – 75) mm Hg LBNP [137]. Tracking leg volume changes at the thigh and the calf, the authors demonstrated that after an initial rapid volume expansion leg volume continued to increase linearly with time demonstrating that the sequestration of plasma volume did not abate over the 10 minutes of their study. The net decrease in plasma volume after 10 minutes was determined to be  $(491 \pm 29)$  ml. Aratow and co-workers studied plasma volume changes during four hours of 30 mm Hg of LBNP and determined a reduction in plasma volume of  $(370 \pm 40)$  ml corresponding

to approximately  $(11.4 \pm 1.2)\%$  [138]. Relatively coarse sampling of their data during the initial period of LBNP prevents an accurate determination of a time constant.

In simulating plasma volume reduction during LBNP, we assume the structure and time constant of the model described in Section 2.4.1. We scale the maximal plasma volume loss according to

$$V_{\max} = (491 \pm 29) \text{ ml} \cdot \frac{P_{\max}}{70 \text{ mm Hg}}.$$

## 2.5 Model Implementation

The hemodynamic model outlined in the previous sections is described mathematically by a set of twenty-one coupled, non-linear, time-varying, first-order differential equations in which the set of compartment pressures assume the role of state variables. We have implemented a standard fourth-order Runge-Kutta integration algorithm [139, p. 712], allowing for adaptive step-size control [139, p. 719], to integrate the equations of state numerically. In order to supply a set of initial conditions for the state variables to the integration routine, we follow the strategy outlined by Davis [11], who solves a set of linearized equations to arrive at an estimate of end-diastolic pressures for a given set of model parameters. Integration steps range from  $6.1 \cdot 10^{-4}$  s during ventricular ejection phase to a user-defined upper limit of 0.01 s during ventricular diastole, with a mean step size of  $5.6 \cdot 10^{-3}$  s.

It can be shown that the model equations allow for a first integral of the equations, or conserved quantity, to be identified. In fact, it is straight forward to demonstrate that this conserved quantity is total blood volume,  $V_t$ :

$$V_t(t = 0) \equiv V_t(t) = \sum_n V_n(\Delta P_n(t), t) = \text{constant}$$

where the summation extends over all compartment volumes,  $V_n$ . Rather than reducing the number of differential equations by one, this algebraic constraint can be used to monitor the quality of the numerical integration scheme, as deviations from the fixed value of total blood volume are purely due to numerical round-off and truncation errors. In Figure 2-25, we show the time series of the volume error, defined as the difference between the fixed, nominal value of total blood volume and the computed total blood volume, for a representative simulation of 500 seconds in duration. Over this period, the maximum absolute volume error is approximately 0.036 ml or  $6.1 \cdot 10^{-4}\%$  of total blood volume. Not only is this value inconsequential physiologically, it is also acceptably small as a cumulative numerical integration error. The relatively small integration steps required to maintain this relative accuracy in total blood volume is in part due to the choice of cardiac pressures as state variables as the time-varying compliances and their derivatives enter the differential equations explicitly. Choosing cardiac volumes instead might allow for bigger time steps to be taken while conserving simulation accuracy.

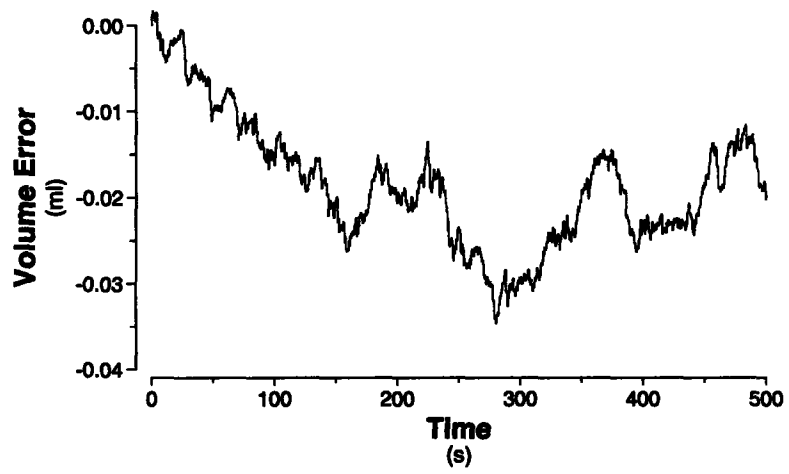


Figure 2-25: Numerical volume error over 500 seconds of simulation time.



# Chapter 3

## Cardiovascular Control System

The cardiovascular system is responsible for supplying the tissues and organs of the body with the oxygen and other nutrients required for their metabolic needs; its timely response to hemodynamic perturbations or to changing metabolic demands is critical for an individual's optimal performance and even survival. To accomplish its task, the cardiovascular system relies on the combined effect of global reflex mechanisms that regulate central hemodynamic variables and local control that modulates regional blood flow in response to changing metabolic demands or to hemodynamic stresses. At either level, the cardiovascular system can recruit a hierarchy of reflex mechanisms, each having different temporal responses, to cope both dynamically and adaptively with a large variety of stresses.

In modeling the cardiovascular control mechanisms relevant to the short-term hemodynamic response to orthostatic stress, we focus on representing the two major neurally-mediated reflex mechanisms, namely the arterial baroreflex, discussed in Section 3.1, and the cardiopulmonary reflex, described in Section 3.2. It will be shown in subsequent chapters that the hemodynamic effects associated with sudden orthostatic stress are quite dramatic so that the neurally-mediated global reflex responses are likely to dominate the immediate circulatory response.

### 3.1 Arterial Baroreflex

The arterial baroreflex is the most potent guardian of short-term blood pressure homeostasis on the high-pressure side of the circulation; when required, its actions can develop full strength well within a few seconds, allowing for a rapid and decisive response to sudden hemodynamic stress. Hard-wired neural pathways connecting arterial pressure sensors to effector organs account for this responsiveness.

The afferent limb of the arterial baroreflex consists of stretch receptors in the arterial wall of the aortic arch and the carotid sinuses, and neural pathways connecting them to the central nervous system. The receptors respond to changes in arterial transmural pressures by changing their rate of depolarization; hypertensive stimuli lead to an increased rate of depolarization whereas hypotensive stimuli have the opposite effect. The resultant electrical impulses propagate via afferent nerve

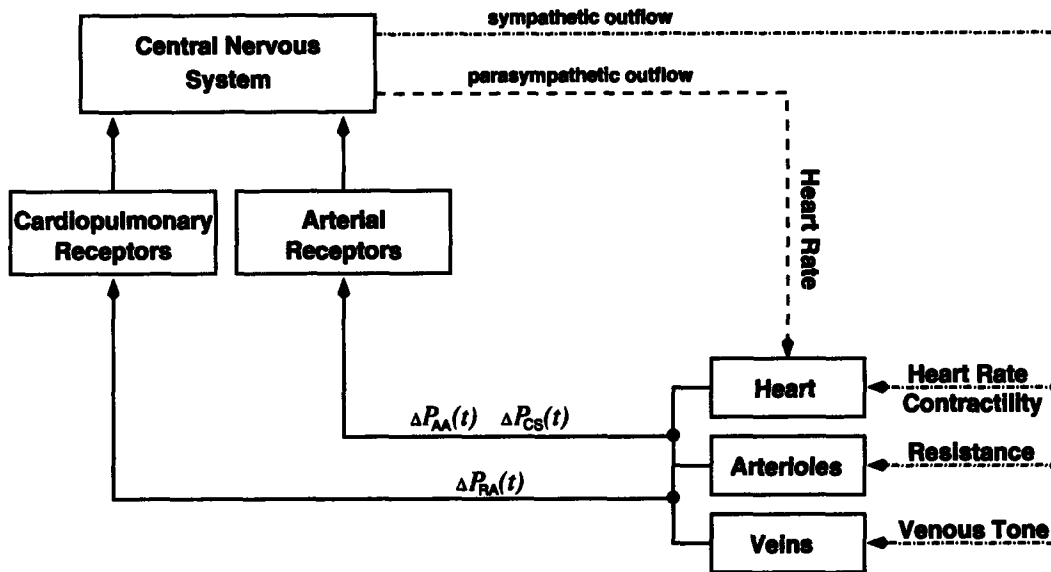


Figure 3-1: Diagrammatic representation of the cardiovascular control model.  $\Delta P_{AA}(t)$ ,  $\Delta P_{CS}(t)$ ,  $\Delta P_{RA}(t)$ : aortic arch, carotid sinus, and right atrial transmural pressures.

fibers traveling alongside the glossopharyngeal nerves (carotid sinus reflex) and vagus nerves (aortic arch reflex) to converge on the *nucleus tractus solitarius* (NTS), a major functional center of autonomic activity in the medulla oblongata. Afferent nerve traffic is thought to have direct inhibitory influence on the NTS, leading to reciprocal effects on the two efferent limbs of the autonomic nervous system: increased afferent nerve traffic reduces efferent sympathetic outflow and increases efferent parasympathetic action. The sympathetic (thoracolumbar) division of the autonomic system is formed by visceral efferent fibers originating from the thoracic and lumbar portions of the spinal cord. At its nerve terminals, the sympathetic nervous system releases norepinephrine, which acts via  $\beta_1$ -sympathetic receptors in cardiac tissue to increase heart rate and cardiac contractility, and via  $\alpha_1$ -sympathetic receptors found in the muscular wall of arterioles and veins to constrict vascular smooth muscle (increasing arteriolar and venous tone). The latter leads to an increase in arteriolar resistance and a decrease in venous zero pressure filling volume. The parasympathetic (craniosacral) division of the autonomic system consists of cranial nerves III (oculomotor), VII (facial), IX (glossopharyngeal), and X (vagus), and spinal nerves  $S_{2-4}$ . Of cardiovascular interest, however, are primarily the vagus nerves that convey efferent signals to the heart and abdominal viscera. The parasympathetic system releases acetylcholine, a rapidly-metabolized neurotransmitter, which acts on the heart primarily by slowing its rate and on the peripheral vasculature by dilating arterioles and venules.

In Figure 3-1 we give a diagrammatic representation of the major functional-anatomical components of the neural reflex loops just described for the arterial baroreflex.

### 3.1.1 Architecture of the Model

In consonance with previous work [11, 31, 140], we model the arterial baroreflex as a set-point controller that aims at minimizing an error signal, namely the deviation of (local) time-averaged arterial pressure from a pre-defined set-point value, by adjusting various effector mechanisms in a feedback configuration. As will be shown, this set-point model is quite powerful in representing the short-term cardiovascular control mechanisms; yet it is also quite abstract in that its functional elements do not necessarily map to any of the functional-anatomical components described above and depicted in Figure 3-1.

The hemodynamic model described in the previous chapter generates samples of aortic arch,  $\Delta P_{AA}(t)$ , and carotid sinus transmural pressures,  $\Delta P_{CS}(t)$ , at a rate determined by the numerical integration stepsize ( $\overline{dt} \leq 10^{-3}$  s). As pointed out by Mukkamala [141], pulsatile arterial blood pressure is band-limited to frequencies below ten times the mean heart rate, while the frequency responses of the autonomically mediated cardiovascular reflex mechanisms are band-limited to frequencies less than the mean heart rate. Relaying every pressure sample to the reflex system is therefore neither computationally advisable nor physiologically necessary. Consequently, as indicated in Figure 3-2, the first processing step on the afferent side involves averaging of the arterial pressure waveforms over an appropriate window of time. We employ a moving average filter over the recent 0.25 s arterial pressure histories and advance the filter every 0.0625 s to generate samples of the respective averaged values,  $\Delta \bar{P}_{AA}[n]$  and  $\Delta \bar{P}_{CS}[n]$ , at a rate of 16 Hz. The discrete-time index  $n$  is used to indicate their relatively coarse sampling compared to the actual pressure waveforms. We implemented the averaging process via backward Euler integration which delays the output by approximately 0.125 s; we will compensate for this delay when considering the overall time delay of the reflex responses.

Instead of modeling the aortic and carotid sinus reflex loops separately, we adopted a hybrid strategy in which we assume the input to a single, lumped arterial baroreceptor to be the arithmetic mean  $\Delta \bar{P}_A[n]$  of  $\Delta \bar{P}_{AA}[n]$  and  $\Delta \bar{P}_{CS}[n]$ . Given the relative paucity of experimental data on the aortic baroreflex, this averaging strategy allows us to maintain the differential influence these receptors exert during respiration or changes in posture, for example. Quite conceivably, though, the equal weighing of

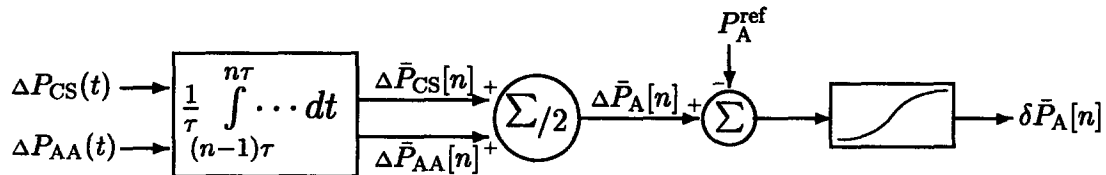


Figure 3-2: Arterial baroreflex model: functional representation of afferent and central nervous pathways.

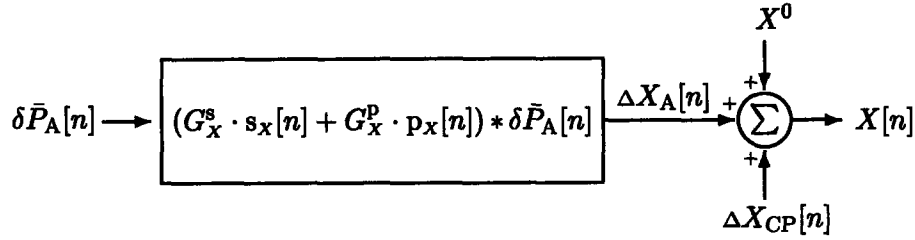


Figure 3-3: Arterial baroreflex model: functional representation of central nervous and efferent processing for an effector variable  $X$ .

aortic arch and carotid sinus transmural pressures might be a strong assumption to make, particularly in situations when one set of receptors senses a substantially different signal than the other. We will revisit this assumption when simulating the transient response to orthostatic stress.

To generate an error signal,  $\delta\bar{P}_A[n]$ , we subtract a pre-defined arterial set-point pressure,  $P_A^{\text{ref}}$ , from the lumped arterial pressure  $\Delta\bar{P}_A[n]$ , and scale the resultant signal as described by deBoer and co-workers [140]:

$$\delta\bar{P}_A[n] = 18 \cdot \arctan \left( \frac{\frac{1}{2}(\Delta\bar{P}_{AA}[n] + \Delta\bar{P}_{CS}[n]) - P_A^{\text{ref}}}{18}} \right) \quad (3.1)$$

to account for the experimentally-observed sigmoidicity of the stimulus-response curves [142]. This scaling limits the error signal to approximately  $\pm 28$  mm Hg.

Figure 3-3 illustrates the efferent side of the arterial baroreflex, where the error signal is convolved with unit-area impulse response functions,  $s_X[n]$  and  $p_X[n]$ , and scaled by static gain values,  $G_X^s$  and  $G_X^p$ , to determine the arterial baroreflex contribution,  $\Delta X_A[n]$ , to the current value of the effector variable  $X[n]$ . For completeness, we also show the effector set-point,  $X^0$ , and the additive contributions of the cardiopulmonary reflex loop,  $\Delta X_{CP}[n]$ , to  $X[n]$ . Here  $X$  denotes any of the four effector mechanisms illustrated in Figure 3-1.  $G_X^s$  and  $G_X^p$  represent the sympathetic and parasympathetic static gain values;  $s_X[n]$  and  $p_X[n]$  denote the sympathetic and the parasympathetic unit-area impulse response functions associated with the effector mechanism represented by  $X$ .

In the case of the arterial resistance and the venous tone effector limbs, the discrete-time values of  $X[n]$  are linearly interpolated to allow for smooth variation of the effector variables  $R(t)$  and  $V_0(t)$ . Interpolation requires that both  $X[n]$  and  $X[n+1]$  be available at time  $t$ , which introduces a delay of 0.0625 s for these two effector loops.

As described in Section 2.2, the cardiac capacitances vary throughout the cardiac cycle between an end-systolic and a diastolic value. The contractility feedback affects the respective end-systolic values,  $C_r^{\text{es}}[i]$  and  $C_1^{\text{es}}[i]$ . Here, we introduced the discrete-time index  $i$  to denote beat number and to emphasize explicitly the beat-by-

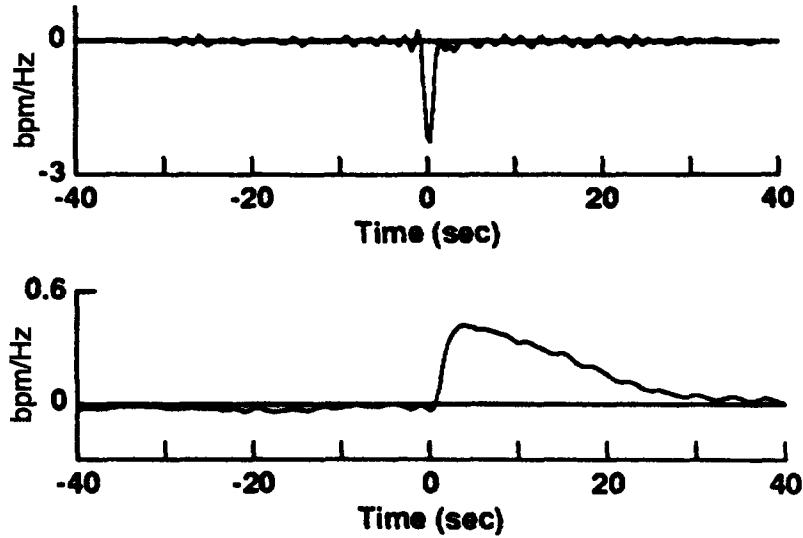


Figure 3-4: Parasympathetic (top) and sympathetic (bottom) canine heart rate impulse response functions. Adapted from Berger et al. [144].

beat nature of variations in contractility as opposed to the smooth variation of  $R(t)$  and  $V_0(t)$ . We implemented the contractility feedback via a sampled-data model in which the reflex signals  $C_{1,r}^{es}[n]$  are sampled at times  $t[i]$ , corresponding to the onset times of cardiac contraction, to establish the end-systolic capacitance values  $C_{1,r}^{es}[i]$  for the ensuing beat. The onset times  $t[i]$  are determined via an Integral Pulse Frequency Modulator (IPFM) model of the sino-atrial node. The latter will be discussed in detail in Section 3.3 where we describe the heart rate limb of the arterial baroreflex.

In summary, the arterial baroreflex is described by a single arterial set-point,  $P_A^{ref}$ , and possibly two static gain values and two normalized impulse response functions for each effector mechanism. The assignment of numerical values to these parameters is the topic of the following section.

### 3.1.2 Parameter Assignments

**Impulse response functions** By directly stimulating the stellate ganglia (sympathetic stimulation) and the vagus nerves (parasympathetic stimulation), Berger [143, 144] identified the canine heart rate impulse response functions for parts of the efferent neural pathways and the sino-atrial node. The impulse response functions so identified are reproduced in Figure 3-4 and confirm common physiological knowledge that vagal stimulation leads to an immediate decrease in heart rate and sympathetic stimulation to an increase over slightly longer time scales. In fact, the parasympathetic impulse response function attains nonzero values before the onset of vagal stimulation (at time zero), suggesting a non-causal heart rate response. Berger [143, p. 133] considers this an artifact of the particular signal processing algorithms employed. More importantly, though, the impulse response functions shown in Fig-

ure 3-4 characterize contribution of the end-organ response and the efferent neural pathways only, omitting the contributions of the receptors, the afferent pathway, and the central nervous system. For pure reflex responses, the latter contributions are described as pure delay elements in series with the former contributions [11]. The triangular shapes of the impulse response functions suggest a parameterization in terms of three timing variables (a delay, a peak, and an end-point). These idealized responses will serve as prototypes for the impulse response functions to be developed for other effector organs.

Having had access to a unique study population, Borst and Karemaker [145] were able to study the latencies of the human arterial baroreflex by directly stimulating the carotid sinus nerves in eleven subjects. Looking at P-P-interval changes, they determined a delay of 0.5–0.6 s for vagally mediated heart rate control. Furthermore, by pacing the heart at a fixed rate while stimulating the carotid sinus nerves, they determined the delay of the  $\alpha$ -sympathetic response to arterial resistance to be 2-3 s.

Several investigators have used periodically varying external neck pressure to stimulate the carotid sinus and thus to elucidate human baroreflex dynamics noninvasively [146–148]. Eckberg found a 0.44 s delay for vagally mediated heart rate control in response to reductions in carotid sinus transmural pressure. Keyl and co-workers [148] found this delay to be  $(0.59 \pm 0.25)$  s. We adopt Keyl's value for the delay and follow Davis' choice for the peak and the end point of the parasympathetic impulse response function [11]. Furthermore, we assign Keyl's estimate of the degree of variability in the delay to all three of the parasympathetic parameters.

Rea and Eckberg [147] measured muscle sympathetic nerve activity at the peroneal nerve in response to changes in external neck pressure. Their data suggest a delay of at least 2.8 s for  $\alpha$ -sympathetically mediated reflex responses which is congruous with the data presented by Borst and Karemaker. We assume this delay to be  $(2.5 \pm 1.0)$  s.

Due to experimental difficulties, little direct experimental evidence exists for the latencies of the  $\beta$ -sympathetic heart rate response or the  $\alpha$ -sympathetic response of venous tone in humans. For dogs, Berger noted that the  $\beta$ -sympathetic filter characteristics shown in Figure 3-4 closely match the results reported by Rosenbaum and Race [149], who studied the canine vascular resistance response. He suggested that this commonality reflects universal kinetic properties of adrenergic receptors and their cellular signaling mechanisms. Studying venous tone feedback in dogs, Shoukas and colleagues [150] observed a significantly longer delay ( $\approx 10$  s) than the ones reported by Berger and Rosenbaum. We assume the delays of the  $\beta$ -sympathetic heart rate response and the  $\alpha$ -sympathetic arterial resistance response to be equal, but we assume a slightly longer delay for the  $\alpha$ -sympathetic response of venous tone as indicated in Table 3.1.

Using system identification techniques, Mullen and co-workers [151] investigated closed-loop cardiovascular regulation. While they do not separate parasympathetic and  $\beta$ -sympathetic responses, it is safe to assume that the tail of their impulse response function is primarily sympathetically mediated, which would suggest an endpoint for the  $\beta$ -sympathetic response at around  $(15.0 \pm 5.0)$  s. Mukkamala [152], from the same laboratory, investigated the human arterial resistance response to step changes in arterial pressure. His data suggest the peak of the impulse response occurs

Table 3.1: Parameterization of the reflex impulse response functions

Type of Response	Delay s	Peak s	End s
parasympathetic	$(0.59 \pm 0.25)$	$(0.70 \pm 0.25)$	$(1.0 \pm 0.25)$
$\beta$ -sympathetic	$(2.5 \pm 1.0)$	$(3.5 \pm 1.0)$	$(15.0 \pm 5.0)$
$\alpha$ -sympathetic to $R$	$(2.5 \pm 1.0)$	$(4.5 \pm 1.0)$	$(30.0 \pm 5.0)$
$\alpha$ -sympathetic to $V_0$	$(5.0 \pm 1.5)$	$(7.0 \pm 1.5)$	$(40.0 \pm 5.0)$

approximately 2 s after the onset of the reflex response. Furthermore, the response seems to equilibrate 30 s after the stimulus was applied. Finally, we assume slightly larger values for the peak and the end-point of the  $\alpha$ -sympathetic response to venous tone.

In assigning a single impulse response function to each effector arc, we neglect a commonly reported experimental finding that the arterial baroreflex responds faster to hypertensive stimuli (average parasympathetic delay  $\approx 0.26$  s) than to hypotensive stimuli (average parasympathetic delay  $\approx 0.44$  s) [146, 153]. Where possible, we selected the timing information associated with hypotensive stimuli, as this is the principal focus of this work.

Finally, we sample the impulse response functions at 0.0625 s and implement them advanced in time to account for the delays introduced by the averaging filter and interpolator described in the previous section.

**Static gain values** While it would be desirable to determine the open-loop gains of each of the four effector mechanisms independently, such experiments are technically very difficult in conscious animals and ethically not permissible in humans. Determination of gain values is therefore commonly based on the closed-loop system in which perturbations in systemic arterial blood pressure are induced pharmacologically or the carotid sinus is stimulated mechanically while the reflex responses of certain effector mechanisms are being observed.

Several studies induced hypertension through bolus-administration of potent vasoconstrictor agents, such as phenylephrine or angiotensin, while the ensuing reflex bradycardia was observed to quantify the stimulus-response curve of R-R-interval to changes in blood pressure [154–158]. Studying 23 normal control subjects, Eckberg and co-workers [155] determined this gain value to be  $(16.0 \pm 8.6)$  ms/mm Hg with a range of  $(5.0 - 35.0)$  ms/mm Hg. Bristow and colleagues [154] report  $(14.8 \pm 9.2)$  ms/mm Hg with a range of  $(3.6 - 29.3)$  ms/mm Hg while Pickering [157] quotes a somewhat higher value of  $(30.0 \pm 4.0)$  ms/mm Hg with a range of  $(13.3 - 48.7)$  ms/mm Hg. Pooling the data from these three studies results in an average R-R-interval gain value of  $(22.7 \pm 9.5)$  ms/mm Hg with a range of  $(3.6 - 48.9)$  ms/mm Hg. We follow deBoer’s [159] suggestion of dividing the gain equally between the sympathetic and the parasympathetic reflex arcs.

Little quantitative information is available on the reflex changes of cardiac con-

Table 3.2: Static gain values of the arterial baroreflex model

Reflex arc		$G^s$	$G^p$
R-R-interval	$\frac{\text{ms}}{\text{mm Hg}}$	$(11 \pm 6)$	$(11 \pm 6)$
Left ventricular contractility	$\frac{\text{ml}}{\text{mm Hg}^2}$	$(0.007 \pm 0.001)$	0
Right ventricular contractility	$\frac{\text{ml}}{\text{mm Hg}^2}$	$(0.022 \pm 0.003)$	0
Arterial resistance	$\frac{\text{PRU}}{\text{mm Hg}}$	$(-0.05 \pm 0.01)$	0
Venous unstressed volume	$\frac{\text{ml}}{\text{mm Hg}}$	$(31 \pm 5)$	0

tractility. Following Davis' reasoning [11], we allow the right and left ventricular end-systolic elastances to attain between 170% and 210% of their respective nominal values in response to maximal carotid sinus stimulation. This translates to gain values of  $(0.007 \pm 0.001) \text{ ml/mm Hg}^2$  and  $(0.022 \pm 0.003) \text{ ml/mm Hg}^2$  for the end-systolic capacitance of the left and the right ventricle, respectively.

Under high orthostatic stress, the cardiovascular system is capable of doubling total peripheral resistance [160, 161]. If we assume that in the limit of life-threatening hypotension, peripheral resistance can be increased to 2.5 – 3.0 PRU, and that this response is overwhelmingly mediated by the arterial baroreflex, we obtain an upper limit for the peripheral resistance gain value of  $(0.05 - 0.07) \text{ PRU/mm Hg}$ . We assign a value of  $(0.05 \pm 0.01) \text{ PRU/mm Hg}$  and assume each of the systemic vascular beds to contribute equally.

Reflex-induced changes in venous unstressed volume are difficult to quantify in humans due to our inability to measure venous volumes directly. Under maximal carotid sinus stimulation, dog experiments have revealed a maximum change in systemic reservoir volume of approximately 12 ml/kg, 6–7 ml/kg of which originate from abdominal vessels [162]. When scaled to a 75 kg human, these data suggest a maximal change in venous unstressed volume of about 900 ml and imply a static gain value of 31 ml/mm Hg, given the limitation of the afferent signal of the arterial baroreflex model. We attribute  $(15 \pm 3) \text{ ml/mm Hg}$  to the splanchnic venous reservoir,  $(8 \pm 2) \text{ ml/mm Hg}$  to the lower body,  $(6 \pm 2) \text{ ml/mm Hg}$  to the upper body, and  $(2 \pm 1) \text{ ml/mm Hg}$  to the kidneys. The static gain values for the arterial baroreflex model are summarized in Table 3.2.

Finally, we assign the value of 91 mm Hg to the set-point pressure of the arterial baroreflex.



## 3.2 Cardiopulmonary Reflex

Neurogenic reflex mechanisms originating from the low pressure side of the circulation and the heart were first described around the same time as their arterial analogs. Today, their role in neurohumoral control of cardiovascular function and fluid-electrolyte balance is hardly questioned; yet their physiological significance in short-term cardiovascular homeostasis is still being debated.

Cardiopulmonary receptors located in the atrio-caval junctions, the atrial and the ventricular walls, and even in the pulmonary vasculature are commonly divided into A-type receptors (mechano-receptors) and B-type receptors (stretch receptors). Afferent signals from these receptors travel along vagal fibers and converge on vagal centers in the medulla oblongata. Cardiopulmonary stimulation is thought to have direct inhibitory influence on medullary vasoconstrictor centers, leading to reciprocal effects on parasympathetic and sympathetic outflow: increased afferent nerve traffic reduces efferent sympathetic outflow and is thought to increase efferent parasympathetic action.

The cardiopulmonary reflex also exerts important longer-term neurohumoral control over cardiovascular function. Direct cardiopulmonary influence on vasopressin (antidiuretic hormone, ADH) and atrial natriuretic peptide (ANP) release allows for low-pressure modulation of renal fluid-electrolyte balance.

Finally, cardiopulmonary-mediated vagal outflow has long been thought to contribute to, if not be causative of, vasovagal syncope during prolonged orthostatic stress or hemorrhage; it is associated with a triad of cardiopulmonary responses (bradycardia, hypotension, and apnea) commonly referred to as Bezold-Jarisch reflex.

The architecture of our cardiopulmonary reflex model is quite similar to the one described for the arterial baroreflex. The sensed variable is right atrial transmural pressure,  $\Delta P_{RA}(t)$ . After averaging and subtraction of the cardiopulmonary set-point pressure,  $P_{CP}^{ref}$ , the scaled error signal  $\delta \bar{P}_{CP}$  is computed according to:

$$\delta \bar{P}_{CP}[n] = 5 \cdot \arctan \left( \frac{\Delta \bar{P}_{CP}[n] - P_{CP}^{ref}}{5} \right) \quad (3.2)$$

The efferent processing steps are again similar to the arterial baroreflex in that the error signal is convolved with unit-area impulse response functions and scaled by effector mechanism-specific static gain values to produce the cardiopulmonary contribution,  $\Delta X_{CP}[n]$ , to the current value of the effector mechanism  $X$  (see Figure 3-3). We also assume the timing of cardiopulmonary control to be described by the same impulse response functions identified in the previous section. What remains to be established, therefore, are the static gain values for the various reflex limbs.

Cardiopulmonary control of heart rate is commonly known under the eponym of Bainbridge reflex. It states that right atrial distention leads to a reflex tachycardia mediated by cardiopulmonary receptors [163, p. 89]. While the Bainbridge reflex has been amply documented in canine experiments, its physiological significance, or even its existence in humans has been questioned. As reviewed by Mark and

Table 3.3: Static gain values of the cardiopulmonary reflex model.

Reflex arc		$G^s$	$G^p$
Arterial resistance	$\frac{\text{PRU}}{\text{mm Hg}}$	$(0.05 \pm 0.01)$	0
Venous unstressed volume	$\frac{\text{ml}}{\text{mm Hg}}$	$(100 \pm 20)$	0

Mancia [164], increasing right atrial pressure in humans through infusion of volume or raising of the legs fails to show the reflex tachycardia seen in dogs with right atrial distention. Furthermore, copious lower body negative pressure experiments confirm that reductions in right atrial pressure fail to elicit a heart rate response until changes in arterial pressure become evident [165, 166]. In a recent study, Desai and co-workers [167] tried to untangle the contributions to the cardiac period of cardiopulmonary, aortic arch, and carotid sinus receptors. Their analyses suggest not only a positive gain value connecting right atrial pressure to R-R-interval (i.e. an inverse Bainbridge reflex), but also that the strength of this coupling is an order of magnitude larger than the influence of carotid sinus pressure on the cardiac period. Given the lack of unequivocal experimental support for a Bainbridge reflex in humans, we decided to set the static gain values for the coupling of right atrial pressure to R-R-interval to zero, i.e. we neglect the Bainbridge reflex. Similarly, we do not account for a possible influence of right atrial pressure on cardiac contractility, given that such a coupling is negated in animal experiments [163, p. 89].

Cardiopulmonary contributions to peripheral resistance feedback can be estimated from LBNP experiments. Low levels of LBNP usually elicit a vasoconstrictor response without increases in heart rate maintaining stable arterial pressures [165, 166]. The data presented by Pawelczyk and Raven [166] suggest a static gain value of 0.05 – 0.06 PRU/mm Hg for the cardiopulmonary – peripheral resistance reflex limb, a value conspicuously similar to the one found for the arterial baroreflex.

Experiments in humans have shown splanchnic blood volume to change by approximately 500 ml in response to a 1000 ml hemorrhage without significant changes in heart rate, cardiac output, and arteriolar resistance [168]. Assuming this response to be mediated by the cardiopulmonary reflex only, we can get a rough estimate of the cardiopulmonary reflex gain to venous tone by assuming that the contribution of the splanchnic circulation is about 60% of the total venoconstriction response. These assumptions would suggest a static venous tone feedback gain of approximately 100 ml/mm Hg as the cardiopulmonary afferent pressure signal is limited to  $\pm 8$  mm Hg. A significantly larger gain value for venous tone feedback on the low pressure side as compared to the analogous gain value of the arterial baroreflex might be explained teleologically by the importance of the venous reservoir to maintain cardiac filling pressure via the Frank-Starling mechanism.

While neurohumoral control of the cardiovascular system plays a significant role

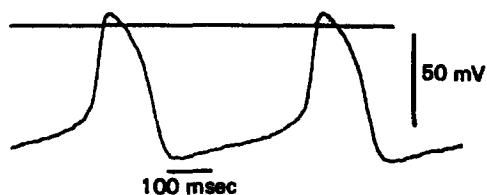


Figure 3-5: Intracellular recording of pacemaker activity recorded within the morphological boundary of the rabbit SA node [170, p. 93].

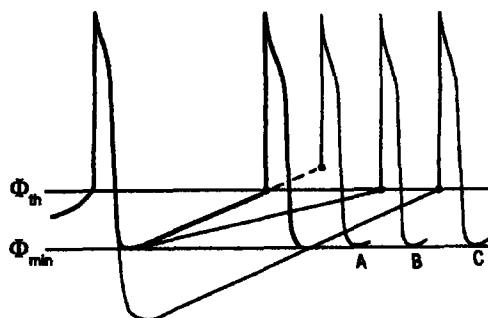


Figure 3-6: Schematic representation of how changes in pacemaker properties lead to cardiac deceleration. Adapted from [171].

in adaptation to prolonged orthostatic stress, its importance to short-term cardiovascular control is questionable. Several studies confirmed that humoral mediators, such as renin, aldosterone, and vasopressin, only attain significant plasma concentrations after 10-15 minutes of sustained orthostatic stress [36, 169]. We therefore ignore neurohumoral control in this work.

Finally, we assign the value of 5 mm Hg to the set-point of the right atrial transmural pressure.

### 3.3 Cardiac Pacemaker

In the healthy heart, cardiac excitation is initiated when specialized cells in the sinoatrial (SA) node depolarize spontaneously — a phenomenon referred to as automaticity of the cardiac pacemaker cells. Due to a progressive increase in cell membrane permeability to sodium and calcium ions during the diastolic portion of the cardiac cycle, the transmembrane potential rises until a cell-specific threshold potential is crossed, at which point the cell membrane rapidly reverses polarity and an action potential is generated (see Figure 3-5). Once generated, the action potential propagates along the cardiac conduction system to reach individual myocardial fibers, where depolarization then leads to a rapid increase in intracellular calcium and ultimately myocyte contraction.

In the absence of external influences, the rate of spontaneous depolarization is constant [172]. In the intact circulation, however, the SA node is richly innervated by sympathetic and parasympathetic nerve fibres whose balanced influence modulates the rate at which action potentials are being generated. Dominance of parasympathetic influence decelerates impulse generation and therefore reduces heart rate; a shift in autonomic balance to sympathetic dominance accelerates action potential generation and therefore increases heart rate. Figure 3-6 shows schematically how cardiac deceleration can be achieved by increasing the threshold potential,  $\Phi_{th}$ , at which an action potential is generated (A), decreasing the slope of diastolic depolar-

ization (B), or by decreasing the diastolic resting potential,  $\Phi_{\min}$ , (C) [173]. Reversal of these parameter changes lead to cardiac acceleration.

In modeling the cardiac pacemaker we are interested in generating a sequence of point events, namely the onset times of cardiac excitation corresponding to the threshold-crossing of the transmembrane potential, based on a representation of automaticity and the time-continuous history of neural input to the cardiac pacemaker. We have modified the approaches taken by Hyndman and Mohn [173] and later deBoer and co-workers [159] who have used an Integral Pulse Frequency Modulator (IPFM) model to represent the dynamics of the transmembrane potential during diastole. The model is based on the idea that the transmembrane potential can be represented as a function  $M(t)$  whose value at time  $t$  depends on the cumulative contribution of automaticity and autonomic activity since the onset of the last cardiac excitation at time  $t_{k-1}$ :

$$M(t) = \int_{t_{k-1}}^t m(t') dt'$$

The function  $m(t)$  can be expressed as  $m(t) = m_0 + m_r(t)$  to represent the automaticity,  $m_0$ , and neural (reflex) input,  $m_r(t)$ . The  $k$ -th beat is initiated at time  $t_k$  when the value of the integral reaches a predefined threshold  $\Gamma$ , corresponding to the threshold potential  $\Phi_{\text{th}}$ , and the absolute refractory period of the cardiac pacemaker cell has passed

$$\int_{t_{k-1}}^{t_k} m(t') dt' = M(t_k) \geq \Gamma \quad \text{and} \quad t_k - t_{k-1} \geq 0.2 \cdot (t_{k-1} - t_{k-2}).$$

where we assumed an absolute refractory period of one fifth of the preceding cardiac cycle length. Once this condition is met, the function  $M(t)$  is reset and the integration process is repeated. We assume  $m_0$  to be constant, which leads to a strictly periodic signal at a rate of  $m_0/\Gamma$  in the absence of neural influence ( $m_r(t) = 0$ ). The neural contribution can increase ( $m_r(t) > 0$ ) or decrease ( $m_r(t) < 0$ ) the rate of beat generation, corresponding to sympathetic or parasympathetic dominance of the efferent autonomic signal, respectively. Neural control of heart rate in this representation therefore modifies the slope of diastolic depolarization, which corresponds to Mechanism B in Figure 3-6.

The reflex system supplies us with a natural choice for the function  $m(t)$ , or its discrete-time analog  $m[n]$ , namely the inverse of the instantaneous R-R-interval  $I[n]$ ,

$$m[n] = \frac{1}{I[n]} \quad \text{where} \quad I[n] = I_0 + \sum_{k=0}^{k=N} \delta \bar{P}_A[n-k] \cdot (G^p \cdot p[k] + G^s \cdot s[k])$$

In the absence of neural control,  $m[n]$  reduces to the constant  $1/I_0$ , the inverse of the set-point R-R-interval. Increased sympathetic outflow is characterized by a negative convolution integral (corresponding to  $m[n] > 1/I_0$ ) whereas parasympathetic dominance leads to a positive convolution integral (corresponding to  $m[n] < 1/I_0$ ). In this representation of  $m[n]$ , the constant  $\Gamma$  is equal to 1.0.

# Chapter 4

## Model Validation

Having detailed the architecture of and the parameter assignments for the cardiovascular model in the previous two chapters, we now turn our attention to its predictions and their comparison with experimental data.

A word on method: We assigned most parameter values on the basis of literature reviews of largely unrelated clinical studies, so we cannot expect the resultant model to generate cardiovascular data in uniform agreement with a large variety of experimental observations without adapting some of the parameter values. We will therefore find it necessary to adjust a small number of model parameters to match certain key variables for each set of comparisons. We refer to this step as *Model Calibration* and will provide the reader with a clear rationale in each case as to why certain parameters need to be adjusted. We chose the term Model Calibration to emphasize its difference from *Model Optimization*. The latter term will be reserved for a strategy to search for parameter values that optimally (by some quantitative measure) represent a given data set in its entirety. Model Optimization is the topic of Chapter 6.

In Section 4.1 we illustrate the closed-loop operation of the model by quantitatively comparing various blood pressure and blood flow numerics to data reported in healthy recumbent subjects. Section 4.2 expands the scope of the simulations to represent not one typical member of a population of normal subjects but to represent the population itself. In Sections 4.3 and 4.4, we compare to experimental data the steady-state and the transient simulated hemodynamic responses of head-up tilt, standing up, and lower-body negative pressure. The simulation of rapid-onset exercise is the focus of Section 4.5; while this topic is not central to the thesis, it does demonstrate the versatility of the developed model. We close this chapter with some remarks about the forward model.

### 4.1 Baseline Simulation

As pointed out in Section 2.1.2 (p. 28), we assigned parameter values with the goal of representing the cardiovascular state of normal, healthy subjects. We also noted that whether or not we achieved this goal can only be judged once the parameter

Table 4.1: Steady-state hemodynamic variables of normal recumbent adults. Comparison of simulations and experimental data.

Variable	Simulations		Measurements	
	Uncalibrated	Calibrated	Mean <sup>†</sup>	Range
Pressures, mm Hg				
Radial artery <sup>†</sup>				
Systolic	98	104	(135 ± 15.7)	(106–164)
Mean	88	91	(91 ± 8.7)	(75–110)
Diastolic	77	77	(71 ± 7.4)	(64–86)
Peripheral vein				
Mean	9	9	(8 ± 2.5)	(4–13)
Right atrium				
Mean	2	2	(0 ± 1.6)	(-2–2)
Right ventricle				
Systolic	21	24	(25 ± 3.4)	(18–30)
End-diastolic	1	1	(2.6 ± 1.4)	(-0.5–4.5)
Pulmonary artery				
Systolic	20	22	(22 ± 3.7)	(13–30)
Mean	15	16	(17 ± 3.1)	(10–21)
Diastolic	10	10	(12 ± 2.6)	(3–15)
Pulmonary capillary wedge*				
Maximum	12	13	(15 ± 2.9)	(8–23)
Mean	10	10	(12 ± 2.0)	(8–15)
Minimum	9	8	(9 ± 2.2)	(5–14)
Left atrium				
Mean	4	5	(7.9 ± 3.0)	(2–12)
Left ventricle				
Systolic	100	106	(118 ± 16)	(90–140)
End-diastolic	8	8	(8.7 ± 2.3)	(5–12)
Left ventricular end-diastolic volume index, ml/m <sup>2</sup>	62	72	(70±20)	(54–120)
Left ventricular end-systolic volume index, ml/m <sup>2</sup>	32	33	(24±10)	(14–45)
Cardiac index, l/min/m <sup>2</sup>	2.4	2.9	(3.5 ± 0.7)	(2.5–5.3)
Stroke index, ml/beat/m <sup>2</sup>	30	39	(46 ± 8.1)	(37–72)
Heart rate, beats/min	80	75	(79 ± 13.8)	(59–113)
Systemic resistance, PRU	1.17	1.02	(0.85 ± 0.17)	(0.56–1.18)

<sup>†</sup>Mean ± population standard deviation.

<sup>†</sup>Compared to aortic root pressure.

\*Compared to pulmonary venous pressure.

values have been assigned, the model assembled, and its predictions compared to experimental data. Such comparison is the topic of this section.

Using the parameter profile and the general architecture of the hemodynamic and the reflex models, we can generate pressure, flow, and volume waveforms from which we can extract beat-to-beat numerical measures of cardiovascular variables. Under the column title "Simulations – Uncalibrated" in Table 4.1, we summarize steady-state numerics for variables commonly used clinically to assess a subject's cardiovascular state, and compare them to measurements reported for healthy recumbent volunteers under resting conditions [60, 174–178]. The model-derived pressures generally tend to agree with the mean values reported for the normal population. The values derived for stroke volume, cardiac output, and systemic vascular resistance, however, lie outside the range for the normal population and suggest a strategy for refinement of some parameter values.

It seems that these deviations can be reconciled by lowering systemic vascular resistance and increasing the diastolic compliances of the left and right ventricles. The former leads to an increase in venous return whereas the latter enhances cardiac output. Referring to Table 2.4, we note that a reduction of each systemic microvascular resistance by 0.5 PRU is compatible with the normal degree of variability of these parameters. Similarly, diastolic ventricular compliances of approximately 20 ml/mm Hg and 9 ml/mm Hg for the right and the left heart, respectively, are in agreement with experimental findings (see Table 2.7). Finally, we increase the set-point of the cardiopulmonary reflex loop by 1 mm Hg to maintain mean right atrial transmural pressure at 6 mm Hg. In the second data column of Table 4.1, we summarize the simulation results using this slightly altered set of parameter values. The discrepancies between simulations and clinical results pointed out previously have been reduced.

The discrepancies between systolic and diastolic radial artery pressure measurements and their simulated equivalents point to an interesting limitation of the lumped-parameter hemodynamic model, namely its inability to reproduce phenomena that arise as a result of the distributed nature of the cardiovascular system. The example at hand is the well-known phenomenon that the morphology of the arterial pressure waveform changes significantly as a function of location within the arterial system: while mean arterial pressure decreases slightly, peak-systolic pressure increases and diastolic pressure decreases the further distal from the heart the pressure is being measured [see, e.g. 179, p. 176]. This behavior has been linked to the geometric non-uniformity of the arterial system [180, p. 134]. In particular, it has been attributed to changes in the vascular impedance that occur along the arterial system at branching points, at the terminal arterioles, and also along the gradually tapered arterial vessels [181]. Measurements reported from a single subject suggest pulse pressure to increase by about 40 % between the aortic root and the femoral artery [179, p. 176]. Since the effect of taper diminishes in the proximal direction, it is the arterial systolic and diastolic pressure at the root of the aorta that is approximated by our lumped parameter representation.

Furthermore, the lack of inertial effects is evident in Figure 4-1 as the central

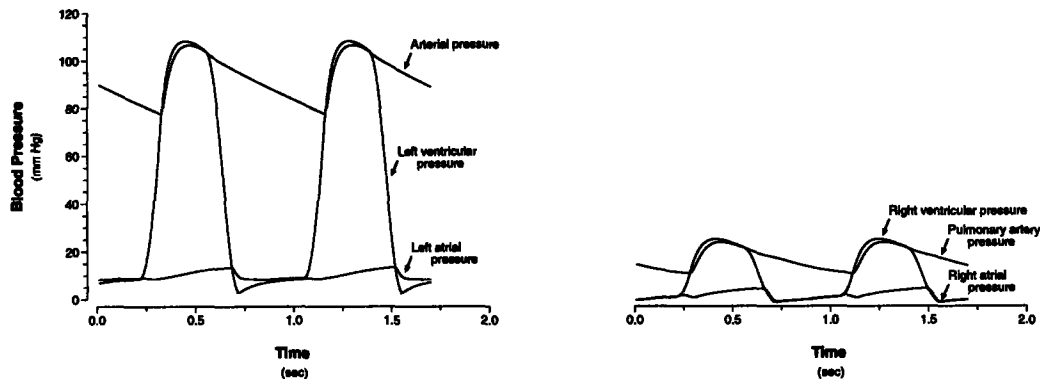


Figure 4-1: Simulated pressure waveforms of the left heart and systemic arterial system (left) and the right heart and the pulmonary artery (right).

arterial and pulmonary arterial waveforms lack the dichrotic notch expected to occur during closure of the semi-lunar valves. Apart from these morphological fine structures, the model represents atrial, ventricular, and peripheral waveforms well.

The analysis so far has centered around the steady-state values of certain cardiovascular variables. In order to probe the dynamic behavior of the cardiovascular model, we need to allow for perturbations of its normal operating conditions. In the sections to follow, we will introduce sudden orthostatic stress as such a challenge to the system. Here, we simply note that the model's response to a simulated Valsalva maneuver reproduces the typical response seen experimentally. Both experimental data and simulations are shown in Figure 4-2, where we simulated the Valsalva maneuver by increasing intra-thoracic and intra-abdominal pressures by 40 mm Hg for a period of 30 s after which the pressures are returned to their normal values.

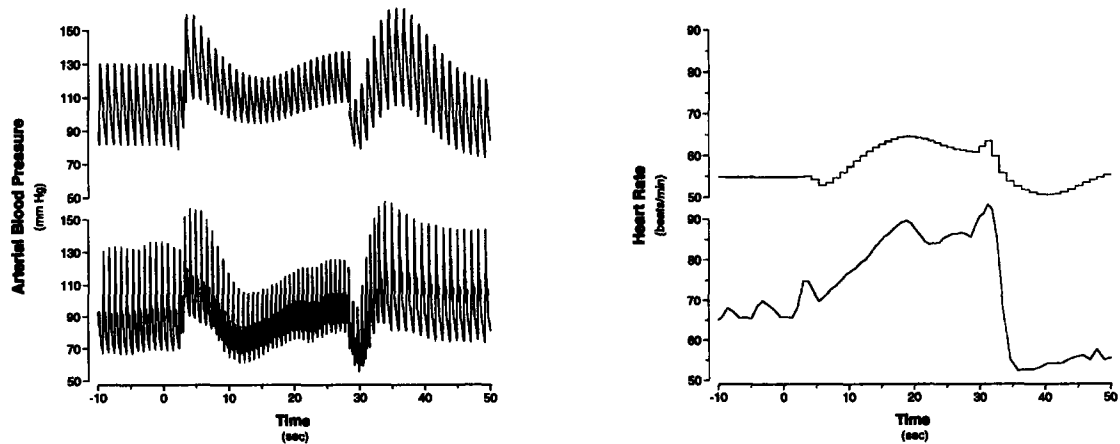


Figure 4-2: Heart rate and arterial blood pressure response to a Valsalva maneuver. Top: simulation result; bottom: experimental recording from one subject.



## 4.2 Population Simulations

The simulations presented in the previous chapter demonstrate that the model is capable of reproducing average cardiovascular variables. Here, “average” refers to the population against which the model response is compared. In this sense, the model framework forms a valid representation of the average cardiovascular state of a healthy population.

Rather than simulating the mean response of a population, a more powerful approach would be to simulate the responses of individual members of the population. On the basis of these responses, one could calculate any desired summary statistic, such as the mean or median response along with their degree of variation. Such an approach presupposes access to a large number of parameter profiles representing the cardiovascular states of the individual members. We could establish such profiles by retracing the arguments presented in Chapters 2 and 3, assuming different anthropometric and cardiovascular variables. This approach would be quite laborious. Instead, we combine the nominal set of parameter values and their standard errors with general allometric scaling laws to generate parameter profiles of subjects with different anthropometric and cardiovascular characteristics. The details of this approach would detract from the theme of this chapter and are therefore presented in Appendix B.

In Table 4.2, we summarize the anthropometric profile of the sampling population based on 500 realizations of the sampling scheme outlined in Appendix B. Table 4.3, presents the population statistics of the numerical cardiovascular measures presented previously in Table 4.1. The data demonstrate that in addition to the mean values, the degrees of variability and the ranges of the population-based simulations generally match their experimental analogs quite well.

Looking ahead, we note that failure of the cardiovascular system to adjust properly to the upright posture is commonly associated with high heart rates and low stroke volumes. We therefore paid particular attention to validating the model’s baseline stroke volume and cardiac output and their response to changes in heart rate. In Figure 4-3, we reproduce the data reported by deSimone and co-workers [62] who studied normalized cardiac output as a function of body weight in children and adults. Our simulations represent adult cardiovascular physiology only and therefore lack the part of the distribution representing children and adolescents. The distribution of

Table 4.2: Anthropometric profile of simulated population.

	Height	Weight	Body Surface Area
	cm	kg	m <sup>2</sup>
Mean	(169 ± 9.1)	(70 ± 14.0)	(1.84 ± 0.21)
Range	(144–202)	(42–117)	(1.38–2.56)

Table 4.3: Comparison of population simulations to steady-state hemodynamic variables of recumbent adults.

Variable	Simulations		Measurements	
	Mean <sup>†</sup>	Range <sup>‡</sup>	Mean <sup>†</sup>	Range
<b>Pressures, mm Hg</b>				
<b>Radial artery*</b>				
Systolic	(107 ± 7.5)	(97–120)	(135 ± 15.7)	(106–164)
Mean	(94 ± 5.1)	(86–103)	(91 ± 8.7)	(75–110)
Diastolic	(79 ± 3.4)	(74–85)	(71 ± 7.4)	(64–86)
<b>Peripheral vein</b>				
Mean	(10 ± 2.8)	(6–15)	(8 ± 2.5)	(4–13)
<b>Right atrium</b>				
Mean	(2 ± 1.7)	(0–5)	(0 ± 1.6)	(–2–2)
<b>Right ventricle</b>				
Systolic	(24 ± 5.9)	(15–35)	(25 ± 3.4)	(18–30)
End-diastolic	(1 ± 2.0)	(–1–4)	(2.6 ± 1.4)	(–0.5–4.5)
<b>Pulmonary artery</b>				
Systolic	(23 ± 6.0)	(13–34)	(22 ± 3.7)	(13–30)
Mean	(17 ± 4.4)	(10–24)	(17 ± 3.1)	(10–21)
Diastolic	(11 ± 3.5)	(8–17)	(12 ± 2.6)	(3–15)
<b>Pulmonary capillary wedge*</b>				
Maximum	(13 ± 3.4)	(8–20)	(15 ± 2.9)	(8–23)
Mean	(10 ± 2.8)	(7–16)	(12 ± 2.0)	(8–15)
Minimum	(9 ± 2.6)	(5–13)	(9 ± 2.2)	(5–14)
<b>Left atrium</b>				
Mean	(5 ± 2.5)	(2–8)	(7.9 ± 3.0)	(2–12)
<b>Left ventricle</b>				
Systolic	(108 ± 7.7)	(98–122)	(118 ± 16)	(90–140)
End-diastolic	(8 ± 2.8)	(5–13)	(8.7 ± 2.3)	(5–12)
<b>Left ventricular end-diastolic volume index, ml/m<sup>2</sup></b>				
	(72 ± 14.7)	(52–96)	(70±20)	(54–120)
<b>Left ventricular end-systolic volume index, ml/m<sup>2</sup></b>				
	(34 ± 9.8)	(18–50)	(24±10)	(14–45)
<b>Cardiac index, l/min/m<sup>2</sup></b>				
	(2.7 ± 0.4)	(2.3–3.4)	(3.5 ± 0.7)	(2.5–5.3)
<b>Stroke index, ml/beat/m<sup>2</sup></b>				
	(38 ± 8.4)	(27–51)	(46 ± 8.1)	(37–72)
<b>Heart rate, beats/min</b>				
	(74 ± 7.8)	(61–87)	(79 ± 13.8)	(59–113)
<b>Systemic resistance, PRU</b>				
	(1.13 ± 0.19)	(0.84–1.48)	(0.85 ± 0.17)	(0.56–1.18)

<sup>†</sup>Mean ± population standard deviation.

\*Compared to aortic root pressure.

<sup>‡</sup>(0.05–0.95) inter-quantile range.

\*Compared to pulmonary venous pressure.

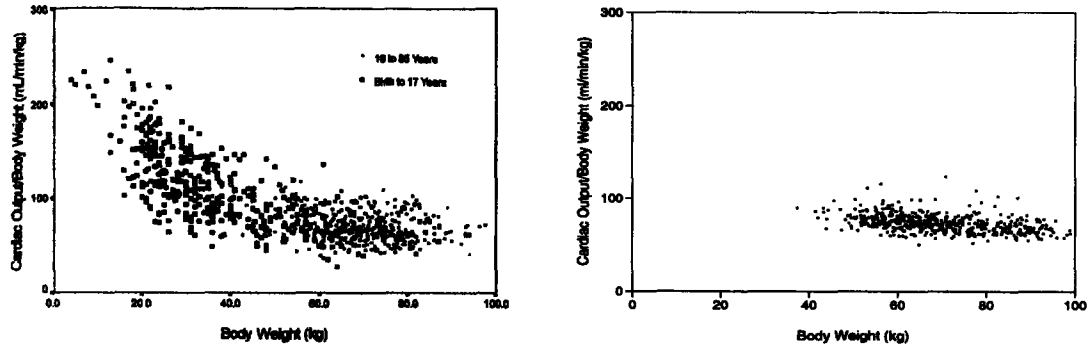


Figure 4-3: Normalized cardiac output as a function of body weight. Experimental data (left) and simulation results (right). Figure on the left adapted from [62].

simulated normalized cardiac output compares quite favorably to the part of the experimental observations it represents.

In Figures 4-4 and 4-5, we reproduce data (solid circles) from an anesthetized canine preparation that demonstrate the effect of heart rate changes on steady-state stroke volume and cardiac output [182]. The data document a reciprocal relationship between heart rate and stroke volume: as heart rate increases, stroke volume decreases monotonically, presumably due to successive shortening of the diastolic ventricular filling phase of the cardiac cycle. Despite the reduction in stroke volume, cardiac output initially increases and subsequently stays relatively constant up to about 200 beats/minute. Further increases in heart rate result in incrementally larger drops in stroke volume and reductions in cardiac output. The latter phenomenon is probably due to sub-optimal relative timing of atrial and ventricular contractions such that the contribution of atrial systolic ejection to ventricular filling volume becomes impaired.

The solid lines in both figures are the mean simulated population responses; the dashed lines bound one standard error of the mean responses. Both simulations and experimental data have been normalized such that the stroke volume and the cardiac output at 160 beats/minute serve as the reference. Simulated and experimental responses agree exceptionally well up to heart rates of about 210 beats/minute when the simulated cardiac output response fails to mimic the pronounced roll-off exhibited by the experimental data. Several explanations seem plausible for this discrepancy. First, the ventricular systolic time interval scales with R-R-interval length according to  $\sqrt{T_{RR}}$ . This relationship is based on a data set not very rich at very high heart rates and might therefore overestimate the systolic and early diastolic time intervals in that regime [98]. Second, we have neglected completely all inertial effects of blood flow, which implies that the cardiac chambers can fill very rapidly. Inclusion of inertial effects will hinder ventricular filling predominantly at high heart rates.

Despite these discrepancies, the model represents well cardiac output in the general population and its behavior as a function of heart rate.

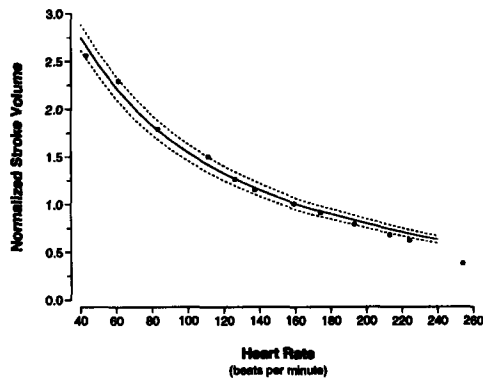


Figure 4-4: Effect of heart rate on stroke volume. Simulation: mean response (solid line)  $\pm$  SE (dashed lines); solid circles: data taken from [182].

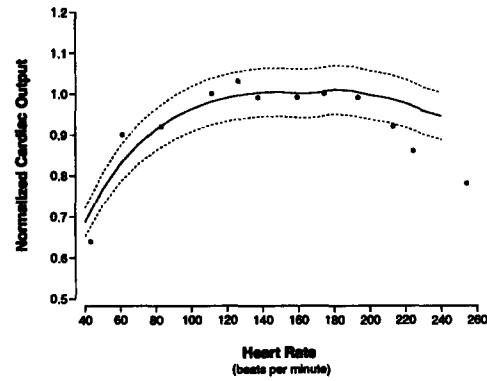


Figure 4-5: Effect of heart rate on cardiac output. Simulation: mean response (solid line)  $\pm$  SE (dashed lines); solid circles: data taken from [182].

### 4.3 Gravitational Stress Simulations

In the previous two sections, we compared the model-predicted steady-state values of several cardiovascular variables to population-averaged data taken from normal subjects in the supine posture. In this section and the section to follow, we will subject the model to orthostatic stress simulations, thus probing the hemodynamic and reflex systems in much greater detail, by comparing the transient hemodynamic responses to experimental data, and also looking at steady-state responses a certain time after the onset of the stress and also

We begin by simulating the experimental protocol by Smith and co-workers [183], who tilted male subjects to various angles for five minutes, with five minutes of supine recovery between tilts. In accordance with their protocol, we report in Figure 4-6 the mean (solid line) simulated change in mean arterial pressure, heart rate, and stroke volume, each averaged over the last three minutes at each level of tilt, along with the approximate 95% confidence limits (dashed lines). At each level of tilt, the simulations are based on 100 realizations from a size-matched population. Figure 4-6 also depicts the experimental data recomputed from [183] to present absolute changes and standard errors (open circles: 15 male subjects of age 20–29; closed circles: 16 male subjects of age 40–49).

In order to achieve these simulations, we estimated from the experimental data a measure of total peripheral resistance [mean arterial pressure/(heart rate  $\cdot$  stroke volume)] at each level of tilt and we adjusted the static gain values of the  $\alpha$ -sympathetic reflex loops to approximate these values of total peripheral resistance at each level of tilt. Furthermore, we had to abandon the equal balance between aortic arch and carotid sinus baroreceptors, and instead hypothesized a dominance of the carotid sinus baroreflex during changes in posture. Teleologically, this hypothesis seems jus-

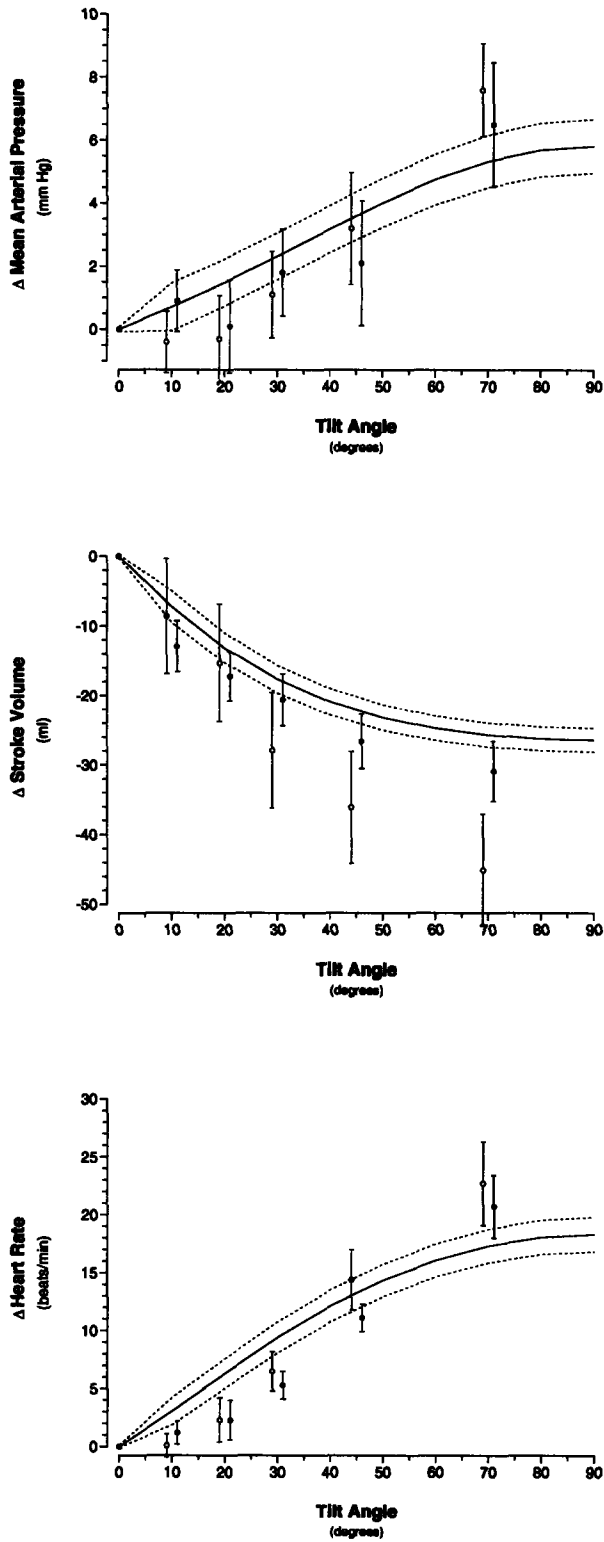


Figure 4-6: Changes in mean arterial pressure (top), stroke volume (middle), and heart rate (bottom) as a function of tilt angle. Simulations: solid lines. Data presented as mean±SE. Open circles: young subjects; closed circles: older subjects. Data adapted from [183].

tifiable given the carotid sinus's importance in maintaining adequate perfusion to the brain and given that the carotid sinus baroreceptors sense a greater fall in arterial blood pressure during changes in posture as compared to the aortic arch receptors. Finally, we increased the sympathetic and the parasympathetic gain values to heart rate slightly.

The experimental results for all three hemodynamic variables are matched quite well by the simulations. Mean arterial pressure and heart rate simulations slightly overestimate the changes seen experimentally at low levels of tilt, possibly suggesting a powerful cardio-pulmonary mediated vasoconstrictor response to be present in humans. The stroke volume simulations generally agree with the experimental data reported for older subjects, but underestimate the changes seen for younger subjects, suggesting that right ventricular filling pressure drops more in the younger population than in our simulations. This could be due to a smaller end-diastolic right ventricular compliance or it could be due to more volume being redistributed to the dependent vasculature during tilt. Despite these minor discrepancies, the simulations approximate the experimental data quite well over the entire range of gravitational stress.

Animal and most human studies agree that the hydrostatic-indifference point on the venous side is located at the level or slightly below the level of the diaphragm [see, e.g., 184]. When simulating a head-up tilt to  $90^\circ$ , the transmural pressure in the inferior vena cava compartment drops whereas the transmural pressure in the abdominal venous compartment rises, indicating that the venous hydrostatic indifference point in our model is located between these two compartments. This result implies that, as in the human circulation, cardiac filling pressure in the model drops on head-up tilt and therefore cardiac performance is dependent on posture.

Figure 4-7 shows the transient responses of mean arterial pressure and heart rate to slow and rapid head-up tilts to  $75^\circ$ , and to standing up, respectively, in ten subjects (lower panels) and the simulations thereof (upper panels). The experimental protocol and results are described in detail in Chapter 7. The simulations are based on 100 realizations from size-matched population simulations; in both figures, we show the mean response (solid line) along with the 95% confidence bands. The experimental data also show the mean response (solid lines) along with the 95% confidence limits (dashed lines).

The simulations are based on a modification of the parameter profile used for the simulations shown in Figure 4-6. Compared to the data shown in Figure 4-7, the data reported by Smith and co-workers [183] show a markedly higher heart rate response at high levels of stress. We therefore returned the sympathetic heart rate gain value to its nominal value and reduced the parasympathetic heart rate gain value slightly below its nominal value. To simulate the transient hemodynamic response to standing, we imposed profiles in external pressures similar to the ones shown in Figure 2-24 of Section 2.4. Measuring rectal pressure changes as surrogates for intra-abdominal pressure changes, Tanaka and co-workers report a peak transient increase of  $(43 \pm 22)$  mm Hg [135]. The transient increase in intra-abdominal pressure occurs at the onset of active standing and lasts for about 2 s. We assumed a somewhat lower value of 18 mm Hg lasting for approximately 3 s.

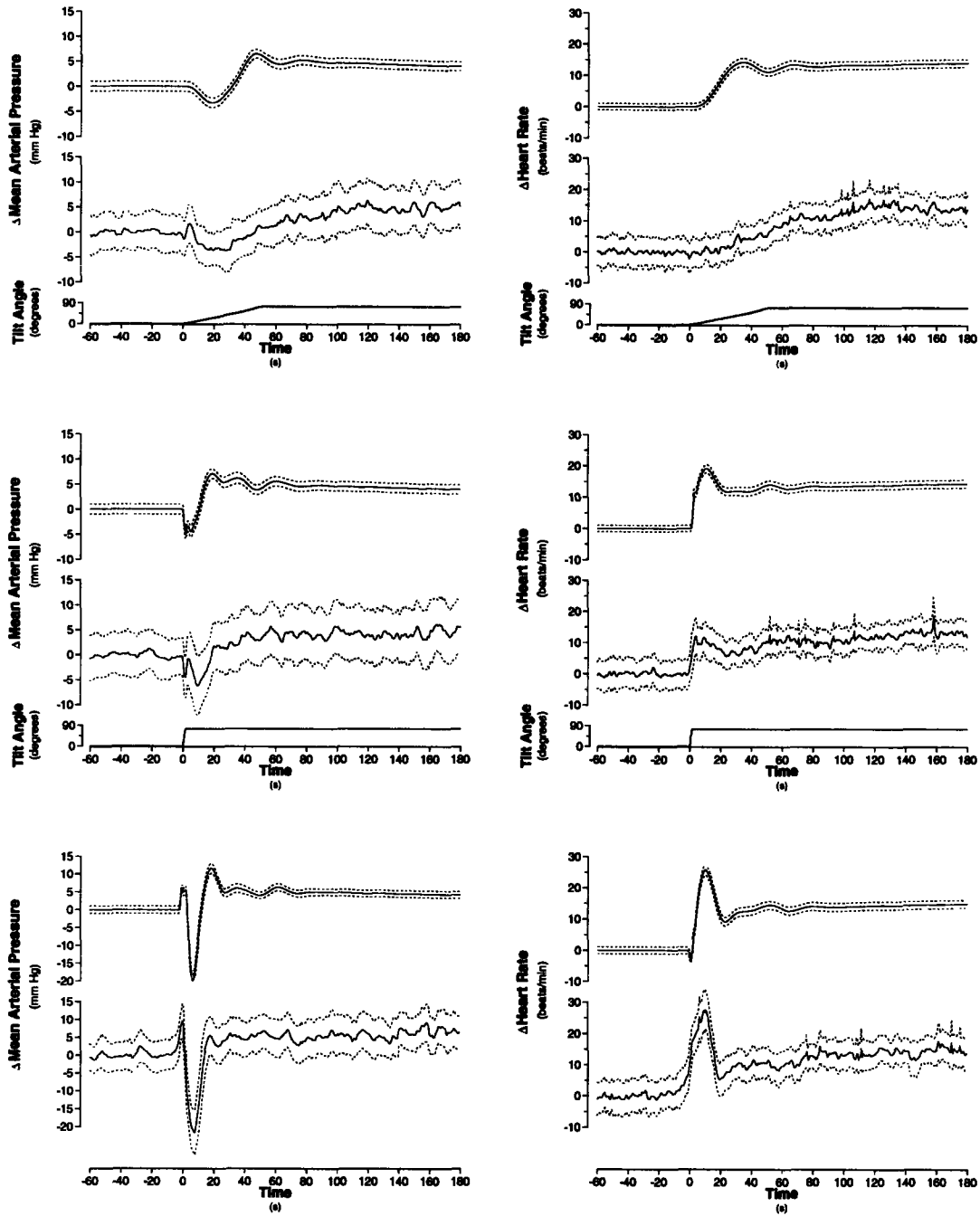


Figure 4-7: Changes in mean arterial pressure (left) and heart rate (right) during slow tilts, rapid tilts, and standing up (top to bottom). Top panels of each figure show simulated responses; bottom panels show experimental data.

While the magnitude and time course of the transient hemodynamic responses to rapid tilt and active standing are well matched by the respective simulations, the simulated response of the slow tilt is less conclusive. The simulations reproduce well the initial drop in mean arterial pressure; the ensuing increases in mean arterial pressure and heart rate, but proceed at a faster rate and generally reflect the profile of the orthostatic stress (which is given by the sine of the tilt angle). The experimental results show a more gradual rise in mean arterial pressure and heart rate. As mentioned above in connection with the steady-state tilt simulations in Figure 4-6, the lack of changes in heart rate at low angles of tilt might be due to a more powerful cardio-pulmonary mediated  $\alpha$ -sympathetic response.

Despite these minor discrepancies of the slow tilt response, the simulated transient responses capture remarkably well the essential features of the transient hemodynamic response to head-up tilt and standing up.

## 4.4 Lower Body Negative Pressure

We based simulations of lower body negative pressure on the work by Ahn and colleagues [160], who studied the hemodynamic response to step-function reductions in external pressure (to  $-20$  mm Hg,  $-40$  mm Hg, and  $-60$  mm Hg) in eight male subjects. Each pressure level was maintained for 5 min, with 30 min of recovery at ambient atmospheric pressure between successive applications of external negative pressures. Due to relatively coarse sampling of the mean arterial blood pressure response in this study, we report in Figure 4-8 experimental data and simulation results at 90 s after the onset of lower body negative pressure. Experimental results are shown as mean changes in hemodynamic variables along with the standard error of the mean. Simulations show the mean population response (solid line) along with the approximate 95% confidence limits of the mean (dashed lines), and are based on 100 realizations at each level of LBNP.

To generate the simulations, we used the parameter profile of the steady-state tilt simulations as the point of departure, and employed the same strategy outlined in the previous section to adjust the peripheral resistance gain values. Specifically, we estimated from the experimental data a measure of total peripheral resistance [mean arterial pressure/(heart rate  $\cdot$  stroke volume)] for each level of LBNP and adjusted the static gain values to match these estimates approximately.

For all three hemodynamic variables, the simulations reproduce the general trend of the data quite well, although a systematic difference in the respective mean responses exist for mean arterial pressure and stroke volume changes.

The hemodynamic response to low-level LBNP is commonly thought to be mediated primarily by the cardio-pulmonary receptors: in response to a drop in right atrial pressure, the low-pressure reflex system responds with vasoconstriction, which keeps mean arterial pressure constant or slightly above baseline despite blood volume being shifted to the leg vasculature. Consistent with this theory, the simulations suggest stable mean arterial pressure and heart rate responses up to about  $-10$  mm Hg despite a reduction in stroke volume. At progressively higher levels of LBNP, the



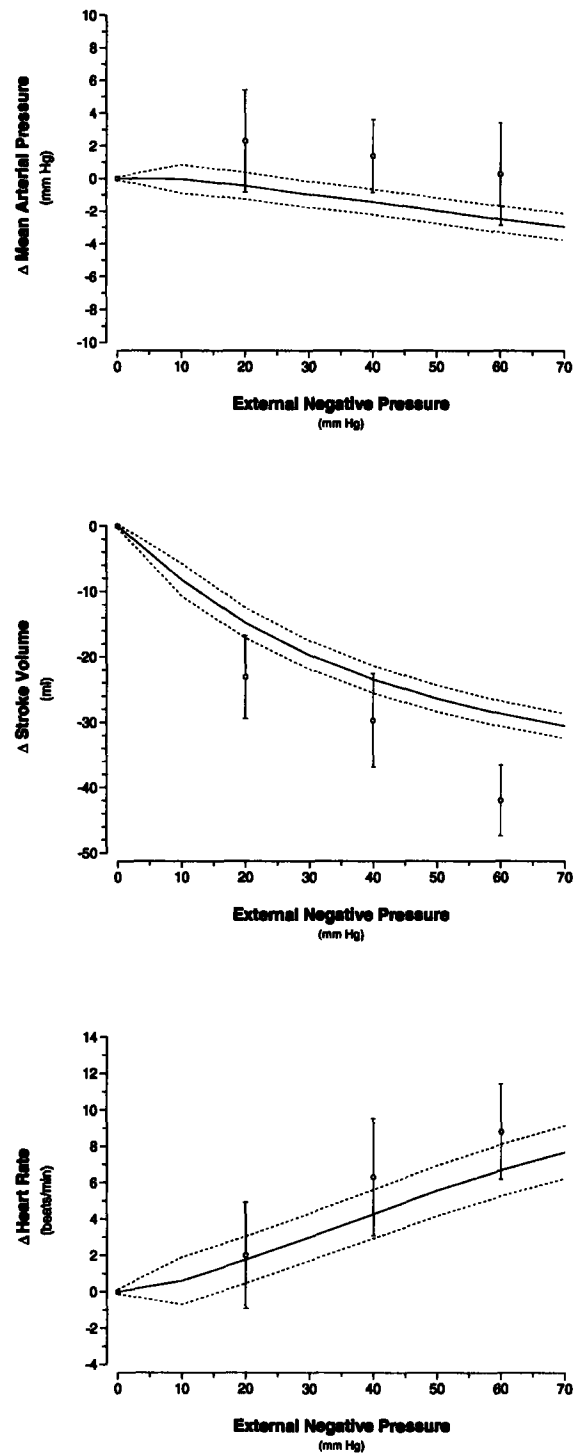


Figure 4-8: Changes in mean arterial pressure (top), stroke volume (middle), and heart rate (bottom) as a function of external negative pressure. Simulations show mean (solid line) and the approximate 95% confidence limits (dashed lines) of the mean. Experimental data (circles; mean $\pm$ SE) are adapted from [160].

arterial baroreceptors become more engaged and the reflex response is mediated by both cardio-pulmonary and arterial baroreceptors, as evidenced by the significant increase in heart rate in simulations and experimental data beyond  $-20$  mm Hg of external pressure. Both simulations and experimental data suggest a gradual decrease in mean arterial pressure at successively higher levels of LBNP. While the simulated mean arterial pressure drops below baseline, the experimental data stay above baseline for each level of LBNP. This might again suggest a more powerful compensatory reflex response in humans as compared to model predictions. However, in this particular experimental study, systolic and diastolic arterial pressures were measured using a sphygmomanometer with Korotkoff sound detection, and mean arterial pressure was inferred with the aid of an empirical formula. The differences in the respective mean arterial pressure responses might very well be within the limits of measurement accuracy using this technique or might be an artifact of the small number of subjects studied. Hisdale [185], for example, reports a drop in mean arterial pressure of 1 mm Hg at the conclusion of a 120 s exposure to  $-20$  mm Hg in twelve subjects. Our simulations predict a drop of approximately 0.5 mm Hg at  $-20$  mm Hg external pressure.

Despite these discrepancies, the simulated hemodynamic response to lower body negative pressure represents the data quite adequately, given that we only matched the peripheral resistance response at each level of LBNP.

## 4.5 Modeling Exercise

From a cardiovascular standpoint, exercise manifests itself primarily through a dramatic increase in cardiac output and blood flow to the exercising muscle groups. Other effects of exercise on the cardiovascular system result from muscular contractions, and include rhythmic muscle-pumping of the leg musculature and an increase in intra-abdominal pressure due to the contraction of abdominal muscles. While changes in breathing pattern might affect intra-thoracic pressure, solid experimental evidence for this is currently sparse. A direct neural coupling between exercising muscle groups and the cardiovascular control center in the brain is possible if not likely. However, little is known about afferent pathways and gains of this reflex loop.

In the following paragraphs, we review the experimental evidence that exists for each of the above mechanisms by which exercise affects cardiovascular function.

**Muscle Blood Flow** Rådegran and Saltin [186] showed that blood flow to an exercising limb increases with a time constant  $\tau \approx 10 - 20$  s. The investigators also demonstrated that the steady-state blood flow to the muscles is linearly related to the exercise intensity over the range of 10 to 70 Watts, and that the longer time constants correspond to the more intense exercise regimes. They report no immediate change in the arterio-venous pressure difference at the level of the femoral artery/vein, which implies that the dramatic increase in blood flow can be attributed to a drop in arteriolar resistance of the leg circulation. At higher exercise intensities (100 to 145 Watts), Pawelczyk and co-workers [187] showed that the leg vascular resistance

fails to decrease further, and that changes in blood flow to the legs are mediated by an increase in perfusion pressure.

The lower body compartment in our model is a lumped representation of the legs, the buttocks, and the pelvic circulation. In order to simulate the increase in leg blood flow and the decrease in total peripheral resistance seen experimentally during exercise, we disconnect the arteriolar resistance of the leg compartment from the arterial and cardiopulmonary reflex control and decrease the leg resistance according to:

$$R_{ll}(t) = R_{ll}^- + (R_f - R_{ll}^-) \cdot (1 - e^{-t/\tau})$$

where  $R_{ll}^-$  is the value of the microvascular resistance of the leg compartment immediately prior to the onset of exercise;  $R_f$  is the final value of the leg vascular resistance for a given level of exercise intensity, and  $\tau$  is the time constant mentioned above.  $R_f$  is determined by matching total peripheral resistance at each level of exercise intensity to the values seen experimentally.

**Muscle Pumps** Arnoldi [134] studied the venous pressure in three different locations in the leg circulation, both at rest and during muscular exercise. He showed that intravascular pressure in the *vena tibialis posterior* changed in phase with muscular contractions. During the contraction phase of the calf muscle, the pressure rose 100 mm Hg above the resting level, whereas during muscular relaxation, the venous pressure dropped approximately 50 mm Hg below the resting level. Venous pressures in two other locations (the *vena poplitea* and the *vena saphena magna*) also showed phasic relationships to muscular contractions. However, the pressure excursions from the respective baselines were modest in comparison to the ones seen in the *vena tibialis posterior*.

The action of a muscle pump is simulated by periodically varying the external bias pressure at the leg compartment. In bicycle ergometry exercise protocols, the angular frequency of cycling is commonly fixed to 1 rev/sec; the exercise intensity is varied through the resistance imposed on the wheels. Thus the sequence of calf muscle contraction and relaxation is periodic with period 1 s. We represented the external pressure at the leg compartment according to:

$$P_{\text{ext}} = \begin{cases} P_{\text{max}} \cdot \frac{1}{2} \cdot (1 - \cos(4\pi t)) & 0 \leq t < 1/4 \\ P_{\text{max}} & 1/4 \leq t < 1/2 \\ P_{\text{max}} \cdot \frac{1}{2} \cdot (1 + \cos(4\pi(t - 1/2))) & 1/2 \leq t < 3/4 \\ 0 & 3/4 \leq t < 1 \end{cases}$$

Here  $P_{\text{max}}$  is the maximal external pressure, which depends on the exercise intensity.

**Intra-Abdominal Pressure** Indirect evidence for a change in intra-abdominal pressure during exercise is given by Williams and Lind [188], who studied esophageal pressures above and below the level of the diaphragm at rest and during static exercise. Their results indicate a modest change in mean intra-abdominal pressure of about 5 mm Hg at a moderate exercise level.

Table 4.4: Parameter assignments for exercise simulations.

Exercise Level	$\tau$	$R_t$	$P_{\max}$	$P_{\text{ext}}^{\max}$	$P_A^{\text{set}}$
Watts	s	PRU	mm Hg	mm Hg	mm Hg
71	15	0.6	7	3	125
97	15	0.52	10	5	155
125	20	0.5	20	10	175
145	20	0.5	30	12	195

To simulate the effects of increased intra-abdominal pressure, we increased the external bias pressure across the abdominal compartments at the onset of exercise according to:

$$P_{\text{ext}} = P_{\text{ext}}^{\max} \cdot (1 - e^{-t/\hat{\tau}})$$

where the time constant  $\hat{\tau}$  is assumed to be on the order of a few seconds and the maximal external pressure  $P_{\text{ext}}^{\max}$  is a function of exercise intensity.

**Mean Arterial Pressure** It is a well established fact that mean arterial pressure rises during dynamic and static exercise and that the increase in mean arterial pressure is both a function of exercise intensity and the number of muscle groups involved in the exercise. Pawelczyk's data indicate that the increase in mean arterial pressure is linear as long as the decrease in total peripheral resistance varies linearly with exercise intensity [187]. Once a further increase in exercise intensity fails to elicit a corresponding decrease in peripheral resistance, mean arterial pressure increases more dramatically probably to maintain adequate blood flow to exercising muscles. Similarly, heart rate and cardiac output increase with exercise intensity presumably to increase the rate of oxygen delivery to the exercising muscle groups.

This behavior suggests that we can no longer assume the cardiovascular control system simply to track mean arterial and mean right atrial pressure in an attempt to keep them constant. Most likely, the cardiovascular control centers receive input from exercising muscles and possibly also from higher centers in the brain. The control system described in Chapter 3 is purely homeostatic in nature, and, if left unaltered, unable to account for the cardiovascular response to exercise. To circumvent this problem, we consider the set-point pressure of the arterial baroreflex an adjustable parameter in this section. We will increase it iteratively to match — at each level of exercise — the increase in mean arterial pressure seen experimentally. Thus, dependent variables like heart rate and stroke volume became amenable to comparison with experimental data.

**Parameter Values** In summary, we have introduced four parameters that need to be specified at each level of exercise. We chose to compare our simulations to the data presented by Pawelczyk, who studied normal healthy volunteers at four different exercise levels. Table 4.4 summarizes the parameter assignments for simulation of his

exercise protocol

The results in Figure 4-9 show the comparison of our simulations to the experimental data presented by Pawelczyk. We generated the simulation of oxygen uptake by multiplying cardiac output,  $CO$ , by the arterio-mixed venous oxygen difference,  $C_{O_2}(a - \bar{v})$  at each level of exercise, i.e.  $\dot{V}_{O_2} = CO \cdot C_{O_2}(a - \bar{v})$ . We took the values of the arterio-mixed venous oxygen difference from Asmussen and Nielsen [189]. The dashed lines in the oxygen uptake simulation represent a one- $\sigma$  confidence level and are based on the standard error of the arterio-mixed venous oxygen difference.

Over the exercise regime considered in the experimental study, the model captures quite well the steady-state changes in heart rate, cardiac output, and oxygen uptake. The simulated changes in stroke volume replicate the ones observed experimentally more qualitatively than quantitatively: an initial increase in stroke volume is followed by decline as the exercise intensity is increased. The faster drop in simulated stroke volume at high exercise intensities might be due to cardiac factors (e.g., inappropriately low inotropic state) or peripheral factors (e.g., inappropriately low venous return).

One should keep in mind, however, that the model was not built with its application to exercise simulation in mind. Given the relatively simple assumptions made in simulating exercise, the results presented in Figure 4-9 are surprisingly good.

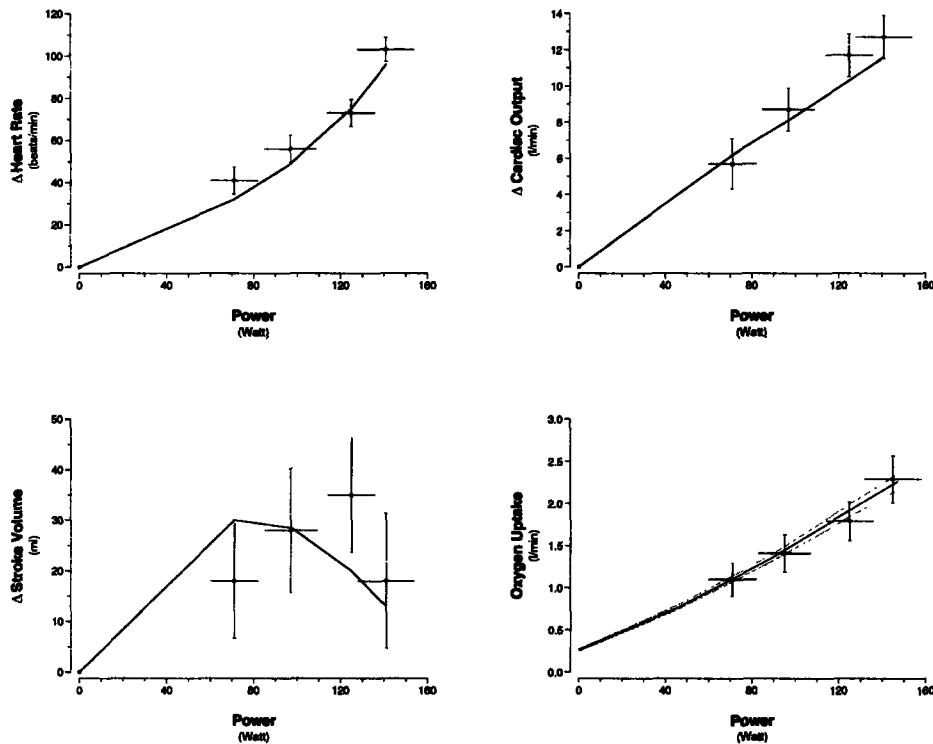


Figure 4-9: Changes in heart rate, cardiac output, stroke volume, and oxygen uptake in response to sudden-onset exercise. Solid lines: simulations; data represent mean  $\pm$  SE, adapted from [187].

## 4.6 Summary Remarks

In this first part of this thesis, we have built and validated a computational model of the cardiovascular system that is capable of representing the short-term steady-state and transient hemodynamic response to orthostatic stress.

To achieve this objective, we chose to model the entire hemodynamic system by a finite set of representative compartments, each of which captures the physical properties of a segment of the vascular system. While this approach is incapable of simulating distributed effects, such as pulse wave propagation, it does reproduce realistic values of beat-by-beat hemodynamic variables, and the simulated steady-state responses to head-up tilt and lower body negative pressure agree well with population averaged experimental observations over a wide range of orthostatic stress levels. In addition, the model is capable of reproducing the transient hemodynamic response to sudden gravitational stress quite well.

For now, we are restricted to simulating the early steady-state response of the cardiovascular system to orthostatic stress, since the reflex control model only represents the major neural control mechanisms that are responsible for short term ( $\lesssim 5$  min) control of blood pressure. Studies have shown that within minutes after the onset of gravitational stress, hormone levels in the circulation rise significantly [36]. The addition of hormone loops in the future might allow us to extend the timescale of our simulations beyond a few minutes.

An inherent limitation to any modeling effort is the degree of uncertainty associated with the numerical values assigned to the various parameters of the model. We have tried as much as possible to give a detailed account of the origin of the parameter values we chose to assign. Where possible, we based nominal parameter values and their standard deviations on the results of clinical studies of normal healthy subjects. When such data was not available, we supplied physiologically plausible mean values, ranges, and standard deviations. This strategy enabled us to estimate error bounds for our simulation results, which generally agree well with those reported in experimental studies.

The degree to which the model reproduces steady-state and transient hemodynamic data suggests that the current model architecture includes all the major features that contribute significantly to the short-term hemodynamic response to orthostatic stress. Residual discrepancies between simulations and experimental observations are likely due to the particular choices of parameter values and not due to structural problems in model architecture. Model Optimization should therefore remedy these residual differences.

Finally, we did not adopt a strategy of minimal modeling. Rather, we built a model with the aim of representing cardiovascular physiology at a resolution that allows for simulation of various hypotheses about the mechanisms of orthostatic intolerance. The model, in its current state, is therefore highly over-parameterized. The sensitivity analysis to follow will identify those parameters of the system that contribute significantly to a particular output of interest, thus reducing the complexity introduced by our modeling approach.

## **Part II**

# **Sensitivity Analyses and Parameter Estimation**





# Chapter 5

## Sensitivity Analysis

When developing the model presented in the previous chapters, we did not strive to find a minimal model capable of representing the experimental observations presented in the previous chapter. Rather, we tried to represent the components of the cardiovascular system that are commonly thought to play significant roles in orthostatic stress physiology. Consequently, the resultant model is quite complex, representing cardiovascular physiology at a variety of time and space scales.

Increasing the complexity of a model can work against its usefulness in many respects: simulation times are increased; parameter values are harder to pick reliably; and it becomes difficult to understand in a fundamental way what parts of the model are actually being exercised and how. The need to develop tools for model analysis becomes quite obvious: only if we are able to identify those components of the model that contribute significantly to a particular simulated response do we actually increase our understanding of the system under study; only if we are able to quantify the effects of parametric uncertainties can we assess the model's range of validity and can we suggest experiments that might help reduce prediction uncertainties<sup>1</sup>. The focus of this chapter is therefore on model analysis and, in particular, on sensitivity studies that help illuminate the influence individual parameters hold over the variability of particular output variables.

We will approach sensitivity analysis from a local perspective, focusing on changes in output variables as the parameters of the model are perturbed about a normal operating point in parameter space. Questions commonly addressed with such local analyses involve propagation of errors or finding a direction in input space along which the output is maximally influenced, thus establishing a local measure of importance of parameters or combinations of parameters.

Section 5.1 serves to introduce the terminology and mathematical routines used in the remainder of this chapter. In Section 5.2, we present the results of the sensitivity analyses. Rather than performing one sensitivity study, we approach the analysis in

---

<sup>1</sup>Uncertainties in mathematical representations of physical or physiological phenomena also arise through the assumed mathematical relationships (structure of the model) and the details of their implementation on computational platforms. We will not pursue these uncertainties here, but assume the model structure and implementation as a framework within which to explore parametric uncertainties.

stages. First, we explore the sensitivities of the uncontrolled hemodynamic system in steady-state. Subsequently, we analyze the controlled cardiovascular system in steady-state, and finally we turn our attention to the steady-state and transient sensitivities during orthostatic stress simulations. We summarize the conclusions of the sensitivity study in Section 5.3.

## 5.1 Local Sensitivity Analysis

When assessing parametric sensitivities, one is interested in the changes  $\Delta \mathbf{y}$  induced in the vector  $\mathbf{y}$  of model outputs as a result of perturbations  $\Delta \boldsymbol{\theta}$  of the vector  $\boldsymbol{\theta}$  of model parameters. Before presenting how  $\Delta \mathbf{y}$  and  $\Delta \boldsymbol{\theta}$  are related in the framework of local sensitivity analysis, we briefly review the nature of the model output  $\mathbf{y}$ .

The cardiovascular model presented in previous chapters generates values for blood pressures, blood flows, vascular volumes, cardiac capacitances, and controlled variables, such as heart rate and arterial resistance, with a temporal granularity of the integration stepsize (on the order of  $10^{-3}$  s). Often, one might be interested in the parameters that affect an entire waveform, such as the arterial or central venous pressure waveforms, for example. In such cases, the output vector  $\mathbf{y}$  consists of the samples of the waveform of interest, and sensitivities are explored for each sample in the waveform. If one is interested in analyzing more than one waveform, the model output  $\mathbf{y}$  can consist of several waveforms, appropriately normalized and stacked on top of each other. Quite frequently, however, one is not interested in the sensitivities of individual samples within a cardiac cycle, but rather in the sensitivities of derived features of these waveforms and how these sensitivities change under transient conditions. Examples of derived features are the mean value, the peak value, or maximum slope of a particular waveform on a beat-by-beat basis. In this case, the output vector  $\mathbf{y}$  consists of all derived features that are of interest, possibly ordered by beat number if transient changes in these features are of interest.

In the analysis to follow, we focus our attention on just four derived output variables, namely cycle-averaged arterial pressure, cycle-averaged central venous pressure, stroke volume, and heart rate, each of which is defined on a beat-by-beat basis. Focusing on the cycle-averaged changes of just four output variables constitutes a significant aggregation of the model's output data. However, these four derived variables are the most significant measures of cardiovascular performance, which is the reason for choosing them.

During the first part of the sensitivity analysis, we will be concerned with the parametric sensitivities of just the steady-state values of these output variables. The output vector  $\mathbf{y}$  in this case simply consists of the steady-state cycle-averaged values of the four variables over one steady-state cycle. Towards the end of this chapter, we will explore the parametric sensitivities of the output variables during the model's transient response to orthostatic stress simulations. For this, the output vector will consist of 2400 samples: each variable is sampled at 2 Hz over one minute of supine baseline and four minutes in the head-up posture. To summarize, the output vector can be written as  $\mathbf{y} = [y_1, y_2, \dots, y_n] \in \mathcal{R}^n$ , where  $n = 4$  for the steady-state analyses

and  $n = 2400$  for the transient sensitivity study. Similarly, the vector of parameters is given by  $\boldsymbol{\theta} = [\theta_1, \theta_2, \dots, \theta_m] \in \mathcal{R}^m$ , where  $m = 107$  is the number of independent parameters of the model.

The effects of parameter changes  $\Delta\theta_j$  on changes  $\Delta y_i$  in a particular output variable can be expressed in terms of a Taylor series expansion:

$$\Delta y_i = \sum_{j=1}^m \frac{\partial y_i}{\partial \theta_j} \Delta \theta_j + \frac{1}{2} \sum_{j=1}^m \sum_{k=1}^m \frac{\partial^2 y_i}{\partial \theta_j \partial \theta_k} \Delta \theta_j \Delta \theta_k + \dots, \quad i = 1, \dots, n$$

The partial derivatives  $\partial y_i / \partial \theta_j$  and  $\partial^2 y_i / \partial \theta_j \partial \theta_k$  are commonly called the first- and second-order local sensitivities [190], respectively, while the matrix of the first partial derivatives

$$\mathbf{J}(\boldsymbol{\theta}) = \frac{\partial \mathbf{y}}{\partial \boldsymbol{\theta}} = \left( \frac{\partial y_i}{\partial \theta_j} \right)_{\substack{i=1, \dots, n \\ j=1, \dots, m}} \in \mathcal{R}^{n \times m}$$

is variously referred to as the sensitivity matrix, the Jacobian matrix, or the Fréchet derivative.

The partial derivative  $\partial y_i / \partial \theta_j$  is an obvious choice for a linear or first-order measure of the local sensitivity of the model output to parameter perturbations, because for small enough  $\Delta \theta_j$  it gives a good approximation to  $\Delta y_i / \Delta \theta_j$  assuming all other parameters stay fixed. The second-order derivative  $\partial^2 y_i / \partial \theta_j \partial \theta_k$  ascertains the sensitivity of the first-order sensitivity  $\partial y_i / \partial \theta_j$  with respect to changes in  $\theta_k$ , and therefore provide information about the quadratic dependence of the model output on parameter changes.

As defined above, however, the numeric values of the sensitivity coefficients depend on the units of measurement of both the output variables and the parameters; in order to compare sensitivities across different input and output variables, the partial derivatives need to be normalized to render them non-dimensional. A commonly used normalization scheme scales the partial derivatives by the nominal outputs and nominal parameter values:

$$\left( \frac{\partial y_i}{\partial \theta_j} \right)_{\substack{i=1, \dots, n \\ j=1, \dots, m}} \rightarrow \left( \frac{\theta_j^0}{y_i^0} \cdot \frac{\partial y_i}{\partial \theta_j} \right)_{\substack{i=1, \dots, n \\ j=1, \dots, m}}$$

$$\left( \frac{\partial^2 y_i}{\partial \theta_j \partial \theta_k} \right)_{\substack{i=1, \dots, n \\ j, k=1, \dots, m}} \rightarrow \left( \frac{\theta_j^0 \theta_k^0}{y_i^0} \cdot \frac{\partial^2 y_i}{\partial \theta_j \partial \theta_k} \right)_{\substack{i=1, \dots, n \\ j, k=1, \dots, m}}$$

to relate fractional changes in output to fractional changes in the parameter values [191].

While efficient methods exist to co-compute accurately the sensitivity matrix along with the actual simulation output, these methods are most powerful when the number of output variables and parameters is small. We rely on a finite-difference approximation to the analytical partial derivatives. Experimentation with the stepsize in a two-sided finite-difference method revealed generally good approximations for stepsizes of about 5% of the nominal parameter values. Owing to the relative efficiency of the

associated computations, we routinely compute the first-order sensitivities,  $\partial y_i / \partial \theta_j$ , and the “pure” second-order sensitivities,  $\partial^2 y_i / \partial \theta_j^2$ , for each parameter. Both are  $O(m)$  computations for fixed  $n$ , where, as above,  $m$  is the number of parameters and  $n$  is the number of output variables. Assessment of the cross-term second-order sensitivities,  $\partial^2 y_i / \partial \theta_j \partial \theta_k$  ( $\forall j, k; j \neq k$ ), is computationally substantially more expensive, namely  $O(m^2)$ .

## 5.2 Results and Discussion

As alluded to in the introductory comments to this chapter, we will perform sensitivity studies in stages, first examining the parametric sensitivities of the steady-state values of the four output variables in the uncontrolled hemodynamic system before repeating the analysis for the controlled system. We then turn our attention to the analysis of the steady-state response to orthostatic stress, and finally investigate the sensitivities of the transient response. Building up the sensitivity studies in such a way allows us to test our understanding of the observed sensitivities at each stage, thus providing more insight into the results than a single sensitivity study would be able to provide.

In the figures to follow, we display the normalized first-order sensitivities (filled circles) along with the normalized pure second-order sensitivities (open circles), ranked in descending order of the magnitudes of the first-order sensitivities. We also display separately the top twenty cross term sensitivities for each analysis, including pure terms if they occur in these top twenty. For each output, we identify by their respective parameter indices<sup>2</sup> the most important parameters (i.e., highest first-order sensitivity) or, in the case of cross sensitivities, parameter combinations.

Figure 5-1 shows the first-order and pure second-order sensitivity spectra for the four output variables when the analysis is applied to the uncontrolled hemodynamic system; Figure 5-2 shows the second-order cross-sensitivities. Before commenting on the importance of particular parameters, several general observations can be made from these graphs. First, the spectra of the first-order sensitivity coefficients for mean arterial pressure, central venous pressure, and stroke volume exhibit the same general structure: a large number of parameters (70% – 80%) have negligible influence on the output variables as evidenced by the long tail of the distributions at very low relative sensitivities; a small number (4 – 10) of parameters hold significant influence over the output variables and are variably offset from the remainder of parameters; a variable number of parameters constitute an intermediate set gradually joining these two extremes. The structure of the three sensitivity spectra confirms our intuition that the model is heavily over-parameterized.

A further observation is that even the largest few of the normalized second-order sensitivities are only a fraction (one half or less) of the largest first-order sensitivities. In the Taylor series expansion, these second-order sensitivities get multiplied by the *square* of the normalized parameter perturbations (and by the further factor of 1/2). It follows that the contribution of the terms involving the second-order sensitivities

---

<sup>2</sup>See Appendix A for the key to parameter indices.

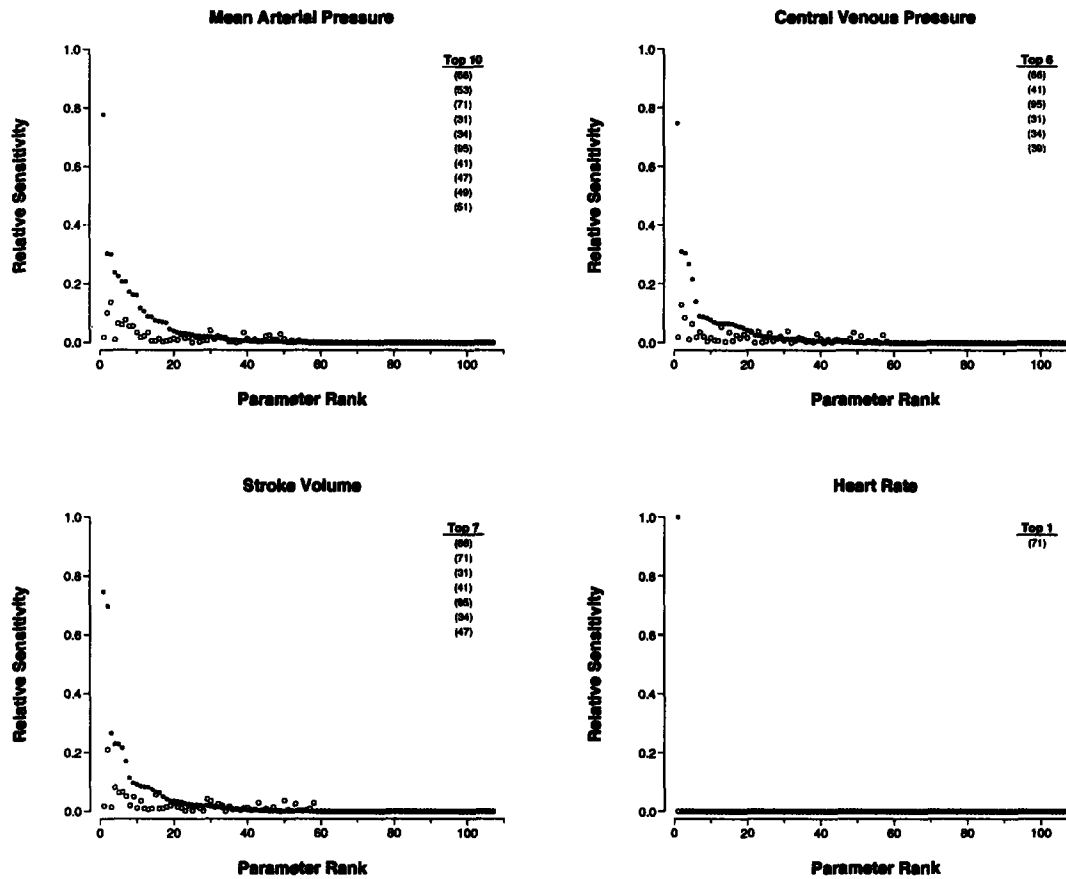


Figure 5-1: Absolute values of relative parametric sensitivities of the uncontrolled hemodynamic model. Solid circles: first-order sensitivities; open circles: “pure” second-order sensitivities.

will be negligible compared to the terms involving the first-order sensitivities, as long as the normalized parameter perturbations are not larger than 10 – 20%. It is also worth remarking that in general the largest second-order sensitivity seem to involve parameters that are also prominent among those with high first-order sensitivities.

The heart rate sensitivity spectrum does not fit the description just given. In the uncontrolled system, heart rate is a parameter rather than a variable whose value is determined in part through the action of the reflex system. Being a parameter, heart rate is trivially dependent on its own set-point value which is reflected in the spectrum by a single relative sensitivity of unit value and a corresponding second-order sensitivity that is identically zero.

As indicated in the figure, there is significant overlap among the top parameters of the four output variables: seven parameters suffice to account for the top five parameters of all four output variables. These seven parameters are distending blood volume (66)<sup>3</sup>, the arteriolar resistance of the splanchnic vascular bed (53), heart rate

<sup>3</sup>Numbers in parentheses indicate parameter indices. See Appendix A for a mapping of parameter

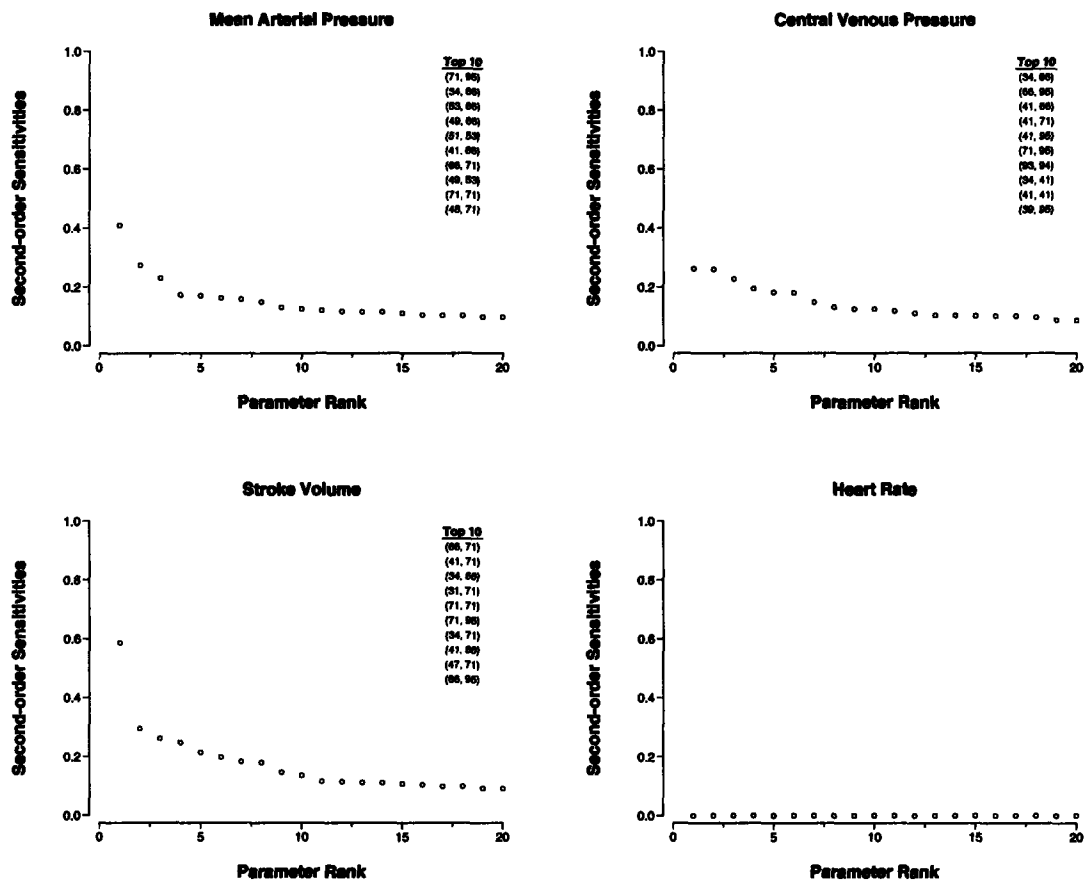


Figure 5-2: Absolute values of the second-order relative parametric sensitivities of the uncontrolled hemodynamic model.

(71), intra-thoracic pressure (31), the venous compliance of the splanchnic vascular bed (34), the ventricular systolic time interval (95), and the right ventricular diastolic compliance (41).

According to the results presented in Figure 5-1, the principal determinants of stroke volume are distending blood volume (66), heart rate (71), intra-thoracic pressure (31), right ventricular diastolic compliance (41), ventricular systolic time interval (95), venous capacitance of the splanchnic vascular bed (34), and left ventricular diastolic compliance (47). To understand these dependencies, we recall that under normal physiological conditions, stroke volume is determined by the end-diastolic filling of the right ventricle. As such, it is dependent on the end-diastolic transmural pressure and the end-diastolic ventricular compliance. The latter is a parameter of the model and features prominently in the hierarchy of sensitivity coefficients. The former involves the luminal right atrial pressure and the intra-thoracic pressure. Thus, intra-thoracic pressure directly affects ventricular filling and therefore stroke volume. Right

---

indices to parameter names.

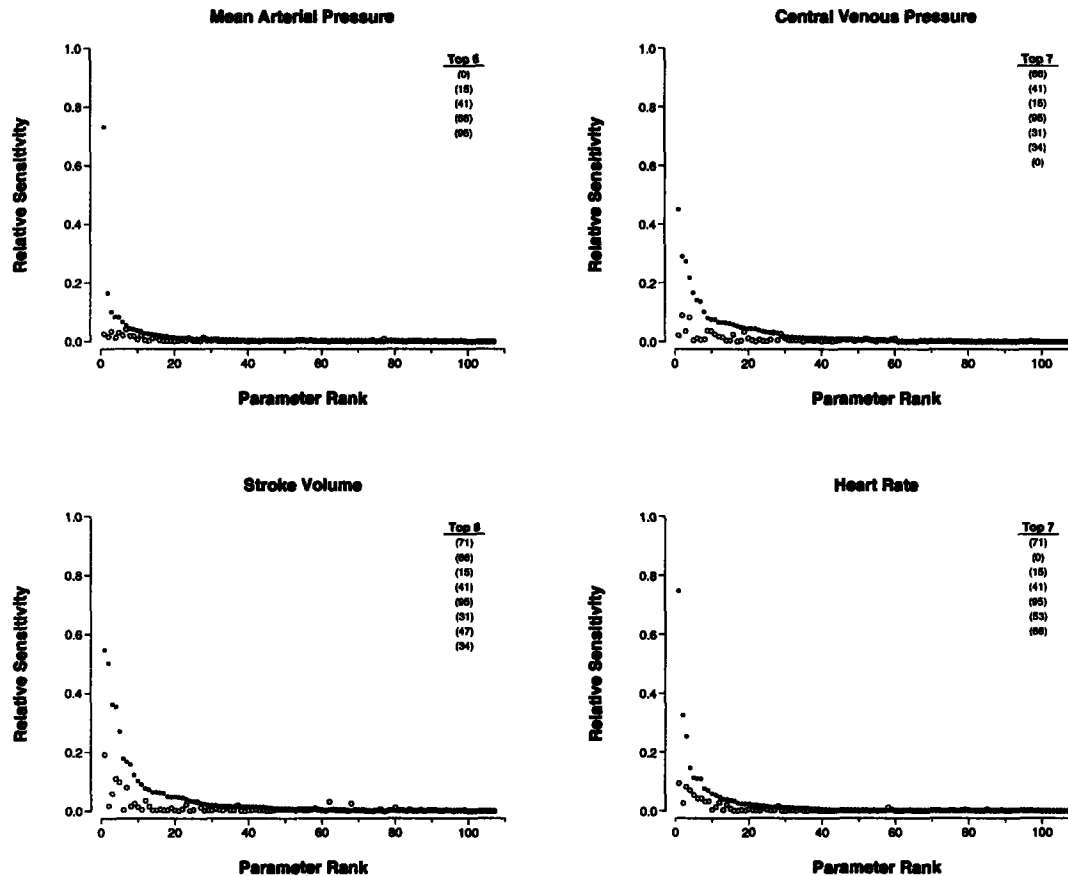


Figure 5-3: Absolute values of relative parametric sensitivities of the controlled hemodynamic model. Solid circles: first-order sensitivities; open circles: “pure” second-order sensitivities.

atrial luminal pressure is largely dependent on distending volume (top sensitivity in the spectrum) and systemic venous compliance. The splanchnic bed has the largest venous compliance of any vascular bed in our model; its influence on cardiac filling pressure is therefore largest, which explains its occurrence in the sensitivity spectrum. Finally, ventricular volume is dependent upon the time available for diastolic filling. This is reflected by the heart rate and possibly systolic time interval sensitivities in the stroke volume spectrum in Figure 5-1. Systolic time interval might also influence stroke volume through the time-varying elastance model as the systolic time interval determines the rate of change of the ventricular elastance and therefore the rate of change of ventricular pressure.

Having understood the sensitivities involved in the steady-state analysis of stroke volume, we only need to note that in addition to the parameters that affect stroke volume, the mean arterial pressure spectrum shows the splanchnic arteriolar resistance (53) as an important parameter. In steady-state, mean arterial pressure is determined to first approximation by cardiac output and total peripheral resistance. Total pe-

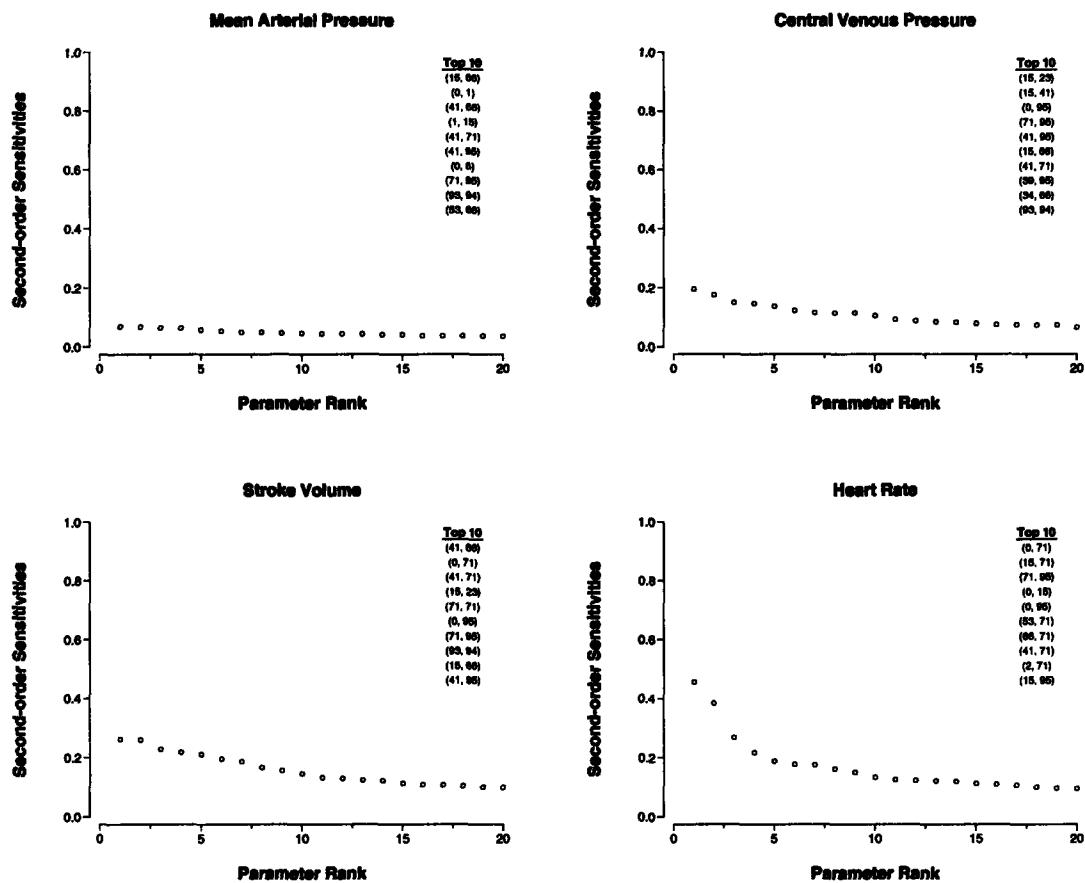


Figure 5-4: Absolute values of second-order relative parametric sensitivities of the controlled hemodynamic model.

ipheral resistance is principally determined by the arteriolar resistances of the four parallel systemic vascular beds. Fractional perturbations to the smallest resistance therefore has the largest impact on total peripheral resistance, which is the reason behind mean arterial pressure being particularly sensitive to changes in splanchnic arteriolar resistance.

Finally, the results presented in Figure 5-1 indicate that central venous pressure is most sensitive to distending blood volume (66), right ventricular diastolic compliance (41), ventricular systolic time interval (95), intra-thoracic pressure (31), splanchnic venous compliance (34), and right atrial diastolic compliance (39). The dependence on right atrial and ventricular diastolic compliances as well as the ventricular systolic time interval is to be expected, because they determine cardiac filling and thus stroke volume, as detailed above. Since most of the distending volume resides in the systemic venous circulation, changes in either the systemic venous capacitance or the distending volume significantly affects central venous pressure, as is reflected in the sensitivity spectrum.

Figure 5-2 shows the top twenty second-order sensitivities of the uncontrolled



system. The second-order sensitivities mostly decline gradually rather than exhibiting the gap structure seen in the first-order spectra. Also, the values of the largest second-order sensitivities for each output variable tend to be smaller in magnitude than the corresponding first-order sensitivities. Finally, the top second-order sensitivities are almost exclusively comprised of combinations of parameters that also feature prominently high in the first-order sensitivity spectra.

Figure 5-3 shows the sensitivity spectra for the four output variables for the *controlled* cardiovascular system. The general appearance of the sensitivity spectra is similar to the one of the uncontrolled system in that the output is sensitive only to a small number of parameters. The peak first-order sensitivities generally tend to be smaller than in the uncontrolled system, which can be ascribed to the homeostatic control of mean arterial and mean right atrial pressure: the parameter perturbations invariably result in perturbations of mean arterial and mean right atrial pressures which lead to reflexive adjustment of effector variables and therefore in reductions of the sensitivity values. Generally, the same parameters that rank high in the sensitivity spectra of the uncontrolled system rank high in the corresponding spectra of the controlled system. In the controlled cardiovascular system, two additional parameters, the arterial baroreflex pressure set-point (0) and the cardiopulmonary reflex pressure set-point (15), enter the top group of parameters.

Since heart rate is now a dependent variable rather than a parameter, its sensitivity spectrum is non-trivial now, and similar in shape to those of the other three output variables. In addition to depending on its own set-point value, heart rate is sensitive to changes in the two reflex set-point pressures and to variables that mostly affect stroke volume and arterial blood pressure. Mean arterial pressure becomes a controlled variable, which is reflected in its strong dependence on its own set-point pressure and the depression of the remaining parameters in its first- and second-order sensitivity spectra.

In Figure 5-5, we examine the parametric sensitivities of the four output variables at the conclusion of a three-minute tilt to the 75° head-up position. We chose this particular time point as it is the recommended reference point for the diagnosis of orthostatic hypotension [29]. The structure of the first-order sensitivity spectra remains almost unchanged from the steady-state analysis of the controlled cardiovascular system. Minor changes in the gap structure and in the ranking of individual parameters are apparent. The distance from the carotid sinus to the aortic root (14), the length of the inferior vena cava compartment (96), and the venous compliance of the legs (35) enter the first-order sensitivity spectra due to their importance in determining the sensed arterial pressure, venous return to the right heart, and the blood volume pooled during orthostatic stress, respectively. The only notable change in the structure of the second-order sensitivity spectra is the isolation of the top three second-order sensitivity coefficients in the spectrum of the steady-state heart rate response. The spectra of the three other output variables largely stay the same.

The sensitivity coefficients of the cycle-averaged quantities we have been examin-

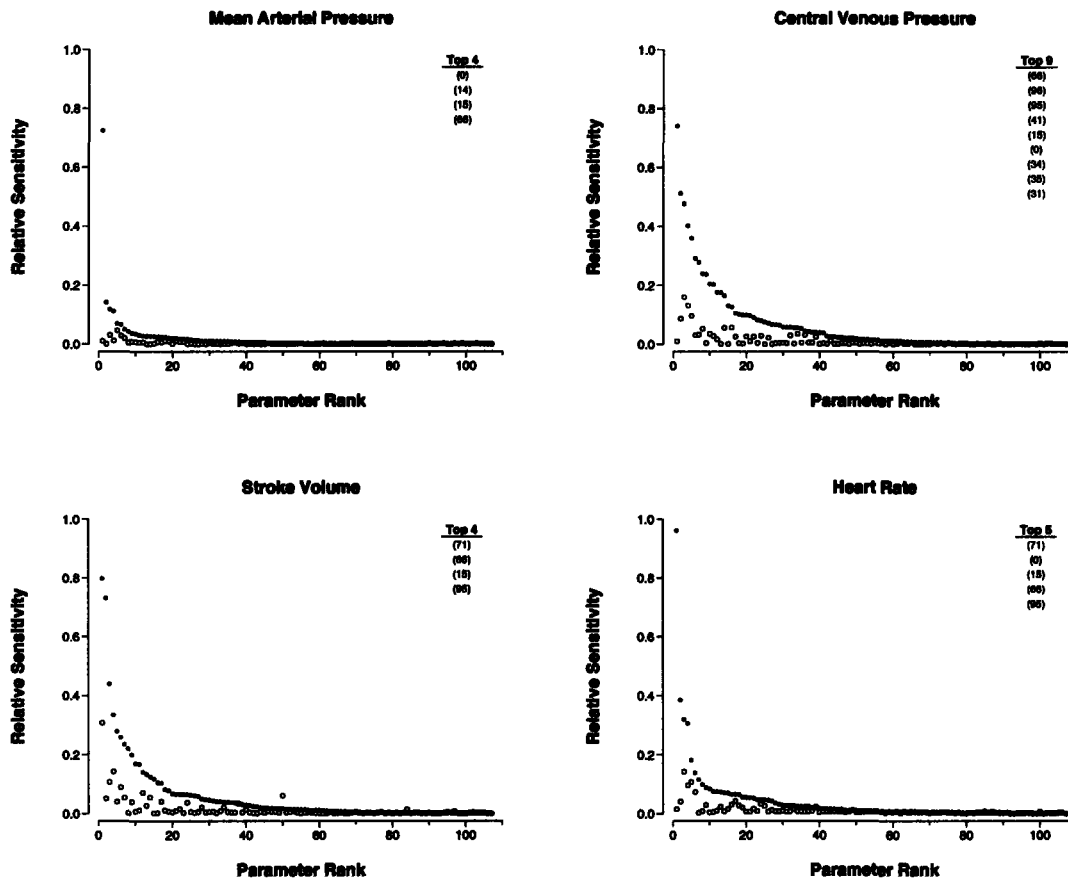


Figure 5-5: Absolute values of relative parametric sensitivities of the controlled hemodynamic system at the conclusion of gravitational stress. Solid circles: first-order sensitivities; open circles: “pure” second-order sensitivities.

ing will evolve from beat to beat if the system is undergoing a transient, rather than being in (cyclic) steady state, for instance during simulations of orthostatic stress tests. Figures 5-1 through 5-6 therefore represent just one snapshot of the continuously evolving sensitivity coefficients. In Figure 5-7, we show the ranges of the absolute values of the beat-to-beat first-order sensitivity coefficients over the entire period of the three-minute tilt to  $75^\circ$ , including a two-minute supine baseline period. The ordering of the parameters is the same as in Figure 5-5.

The general shape of the sensitivity spectra in Figure 5-7 is quite comparable to the ones discussed in previous figures. However, the numerical values of the sensitivity coefficients, and therefore the relative importance of particular parameters, depend quite strongly on when the sensitivities are computed, as indicated by rather large numeric ranges observed for some parameters.

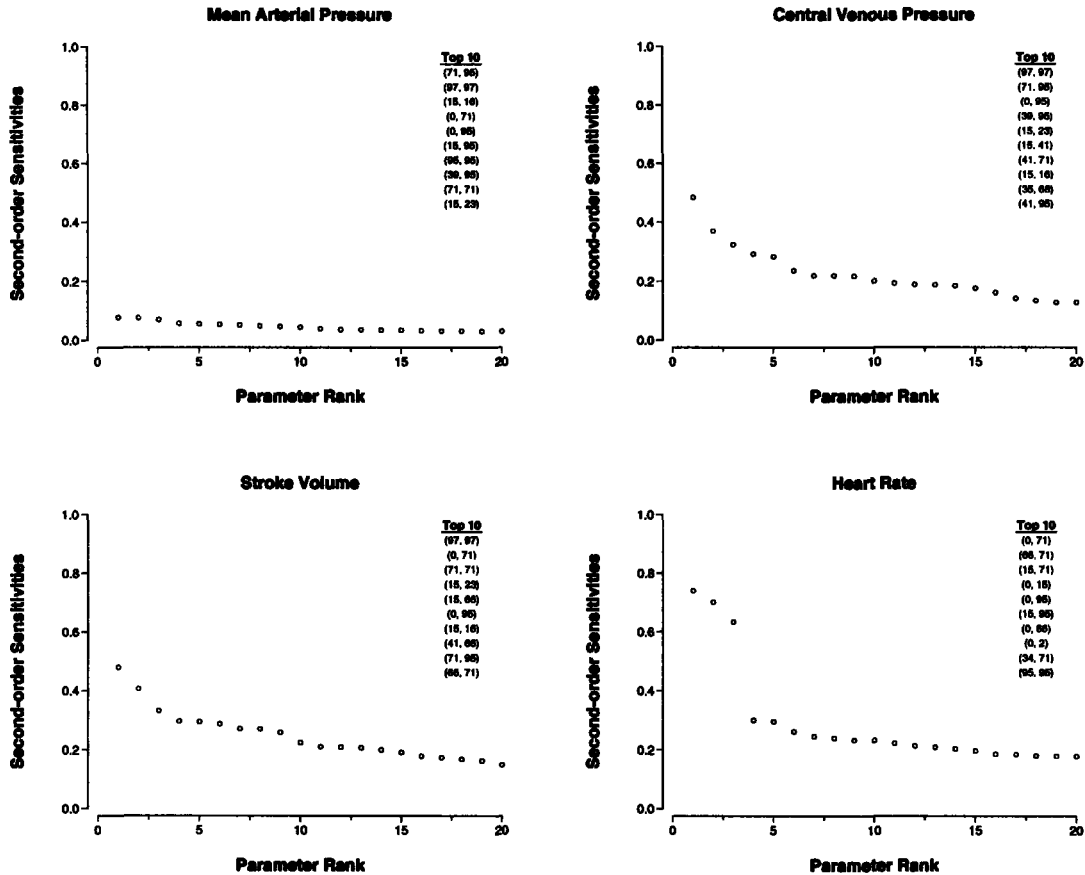


Figure 5-6: Absolute values of second-order relative parametric sensitivities at the conclusion of gravitational stress.

### 5.3 Summary and Conclusions

In the previous section, we have investigated the local first- and second-order sensitivities of four output variables to the 107 parameters of the model. While we have focused our attention on ranking the parameters from very important to non-influential on the basis of the magnitudes of their first-order sensitivity coefficients, we have to keep in mind that the analysis presented is truly local, in the sense that it is only valid in the neighborhood of the local operating point. Furthermore, we have seen that during transient simulations, the sensitivity spectra depend quite strongly on time. The notion of a parameter hierarchy therefore becomes a function of time and operating point rather than being a universal concept. However, several general conclusions can still be drawn from the results presented in the previous section.

As elaborated on in the previous section, the normalized first-order sensitivity spectra all exhibit a similar structure: a long tail at very low relative sensitivities, a small number of parameters at high relative sensitivities, and an intermediate zone of variable length joining the two extremes. For the steady-state analyses shown

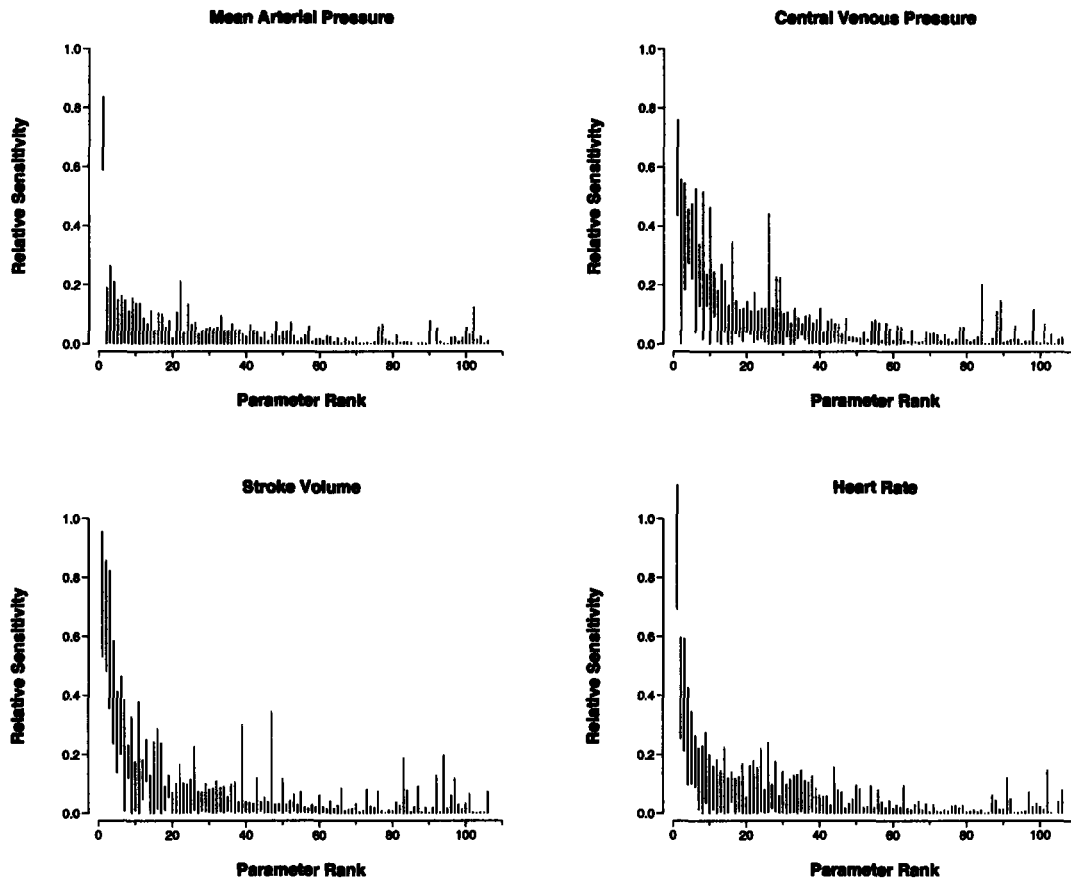


Figure 5-7: Ranges of the relative parametric sensitivities of the controlled hemodynamic system during gravitational stress. Ordering of parameters is the same as in Figure 5-5.

in Figures 5-1 – 5-5, approximately 70 – 80% of parameters can be labeled non-influential while only about 5% of the parameters have significant impact on the steady-state values of the four output variables. The second-order sensitivities are sufficiently small that their effect is negligible for normalized parameter variations of up to 10 – 20%.

Several parameters rank consistently high in the sensitivity analysis and are variably offset from the remainder in the first-order sensitivity spectra. These are the arterial baroreflex set-point pressure (0), the cardio-pulmonary set-point pressure (15), distending blood volume (66), and the heart rate set-point (71). The ventricular systolic timing parameter (95) and the right ventricular diastolic compliance (41) complement the list of top-ranking parameters for stroke volume and central venous pressure.

The arterial baroreflex and the cardio-pulmonary reflex set-point pressures determine the steady-state values of mean arterial and mean right atrial pressure, respectively. However, they also affect the transient response to gravitational stress through their influence on the effector variables. In the absence of homeostatic blood

pressure control, the heart rate set-point determines heart rate completely. In the presence of neural control, it only partially determines heart rate, as reflex fluctuations contribute to the instantaneous heart rate signal. Nevertheless, the heart rate set-point remains an important determinant of the instantaneous heart rate signal. It also affects, along with the systolic ventricular timing parameter, the time period for cardiac filling, thus affecting central venous pressure and stroke volume. Finally, distending volume is universally important to all four output variables.

Several other parameters enter the hierarchy of top parameters, depending on the intervention being simulated, on when in the intervention the analysis is performed, and where in parameter space the model is being exercised.



# Chapter 6

## Parameter Estimation

Our modeling strategy has focused on building a computational model based on our understanding of the cardiovascular system. More specifically, in Chapters 2 and 3 we developed the model based on analysis of the physical and dynamic properties of the various segments of the vasculature and the reflex system. The resultant model has relatively high spatial and temporal resolution for its ultimate application, involves a large number of parameters, and exhibits rich dynamic behavior spanning several time scales. Such an approach, in which a model is built from detailed analysis of the underlying physical processes, is commonly referred to as *forward modeling*.

In this chapter, we will change perspective and use data in conjunction with our model to estimate the values of some of the model parameters. Such a strategy falls under the general umbrella of *inverse methods* in which attributes of a system are estimated based on measurements that are only indirectly related to these attributes [192]. In parameter estimation problems, the parameters of a model are tuned such that a measure of error between the model output and a corresponding set of observations is minimized. Methods for solving this minimization problem depend quite naturally on the error criterion and on the structure of the model. Furthermore, the quality of the resultant parameter estimates also depends on the fidelity of the available data.

The signals available from physiological experiments are usually very few in number. Quite often, the only signals recorded are beat-to-beat mean arterial pressure and heart rate. Thus a disparity exists between the high resolution and rich dynamic behavior of the model and the low resolution and limited dynamic behavior of the measurements. In Chapter 5, we have already encountered one aspect of this mismatch between high detail of the model and low richness of cycle-averaged data: the four output variables of the sensitivity analysis were insensitive to perturbations in a large number of model parameters. In the parameter estimation setting, this disparity leads to a very sensitive, or *ill-conditioned*, estimation problem. Any parameter estimation scheme in this setting needs to address this ill-conditioning.

In Section 6.1, we discuss the error criterion and the method of solving the minimization problem. In particular, we will discuss the method of *subset selection* to overcome ill-conditioning of the estimation problem. In Section 6.2, we present the results of the parameter estimation algorithm when applied to the transient hemo-

dynamic response to head-up tilt. We conclude in Section 6.3 by summarizing the results.

## 6.1 Non-linear Least Squares and Subset Selection

If the model outputs are linear functions of the model parameters, and if the error measure is chosen to be the sum of squares of the prediction error on each output, the resultant minimization problem is the well-known *linear least squares problem*. If the model output is a *non-linear* function of the parameters, the minimization problem is usually solved iteratively through a sequence of linear least squares problems that involve the gradient or higher-order derivatives of the cost function.

Below, we first discuss a particular iterative scheme, known as the Gauss-Newton method. We subsequently point out the manifestation of ill-conditioning in terms of the condition number of the Hessian matrix  $H$ , and describe the subset selection algorithm that aims to overcome this ill-conditioning. We conclude by giving implementational details and describing the formulation of the estimation experiments, the results of which will be presented in the next section.

### 6.1.1 Non-linear Least Squares Estimation

Let  $\Phi(\hat{\mathbf{y}}(\boldsymbol{\theta}), \mathbf{y})$  denote a non-negative measure of error, or cost function, between model output  $\hat{\mathbf{y}}(\boldsymbol{\theta}) \in R^n$  and experimental data  $\mathbf{y} \in R^n$ . Through the model output,  $\Phi$  is an implicit function of the vector of model parameters  $\boldsymbol{\theta} \in R^m$  and can therefore be considered a function from  $R^m$  to the non-negative real line,  $\Phi = \Phi(\boldsymbol{\theta}) : R^m \rightarrow R^+ \cup \{0\}$ , for a given experimental data set. Since we aim to minimize this measure of error iteratively, we seek a computational scheme that provides us with a new parameter vector  $\boldsymbol{\theta}_1$  such that  $\Phi(\boldsymbol{\theta}_1) < \Phi(\boldsymbol{\theta}_0)$  given an initial best guess  $\boldsymbol{\theta}_0$ . Once such a  $\boldsymbol{\theta}_1$  has been identified, it can assume the role of  $\boldsymbol{\theta}_0$ , and we can repeat the computational scheme in an effort to reduce the measure of error even further.

Let us assume that a second-order Taylor series approximation  $\Psi$  of  $\Phi(\boldsymbol{\theta})$  is a good approximation of the local behavior of the cost function for small perturbations  $\Delta\boldsymbol{\theta} = \boldsymbol{\theta} - \boldsymbol{\theta}_0$  around the initial parameter estimate. [ $\Psi(\boldsymbol{\theta})$  is the best second-order approximation to the surface defined by  $\Phi(\boldsymbol{\theta})$  around  $\boldsymbol{\theta}_0$ .]  $\Psi(\boldsymbol{\theta})$  is given by

$$\Psi(\boldsymbol{\theta}) = \Phi(\boldsymbol{\theta}_0) + \left[ \frac{\partial\Phi}{\partial\boldsymbol{\theta}} \right]_{\boldsymbol{\theta}_0} \Delta\boldsymbol{\theta} + \frac{1}{2} \Delta\boldsymbol{\theta}^T \left[ \frac{\partial^2\Phi}{\partial\boldsymbol{\theta}^2} \right]_{\boldsymbol{\theta}_0} \Delta\boldsymbol{\theta}$$

where  $[\partial\Phi/\partial\boldsymbol{\theta}]_{\boldsymbol{\theta}_0}$  and  $[\partial^2\Phi/\partial\boldsymbol{\theta}^2]_{\boldsymbol{\theta}_0}$  are the appropriate matrices of the first- and second-order derivatives evaluated at the current best guess of the parameter vector as indicated by the subscript  $\boldsymbol{\theta}_0$ . To find its minimum, we equate to zero the gradient of  $\Psi(\boldsymbol{\theta})$ :

$$\frac{\partial}{\partial\boldsymbol{\theta}} \Psi(\boldsymbol{\theta}) = \left[ \frac{\partial\Phi}{\partial\boldsymbol{\theta}} \right]_{\boldsymbol{\theta}_0} + \left[ \frac{\partial^2\Phi}{\partial\boldsymbol{\theta}^2} \right]_{\boldsymbol{\theta}_0} \Delta\boldsymbol{\theta} = 0$$



which leads to the following condition for the stationary point  $\theta_1$ :

$$\left[ \frac{\partial^2 \Phi}{\partial \theta^2} \right]_{\theta_0} (\theta_1 - \theta_0) = - \left[ \frac{\partial \Phi}{\partial \theta} \right]_{\theta_0}$$

If the inverse of the second-order derivative matrix exists, the stationary point is given by:

$$\theta_1 = \theta_0 - \left[ \frac{\partial^2 \Phi}{\partial \theta^2} \right]_{\theta_0}^{-1} \cdot \left[ \frac{\partial \Phi}{\partial \theta} \right]_{\theta_0} \quad (6.1)$$

It can be shown that  $\Phi(\theta_1) < \Phi(\theta_0)$  if and only if the matrix of second-order derivatives is positive definite [193, p. 86].

Note that we have not yet specified the cost function  $\Phi$ . The results obtained so far only require it to be twice differentiable. Let us assume now that we are aiming to minimize the square of the residual error  $\mathbf{r}(\theta) = \hat{\mathbf{y}}(\theta) - \mathbf{y}$  between model output and actual measurements, that is

$$\Phi(\theta) = \frac{1}{2} \cdot \|\mathbf{r}(\theta)\|^2 = \frac{1}{2} \cdot \|\hat{\mathbf{y}}(\theta) - \mathbf{y}\|^2 = \frac{1}{2} \cdot \mathbf{r}^\top \mathbf{r} \rightarrow \min$$

where the factor of 1/2 has been included for convenience, and the superscript  $\top$  denotes transposition. The gradient of this cost function is given by:

$$\left[ \frac{\partial \Phi}{\partial \theta} \right] = \mathbf{J}^\top \cdot \mathbf{r}(\theta) \quad \text{where} \quad J_{ij} = \frac{\partial r_i(\theta)}{\partial \theta_j} = \frac{\partial \hat{y}_i(\theta)}{\partial \theta_j}$$

$\mathbf{J} \in R^{n \times m}$  denotes the Jacobian matrix of the error vector with respect to the parameter vector. Similarly, we can compute the elements of the Hessian matrix  $\mathbf{H} \in R^{m \times m}$  of second derivatives of the cost function:

$$H_{ij} = \frac{\partial^2 \Phi}{\partial \theta_i \partial \theta_j} = (\mathbf{J}^\top \mathbf{J})_{ij} + \sum_{l=1}^n r_l \cdot \frac{\partial^2 r_l}{\partial \theta_i \partial \theta_j} \quad (6.2)$$

Note that for small residuals, the Hessian can be approximated by

$$H_{ij} = \frac{\partial^2 \Phi}{\partial \theta_i \partial \theta_j} \approx (\mathbf{J}^\top \mathbf{J})_{ij} \quad (6.3)$$

since the second term involves the elements of the vector of residuals directly. This approximation is known as the Gauss-Newton approximation to the Hessian.

Inserting the expressions for the derivatives into Equation 6.1, we obtain the iterative parameter updates of the Newton method:

$$\mathbf{H} \cdot (\theta_{i+1} - \theta_i) = -\mathbf{J}^\top \cdot \mathbf{r} \quad (6.4)$$

and the Gauss-Newton approximation thereof:

$$\mathbf{J}^\top \mathbf{J} \cdot (\theta_{i+1} - \theta_i) = -\mathbf{J}^\top \cdot \mathbf{r} \quad (6.5)$$

Let  $\mathbf{R}$  denote either the full Hessian  $\mathbf{H}$  or its Gauss-Newton approximation  $\mathbf{J}^T \mathbf{J}$ . If  $\mathbf{R}$  has full column rank, Equations 6.4 and 6.5 can be solved exactly or in a least squares sense, depending on whether or not  $\mathbf{J}^T \cdot \mathbf{r}$  is in the column space of  $\mathbf{R}$ . In either case, however, the solution is unique, and efficient algorithms exist to solve the set of linear equations numerically [see, e.g., 194, Chapter 5]. If, on the other hand,  $\mathbf{R}$  is rank-deficient, then the  $m$  columns of  $\mathbf{R}$  actually contain less than  $m$  linearly independent vectors. As a consequence,  $\mathbf{R}$  is semi-definite with at least one of its eigenvalues at zero. The following argument by Burth and co-workers [195] illustrates the problem of a singular matrix  $\mathbf{R}$  in the context of parameter estimation. Assume  $\mathbf{R}$  has a single eigenvalue at zero with some associated eigenvector  $\boldsymbol{\vartheta}$ . Within the limits of our second-order approximation,  $\boldsymbol{\vartheta}$  can be added to any step direction without affecting the error criterion, since

$$\mathbf{R} \cdot (\boldsymbol{\theta}_{i+1} - \boldsymbol{\theta}_i + \boldsymbol{\vartheta}) = \mathbf{R} \cdot (\boldsymbol{\theta}_{i+1} - \boldsymbol{\theta}_i) + \mathbf{R} \cdot \boldsymbol{\vartheta} = \mathbf{R} \cdot (\boldsymbol{\theta}_{i+1} - \boldsymbol{\theta}_i) = -\mathbf{J}^T \cdot \mathbf{r}$$

This implies that we can arbitrarily change parameter values along the direction of  $\boldsymbol{\vartheta}$  without affecting the error criterion. Such indeterminacy suggests that the parameters of the model cannot be estimated uniquely from the given measurements; the estimation problem is said to be ill-conditioned.

Frequently, the matrix  $\mathbf{R}$  is not exactly rank deficient but quite nearly so, in the sense that the largest eigenvalue is orders of magnitude larger than the smallest eigenvalue. Closeness to singularity is measured by the condition number  $\kappa(\mathbf{R})$  which, for real, symmetric matrices, is given by the ratio of the largest to the smallest eigenvalue.

Burth reviews several related consequences of a large condition number for estimation problems [195]. We simply note here that a hallmark of an ill-conditioned problem is its extreme sensitivity to small perturbations in either the experimental data or the elements of the matrix  $\mathbf{R}$ . In the following section, we discuss subset selection as an approach to overcome this ill-conditioning.

## 6.1.2 Subset Selection

Subset selection aims to determine which parameter axes lie closest to the singular directions of the Hessian matrix [196]. Changes in the corresponding parameters do relatively little to change the fit of the model to the data, and therefore these parameters are hard to estimate reliably. Once these ill-conditioned parameter axes are identified, one can fix the associated parameters at prior values throughout the estimation process, thus improving the conditioning of the resultant reduced-order estimation problem. Fixing values of the ill-conditioned parameters has the effect of introducing some bias error into the model, but by removing these parameters from the estimated set, we improve the reliability with which the remaining parameters are estimated.

Subset selection is most powerful if the eigenvalue spectrum of the Hessian matrix exhibits a large gap between  $\rho$  large eigenvalues and  $m - \rho$  small ones. Such a situation suggests that the Hessian matrix has numerical rank  $\rho$  and that  $m - \rho$

appropriately chosen parameters should be fixed. Equations 6.4 and 6.5 then only involve reduced-order Hessian and Jacobian matrices, which we will denote by  $\mathbf{H}_\rho$  and  $\mathbf{J}_\rho$ , respectively.

The following subset selection algorithm for non-linear least squares estimation is based on the work of Vélez-Reyes [196] and is essentially an extension of a subset selection algorithm for the linear least squares problem [194, 197].

1. Given an initial estimate  $\boldsymbol{\theta}_0$ , compute the Hessian  $\mathbf{H}(\boldsymbol{\theta}_0)$  and its eigenvalue decomposition  $\mathbf{H} = \mathbf{V}\boldsymbol{\Lambda}\mathbf{V}^\top$ .
2. Determine  $\rho$  and an ordering of the eigenvalues in the decomposition such that the first  $\rho$  eigenvalues of  $\mathbf{H}$  are much larger than the remaining  $m - \rho$ .
3. Partition the matrix of eigenvectors according to  $\mathbf{V} = [\mathbf{V}_\rho \ \mathbf{V}_{m-\rho}]$ .
4. Determine a permutation matrix  $\mathbf{P}$  by constructing a QR decomposition with column pivoting [194, p. 248] for  $\mathbf{V}_\rho^\top$ , i.e. determine  $\mathbf{P}$  such that

$$\mathbf{V}_\rho^\top \cdot \mathbf{P} = \mathbf{Q} \cdot \mathbf{R}$$

where  $\mathbf{Q}$  is an orthogonal matrix and the first  $\rho$  columns of  $\mathbf{R}$  form an upper triangular matrix.

5. Use  $\mathbf{P}$  to re-order the parameter vector  $\boldsymbol{\theta}$  according to  $\tilde{\boldsymbol{\theta}} = \mathbf{P}^\top \boldsymbol{\theta}$ .
6. Make the partition  $\tilde{\boldsymbol{\theta}} = [\tilde{\boldsymbol{\theta}}_\rho^\top \ \tilde{\boldsymbol{\theta}}_{m-\rho}^\top]^\top$ , where  $\tilde{\boldsymbol{\theta}}_\rho^\top$  contains the first  $\rho$  elements of  $\tilde{\boldsymbol{\theta}}$ . Fix  $\tilde{\boldsymbol{\theta}}_{m-\rho}$  at a prior estimate  $\hat{\tilde{\boldsymbol{\theta}}}_{m-\rho}$ .
7. Compute the new estimate of the parameter vector  $\hat{\tilde{\boldsymbol{\theta}}}$  by solving the reduced-order minimization problem

$$\hat{\tilde{\boldsymbol{\theta}}} = \arg \min_{\tilde{\boldsymbol{\theta}}} \Phi(\tilde{\boldsymbol{\theta}}) \quad \text{subject to} \quad \hat{\tilde{\boldsymbol{\theta}}}_{m-\rho} = \tilde{\boldsymbol{\theta}}_{m-\rho}$$

The eigenvalue decomposition in the first step is a pre-requisite for the determination of the numerical rank of  $\mathbf{H}$  and the subset selection step. The rank determination in step 2 is based on reasonably sized gaps in the eigenvalue spectrum. Such gaps might not exist, and in those cases subset selection is only of limited help. Usually several gaps of differing sizes can be identified and one has to choose between including more parameters and keeping the condition number of the reduced order Hessian  $\mathbf{H}_\rho$  small. The former choice usually increases the reduced-order model's ability to represent experimental data, while the latter leads to more reliable estimation of the remaining parameters. The numerical rank estimate tells us how many parameters to include in our analysis. Step 4, the actual subset selection step, determines *which* parameters to include. This information is encoded in the permutation matrix  $\mathbf{P}$ . Step 5 reorders the parameter vector  $\boldsymbol{\theta}$  such that the  $\rho$  dominant parameters move to the top of the vector. Steps 6 and 7 describe the reduced-order estimation step.

### 6.1.3 Numerical Implementation

The computations of the Jacobian and Hessian matrices have been described in Section 5.1.

There are three major computational steps associated with the subset selection algorithm outlined above: the eigenvalue decomposition of the Hessian matrix; the QR-decomposition with column pivoting of the matrix of eigenvectors; and the least-squares estimation of the reduced-order problem.

To solve the eigenvalue problem, we were guided by Algorithms 8.3.1 – 8.3.3 from Golub and van Loan [194, p. 415–421]. We start by converting the real, symmetric Hessian matrix  $H$  to a symmetric tridiagonal matrix through a sequence of similarity transformations based on Householder reflections [198]. Subsequently, the lower right-hand tridiagonal 2-by-2 submatrix is diagonalized iteratively through a sequence of implicit, symmetric QR steps with Wilkinson shifts using Givens rotations [199]. This step is repeated on the next trailing lower right-hand tridiagonal 2-by-2 submatrix until the entire tridiagonal matrix is diagonalized. The resultant matrix carries the eigenvalues of the Hessian along the diagonal. By accumulating the sequence of similarity transformations, we assemble the matrix of eigenvectors. Finally, we apply permutation matrices to reorder the columns of the eigenvalue and the eigenvector matrices such that the diagonal matrix contains the eigenvalues in descending order of their magnitudes.

We implemented the QR-decomposition of the eigenvector matrix  $V$  according to Businger and Golub [200]. The algorithm applies a sequence of Householder reflections to the columns of  $V$  so that the lower diagonal portion of each column is successively set to zero. At each step of this reduction to upper triangular form, the algorithm chooses the column with the largest sum of squares to be reduced next, thus implementing the column pivoting strategy. The same QR-decomposition is at the core of the algorithm for solving the reduced-order least-squares problem. The algorithm consists of a QR-decomposition of the reduced Jacobian matrix, the application of the transposed orthogonal matrix  $Q^T$  to the vector of residuals, and solution of the resultant set of equations through backsubstitution. Finally, we use an iterative refinement scheme to improve the estimate of the solution vector.

We implemented the subset selection algorithm in the C programming language and extended the program to run on a five nodes, ten processors, Linux-based parallel computational platform using the message-passing interface.

### 6.1.4 Formulation of the Estimation Problem

In the following section, we apply the subset selection algorithm to the problem of estimating parameter values from the transient hemodynamic response of transitions from supine to the upright posture. In keeping with the analysis of the previous chapter, the vector of output variables consists of cycle-averaged arterial pressure, cycle-averaged central venous pressure, stroke volume, and heart rate. Each variable is computed on a beat-by-beat basis, linearly interpolated between beats, and re-sampled at 2 Hz. We include one minute of supine baseline data and four minutes in

the upright posture leading to an output vector  $\hat{\mathbf{y}}(\boldsymbol{\theta})$  that contains 2400 samples. We normalize this output vector by the samples of the data vector  $\mathbf{y}$ , so the elements of the output vector are unitless. Thus, we aim to minimize the *relative* error between simulation output and measurements:

$$\tilde{\Phi}(\boldsymbol{\theta}) = \frac{1}{2} \cdot \tilde{\mathbf{r}}^\top \tilde{\mathbf{r}} \quad \text{where} \quad \tilde{r}_i = \frac{\hat{y}_i(\boldsymbol{\theta}) - y_i}{y_i}$$

We similarly normalize the columns of the Jacobian matrix by the elements of the target vector.

In this chapter, we are interested in evaluating the performance of the subset selection algorithm as applied to our computational model. In order to do so, we need to know the true parameter values underlying the experimental data that the algorithm is supposed to match. We therefore use the cardiovascular model in a forward sense to generate synthetic “measurements” that serve as the target for the estimation routine.

We will approach the evaluation in two stages. In the first stage, we will fix the ill-conditioned parameters at their “true” values; the only parameter values that differ between  $\boldsymbol{\theta}_0$  and the target “measurements” are the well-conditioned parameters. This approach allows us to assess the quality of the resultant parameter estimates in the absence of possible influences from the ill-conditioned parameters. In the second stage, we vary all parameters to generate the target data. More precisely, we generate the “measurements” by randomly perturbing the parameter vector  $\boldsymbol{\theta}$  around its nominal value  $\boldsymbol{\theta}_0$  using a Gaussian density with mean  $\boldsymbol{\theta}_0$  and standard deviation of 10 % of each parameter’s nominal value. In both stages, we generated the target vector by simulating the transient response to a 75° degree head-up tilt using the perturbed parameter vector. We subsequently reset the parameter vector to  $\boldsymbol{\theta}_0$  in order to start the estimation procedure.

To assess the estimation algorithm’s sensitivity to noise in the target data, we added to the target vector zero-mean Gaussian white noise with a standard deviation of 2.5 % of each target sample.

Finally, we will exclusively work with the Gauss-Newton approximation of the Hessian matrix since it is computationally much less expensive to compute than the full Hessian.

## 6.2 Results

Figure 6-1 shows the eigenvalue spectrum  $\{\lambda_i\}$  of the approximate Hessian matrix  $\mathbf{H}(\boldsymbol{\theta}_0) = \mathbf{J}^\top \mathbf{J}$ . Since the spectrum covers almost eight orders of magnitude, we plot the eigenvalues on a logarithmic scale. The corresponding condition number of the full-order Hessian matrix is  $\kappa(\mathbf{H}) = 3.4 \cdot 10^7$ , indicating substantial ill-conditioning if attempts were made to solve the full-order estimation problem. Figure 6-2 shows the gap structure  $\{\lambda_i/\lambda_{i+1}\}$  of the eigenvalue spectrum. It is evident from the two figures that no single dominantly large gap exists that would suggest an obvious choice for the rank estimate. However, Figure 6-2 does show three breakpoints that are sufficiently

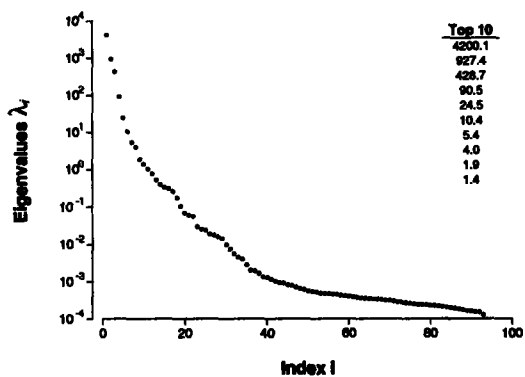


Figure 6-1: Eigenvalue spectrum of the Hessian matrix.

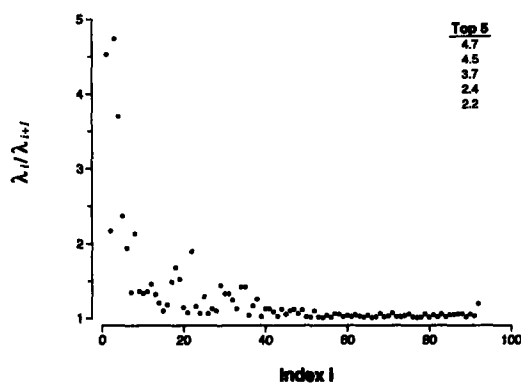


Figure 6-2: Gaps  $\lambda_i/\lambda_{i+1}$  of the eigenvalue spectrum.

removed from the remainder of the spectrum. They correspond to the rank estimates  $\rho_1 = 3$ ,  $\rho_2 = 1$ , and  $\rho_3 = 4$ , where  $\rho_1$  corresponds to the largest gap,  $\rho_2$  to the second largest and so on. We will explore each of these rank estimates along with a fourth one,  $\rho = 15$ , to demonstrate the effect ill-conditioning can have on the parameter estimates.

In the first stage of our analysis, we are interested in whether the optimization algorithm can recover the well-conditioned parameters when the ill-conditioned parameters are fixed at their “true” values. The results of this analysis are shown in Figures 6-3 and 6-4. For each parameter included in the optimization, we display the relative error between the parameter’s starting value and its true target value by a blue diamond. The red solid circles indicate the relative error between the final parameter estimate and the parameter’s true value. Parameter estimates were accepted, once the cost function  $\tilde{\Phi}(\theta)$  met the preset termination criterion,  $\tilde{\Phi}(\theta) < \gamma$ , where  $\gamma$  is an appropriately small constant. Each result is based on ten runs of the estimation algorithm for different noise realizations of the target vector.

The results in Figure 6-3 demonstrate that in each of the reduced-order estimation problems, the algorithm returns parameter estimates that are very close to, if not indistinguishable from, their true values (mean relative error of zero), despite initial relative errors of up to 26%. In fact, the residual bias in some of the parameter estimates can be reduced even further by using a more stringent termination criterion. The parameters identified are the arterial baroreflex pressure set-point (0), the right ventricular end-diastolic compliance (45), distending blood volume (70), and the heart rate set-point (90)<sup>1</sup>.

Figure 6-3 also demonstrates that the reduced-order parameter estimates are extraordinarily insensitive to perturbations of the target “measurements”. In fact, for

<sup>1</sup>Numbers in parentheses indicate parameter indices. See Appendix A for a mapping of parameter indices to parameter names.

Table 6.1: Mean relative errors of estimated parameters with respect to their true values. Numeric values are given in %.

	$\kappa(\mathbf{H}_\rho)$	Parameter Indices			
		0	45	70	90
$\rho = 4$	55.3	(-0.9±0.3)	(0.1±0.2)	(0.4±0.1)	(0.7±0.4)
$\rho = 15$	$8.0 \cdot 10^4$	(-21.1±2.5)	(4.6±4.2)	(-5.6±1.2)	(32.1±6.8)

each parameter estimate shown in the figure, there are ten red circles corresponding to the ten runs of the algorithm for different noise realizations. For most estimates, it is impossible to resolve visually more than two of these red circles.

This situation changes dramatically, however, if we attempt to identify ill-conditioned parameters. The results of such an attempt are shown in Figure 6-4, where we included 15 parameters in the analysis. The results demonstrate that inclusion of ill-conditioned parameters leads to failure to converge to the true parameter values (large bias) and severe sensitivity of the parameter estimates to perturbations of the target “measurements” (large variances of the parameter estimates). Mean relative errors between the parameter estimates and the true target parameter values are as high as 450 % with standard deviations as high as 180 %. In Table 6.1, we summarize the results of the well-conditioned estimation problem shown in the bottom panel of Figure 6-3 along with the estimates of the same parameters as derived from the ill-conditioned problem of Figure 6-4. A large condition number of the Hessian corresponds to large mean relative errors and comparatively larger variances.

We want to emphasize that the parameter estimation runs shown in Figure 6-3 and 6-4 used the same termination criterion. This implies that no assessment of the quality of the parameter estimates can be based on the residual error or its norm.

In any realistic situation, we cannot assume that the ill-conditioned parameters remain at their “true” values. This issue is addressed in the second stage of our analysis, where we allow all parameters to vary from their respective nominal values when generating the target response. The ill-conditioned parameters are subsequently set to their nominal values for the estimation algorithm, and only the well-conditioned parameters are estimated. The results of this second stage are shown in Figures 6-5 and 6-6.

In Figure 6-5, we show the results of the well-conditioned problem. As in Figure 6-3, the parameter estimates are quite close to the true target parameter values. Furthermore, the parameter estimates are again extraordinarily insensitive to perturbations of the target “measurements”. However, as compared with the corresponding results shown in Figure 6-3, the bias of the some parameter estimates is larger, because these estimates attempt to compensate for the incorrect (nominal) values assumed for the ill-conditioned parameters. Despite the gentle increase in bias in some estimates, the estimation results of the well-conditioned problem is still good, with a maximum relative error of approximately 3 %.

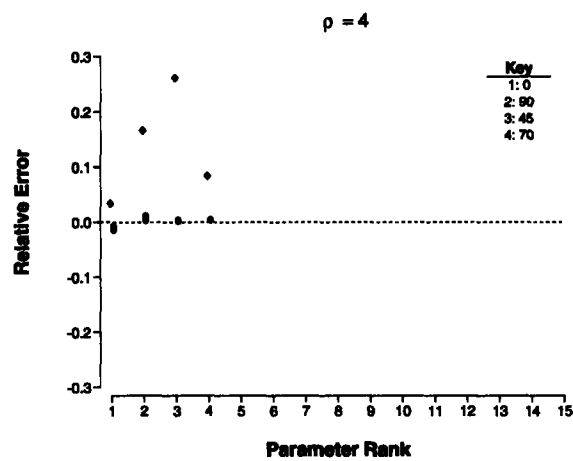
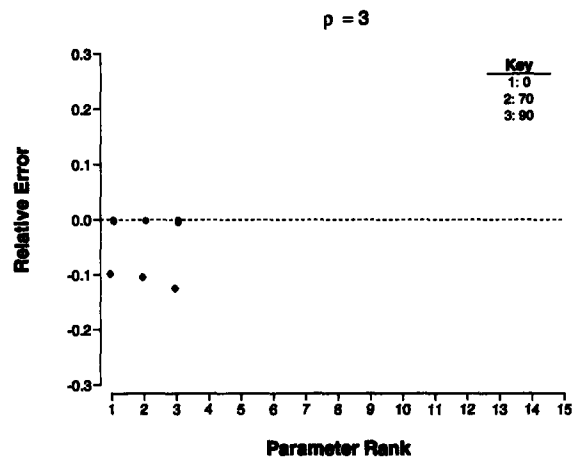
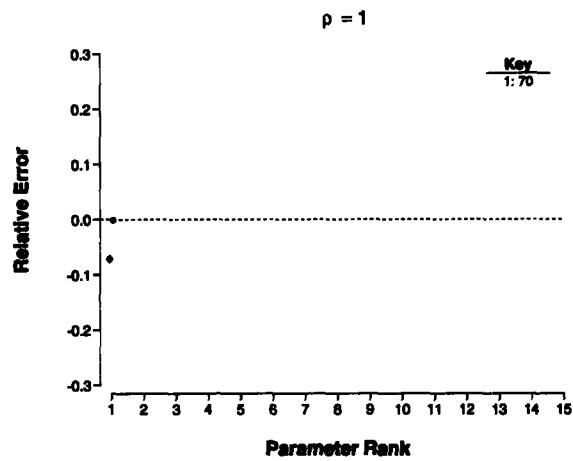


Figure 6-3: Relative errors between initial parameter values and target values (blue diamonds) and final parameter estimates and target values (red circles) for three rank estimates. Ill-conditioned parameters kept at their “true” values. They key in each figure relates the parameter rank to the respective parameter index.



Figure 6-6 displays the results of the parameter estimation if ill-conditioned parameters are once more included in the analysis. The results are as unstable as the ones presented in Figure 6-4.

### 6.3 Summary and Conclusions

This chapter focused on estimating parameters of the cardiovascular model from “experimental” data. In particular, we employed a non-linear least squares optimization routine with subset selection. The latter was necessary to overcome the severe ill-conditioning of the estimation problem.

The results presented are quite promising in that the parameter estimates derived from solving reduced-order problems are quite well-conditioned and have little bias even if the ill-conditioned parameters are allowed to vary.

We consider the work presented in this chapter the beginning of our effort to estimate parameters from experimental data. Future work needs to analyze the quality of the parameter estimates in relation to the number of signals included in the analysis. We did not address the issue of row and column scaling of the Hessian matrix, but simply remark here that subset selection results are not scaling-invariant. One could potentially exploit such a fact to improve the estimates of parameters that are currently ill-conditioned.

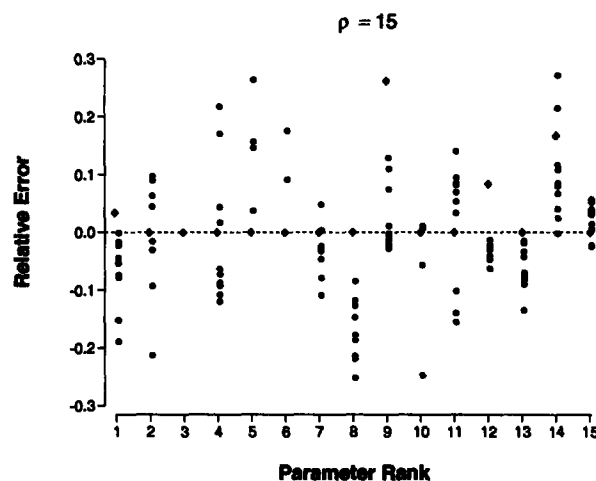


Figure 6-4: Relative errors between initial parameter values and target values (blue diamonds) and final parameter estimates and target values (red circles).  $\rho = 15$ . Ill-conditioned parameters kept at their “true” values.

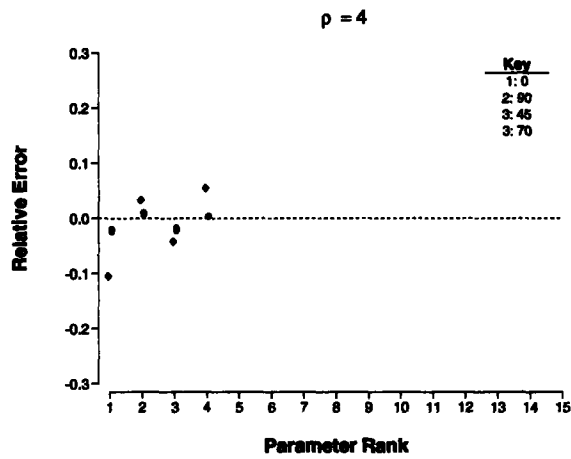
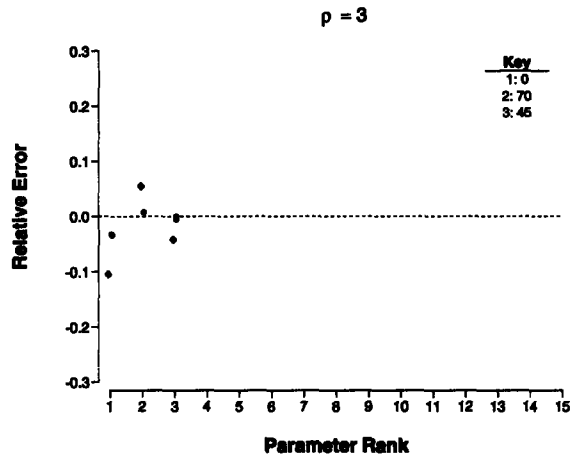
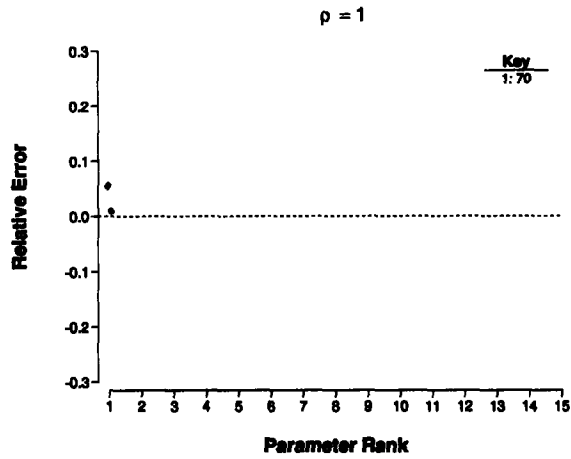


Figure 6-5: Relative errors between initial parameter values and target values (blue diamonds) and final parameter estimates and target values (red circles) for three rank estimates. Ill-conditioned parameters not kept at their “true” values. The key in each figure relates the parameter rank to the respective parameter index.

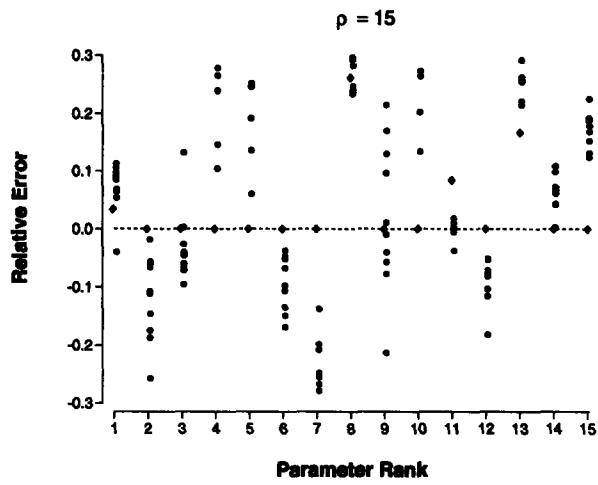


Figure 6-6: Relative errors between initial parameter values and target values (blue diamonds) and final parameter estimates and target values (red circles).  $\rho = 15$ . Ill-conditioned parameters not kept at their “true” values.



## **Part III**

# **Clinical Study and Model-based Data Analysis**



# Chapter 7

## Clinical Study

The transient cardiovascular response to changes in posture has been under investigation by various groups of researchers over the past three decades. Of particular interest has been the question of whether active standing and passive tilting elicit the same sequence of hemodynamic events.

In a series of publications, Rossberg and co-workers [201–203] investigated the transient heart rate response to rapid head-up tilt. They report that rapid tilt to 70° (over 1.5–2 s) elicits a strong reflexive increase in heart rate, comparable in magnitude and timing to the ones observed during active standing [204]. Borst and co-workers had previously hypothesized that the initial heart rate response to active standing was at least in part due to a central command-mediated muscular exercise reflex [204]. This mechanism would clearly be absent during passive tilt and, therefore, would not explain the purported similarity of the two responses. Subsequent studies of the heart rate response to active and passive changes in posture failed to reproduce the dramatic responses reported by Rossberg [136, 205–207].

Similarly, several investigators have focused on the arterial blood pressure response to active and passive changes in posture [135, 136, 206–208]. The data presented by Sprangers and co-workers suggest no significant [206] or only a modest drop in arterial blood pressure for a very brief period of time ( $\lesssim 5$  s) in response to rapid tilts [136, 207]. The data presented by Tanaka and colleagues [135] suggest, however, that the timing of arterial blood pressure drop and heart rate response are intimately linked and are approximately the same for active and rapid passive changes in posture. Consistent with Sprangers' findings, Tanaka reports a smaller increase in heart rate and a smaller drop in mean arterial pressure for rapid tilts than for standing up.

To understand better the transient hemodynamic events during active and passive changes in posture, and in the of hope resolving some of the discrepancies between various reports in the literature, we designed a clinical study that aimed at elucidating the hemodynamic response during the first 180 s after the onset of orthostatic stress. In particular, we were interested in identifying the continuous transient response of arterial blood pressure and heart rate to active standing, rapid tilting, and slow tilting.

## 7.1 Methods

**Subjects** We recruited ten healthy volunteers (five males, five females) to participate in this study. The mean age was ( $28.7 \pm 1.2$ ) years, the mean body height was ( $172.8 \pm 4.0$ ) cm, and the mean body weight was ( $70.6 \pm 4.5$ ) kg (see Table 7.1 for individual subject information)<sup>1</sup>. Participants regularly engaged in light to moderate physical activity (none was a performance athlete) and had no sign of cardiovascular disease.

Table 7.1: Subject information.

Subject ID	Gender	Age years	Height cm	Weight kg
12726	M	28	170	64
12734	M	30	165	64
12744	M	28	180	100
12754	F	26	160	61
12755	M	32	192	83
12814	F	27	165	56
12815	F	22	185	73
12819	F	28	155	55
12821	F	32	173	77
13960	M	34	183	83
		$28.7 \pm 1.2$	$172.8 \pm 4.0$	$70.6 \pm 4.5$

**Data acquisition and signal processing** Using a standard clinical ECG monitor (Hewlett-Packard 1500A Electrocardiograph), we recorded a single-channel ECG in an approximate lead II configuration to maximize the QRS-complex amplitude. Blood pressure was measured non-invasively at the second phalanx of the left middle finger with the aid of a volume clamp-based pressure monitoring device (2300 Finapres BP monitor, Ohmeda, Madison, WI). The hand was secured at the level of the sternal angle to minimize motion and hydrostatic artifacts during changes in posture.

ECG and the arterial pressure waveforms were recorded throughout the duration of the experiment. Analog signals of the electrocardiogram, arterial blood pressure, tilt angle, and event marker were recorded simultaneously to a TEAC RD-135T digital audio tape data recorder (TEAC America, Inc., Montebello, CA) and, for data redundancy purposes, to a Sony laptop using a BIOPAC MP System (BIOPAC Systems, Inc., Goleta, CA) data acquisition module. The TEAC QuickVu-RD/WIN software (version 1.0.5) was used to retrieve the data from the digital audio tapes in digitized form at a system-determined sampling frequency of 24 kHz. The data were

<sup>1</sup>Unless otherwise indicated, data are presented as population mean  $\pm$  standard error of the mean throughout this chapter.



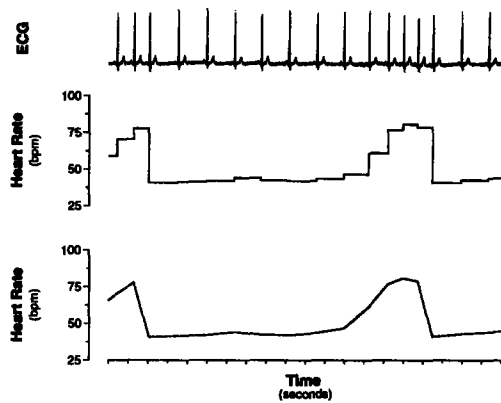


Figure 7-1: Derivation of instantaneous heart rate signal from the electrocardiogram.

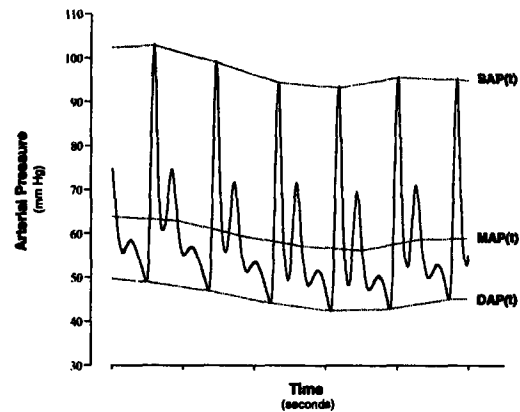


Figure 7-2: Derivation of systolic, mean, and diastolic arterial pressure time series from the arterial pressure waveform.

transferred to a PC running the LINUX operating system, converted to the WFDB data format [209], and down-sampled to a sampling rate of 250 Hz for subsequent off-line analysis. We used a curve length-based QRS detection algorithm, as described in [210] and available from [211], to detect the onset of ventricular depolarizations. As shown in Figure 7-1, time series of instantaneous heart rate signals for constant (middle panel) and linear (bottom panel) interpolation between contractions were derived from consecutive QRS detections. Similarly, we extracted beat-by-beat numerical values from the arterial pressure waveform after identifying the onset of each arterial pressure pulse using a slope-based detection algorithm [212]. Time series for systolic arterial pressure,  $SAP(t)$ , mean arterial pressure,  $MAP(t)$ , and diastolic arterial pressure,  $DAP(t)$ , were generated through linear interpolation between the respective beat-by-beat values, as shown in Figure 7-2.

**Protocol** During the experimental session, each subject underwent each of the following three interventions twice:

1. Rapid Tilt:

After recording a 5-minute supine baseline of ECG and arterial blood pressure, we unlocked the tilt table from its secured horizontal position. Two operators manually moved the table to the  $75^\circ$  head-up position over a 2-second interval. After three minutes in the upright position, the subject was tilted back to the horizontal at the same rate and the tilt table was locked again.

2. Standing Up:

After recording a 5-minute supine baseline of ECG and arterial blood pressure, we asked the subject to perform a standard lying-to-standing maneuver which generally took less than three seconds to complete. The subjects remained motionless in the standing position for the ensuing three minutes before they were asked to resume the supine position.

### 3. Slow Tilt:

After recording a 5-minute supine baseline of ECG and arterial blood pressure, the slow tilt was initiated by activating the tilt table's motor. The subject was tilted to 75° head-up over approximately 50 seconds and remained in the head-up position for three minutes.

At the conclusion of the final intervention, the subject was returned to the horizontal position for a final five minutes of supine baseline recording. The sequence of 6 interventions (2 Rapid Tilts, 2 Stand-Ups, and 2 Slow Tilts) was randomized for each subject.

The study protocol was approved by MIT's Committee On the Use of Humans as Experimental Subjects (COUHES Application # 2895) and the Advisory Board of the MIT-MGH General Clinical Research Center (MIT CRC # 512). Each volunteer gave written, informed consent prior to participation in the study. The study was carried out at the MIT General Clinical Research Center.

## 7.2 Results

### 7.2.1 Steady-state Results

In Table 7.2, we list the average values of HR, SAP, MAP, and DAP 50s before (Rest) and 140s after assumption of the head-up (HU) position along with the difference between the two ( $\Delta$ ) for rapid tilt (RT), slow tilt (ST), and standing-up (SU), respectively.

Statistical comparisons are based on two-sided tests of significance for comparisons between different interventions (e.g., comparison of resting HR between RT and SU) and one-sided tests of significance for HU vs. Rest comparisons. Each intervention led to statistically significant ( $P < 0.005$ ) increases in HR, MAP, and DAP. Neither intervention led to a statistically significant change in SAP. With two exceptions, no statistically significant difference was observed between the resting steady-state hemodynamic variables for the three interventions or between the head-up steady-state hemodynamic variables for the three interventions.

### 7.2.2 Transient Responses

On the following pages, we present the population-averaged transient hemodynamic responses to the three stress tests. In Figure 7-3, we show the hemodynamic responses of systolic, mean, and diastolic arterial blood pressure and heart rate. To emphasize the dynamic response, we display the changes in mean arterial pressure and heart rate from their respective supine baseline values in Figure 7-4. All figures show the mean response (solid lines) along with the approximate 95% confidence limits (dashed lines).

It is evident from Figures 7-3 and 7-4 that each intervention leads to a somewhat different transient response. Clearly standing up elicits the most dramatic transient

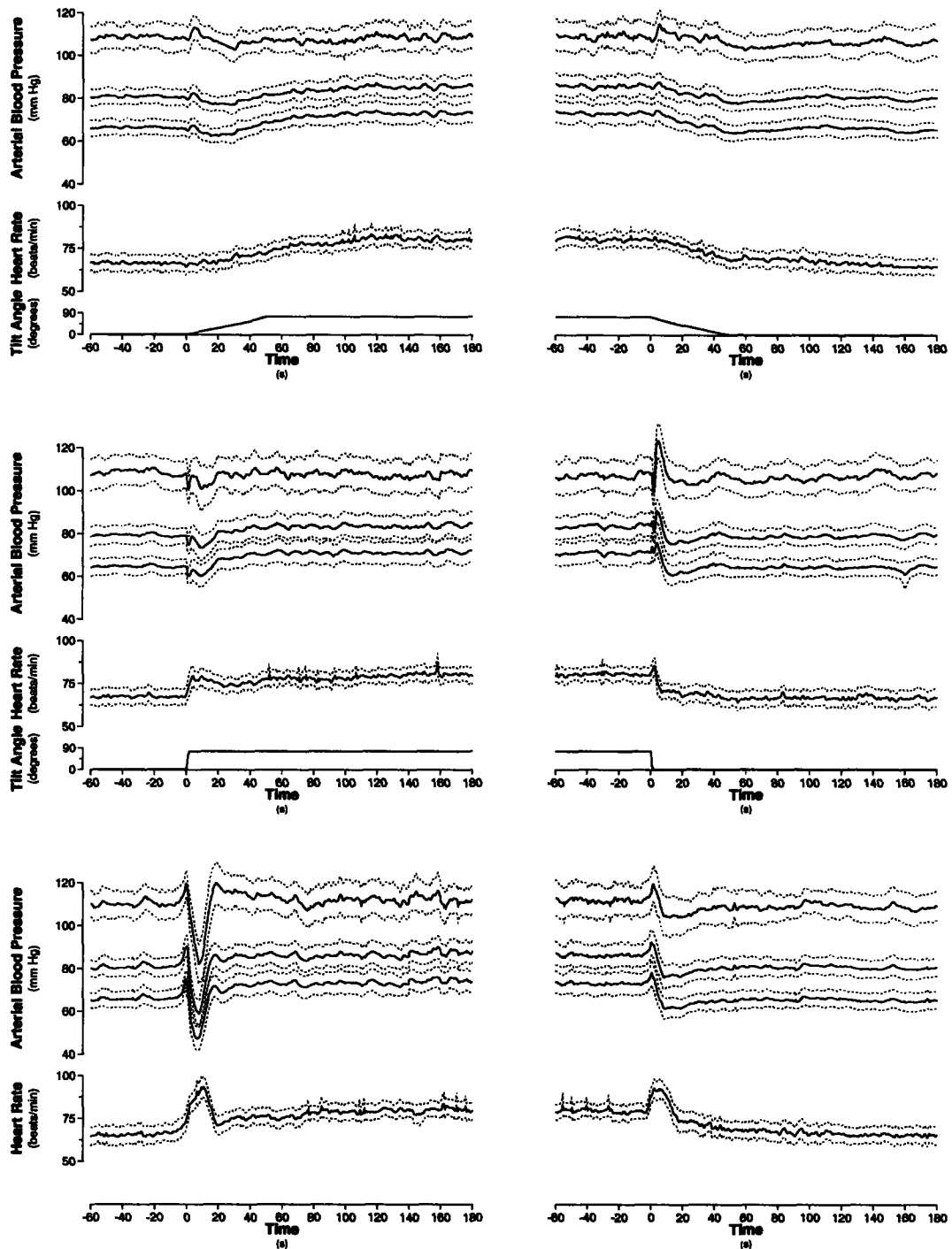


Figure 7-3: Hemodynamic response to slow tilt (top), rapid tilt (middle) and standing up (bottom). Left panels show transition from supine to the head up posture. Right panels show the transition back to the supine.

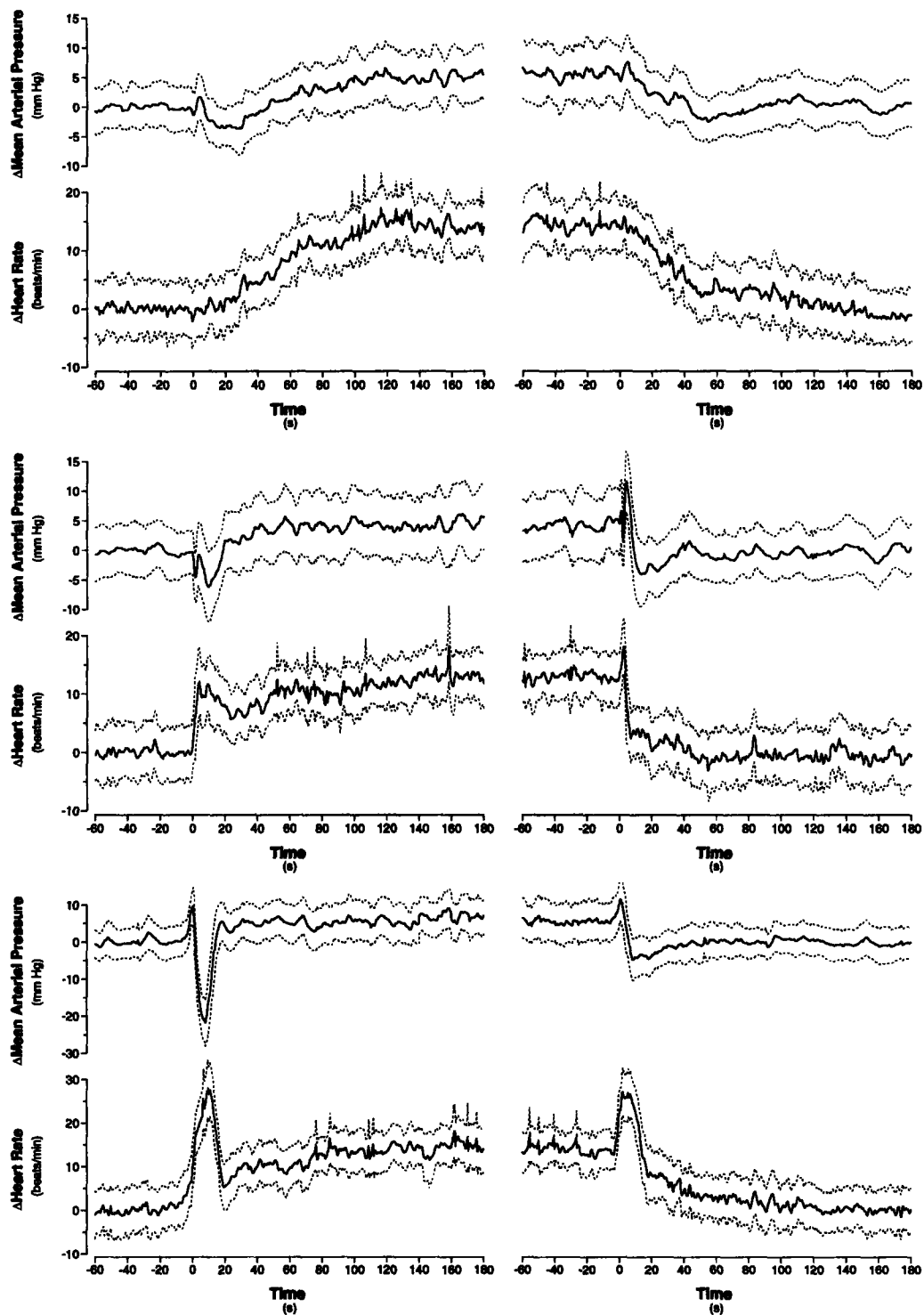


Figure 7-4: Changes in mean arterial pressure and heart rate during slow tilt (top), rapid tilt (middle) and standing up (bottom). Note difference in amplitude scale between tilt and stand-test data.

Table 7.2: Steady-state numerics of heart rate, systolic, mean, and diastolic arterial pressure. RT: rapid tilt; ST: slow tilt; SU: standing up; Rest: supine posture; HU: head-up posture.

	Rest	HU	$\Delta$
Heart rate (beats/min)			
RT	67.2 $\pm$ 2.4	80.1 $\pm$ 2.1*	13.0 $\pm$ 1.5
ST	66.5 $\pm$ 2.4	81.1 $\pm$ 2.2*	14.6 $\pm$ 1.8
SU	65.1 $\pm$ 2.6 <sup>†</sup>	79.0 $\pm$ 2.2*	13.9 $\pm$ 1.5
Systolic arterial pressure (mm Hg)			
RT	108.5 $\pm$ 3.5	106.6 $\pm$ 3.8	-1.9 $\pm$ 1.7
ST	108.4 $\pm$ 2.9	108.8 $\pm$ 2.9 <sup>†</sup>	0.4 $\pm$ 2.2
SU	109.8 $\pm$ 3.2	111.5 $\pm$ 3.7	1.7 $\pm$ 1.9
Mean arterial pressure (mm Hg)			
RT	69.3 $\pm$ 2.1	73.3 $\pm$ 2.6*	4.0 $\pm$ 1.2
ST	70.7 $\pm$ 1.8	75.5 $\pm$ 2.1*	5.7 $\pm$ 1.4
SU	70.5 $\pm$ 2.1	75.7 $\pm$ 2.6*	5.2 $\pm$ 1.4
Diastolic arterial pressure (mm Hg)			
RT	54.8 $\pm$ 1.9	60.9 $\pm$ 2.6*	6.3 $\pm$ 1.2
ST	56.3 $\pm$ 1.8	63.0 $\pm$ 2.2*	6.8 $\pm$ 1.2
SU	55.6 $\pm$ 1.9	62.5 $\pm$ 2.5*	6.9 $\pm$ 1.3

\*P<0.005 HU vs. Rest; <sup>†</sup>P<0.05 SU vs. RT

response in arterial blood pressure and heart rate. The arterial pressure response to standing up is characterized by a brief increase followed by a dramatic decrease in blood pressure. The initial brief increase is due to a Valsalva-type maneuver (contraction of the abdominal and thoracic muscles to stiffen the torso) that allows for raising of the upper body off the tilt table. Heart rate transiently increases dramatically in response to the drop in arterial pressure. During rapid tilt, the subjects are tilted passively with minimal muscular effort on their part. It is therefore not surprising that the initial Valsalva-related blood pressure rise preceding the change in posture seen during standing up is absent during rapid tilt. However, the blood pressure response to rapid tilt does show a bi-phasic behavior: a brief drop in arterial pressure is followed by an increase, which in turn is followed by an even larger decrease. Whether the intermittent increase in pressure is caused by a transient increase in cardiac output, as suggested by Toska and colleagues [208], or is due to reflexive muscle contraction in response to the rapid tilt (a startle response), or is a measurement artifact requires further elucidation. The heart rate response to rapid tilt shows a transient increase similar in duration to the one seen during standing up. The cardiovascular response to slow tilt is characterized by very gradual changes in both heart rate and mean arterial pressure. Interestingly, a small increase in arterial pressure, very similar in morphology to the one observed during rapid tilt, is also seen at the onset of slow tilt.

In Figures 7-5 and 7-6, we directly compare the dynamic responses of mean arterial

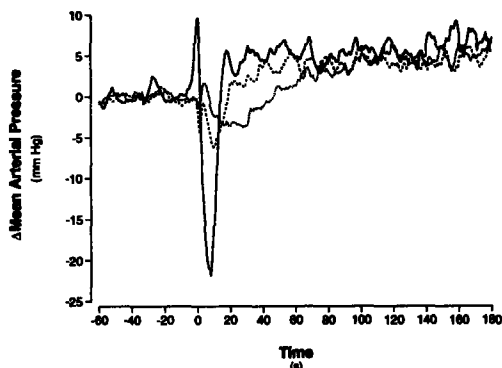


Figure 7-5: Comparison of transient mean arterial pressure responses. Solid line: stand test; dashed line: rapid tilt; dotted line: slow tilt.

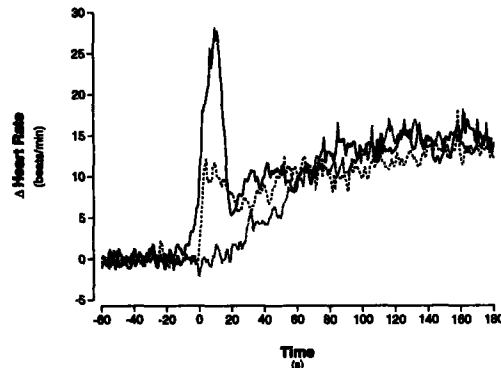


Figure 7-6: Comparison of transient heart rate responses. Solid line: stand test; dashed line: rapid tilt; dotted line: slow tilt.

pressure and heart rate during standing-up (solid lines), rapid tilt (dashed lines), and slow tilt (dotted lines). Clear and statistically significant differences exist in the amplitudes of the initial blood pressure drop and heart rate increase between rapid tilt and standing up. Yet the timing of the initial transient responses of these two variables is well preserved, i.e. differences are confined to the first 20 s of the transient response. In contrast, the hemodynamic response to slow tilt lacks completely the initial transient complex seen during standing-up and rapid tilt. In fact, despite a drop in mean arterial pressure, heart rate fails to increase for the first 20 s in response to slow tilt.

### 7.3 Pilot Study

In a follow-up pilot study, we investigated the origin of the difference in the amplitude response seen between standing up and rapid tilt. One obvious mechanistic difference between the two interventions is the contraction of abdominal and leg muscles in the process of standing up. We hypothesized that the transient response to standing can be mimicked by a rapid tilt with prior muscle contraction. To test this hypothesis, we conducted a pilot study in which two volunteers underwent a protocol similar to the one outlined above. Just prior to the rapid tilts, however, the subjects were asked to raise their feet a few centimeters off the tilt table for a short period of time ( $\lesssim 3$  s). Upon return of feet to the tilt table, the subjects were immediately tilted up rapidly to the 75° head-up posture.

The results of this pilot study are shown in Figures 7-7 and 7-8 and are based on two volunteers with a total of six rapid tilts with muscle contraction (dashed lines) and six stand tests (solid lines). It is obvious that muscular contraction prior to rapid tilting gives rise to transient changes in mean arterial pressure and heart rate that are very similar, if not indistinguishable, from those elicited by actively standing up.

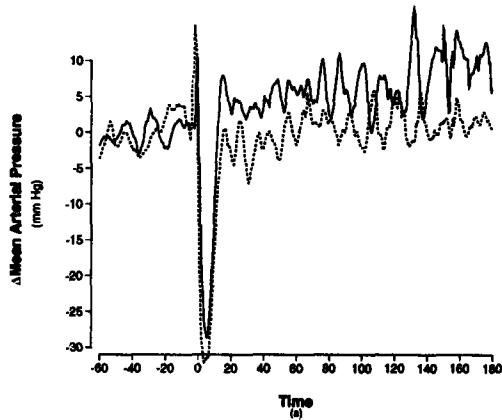


Figure 7-7: Comparison of transient mean arterial pressure responses. Solid line: stand test; dashed line: rapid tilt with prior muscle contraction.

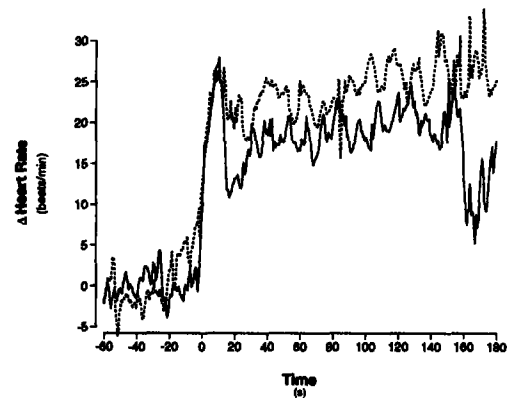


Figure 7-8: Comparison of transient heart rate responses. Solid line: stand test; dashed line: rapid tilt with prior muscle contraction.

## 7.4 Discussion

This study was designed to elucidate the short-term ( $\leq 3$  min), transient hemodynamic response for transitions to the upright posture for three different modes of transition, namely rapid tilt, slow tilt, and standing-up. As can be seen from Table 7.2, the steady-state responses of MAP, DAP, and HR are independent of the mode of transition to the head-up position. It seems physiologically intuitive that the steady-state response depends only on the amount of blood volume that is translocated to the dependent vasculature and that the mode of transition is irrelevant in the long run. The results in Table 7.2 confirm this notion.

Significant differences exist, however, between the three modes of transition during the first 20-30 seconds. As mentioned above, the timing of the initial transient complex during standing up and rapid tilt is well preserved. In both interventions, the gravitational stress is brought on rapidly and can be considered a quasi step-functional change in gravitational stress. Rapid vagal withdrawal is the body's first line of defense, leading to a rapid, almost immediate increase in heart rate. The sympathetic system is known to have longer latency and impulse response and therefore responds slower to the gravitational stimulus. We attribute the fact that the hemodynamic response to standing up and rapid tilt is essentially the same after  $\approx 20$  seconds to the intrinsic equilibration of sympathetic outflow and vagal withdrawal. Further slow increases in heart rate are seen in all three interventions and are probably related to extravasation of plasma volume into the interstitial fluid compartment.

Cardiovascular adaptation to slow tilt exhibits a more gradual change in both heart rate and mean arterial pressure, lacking the initial transient complex seen during both rapid tilt and standing up. We attribute this behavior to the slow change in gravitational stress, which essentially allows for equilibration of the reflex responses during transition to the head-up posture. This explanation is supported by the fact

that the hemodynamic response to slow tilt becomes indistinguishable from those seen during rapid tilt and standing up about 50 s after the onset of gravitational stress; this is the time it takes for the slow tilt to be completed.

Finally, a small pilot study suggests that the difference between the hemodynamic responses seen during rapid tilt and standing up can be explained on the basis of transient muscle contractions. Our results are therefore consistent with Tanaka's findings, in that the timing but not the amplitude of the hemodynamic response is preserved between standing up and rapid tilt. Mechanistically, muscular activity seems to account for the difference in amplitudes. Whether the large drop in mean arterial pressure and the large increase in heart rate are mediated through peripheral vasodilation and central command, respectively, as advocated by some [135, 136] or whether mechanical factors such as transient changes in venous return due to abdominal contraction play a dominant role remains to be elucidated. Given what we know about the latencies of the sympathetic nervous system, it is unlikely that a powerful vasodilation response can be mounted over a few seconds to account for the dramatic difference in the arterial pressure response between standing up and rapid tilt.



# Chapter 8

## Post-spaceflight Orthostatic Intolerance

A reduction in cardiovascular performance following exposure to the microgravity environment has been one of the first documented physiological consequences of manned spaceflight. In particular, a large number of astronauts show signs of maladaptation to the upright posture upon return to the normal gravitational environment. A number of mechanisms underlying this post-spaceflight orthostatic intolerance have been suggested and studied over the past forty years. Proving or rejecting a scientific hypothesis in the spaceflight setting is complicated by a host of possible confounding factors not usually seen in ground-based clinical trials: heterogeneity of the study population (pilot/commander vs. mission specialist, rookie vs. veteran astronaut, male vs. female astronaut), environmental heterogeneity (duration of flight, work schedule, astronaut participated in extra-vehicular activities), possible lack of compliance with to protocol, inability to randomize treatment, possible lack of predictability of re-entry, and — above all — a very small number of subjects studied on any given mission.

In the context of post-spaceflight orthostatic intolerance, the interpretation of limited experimental data can be greatly aided by a mathematical model that simulates the critical components and behaviors of the cardiovascular system. A reasonably complete and validated mathematical model allows researchers to simulate the systems-level effects a particular cardiovascular alteration might have, and to test the compatibility of physiological hypotheses against human experimental data. In this chapter, we will use such a modeling approach to test hypotheses regarding the cardiovascular system's failure to adjust properly to the upright posture post-flight.

In Section 8.1, we provide a historical perspective on post-flight orthostatic intolerance. Section 8.2 reviews the current literature on human cardiovascular adaptation to microgravity and presents the phenomenology of post-flight orthostatic intolerance. In Section 8.3, we use our computational model to test the system-level effects of detrimental changes in particular cardiovascular parameters.

## 8.1 Historical Perspective

The first indication of spaceflight-induced changes in cardiovascular performance came at the conclusion of the third orbital manned spaceflight during Project Mercury in 1962. After spending nine hours orbiting the earth in weightlessness, Astronaut Walter Schirrer's post-flight physical examination was unremarkable except for one finding that was deemed noteworthy: when moving from the supine to the upright position, his heart rate increased from 70 beats per minute to over 100 beats per minute with a concomitant decrease in systolic blood pressure [213, p. 34]. While these symptoms disappeared by hour 21 after landing, the medical staff recognized that "*such a hemodynamic phenomenon may have serious implications for a longer mission*" [213, p. 35], and suggested that an in-flight exercise program might be needed to prevent these symptoms from interfering with a possible emergency egress soon after landing. These suggestions proved to be remarkably prophetic. The subsequent Mercury-Atlas 9 mission sent Astronaut L. Gordon Cooper to space for a U.S. record-breaking 34 hours. And while his health prior and during flight was excellent, egress from the space capsule imposed a substantial burden on his cardiovascular system:

The postflight examination began prior to egress from the spacecraft. Approximately 40 minutes after landing, two measurements of the astronaut's [Cooper's] blood pressure were recorded while he was still lying in the spacecraft on the deck of the recovery ship. He was then able to egress from the spacecraft without assistance and stand erect on the deck while his blood pressure was again recorded on the onboard tape. Later examination of this 3 1/2 minute record shows that, while he was still in the spacecraft, his blood pressures were 101/65 and 105/87, with a corresponding heart rate of 132 beats per minute. During egress and immediately thereafter while standing upright on the deck, his heart rate rose to 188 beats per minute with atrioventricular dissociation. At that point, another blood pressure recording was attempted and, although the apparatus appeared to cycle normally, no pressure pulses were seen on the recording. His heart then returned to a normal sinus rhythm with a rate of 92 beats per minute at sensor disconnect.

After standing on the deck for approximately a minute, the pilot began to look pale and, although his face was already wet, new beads of perspiration appeared on his forehead.

He swayed slightly and reported symptoms of impending loss of consciousness including lightheadedness, dimming of vision, and tingling of his feet and legs. [214, p. 317]

Astronaut Cooper underwent a series of tilt table studies to investigate further the presence and time course of orthostatic symptoms. These symptoms disappeared by hour 19 after splashdown. The practice of assessing orthostatic tolerance by means of provocative tilt table experiments pre- and post-flight was adopted into the standard medical protocol and continued throughout the subsequent Gemini program.

During the ten manned Gemini missions, astronauts stayed in orbit between 4 hours and 13 days, logging a combined 2000 man-hours in the weightless environment. Post-flight tilt table testing (15 minutes in the 70° head-up posture) consistently showed orthostatic heart rate increases 17% – 105% larger than those recorded pre-flight [215, p. 206]. In addition, leg volume in the upright posture post-flight was consistently larger when compared with the appropriate pre-flight values. Furthermore, hematologic studies on six astronauts revealed reductions in red-cell mass ranging from 5%–20%. Signs of orthostatic hypotension persisted for up to 50 hours after landing [216]. To simulate blood pooling in the lower extremities, two Gemini astronauts wore intermittently occlusive lower limb cuffs for either half or the entire duration of space travel. Neither astronaut showed an improved tolerance to the upright posture post-flight, and this early experimental countermeasure was discontinued.

In demonstrating that astronauts tolerate extended exposures to the weightless environment without any notable decrement in performance or health, Project Gemini achieved an important biomedical goal in preparation for the planned Apollo missions. The Apollo program had very specific yet enormously ambitious aims, namely to land man on the moon, to allow him to explore the lunar surface, and to return him safely to earth. Given the technological and operational challenges of such an endeavor, physiological testing and medical monitoring pre-flight, in-flight, and post-flight were constrained by crew availability and therefore naturally limited to those measurements deemed absolutely vital for the success of the program [217, p. 227]. The continued occurrence of variable degrees of orthostasis post-flight, however, led to the inclusion of extensive cardiovascular and fluid-electrolyte evaluations in the routine medical examinations. Throughout the Apollo program, orthostatic stress tests were scheduled approximately 30, 15, and 5 days before spaceflight, shortly after splashdown, and at intervals of 24 hours thereafter until astronauts regained their pre-flight tolerance levels [217, p. 232]. An operational shift was made from tilt table to lower body negative pressure experiments and passive stand tests to test for orthostatic hypotension. Other measurements made included calf volume changes during LBNP, changes in body weight, resting calf girth, volume of the lower legs, stroke volume, and chest X-rays to determine changes in heart size. Fluid volume, electrolyte balances, and hormonal changes were determined from blood and urine samples. In anticipation of the 28-day and 56-day Skylab missions, and partly in response to anecdotal evidence that astronauts of the 18-day Soviet Soyuz 9 mission had to rely on assisted egress after landing because of difficulties standing up, two Apollo crewmen tested experimental anti-hypotensive garments (anti-G suits).

Orthostatic hypotension, including several pre-syncopal episodes, was generally observed post-flight for up to three days following splashdown and was characterized by marked tachycardias and reductions in systolic blood pressure and in stroke volume as compared with the respective pre-flight values [217, p. 256]. Body weight was reduced on average by approximately 5% post-flight but showed a one-third recovery over the first 24 hours after landing [218, p. 166]. Plasma volume was reduced on average by 4.4% but was restored to pre-flight levels within one day after recovery; red-cell mass was variably changed post-flight, ranging from -2% to -10% with a relatively

slow recovery over weeks following spacetravel [219, p. 204]. These findings, along with a reduction in maximal calf girth and a decreased cardiothoracic ratio, implicated a reduction in circulating volume as a principal contributor to the post-flight orthostatic intolerance phenomenon [220, p. 576]. The positive pressure garment appeared to provide some level of protection as measured by a somewhat reduced orthostatic tachycardia with the suit inflated [217, p. 254].

At the conclusion of the Apollo missions, the U.S. space program had successfully executed 27 manned missions, ranging from 15 minutes to 13 days in duration, had achieved six lunar landings, and had sent a total of 34 astronauts to space. The overwhelming medical evidence suggested that humans adapt quickly to and function well in the new environment. Pre- and post-flight medical testing established a number of physiological changes that were thought to be adaptive to the weightless environment yet largely self-limiting. In-flight medical surveillance was focused on monitoring crew health; only limited in-flight experiments were performed to establish the proximal physiological response to weightlessness.

The subsequent Skylab program provided an environment in which such in-flight medical and physiological experiments could be performed. It also successively extended the exposure to weightlessness to a maximum of 84 days. The cardiovascular experiments performed during the three manned Skylab missions point to an adaptive process — commonly referred to as *cardiovascular deconditioning* — that occurs during flight and that stabilizes over a period of four to six weeks [221, p. 412]. In-flight lower body negative pressure experiments of the three Skylab 4 astronauts revealed a more rapid loss of orthostatic tolerance, as indicated by a significantly elevated heart rate response to  $-50$  mm Hg of LBNP by day 3 in orbit [222, p. 286]. Post-flight stroke volume was found to be reduced in two of the three astronauts; echocardiographic examinations revealed this observation to be consequent to reduced cardiac filling rather than due to changes in cardiac function [223, p. 370]. At the conclusion of the Skylab program, orthostatic intolerance and reduced exercise capacity following spaceflight were both thought to be primarily linked to reduced circulating blood volume, although possible contributions of reduced venous tone to the etiology were suggested [221, p. 412].

The advent of the Space Transportation System, commonly known as the *Space Shuttle*, opened the opportunity to investigate systematically hypotheses regarding the body's adaptation to the microgravity environment. In particular, the relatively large shuttle fleet allowed for up to nine spaceflights a year, each carrying up to seven astronauts. Dedicated life science missions (such as Spacelab 1, Spacelab 2, and Neurolab) and routine pre- and post-flight medical examinations opened the possibility for meaningful statistics to be obtained. The prevalence of orthostatic intolerance following shuttle flights varies from 9% to 30% for short-duration missions (4-10 days) [224, 225] to over 60% for longer shuttle missions (9-14 days) [53]. Estimates vary depending on the definition of orthostatic intolerance and the number of astronauts included in the studies. Retrospective analysis of records from 140 male and 25 female astronauts revealed a prevalence of orthostatic intolerance of 7% among male and 28% among female astronauts if occurrence of pre-syncopal signs is used as a positive endpoint of tilt test experiments [226]. When studying smaller populations of astronauts,

these figures can be as high as 20% for men and 100% for women, respectively [227]. Other estimates put the overall prevalence of post-spaceflight orthostatic intolerance at 20% with existing countermeasure programs in place [228]. Repeated exposure to weightlessness does not seem to alter an astronaut's predisposition to orthostatic intolerance: 90% of second-time and 86% of third-time fliers show the same outcome to orthostatic stress tests that was established after their first shuttle mission [228].

Long-duration missions became possible for U.S. astronauts in the mid-90s through the Shuttle-MIR program and more recently through the completion of the International Space Station. Both programs enabled repeated assessment of individual astronauts' gravitational tolerance. Comparison with the appropriate results from short-duration flights indicate that five out of six astronauts became pre-syncope during a 10-minute tilt test after long-duration missions (129–190 days) whereas only one out of the six astronauts showed signs of pre-syncope after short-duration missions (8–16 days) [30]. These results have important implications for the future planning of long-duration missions.

To date, more than 400 astronauts in the combined Russian and U.S. space programs have experienced the weightless environment. Yet despite considerable effort of the past forty years, post-spaceflight orthostatic intolerance remains one of the most important cardiovascular challenges of spaceflight. In the section to follow, we will review the most common hypotheses regarding the etiology of post-flight orthostatic intolerance and review mechanistic studies that support them.

## 8.2 Mechanistic Studies

Many hypotheses concerning the mechanisms underlying post-spaceflight orthostatic intolerance have been the focus of in-flight and ground-based experimental studies in the past, and some are presently under investigation in both human and animal studies. In Table 8.1, we summarize these hypothesized mechanisms and group them according to the system with which they are primarily associated.

**Blood volume** A reduction in blood volume is thought to be adaptive to the microgravity environment in that a loss of gravitational gradients in the cardiovascular system leads to a translocation of blood from the dependent vasculature into the thorax. The resultant distention of the right atrium is thought to promote the loss of water and sodium through the activation of atrial stretch receptors and the release of atrial natriuretic peptide (ANP). Through the action of the sympathetic system, atrial stretch promotes vasodilation, suppression of the release of antidiuretic hormone, and reductions in the release of renin. ANP has similarly diverse effects, acting as a vasodilator and by directly promoting water and sodium loss through action on the collecting tubules.

A decrease in total blood volume is probably the best documented and unequivocally accepted cardiovascular response to microgravity. Fischer reported an average reduction in plasma volume on landing day of 7.5% in four Gemini astronauts and an increase of approximately 10% in two more astronauts [239]. He also noted a

Table 8.1: Hypothesized mechanisms of post-spaceflight orthostatic intolerance.

Mechanism	Reference
<b>Hemodynamic mechanisms</b>	
Hypovolemia	[39, 218, 229, 230]
Increased venous capacitance	[231, 232]
Reduced cardiac performance	[41, 42, 233, 234]
<b>Autonomic mechanisms</b>	
Sympatho-adrenal dysfunction	[51, 235, 236]
<b>Non-cardiovascular mechanisms</b>	
Reduced exercise capacity	[237]
Neuro-vestibular plasticity	[47, 238]

15 % decrease in red cell volume. Leach reported a reduction in plasma volume of 4 % for the three Apollo 17 astronauts [218]; landing day red cell volumes were variably reduced between 2 % and 10 % during the Apollo program [219]. The data presented by Leach suggest that plasma volume is restored within one day after landing. During the Skylab missions, plasma volume reductions of 10 % to 14 % were noted; reductions in red cell mass ranged from 4 % to 20 % with a mean of 12 % [229]. Leach and co-workers report a reduction in plasma volume of 9 % from two Spacelab missions (Space Life Sciences 1, SLS-1, and Space Life Sciences 2, SLS-2) [230]; Alfrey reports a reduction in red cell volume of 10 % to 14 % for the same missions [240]. More recently, Waters reported a 7 % reduction in plasma volume and a 6 % reduction in red cell mass in male astronauts who became pre-syncopal on landing day, whereas spaceflight-induced plasma and red cell mass losses are as high as 19.5 % and 7 % in female astronauts who have pre-syncopal events on landing day [227].

**Venous capacitance** Early reports correlated the occurrence of post-flight orthostatic intolerance with engorgement of all dependent leg veins upon standing; *feet and legs rapidly took on a dusky, reddish-purple color following standing* [213, p. 34]. Increased venous pooling in the dependent vasculature therefore seemed to be a plausible contributing mechanism worth exploring further, and has thus been studied intensely in-flight and in ground-based bed rest studies. During the Skylab 4 mission, changes in the distensibility of the leg veins were determined using in-flight venous occlusion plethysmography. The results suggest that early in flight, venous leg volume is significantly increased for a given occlusion pressure [231]. These results are difficult to interpret in terms of changes of the capacitive properties of the leg veins. Venous pressure-volume relationships are non-linear; changes in the incremental venous capacitance might occur simply because the leg venous transmural pressure has shifted to a more compliant region of the relationship. Furthermore, we note that venous occlusion plethysmography is incapable of separating changes in the capacitive properties of the vessels from changes in vasomotor tone (venous tone). Plethysmography

results, however, are commonly interpreted as changes in the physical characteristics of the veins only, and we will report them as such.

Watenpaugh and co-workers [241] and Buckey et al. [242] studied the leg circulation in SLS-1 and SLS-2 astronauts. Watenpaugh noted a difference in leg blood flow but did not detect a difference in the capacitive properties of the legs on landing day. Buckey showed that total leg volume after spaceflight was smaller than before, yet the increase in total leg volume at the conclusion of a stand test was basically the same before and after flight. Furthermore, he documented that the volume pooled in the leg circulation by those astronauts capable of finishing a landing-day tilt test is quite comparable to the volume pooled by those who become pre-syncope.

Numerous results from bedrest studies suggest an increase in the venous compliance of the legs at the conclusion of bedrest [53, 232, 243, 244]. However, it is generally thought that such changes are at most secondary in importance in contributing to post-bedrest or post-spaceflight orthostatic intolerance [81, 241, 245, 246].

**Cardiac atrophy** Evidence for alterations in cardiac performance have frequently been based on observations of reduced end-systolic, end-diastolic, or stroke volume indices on landing day. Bungo reported a reduction of 22 % in the left ventricular end-diastolic volume index (EDVI) on landing day in seven astronauts [247]. In a group of seventeen astronauts, he was still able to detect a reduction in EDVI of 11 % 7-14 days after landing. In a group of 24 astronauts, Mulvagh and co-workers noted a reduction in left ventricular EDVI of 11 % on landing day after short-duration missions lasting 4-5 days [50]. Their data, however, suggest recovery to pre-flight values within 48 hours of landing. Martin and co-workers showed a reduction in left ventricular EDVI of approximately 10 % after short-duration missions (4-17 days) yet only about 5 % after long-duration missions (129-144 days) [44]. Neither change was statistically significant. Further conflicting results exist for long-duration missions. Atkov reported a mean reduction in left ventricular EDVI of 23 % in ten Solyut-6 astronauts whose missions ranged from 75 to 185 days and five astronauts who stayed aboard Solyut-7 for seven to eight months [248]. Hérault and co-workers examined six MIR astronauts after six months in space and did not detect a statistically significant shift in their left ventricular EDVI [249]. Using an empirical formula to assess myocardial mass echocardiographically, Martin reported a reduction in cardiac mass of about 12 % after long-duration missions; he failed to detect any significant change after short-duration missions [44]. In four SLS-2 astronauts, post-flight MRI examinations revealed changes in cardiac mass ranging from +7 % to -28 % [mean:  $(-12 \pm 6.9) \%$ ] compared to pre-flight values [43, 250].

Reductions in end-systolic and end-diastolic volume indices might simply reflect a hypovolemic state and might not necessarily be indicative of structural and functional impairment of the heart. Similarly, it is unclear whether a reduction in cardiac mass is simply a reflection of a hypovolemic state or whether it indicates a *functionally atrophic* process that causes a reduction in the number of cardiac myocytes or their cellular machinery, resulting in impairment of cardiac contraction or relaxation.

Evidence for the latter has been given by Barańska [251], Philpott [252], and Gold-

stein [253], who have performed histological examinations on hearts from space-flown rats. Their results indicate a decrease in the relative number and volume fraction of mitochondria [251, 252], the energy-producing cells, and a reduction in cross-sectional area of papillary muscle myofibers [253]. Both results point to ultrastructural changes at the sub-cellular level. More recently, however, Ray and co-workers could not find a statistically significant difference between space-flown and control rats [254]. Furthermore, their data shows no statistically significant difference between left ventricular  $(dP/dt)_{\max}$  between space-flown rats and controls, suggesting no significant alteration in ventricular contractility. The authors acknowledged Buckley [242] and attribute failure to maintain blood pressure after short duration spaceflight to changes in the periphery rather than cardiac deterioration.

However, this view is not shared by Levine and co-workers, who have studied the cardiac adaptation to head-down bedrest in a series of experiments [41–43, 255]. Their major finding is a leftward shift of the left-ventricular end-diastolic pressure-volume relation, leading to a smaller end-diastolic volume for a given end-diastolic pressure, or — alternatively — to a steeper Starling curve post-bedrest. This phenomenon seems independent of the hypovolemic state of the subjects [42]. The authors speculate that their findings may play an important role in the genesis of post-spaceflight orthostatic intolerance, in particular after long-duration missions [43].

As should be evident from this review, whether or not changes in cardiac performance contribute significantly to post-flight orthostatic intolerance is still very much an open and hotly debated question.

**Autonomic dysfunction** Given the importance of autonomic dysfunction in ground-based, non-spaceflight related orthostatic intolerance syndromes, much effort has been spent analyzing the integrity of the autonomic nervous system pre-flight, in-flight, and post-flight. Using a neck-cuff to stimulate the carotid sinus receptors, Fritsch and co-workers identified a blunted vagally-mediated baroreflex control of heart period in the supine posture following space travel [256]. In a follow-up study, the author confirmed her previous results and noted that supine plasma epinephrine and norepinephrine levels on landing day were significantly higher when compared to pre-flight levels, indicating a shift in the balance between sympathetic and parasympathetic control [38]. Whitson reported significantly elevated levels of plasma catecholamines in the supine and in the upright posture on landing day when compared to pre-flight levels, and concluded that decreased orthostatic tolerance following spaceflight is largely due to a 26 % reduction in stroke volume [51]. However, she did not separately report the hemodynamic responses of those astronauts who did (non-finishers) and those who did not (finishers) become pre-syncopal during an orthostatic stress test on landing day. Such an analysis, subsequently reported by Buckley [242] and Fritsch-Yelle [235], revealed that non-finishers failed to increase total peripheral resistance to the extent that the finishers were able to do. This failure to vasoconstrict correlated with a failure to increase plasma norepinephrine levels sufficiently [235]. Recently, Meck and co-workers showed that failure to mount a norepinephrine response upon standing post-flight is not related to impaired synthesis of norepinephrine or failure of the



end-organ to respond to norepinephrine [236]. Rather, the central nervous system's release of norepinephrine in the non-finishers seems to be inappropriate, given the level of orthostatic stress [236]. Levine and co-workers measured muscle sympathetic nerve activity during tilt tests in six astronauts on landing day; they noted an elevation in nerve traffic both in the supine and in the head-up posture, when compared to pre-flight levels [257]. Given that none of the subjects in Levine's study became pre-syncopal, his results do not conflict with Meck's hypothesis of central autonomic dysfunction as a principal contributor to post-flight orthostatic intolerance [227, 236].

As mentioned above, inappropriately low levels of plasma norepinephrine have been correlated with a failure to increase total peripheral resistance upon standing post-flight. A reduced arteriolar vasoconstrictor response has therefore been implicated in the genesis of pre-syncope following space travel [242, 246]. Of similar or even higher importance, however, might be failure of veins to contract in response to standing, thus leading to an inappropriate attenuation of venous return in the upright posture.

**Vascular adaptation** Vascular adaptation to microgravity in humans has most frequently been studied by focusing on the system-level total peripheral resistance response to post-flight tilt tests. This approach, however, does not specifically probe alterations in vascular properties but rather examines alterations of the entire baroreflex loop. Unfortunately, only limited information exists on the adaptation of arterial and venous vessels in humans to spaceflight. Meck's study [236], described above, is a notable exception, as is the study by Herval and co-workers [249]. In the latter study, the investigators determined vascular flows and diameters using ultrasound before, during, and after spaceflight. They noted a significant increase in the diameter of the femoral vein and speculated that prolonged venous distention might affect the physical properties of the vascular wall and its ability to vasoconstrict. Unfortunately, their morphometric analyses were not coupled to pharmacological dose response studies to test this hypothesis.

Wilson and co-workers studied cutaneous vasoreactivity in 22 subjects undergoing a head-down tilt bedrest protocol [258]. They found that cutaneous vasoconstriction in the arms and legs in response to exogenous norepinephrine administration remained unaffected by 14 days of head-down bedrest.

Ground-based rodent studies have provided a wealth of physiological and histological insight into arterial remodeling and vascular reactivity that point to heterogeneous adaptation of different vascular beds to simulated microgravity (hindlimb suspension) [see, e.g., 54]. How to extrapolate these results to humans remains unclear, however.

Several conclusions can be drawn from the literature review above. First, astronauts on landing day are hypovolemic by about 6–7% of total blood volume. Second, cardiovascular function following spaceflight is characterized by low stroke volume in the supine and in the head-up posture when compared to the respective values pre-flight. This observation holds for both astronauts who do and who do not become pre-syncopal on landing day. The etiology of this observation is unclear; several

mechanisms affecting venous return (such as hypovolemia and increased venous compliance of the legs) and cardiac performance (cardiac atrophy) have been implicated, yet no conclusive proof has been established for any of these mechanisms. Third, pre-syncopal astronauts fail to increase their peripheral resistance upon standing to the extent that non-pre-syncopal astronauts do.

This phenomenon is correlated with low circulating norepinephrine levels in the supine posture. Furthermore, pre-syncopal astronauts fail to increase their plasma norepinephrine levels in the upright posture to the extent that non-pre-syncopal astronauts do. Recent evidence implicates central nervous plasticity rather than failure of the end-organs.

### 8.3 Testing Hypotheses

Using the model developed and validated in previous chapters, we can gain insight into the cardiovascular system's failure to adapt to the upright posture post-flight by simulating the system-level hemodynamic response to a tilt or a stand test while varying certain key parameters. This approach can be viewed as a targeted sensitivity analysis that differs from the more general explorations presented in Chapters 5 and 6, in that the parameters to vary are selected based on physiological considerations. Furthermore, the parameter values will be subjected to larger perturbations than in to the more narrow local analysis of Chapter 5.

In selecting parameters for our analysis, we are guided by the literature review of the previous section, and choose parameters that have been implicated in contributing to the post-flight orthostatic intolerance phenomenon. Our analysis therefore includes total blood volume, the venous compliance of the legs, the end-diastolic compliance of the right ventricle, and the static gain values (both arterial and cardiopulmonary) of arteriolar resistance and venous tone. We will mostly assess the impact of parameter perturbations by analyzing the changes they induce in the mean arterial pressure and heart rate responses to a 75° head-up tilt. In particular, we will seek answers to the following three questions:

1. Which of the parameters included in the analysis has the greatest impact on mean arterial pressure and heart rate?
2. Assuming the same fractional decrement in arteriolar resistance and venous tone gains, which of the two autonomic control mechanisms affect mean arterial pressure and heart rate more?
3. Which of the parameters included in the analysis affects steady-state stroke volume most?

The answer to the first question allows us to establish a hierarchy of mechanisms contributing to orthostatic intolerance in much the same way that we rank-ordered the importance of parameters in Chapter 5. The second question addresses the issue, raised in the previous section, of whether changes in the reactivities of arteriolar

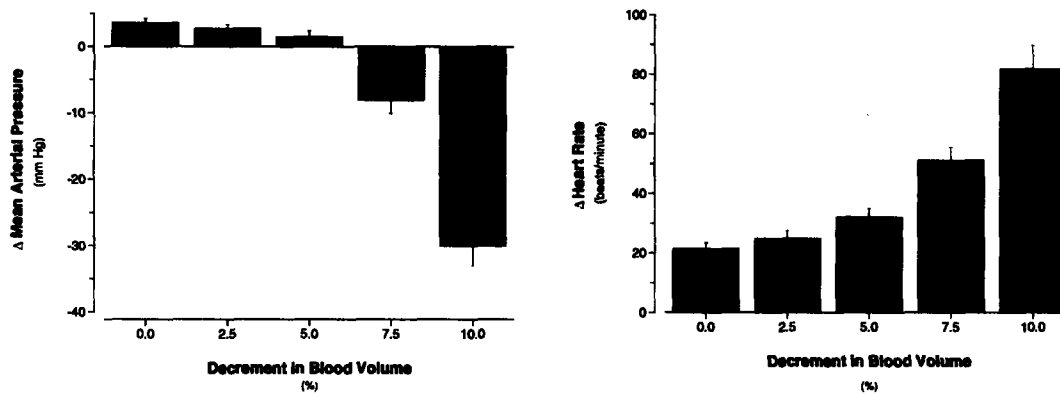


Figure 8-1: Mean arterial pressure and heart rate changes induced by head-up tilt to 75°. Dependence on volume status. Mean response  $\pm$  SE based on 20 simulations.

resistance or venous tone have greater impact on the outcome of tilt tests. The third question is motivated by the observation that astronauts on landing day have lower baseline stroke volumes when compared to pre-flight levels. It seeks to establish which, if any, parameters exert the greatest influence over steady-state stroke volume<sup>1</sup>

We address the first question by repeatedly simulating tilt experiments while varying each of the parameters by a certain percentage of their nominal values. In Figure 8-1, we report the changes in mean arterial pressure and heart rate from their respective supine baselines in response to a four-minute head-up tilt to 75° for varying levels of total blood volume. In Chapter 7, we noted that head-up tilt usually results in a slight increase in mean arterial pressure measured at heart level, with a concomitant increase in heart rate. Figure 8-1 reflects this fact as the baseline simulation (0% decrement in total blood volume) shows an increase in mean arterial pressure of about 4 mm Hg and an increase of approximately 20 beats/minute in heart rate. As blood is withdrawn, the gentle rise in mean arterial pressure is diminished but generally maintained up to volume decrements of 5%. Beyond that, the system increasingly fails to maintain mean arterial pressure despite incrementally larger increases in heart rate. The reason for this behavior becomes clear when we consider blood pooling in the dependent vasculature during tilt as a function of hydration status. With increasing degree of hypovolemia, the amount of blood volume pooled in the lower extremities becomes an increasingly larger fraction of distending volume. It is therefore increasingly difficult for the cardiovascular system to maintain mean arterial pressure during tilt.

In Figure 8-2, we display the results of the same analysis for the venous compli-

<sup>1</sup>We want to emphasize that stroke volume is dependent on heart rate, ventricular filling pressure, arterial pressure, and cardiac parameters, and is therefore not an indicator of cardiac performance *per se*.

ance of the legs, the right-ventricular end-diastolic compliance, and the arterial and venous tone feedback gain values (top to bottom). Each of the simulations underlying Figure 8-2 starts with the same baseline blood volume, which, for future reference, we term the euvoletic baseline state. When comparing the results in Figure 8-2 with the volume loss results in Figure 8-1, it is obvious that deleterious changes in any of the parameters shown in Figure 8-2 have only marginal impact on the hemodynamic response to tilt if the volume status is euvoletic. In other words, in the absence of hypovolemia, the body can tolerate significant detrimental changes in any of the other parameters without developing a seriously compromised hemodynamic response to tilt.

Next, we demonstrate that this behavior can change drastically if the baseline volume status is changed. In Figure 8-3, we vary the four parameters of Figure 8-2 by the same fractional changes, yet their variation is superimposed on a baseline state that is 5% hypovolemic compared to the euvoletic baseline states of Figures 8-1 and 8-2. The results demonstrate that even a modest 5% to 10% detrimental change in each of the parameters can have a significant impact on the hemodynamic response to tilt if the baseline hydration state is borderline hypovolemic.

The results of the simulations show that the level of hydration has by far the greatest impact on blood pressure homeostasis during tilt. Furthermore, the impact of changes in other parameters varies significantly with the level of hydration. In the euvoletic state, changes in the four parameters considered in Figures 8-2 and 8-3 have similar effects on the mean arterial pressure and heart rate responses. In the hypovolemic case, changes in venous tone seem to impact the hemodynamic response to tilt more when compared with the same fractional changes in the other parameters, yet none of the parameters considered has negligible influence over heart rate and mean arterial pressure.

In Figure 8-4, we compare side-by-side the effects of changes in arteriolar resistance and venous tone gains superimposed on a 5% hypovolemic baseline state. We know from the literature review in the previous section that pre-syncopal astronauts fail to increase plasma norepinephrine [235], which can be interpreted as a reduction in the resistance and venous tone gain values. The simulations in Figure 8-4 suggest that mean arterial pressure homeostasis is sacrificed to a larger extent by changes in venous tone feedback than arterial resistance feedback.

In Figure 8-5, we show the steady-state supine stroke volume as a function of reductions in blood volume. Figure 8-6 summarizes the same information if fractional changes in the four other parameters are superimposed on a 5% hypovolemic baseline state. The simulations suggest again that detrimental changes in blood volume have the largest impact on steady-state supine stroke volume. The gain of the venous tone feedback and the end-diastolic compliance of the right ventricle have similarly deleterious effects when a hypovolemic state is assumed.

The simulations presented in this section demonstrate the importance of blood volume in maintaining baseline stroke volume and mean arterial pressure during orthostatic stress. Changes in the other parameters included in this analysis are largely inconsequential if total blood volume is normal. However, if the baseline state is

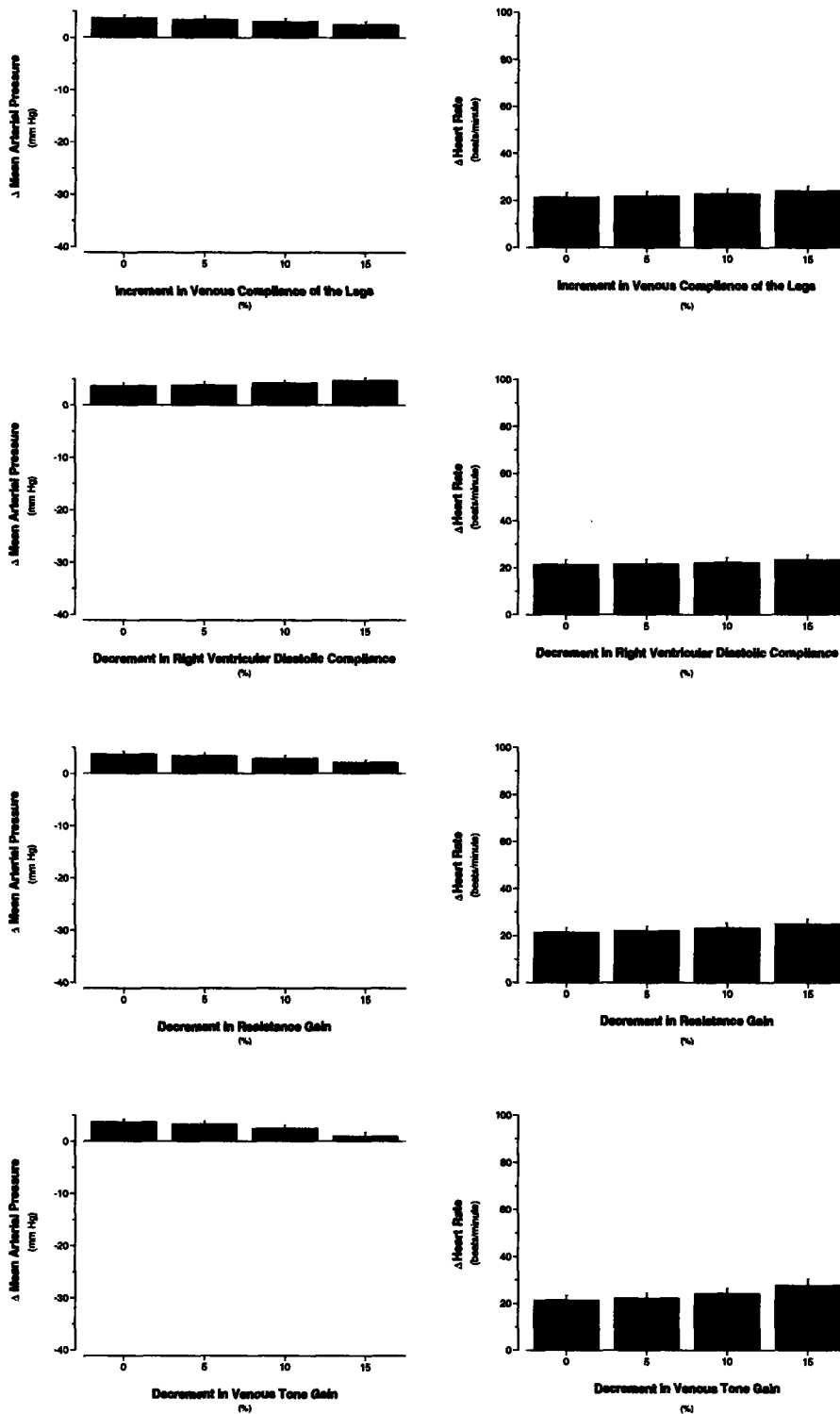


Figure 8-2: Mean arterial pressure and heart rate changes in response to a 75° head-up tilt under varying parametric conditions. Baseline volume status is euvoletic. Mean response  $\pm$  SE based on 20 simulations.

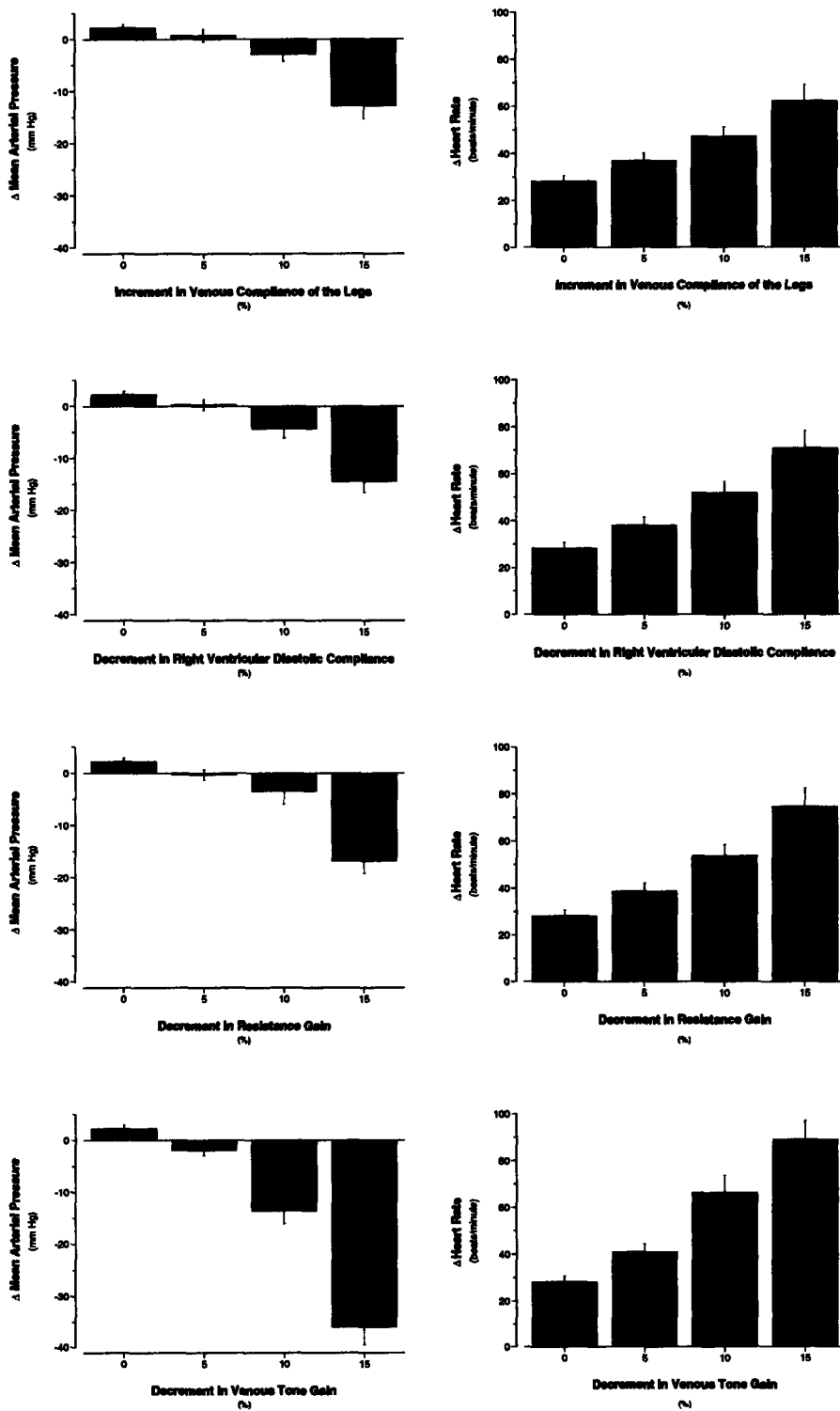


Figure 8-3: Mean arterial pressure and heart rate changes in response to a 75° head-up tilt under varying parametric conditions. Baseline volume status is 5% hypovolemic. Mean response  $\pm$  SE based on 20 simulations.

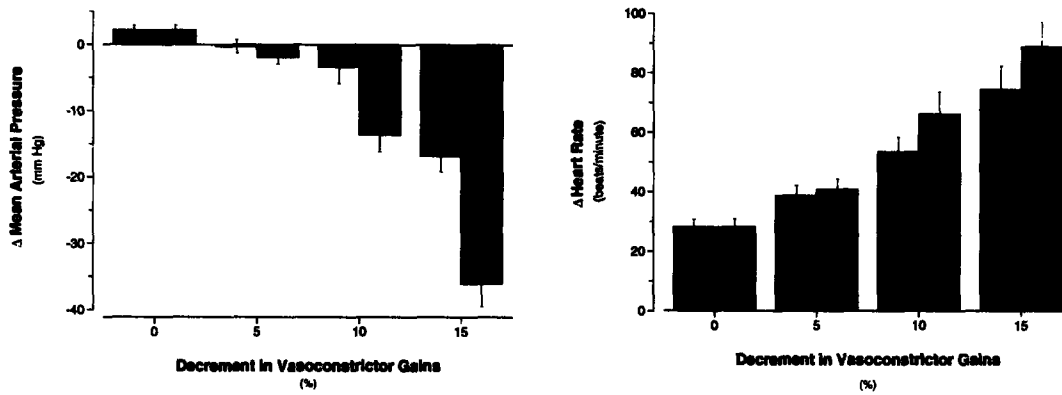


Figure 8-4: Mean arterial pressure and heart rate changes induced by head-up tilt to 75°. Black bars: decrements in venous tone gains; gray bars: decrements in resistance gains. Baseline volume status is 5% hypovolemic. Mean response  $\pm$  SE based on 20 simulations.

hypovolemic, even moderate changes in these parameters can aggravate the cardiovascular system's failure to adapt properly to the upright posture. Reductions in both the arterial resistance gains and the venous tone gains affect mean arterial pressure; impairment of the venous tone feedback, however, has a stronger effect when the same fractional decrements in the nominal values are considered.

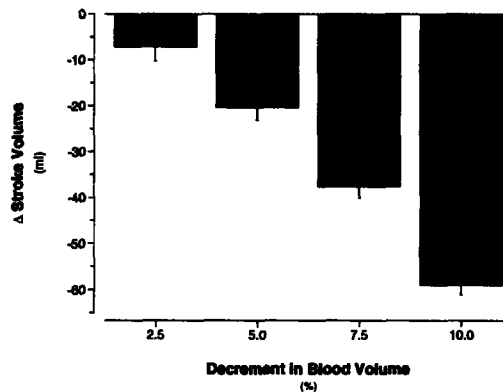


Figure 8-5: Changes in supine stroke volume on volume status. Baseline volume status is euvoletic. Mean response  $\pm$  SE based on 20 simulations.

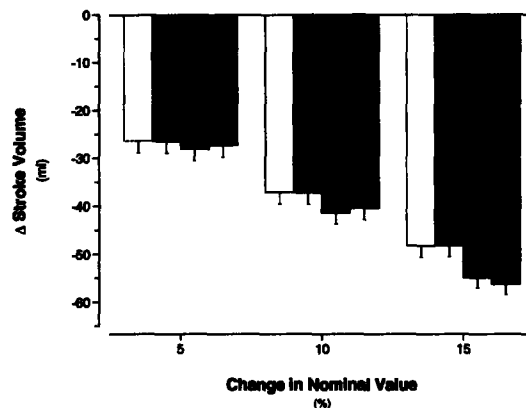


Figure 8-6: From left to right (white to black): increments in venous compliance of the legs, decrements in arterial resistance gains, decrements in right-ventricular end-diastolic compliance; decrements in venous tone gains. Baseline volume status is 5% hypovolemic. Mean response  $\pm$  SE based on 20 simulations.

## 8.4 Model-based Data Analysis

Many astronauts undergo orthostatic stress testing before space travel and on landing day. Currently, the standard protocol calls for such testing for rookie astronauts, for astronauts who have experienced orthostatic intolerance following previous missions, and for astronauts returning from long-duration missions. The data is usually collected by staff from the Cardiovascular Laboratory at Johnson Space Center.

Figure 8-7 shows heart rate and mean arterial pressure recordings in response to a stand test in the same astronaut approximately ten days before lift-off (left panel) and on landing day (right panel). The post-flight data suggest that despite a more dramatic increase in heart rate, mean arterial pressure during orthostatic stress falls below supine levels. This is not seen in the pre-flight recording.

Figure 8-8 shows the same experimental data (dashed lines) along with simulations thereof (solid lines). To obtain the simulations, we applied the subset optimization algorithm described in Chapter 6 to identify the best-fit simulations to the heart rate and mean arterial pressure recordings pre- and post-flight. Six parameters were included in the optimization procedure. Except for a slight overshoot following the initial transient reductions in mean arterial pressures, the simulations generally fit the experimental data quite well, both in amplitude and in time course.

When comparing the parameter profiles of the two simulations, one notices that the post-flight simulations are characterized by a reduction in total blood volume by approximately 9%, an increase in the pressure set-point of the arterial baroreflex by approximately 20%, and an increase in the heart rate set-point by approximately 16%. The reduction in blood volume is certainly consistent with the analysis and the literature review in previous sections. The changes in arterial pressure and heart



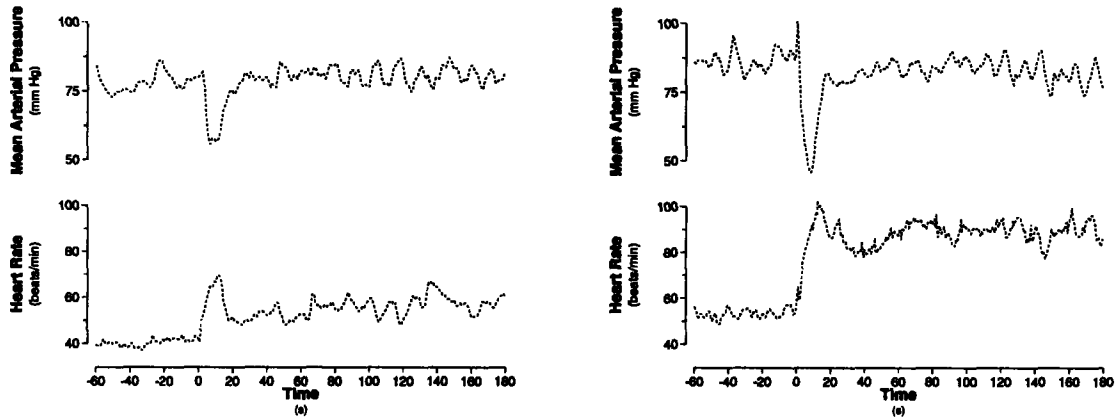


Figure 8-7: Heart rate and mean arterial pressure during stand test in one astronaut before space travel (left panel) and on landing day (right panel).

rate set-points are less readily interpretable. Possible explanations certainly include a plasticity of arterial baroreflex: due to the adaptation to microgravity, heart rate and arterial pressure might be regulated at different values following space travel.

We included this example of model-based data analysis not to give a definite explanation of the observed increase in heart rate and drop in mean arterial pressure post-flight but to give an example of how we intend to use the optimization algorithm along with real data from astronauts pre- and post-flight. However, it is reassuring that the amount of blood volume reduction predicted by the model is well within the range of what has been reported in astronauts following short-duration missions.

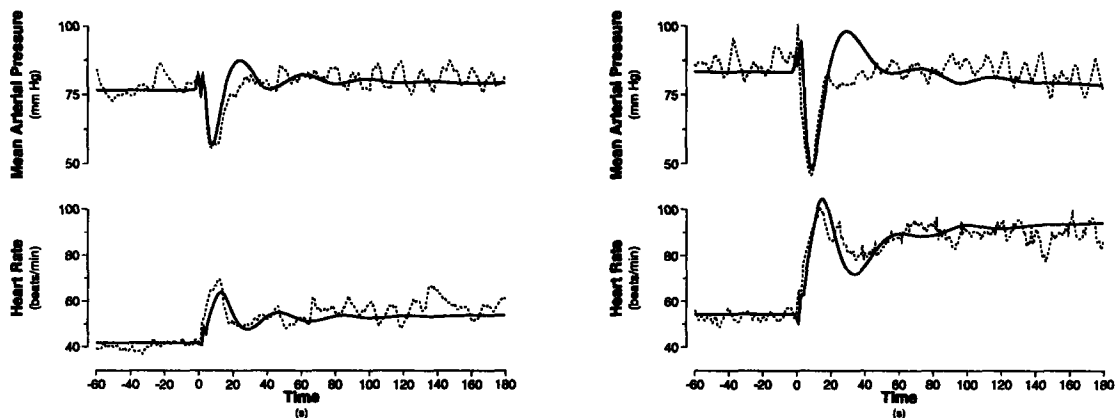


Figure 8-8: Heart rate and mean arterial pressure during stand test in one astronaut before space travel (left panel) and on landing day (right panel) and best-fit simulations thereof (dashed lines).

## 8.5 Summary and Conclusions

In this chapter, we reviewed the evolution of post-spaceflight orthostatic intolerance from the earliest manned American space missions to the most recent long-duration missions. We also reviewed the wealth of mechanistic studies that aimed at elucidating the etiology of post-flight orthostatic intolerance. Our simulations indicate that changes in total blood volume have the biggest detrimental impact on blood pressure homeostasis in the head-up posture. If the baseline volume status is borderline hypovolemic, changes in other parameters can significantly impact the cardiovascular system's ability to maintain mean arterial pressure constant in the upright posture. In particular, any deleterious changes in the venous tone feedback impairs blood pressure homeostasis significantly. This result has important implications as it suggests that  $\alpha_1$ -adrenergic agonists (such as midodrine) might help alleviate the orthostatic syndrome seen post-spaceflight.

Many countermeasures have been tried in the past, and most aim at increasing intra-vascular volume in-flight. Countermeasures that have been tested include in-flight lower body negative pressure (LBNP), LBNP with fluid loading, oral hydration using isotonic saline, oral pharmacological treatment (fludrocortisone) [259, 260] and thigh cuffs [249]. None of these interventions significantly improved orthostatic tolerance postflight. Oral hydration (8 g of NaCl with 960 ml fluid) [259, 261] two hours before re-entry is currently the countermeasure of choice, along with the use of an anti-g suit to prevent excessive blood pooling in the legs, and a liquid-cooling garment to prevent vasodilation during reentry [261]. However, if volume regulation is intact in-flight — and we have every reason to believe that it is — fluid loading before re-entry will merely increase the astronauts' discomfort and urine output rather than expanding intra-vascular volume for a significant amount of time. The suggestion that an  $\alpha_1$ -agonist can prevent post-flight orthostatic intolerance is not new. Midodrine has been used successfully to treat ground-based orthostatic hypotension secondary to pure autonomic failure [262], has been demonstrated to reduce orthostatic intolerance following 6° head-down bed-rest (a ground-based analog of microgravity) [263], and has recently proved efficacious in the prevention of post-spaceflight orthostatic intolerance in one astronaut who experienced pre-syncope following a previous mission [264]. Our results confirm the importance of venous tone in cardiovascular regulation in the upright posture and suggest that the vasoconstrictor effect of midodrine might be more important on the venous than the arterial side of the circulation.

We concluded this chapter by applying the optimization algorithm to the heart rate and blood pressure recordings of one astronaut before and after exposure to microgravity. The parameter estimates point to a volume problem along with changes in the control system that are somewhat harder to interpret. More work certainly needs to be done in order to gain confidence in the results of this matching procedure.

# Chapter 9

## Conclusions and Further Research

The cardiovascular response to postural changes has been the focus of several mathematical modeling studies and numerous experimental investigations in the past. Our work naturally builds on former studies but also extended previous work in important ways.

In this thesis, we set out to develop a comprehensive lumped-parameter model of the cardiovascular system and its short-term homeostatic control mechanisms with a particular application in mind, namely to simulate the short-term transient hemodynamic responses to various orthostatic stresses. Our effort to couple model building with model analysis, to gain insight into the mechanisms that contribute significantly to the cardiovascular system's adaptation to the head-up posture, distinguishes our work from previous modeling approaches.

In this final chapter, we summarize the main results and contributions of this effort before suggesting directions for future research.

### 9.1 Summary and Contributions

In Part I (Chapters 2 – 4), we built and validated a computational model of the cardiovascular system and its neural control mechanisms with the specific purpose of simulating the short-term ( $\lesssim 5$  min), transient hemodynamic response to orthostatic stress tests such as tilt, stand-up, and lower body negative pressure. Part II (Chapters 5 and 6) was dedicated to the analysis of the model and its application to the problem of parameter estimation. In Part III, we presented a clinical study (Chapter 7) of the short-term hemodynamic response to three different head-up maneuvers and subsequently used the model to explore hypotheses regarding the etiology of post-spaceflight orthostatic intolerance (Chapter 8).

In Chapter 2, we presented the architecture of and the parameter assignments for the models of the systemic circulation, the cardiac chambers, and the pulmonary circulation. Furthermore, we detailed the implementations of the various orthostatic stress maneuvers. We took great care to base the parameter values on sizable clinical studies of normal healthy volunteers. In this, we see a major contribution to the field of lumped-parameter modeling of the cardiovascular system, as it is — to our

knowledge — the first comprehensive attempt to justify parameter values rigorously. In Section 2.4, we reviewed the pertinent literature on changes in plasma volume during orthostatic stress and proposed a heuristic model to account for the sequestration of intra-vascular volume into the interstitial fluid compartment. All previous cardiovascular models have neglected fluid shifts during orthostatic stress between these two fluid compartments. Our literature review revealed that such shifts can be quite substantial in magnitude and occur with a time constant ( $\tau \approx 5$  min) that makes them quite relevant during short-term gravitational stress.

In Chapter 3, we described the architecture of and the parameter assignments for the cardiovascular control model. The latter consists of the two major neurally-mediated reflex loops, namely the arterial baroreflex and the cardiopulmonary reflex. The arterial baroreflex senses arterial transmural pressure and affects R-R-interval, venous zero pressure filling volume, arterial resistance, and right and left ventricular contractility. The cardiopulmonary reflex senses right atrial transmural pressure and affects venous zero pressure filling volume and arterial resistance only. Both reflex mechanisms were implemented using set-point models. As in Chapter 2, we tried as best as possible to justify the numerical values assigned to the reflex parameters. Given the substantial difficulties in studying these reflex mechanisms in human subjects, however, the resultant estimates of static gain values have considerable uncertainties associated with them.

Chapter 4 was dedicated to the validation of the model assembled in the previous two chapters. Here, we compared the steady-state values of hemodynamic variables to the population-averaged values found in a large number of healthy individuals. We extended this analysis by performing population simulations, the details of which are presented in Appendix B. The simulated population means, standard errors, and ranges of the steady-state values of hemodynamic variables compare quite favorably with their experimental analogs. In Section 4.3, we demonstrated that the model is capable of reproducing the changes in heart rate, mean arterial pressure, and stroke volume reported for changes in posture to different levels of elevation. Furthermore, we showed that the model reproduced the transient hemodynamic responses to rapid tilt and standing up. Both the temporal behavior and the magnitudes of the changes in heart rate and mean arterial pressure match the experimental data quite well. Similarly, the model is capable of reproducing the changes seen in mean arterial pressure, heart rate, and stroke volume in response to different levels of external negative pressure. The model's versatility has also been documented by demonstrating that it can reproduce the changes in hemodynamic variables due to exercise, with minimal additional modeling assumptions. The tilt, stand-up, and lower body negative pressure simulations have all been performed using the same parameter profile. We consider this further evidence that the baseline cardiovascular model represents the physiological response to orthostatic stress in the normal population quite well. The simulations in Section 4.3 suggest that the changes and relative timing in intra-thoracic pressure, intra-abdominal pressure, and the pressure external to the legs are quite important in generating the hemodynamic response to standing up. Only very few experimental studies have touched upon the possible contribution of changes in extra-vascular pressures to the genesis of the transient hemodynamic response to active and passive

changes in posture. Our simulations revealed a gap in our understanding and suggest that experimental studies be performed to identify time course and magnitude of these pressure changes (see Section 9.2).

In Chapter 5, we performed a local sensitivity analysis to identify which model parameters significantly impact cycle-averaged arterial pressure, cycle-averaged central venous pressure, stroke volume, and heart rate. We analyzed the sensitivities both in steady-state and during transients induced by head-up tilt simulations. As expected, the vast majority of model parameters do not impact the four output variables significantly. This is in part due to the fact that cycle-averaged variables constitute a highly aggregated form of model output. Mostly, however, the sensitivity analysis indicates that the model is highly over-parameterized for the simulation of only four output variables. Several parameters rank consistently high in the first-order analysis and are variably offset from the remainder in the sensitivity spectra. These are the arterial baroreflex set-point pressure, the cardio-pulmonary set-point pressure, distending blood volume, and the heart rate set-point. The ventricular systolic timing parameter and the right ventricular diastolic compliance complement the list of top-ranking parameters for stroke volume and central venous pressure. We did not address in this thesis how to use the results of the sensitivity studies to change the model structure. This will be an important area for future research.

In Chapter 6, we focused our attention on the problem of estimating parameter values of the cardiovascular model from experimental data. We reviewed non-linear least squares optimization methods and discussed the effects of ill-conditioning on parameter estimates. We implemented a Gauss-Newton gradient-based optimization algorithm coupled to subset selection to overcome ill-conditioning of the Hessian matrix. The latter method partitions the parameter vector into a well-conditioned and an ill-conditioned part. The parameters giving rise to ill-conditioning are fixed at a priori values and the remaining parameters are estimated via a reduced-order optimization scheme. The reduced-order parameter estimates generally have little bias and are insensitive to perturbations of the experimental data. Throughout the chapter, we used synthetic data, generated by the model, as “experimental” data so that the true parameter values are known to us. The results of Chapter 6 are quite promising and warrant further exploration. To our knowledge, this is the first attempt at extracting physiologically meaningful parameters from the transient hemodynamic response to gravitational stress.

In Chapter 7, we summarized the results of our clinical study, where we investigated the hemodynamic response to sudden rapid tilt, to slow tilt, and to standing up. This study was motivated in part by conflicting experimental results in the medical literature. Some claimed a significant difference exists between the hemodynamic response to active and passive changes in posture, while others presented data that indicated otherwise. Our own investigation showed that significant differences between rapid tilt and standing up exist only during the first twenty seconds after the onset of the change in posture. Thereafter, the arterial blood pressure and heart rate responses become statistically indistinguishable. In a follow-up pilot study, we tested the hypothesis of whether abdominal and leg muscle contraction can account for the observed differences during the first twenty seconds. The results are quite compelling,

in that the hemodynamic responses to rapid tilt with prior muscle contraction and standing up are almost indistinguishable. The results of this study suggest further that the roles of intra-thoracic pressure, intra-abdominal pressure, and external pressures of the leg veins be investigated for their contribution and importance in the genesis of the hemodynamic response to standing up.

In Chapter 8, we reviewed the evolution of post-spaceflight orthostatic intolerance from the earliest manned American space missions to the most recent long-duration missions. We also reviewed the wealth of mechanistic studies that aimed at elucidating the etiology of post-flight orthostatic intolerance. Based on current hypotheses, we simulated the effect of fractional changes in some of the cardiovascular parameters that have been implicated in contributing to the orthostatic intolerance phenomenon. Our simulations indicate that changes in total blood volume have the biggest detrimental impact on blood pressure homeostasis in the head-up posture. If the baseline volume status is borderline hypovolemic, changes in other parameters can significantly impact the cardiovascular system's ability to maintain mean arterial pressure constant in the upright posture. In particular, any deleterious changes in the venous tone feedback impairs blood pressure homeostasis significantly. This result has important implications as it suggests that  $\alpha$ -adrenergic agonists (such as midodrine) might help alleviate the orthostatic syndrome seen post-spaceflight.

## 9.2 Suggestions for Further Research

Despite our best intentions and efforts, the research presented in the previous eight chapters only partially succeeded in answering the questions it set out to address. As with any research agenda, this work seemingly raised as many new questions as it provided answers to old ones. Below, we provide a list of possible future research projects that were motivated by our work.

**Cycle-averaged models** At the system level, time-varying ventricular elastance models have proven to be useful representations of the right and left heart. When coupled to appropriate models of the peripheral systemic and pulmonary circulations, such models allow for simulation of realistic pulsatile, quasi-periodic pressure and flow waveforms. However, throughout the majority of this thesis, we were not interested in an instantaneous value of a particular variable, or in the details of a specific waveform, but rather in the response of the variable's short-term average to perturbations in its parameters. This response typically occurs over time scales that are large compared to the dynamics of cardiac contraction. In these cases, a cycle-averaged model, which tracks cycle-to-cycle (i.e. inter-cycle) dynamics rather than intra-cycle dynamics, seems desirable for several reasons. First, by ignoring the fine intra-cycle structure of each waveform, one can expect to reduce computational cost significantly. Second, one can anticipate that analysis of the dynamics of interest can be simplified if the model structure is reduced sufficiently. Third, it is typically the time-averages and not instantaneous values of key state variables that are regulated through feedback control.

Some nascent work in our group is aimed at developing dynamic cycle-averaged models from pulsatile ones [32–35]. We have begun analytical and computational studies of averaging [32, 35] and sampled-data modeling [33, 34] on a highly simplified model (single heart chamber, single circulatory loop, no control). Much more remains to be done in order to extend these results to more established models that include cardiovascular control mechanisms. Since lumped-parameter pulsatile representations are quite common in modeling of physiological systems, we expect cycle-averaging to have application beyond the cardiovascular domain.

**Model reduction and Parameter estimation** The sensitivity analysis of Chapter 5 addressed the question of which parameters influence particular output variables. This knowledge is in turn critical to matching a model to experimental data by parameter tuning, and to determining which parts of a dynamic model are significantly exercised in generating particular outputs. The sensitivity analysis did not determine where aggregation or simplification or reduction of the model may be allowed, and where refinement or elaboration may be needed.

The parameter estimation algorithm in Chapter 6 performed quite well in estimating the parameters of the reduced-order problems. Further explorations should investigate the relationship between the number of signals included in the analysis and the quality of the resultant parameter estimates. Subset selection is not invariant under multiplicative row or column scaling. It is worth examining whether this fact can be exploited in order to estimate more parameters from a given response or to estimate the same number of parameters better (smaller variance or smaller bias).

**Further tilt studies** Our tilt study confirmed previous work in that the hemodynamic response to a sudden tilt is different from the hemodynamic response to a stand-up maneuver. When comparing the time series of heart rate and mean arterial pressure (see Figures 7-5 and 7-6), one realizes that this difference is confined to the first twenty seconds after the onset of the change in posture. Our simulations and our pilot study suggest that leg and abdominal muscle contractions, as well as changes in intra-thoracic pressure might be important contributors to the more pronounced stand-up response. This hypothesis directly challenges the established view that the difference in the two responses is due to cardiopulmonary-mediated transient vasodilation. Surprisingly little information is available in the medical literature regarding the time course and magnitude of changes in intra-thoracic and intra-abdominal pressures during active and passive changes in posture.

A definitive experiment to test this hypothesis would be quite invasive. One would ideally monitor right atrial pressure, intra-thoracic pressure, intra-abdominal pressure, and leg venous pressure during active stand-ups and passive tilts. A less invasive but more indirect investigation involves esophageal and gastric pressures as surrogates for intra-thoracic and intra-abdominal pressures. Both could be measured with a single double-lumen balloon catheter that would be swallowed by the study subjects.

**Hypovolemia studies** In Chapter 8, we established that reductions in total blood volume significantly impact the blood pressure response to the head-up posture. Our analyses in Chapter 6 revealed that distending blood volume is one of the well-conditioned parameters that yields reliable estimates.

Our modeling approach would find an important application if one could estimate with sufficient sensitivity the degree of hypovolemia from arterial blood pressure and heart rate recordings given appropriate euvoletic reference recordings. In order to test the sensitivity of such an approach, we would need to study the hemodynamic response of normal volunteers in the euvoletic and hypovolemic states. Such a population could potentially be found in blood donors.



# Appendix A

## Parameters of the Cardiovascular Model

Table A.1: Parameters of the cardiovascular model.

Index	Description	Unit	Value
0	Arterial baroreflex set-point pressure	mm Hg	(98±1)
1	Arterial baroreflex scaling factor	mm Hg	18
2	R-R-interval sympathetic gain	$\frac{\text{ms}}{\text{mm Hg}}$	(9±1)
3	R-R-interval parasympathetic gain	$\frac{\text{ms}}{\text{mm Hg}}$	(9±1)
4	Arterial baroreflex $R_{\text{up}}$ gain	$\frac{\text{PRU}}{\text{mm Hg}}$	(-0.05±0.01)
5	Arterial baroreflex $R_{\text{k}}$ gain	$\frac{\text{PRU}}{\text{mm Hg}}$	(-0.05±0.01)
6	Arterial baroreflex $R_{\text{sp}}$ gain	$\frac{\text{PRU}}{\text{mm Hg}}$	(-0.05±0.01)
7	Arterial baroreflex $R_{\text{ll}}$ gain	$\frac{\text{PRU}}{\text{mm Hg}}$	(-0.05±0.01)
8	Arterial baroreflex $V_{\text{up}}$ gain	$\frac{\text{ml}}{\text{mm Hg}}$	(5±2)
9	Arterial baroreflex $V_{\text{k}}$ gain	$\frac{\text{ml}}{\text{mm Hg}}$	(2±1)
10	Arterial baroreflex $V_{\text{sp}}$ gain	$\frac{\text{ml}}{\text{mm Hg}}$	(13±3)
11	Arterial baroreflex $V_{\text{ll}}$ gain	$\frac{\text{ml}}{\text{mm Hg}}$	(7±2)
12	Arterial baroreflex $C_{\text{rv}}^{\text{es}}$ gain	$\frac{\text{ml}}{\text{mm Hg}^2}$	(0.022±0.003)
13	Arterial baroreflex $C_{\text{lv}}^{\text{es}}$ gain	$\frac{\text{ml}}{\text{mm Hg}^2}$	(0.007±0.001)
14		cm	(6±1)
15	Cardio-pulmonary reflex set-point pressure	mm Hg	(6±1)
16	Cardio-pulmonary reflex scaling factor	mm Hg	5
17	Cardio-pulmonary reflex $R_{\text{up}}$ gain	$\frac{\text{PRU}}{\text{mm Hg}}$	(0.05±0.01)
18	Cardio-pulmonary reflex $R_{\text{k}}$ gain	$\frac{\text{PRU}}{\text{mm Hg}}$	(0.05±0.01)
19	Cardio-pulmonary reflex $R_{\text{sp}}$ gain	$\frac{\text{PRU}}{\text{mm Hg}}$	(0.05±0.01)

*continued on next page*

Table A.1: *continued*

Index	Description	Unit	Value
20	Cardio-pulmonary reflex $R_{II}$ gain	$\frac{\text{PRU}}{\text{mm Hg}}$	(0.05±0.01)
21	Cardio-pulmonary reflex $V_{up}$ gain	$\frac{\text{ml}}{\text{mm Hg}}$	(13±2)
22	Cardio-pulmonary reflex $V_k$ gain	$\frac{\text{ml}}{\text{mm Hg}}$	(3±1)
23	Cardio-pulmonary reflex $V_{sp}$ gain	$\frac{\text{ml}}{\text{mm Hg}}$	(64±12)
24	Cardio-pulmonary reflex $V_{II}$ gain	$\frac{\text{ml}}{\text{mm Hg}}$	(30±5)
25	Delay parasympathetic impulse response	s	(0.59±0.25)
26	Peak parasympathetic impulse response	s	(0.70±0.25)
27	End parasympathetic impulse response	s	(1.0±0.25)
28	Delay $\beta$ -sympathetic impulse response	s	(2.5±1.0)
29	Peak $\beta$ -sympathetic impulse response	s	(3.5±1.0)
30	End $\beta$ -sympathetic impulse response	s	(15.0±5.0)
31	Intra-thoracic pressure	mm Hg	(-3.0±0.5)
32	<i>Unassigned</i>		
33	<i>Unassigned</i>		
34	<i>Unassigned</i>		
35	<i>Unassigned</i>		
36	Upper body venous compliance	$\frac{\text{ml}}{\text{mm Hg}}$	(7.0±2.0)
37	Kidney venous compliance	$\frac{\text{ml}}{\text{mm Hg}}$	(5.0±1.0)
38	Splanchnic venous compliance	$\frac{\text{ml}}{\text{mm Hg}}$	(50.0±7.5)
39	Lower body venous compliance	$\frac{\text{ml}}{\text{mm Hg}}$	(20.0±3.0)
40	Abdominal venous compliance	$\frac{\text{ml}}{\text{mm Hg}}$	(1.3±0.1)
41	Inferior vena cava compliance	$\frac{\text{ml}}{\text{mm Hg}}$	(0.5±0.1)
42	Superior vena cava compliance	$\frac{\text{ml}}{\text{mm Hg}}$	(1.3±0.1)
43	Right atrial diastolic elastance	$\frac{\text{mm Hg}}{\text{ml}}$	(0.3±0.1)
44	Right atrial end-systolic elastance	$\frac{\text{mm Hg}}{\text{ml}}$	(0.74±0.1)
45	Right ventricular diastolic elastance	$\frac{\text{mm Hg}}{\text{ml}}$	(0.07±0.03)
46	Right ventricular end-systolic elastance	$\frac{\text{mm Hg}}{\text{ml}}$	(1.3±0.8)
47	Pulmonary arterial compliance	$\frac{\text{ml}}{\text{mm Hg}}$	(3.4±1.8)
48	Pulmonary venous compliance	$\frac{\text{ml}}{\text{mm Hg}}$	(9.0±3.7)
49	Left atrial diastolic elastance	$\frac{\text{mm Hg}}{\text{ml}}$	(0.50±0.10)
50	Left atrial end-systolic elastance	$\frac{\text{mm Hg}}{\text{ml}}$	(0.61±0.07)
51	Left ventricular diastolic elastance	$\frac{\text{mm Hg}}{\text{ml}}$	(0.13±0.02)
52	Left ventricular end-systolic elastance	$\frac{\text{mm Hg}}{\text{ml}}$	(2.5±0.6)

*continued on next page*

Table A.1: *continued*

Index	Description	Unit	Value
53	Upper body microvascular resistance	PRU	(4.9±1.7)
54	Upper body venous outflow resistance	PRU	(0.11±0.05)
55	Renal microvascular resistance	PRU	(5.2±1.0)
56	Renal venous outflow resistance	PRU	(0.11±0.05)
57	Splanchnic microvascular resistance	PRU	(3.3±1.0)
58	Splanchnic venous outflow resistance	PRU	(0.07±0.04)
59	Lower body microvascular resistance	PRU	(4.5±1.8)
60	Lower body venous outflow resistance	PRU	(0.10±0.05)
61	Abdominal venous resistance	PRU	(0.019±0.007)
62	Inferior vena cava resistance	PRU	(0.008±0.003)
63	Superior vena cava resistance	PRU	(0.028±0.014)
64	Tricuspid valve resistance	PRU	(0.005±0.001)
65	Right ventricular outflow resistance	PRU	(0.006±0.003)
66	Pulmonary microcirculation resistance	PRU	(0.07±0.04)
67	Pulmonary venous outflow resistance	PRU	(0.006±0.003)
68	Mitral valve resistance	PRU	(0.010±0.001)
69	Left ventricular outflow resistance	PRU	(0.007±0.002)
70	Total blood volume	ml	(5150±103)
71	<i>Unassigned</i>		
72	Maximal lower body venous distending volume	ml	(1000.0±103)
73	<i>Unassigned</i>		
74	Maximal plasma loss (tilt)	ml	(700±41)
75	Total zero pressure filling volume	ml	4166
76	<i>Unassigned</i>		
77	Upper body ZPFV	ml	(645±40)
78	Renal ZPFV	ml	(30±10)
79	Splanchnic ZPFV	ml	(1146±100)
80	Lower body ZPFV	ml	(716±50)
81	Abdominal venous ZPFV	ml	(79±10)
82	Inferior vena cava ZPFV	ml	(33±4)
83	Superior vena cava ZPFV	ml	(16±4)
84	Right atrial ZPFV	ml	(14±1)
85	Right ventricular ZPFV	ml	(46±21)
86	Pulmonary arterial ZPFV	ml	(160±20)

*continued on next page*

Table A.1: *continued*

Index	Description	Unit	Value
87	Pulmonary venous ZPFV	ml	(430±50)
88	Left atrial ZPFV	ml	(24±13)
89	Left ventricular ZPFV	ml	(55±10)
90	Nominal heart rate	beats/min	(67±11)
91	<i>Unassigned</i>		
92	<i>Unassigned</i>		
93	<i>Unassigned</i>		
94	<i>Unassigned</i>		
96	Maximal plasma loss (LBNP)	ml	(491±29)
97	Ascending aorta compliance	$\frac{\text{ml}}{\text{mm Hg}}$	(0.28±0.04)
98	Brachiocephalic arteries compliance	$\frac{\text{ml}}{\text{mm Hg}}$	(0.13±0.02)
99	Descending thoracic aorta compliance	$\frac{\text{ml}}{\text{mm Hg}}$	(0.21±0.03)
100	Upper body arteries compliance	$\frac{\text{ml}}{\text{mm Hg}}$	(0.42±0.10)
101	Abdominal aorta compliance	$\frac{\text{ml}}{\text{mm Hg}}$	(0.10±0.01)
102	Renal arteries compliance	$\frac{\text{ml}}{\text{mm Hg}}$	(0.21±0.05)
103	Splanchnic arteries compliance	$\frac{\text{ml}}{\text{mm Hg}}$	(0.42±0.05)
104	Leg arteries compliance	$\frac{\text{ml}}{\text{mm Hg}}$	(0.42±0.05)
105	Brachiocephalic arteries resistance	$\frac{\text{ml}}{\text{mm Hg}}$	(0.003±0.001)
106	Descending thoracic aorta resistance	$\frac{\text{ml}}{\text{mm Hg}}$	(0.011±0.002)
107	Upper body arteries resistance	$\frac{\text{ml}}{\text{mm Hg}}$	(0.014±0.004)
108	Abdominal aorta resistance	$\frac{\text{ml}}{\text{mm Hg}}$	(0.010±0.003)
109	Renal arteries resistance	$\frac{\text{ml}}{\text{mm Hg}}$	(0.10±0.05)
110	Splanchnic arteries resistance	$\frac{\text{ml}}{\text{mm Hg}}$	(0.07±0.04)
111	Leg arteries resistance	$\frac{\text{ml}}{\text{mm Hg}}$	(0.09±0.05)
112	Delay $\alpha$ -sympathetic response (veins)	s	(5.0±1.5)
113	Peak $\alpha$ -sympathetic response (veins)	s	(7.0±1.5)
114	End $\alpha$ -sympathetic response (veins)	s	(40.0±5.0)
115	Delay $\alpha$ -sympathetic response (arteries)	s	(2.5±1.0)
116	Peak $\alpha$ -sympathetic response (arteries)	s	(4.5±1.0)
117	End $\alpha$ -sympathetic response (arteries)	s	(30.0±5.0)
118	P-R-interval	s	0.19
119	Atrial systole	s	0.25
120	Ventricular systole	s	0.37

*continued on next page*

Table A.1: *continued*

Index	Description	Unit	Value
121	Ascending aorta (vertical length)	cm	10.0
122	Brachiocephalic arteries (vertical length)	cm	4.5
123	Upper body arteries (vertical length)	cm	20.0
124	Upper body veins (vertical length)	cm	20.0
125	Superior vena cava (vertical length)	cm	4.5
126	Descending thoracic aorta (vertical length)	cm	16.0
127	Abdominal aorta (vertical length)	cm	14.5
128	Renal arteries (vertical length)	cm	0
129	Renal veins (vertical length)	cm	0
130	Splanchnic arteries (vertical length)	cm	10.0
131	Splanchnic veins (vertical length)	cm	10.0
132	Leg arteries (vertical length)	cm	106
133	Leg veins (vertical length)	cm	106
134	Abdominal veins (vertical length)	cm	14.5
135	Inferior vena cava (vertical length)	cm	6.0
136	Ascending aorta ZPFV	ml	(21±3)
137	Brachiocephalic arteries ZPFV	ml	(5±1)
138	Descending thoracic aorta ZPFV	ml	(16±2)
139	Upper body arteries ZPFV	ml	(200±40)
140	Abdominal aorta ZPFV	ml	(10±1)
141	Renal arteries ZPFV	ml	(20±5)
142	Splanchnic arteries ZPFV	ml	(300±50)
143	Leg arteries ZPFV	ml	(200±20)
144	Body height	cm	(169±1.5)
145	Body weight	kg	(70.3±2.1)
146	Body surface area	m <sup>2</sup>	(1.83±0.02)



## Appendix B

# Allometry of the Cardiovascular System

In Chapters 2 and 3, we have concerned ourselves with the architecture of and the parameter assignments for our cardiovascular model. In particular, we have assigned numerical values to the physical parameters of the model, assuming certain values for anthropometric measures and cardiovascular variables. These values were deemed characteristic of the population we aim to represent (see Table 2.1). We referred to this set of parameter values as the *nominal parameter profile* or the *base state* of the model. We also strove to assess the degree of variability of each parameter value within the population by estimating the respective standard errors.

The purpose of this appendix is to combine the nominal set of parameter values and their standard errors with general allometric scaling laws so we can generate parameter profiles of subjects with different anthropometric and cardiovascular characteristics, as if they were recruited at random from a large population. This sampling will enable us to repeat simulations for different subjects (i.e., different parameter profiles) and therefore establish population-averaged responses.

Knowing the nominal parameter values and their standard deviations, we could assume appropriate probability density functions (e.g., uniform, Gaussian, or log-normal) to sample each parameter independently. However, this sampling scheme would neglect important correlations that exist between physiological parameters: Figures B-1 and B-2 demonstrate that ‘size matters’ in physiological systems, where size is commonly quantified in terms of body weight. Figure B-1 demonstrates that height, and therefore gravitational stress, increases on average with increasing size. Figure B-2 shows that total blood volume also increases on average with increasing size. In fact, most cardiovascular variables are extrinsic; their values scale with the size of the organism, not only between different species but also intra-specifically (blood pressure being an important exception [265, p. 827]). Mathematically, this phenomenon is described by allometric scaling laws, which take the form of power-law monomials

$$Y_i = a_i \cdot W^{k_i} \tag{B.1}$$

where  $Y_i$  is a physiological variable of interest such as, for example, basal metabolic

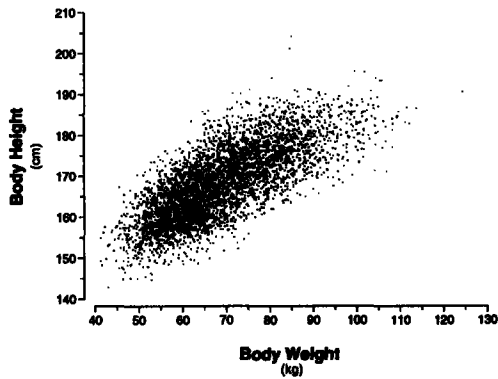


Figure B-1: Correlation of body height and body weight. Data adapted from [61].

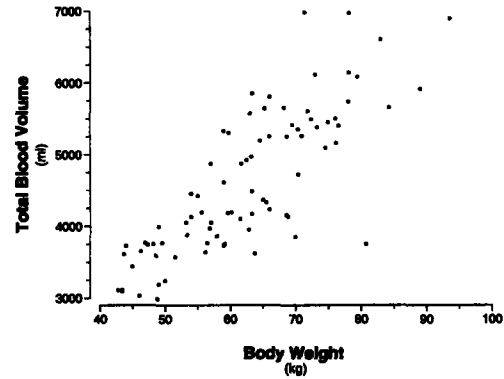


Figure B-2: Correlation of total blood volume and body weight. Data adapted from [57].

rate, vascular compliance, limb length, or heart rate.  $W$  is the representative weight of an organism if one is interested in inter-specific variation of  $Y$ , or it can be the weight of different representatives of the same species if one is interested in intra-specific variation of  $Y$ . Pragmatically, the coefficient  $a_i$  and the exponent  $k_i$  both have to be estimated from data to establish the exact scaling law for the particular variable  $Y_i$ . This approach would not help us as we would need a large volume of data to correlate each parameter or class of parameters (compliances, resistances, volumes) to body weight.

Theoretical frameworks have been developed to predict the scaling exponents for different physiological parameters, given a set of fundamental assumptions [266, 267]. Two commonly used models are based on the principles of geometric and elastic similarity, respectively [268]. Geometric similarity is based on the assumption that a set of related animals have the same shape but differ in size. Mathematically, geometric similarity is based on proportional scaling of all variables of linear dimension. In particular,  $L \propto D$ , where  $L$  is the dimension of a characteristic length variable (such as the length of the femur), and  $D$  is the associated transverse dimension (such as the diameter of the femur neck)<sup>1</sup>. Elastic similarity, on the other hand, asserts that larger animals are more strongly built than smaller ones [268]. In particular, it states that two variables are scaled in proportion to their characteristic elastic properties. Mathematically, elastic similarity is described by an affine transformation that scales the transverse dimensions relatively more than the longitudinal dimensions ( $L \propto D^{\frac{2}{3}}$ ).

If one assumes constant tissue density among or within species, weight scales according to volume,  $W \propto L \cdot D^2$ , so  $L \propto W^{\frac{1}{3}}$  assuming geometric similarity and  $L \propto W^{\frac{1}{4}}$  when the model of elastic similarity is employed. Alternatively,  $D \propto W^{\frac{1}{3}}$  and  $D \propto W^{\frac{3}{8}}$  under the geometric and elastic model, respectively. By computing the exponents  $k_i$  for various anthropometric and cardiovascular variables, we can decide which of the two models is more appropriate in describing the population data

<sup>1</sup>The sign  $\propto$  signifies proportionality.



Table B.1: Allometric exponents of the human cardiovascular system.

Variable	Dimensions	Exponent $k$		Reference	
		Predicted			Observed <sup>†</sup>
		Geometric similarity	Elastic similarity		
Body height	L	0.333	0.250	(0.223 ± 0.003)	[61]
		0.333	0.250	(0.221 ± 0.026)	[57]
Leg height	L	0.333	0.250	(0.228 ± 0.004)	[61]
Chest circumference	D	0.333	0.375	(0.405 ± 0.003)	[61]
Calf girth	D	0.333	0.375	(0.347 ± 0.004)	[61]
Thigh girth	D	0.333	0.375	(0.350 ± 0.005)	[61]
Body surface area	LD	0.667	0.625	(0.602 ± 0.019)	[57]
Cardiac output	LD <sup>2</sup> T <sup>-1</sup>	0.667	0.75	0.71	[62]
Blood volume	LD <sup>2</sup>	1.0	1.0	(0.936 ± 0.074)	[57]

<sup>†</sup>Mean ± standard error.

presented in Chapter 2. Table B.1 shows the results of the regression analysis and indicates that the data favor elastic over geometric similarity.

As mentioned above, blood pressure does not scale with body size, that is  $P \propto W^0$ . Combining this information with the fact that blood volume scales proportional to body size, we can determine that vascular compliance scales according to  $C \propto W$ . To determine how resistance scales, we need to understand how blood flow scales. McMahon [268] argues and presents experimental confirmation that dynamic variables of metabolic importance such as blood flow, minute respiration, and metabolic oxygen consumption all scale according to  $W^{\frac{3}{4}}$  under the elastic similarity assumption. Resistance therefore scales as  $R \propto W^{-\frac{3}{4}}$  and physiological time scales according to  $T \propto W^{\frac{1}{4}}$ .

To sample different parameter profiles from the population of subjects we are aiming to represent, we start with the nominal parameter profile and adopt the following sampling and scaling strategy:

1. Sample from an empirical distribution function of body weights to obtain a new weight  $W_1$ .
2. Normalize the nominal parameter  $\theta_0^i$  and its standard deviation  $\Delta\theta_0^i$  by the appropriately scaled nominal body weight  $W_0$ :

$$\hat{\theta}_0^i = \frac{\theta_0^i}{W_0^{k_i}}, \quad \Delta\hat{\theta}_0^i = \frac{\Delta\theta_0^i}{W_0^{k_i}}$$

3. Sample a new normalized value  $\hat{\theta}_1^i$  from some appropriately chosen probability distribution function  $F_i$ :

$$\hat{\theta}_1^i \sim F_i(\hat{\theta}_0^i, \Delta\hat{\theta}_0^i)$$

4. Scale the new normalized parameter value by the appropriate power law to obtain the extensive value  $\theta_1^i$ :

$$\theta_1^i = \hat{\theta}_1^i \cdot W_1^{k_i}$$

We chose the normal distribution for the sampling step (Step 2), but constrained the samples to lie between pre-defined minima and maxima to account for the fact that under normal conditions, cardiovascular variables do not assume extremely large or negative values.

# Bibliography

- [1] C.J. Dickinson. A digital computer model of the effects of gravitational stress upon the heart and venous system. *Medical & Biological Engineering*, 7:267–275, 1969.
- [2] T.L. Ozawa, K.E. Bottom, X. Xiao, and R.D. Kamm. Numerical simulation of enhanced external counterpulsation. *Annals of Biomedical Engineering*, 29(4):284–297, 2001.
- [3] K. Peterson, E.T. Ozawa, G.M. Pantalos, and M.K. Sharp. Numerical simulation of the influence of gravity and posture on cardiac performance. *Annals of Biomedical Engineering*, 30(2):247–259, 2002.
- [4] V.K. Sud, R. Srinivasan, J.B. Charles, and M.W. Bungo. Effects of lower body negative pressure on blood flow with applications to the human cardiovascular system. *Medical & Biological Engineering & Computing*, 31(6):569–575, 1993.
- [5] X. Xiao, E.T. Ozawa, Y. Huang, and R.D. Kamm. Model-based assessment of cardiovascular health from noninvasive measurements. *Annals of Biomedical Engineering*, 30(5):612–623, 2002.
- [6] D.G. Boyers, J.G. Cuthbertson, and J.A. Luetscher. Simulation of the human cardiovascular system: A model with normal response to change in posture, blood loss, transfusion, and autonomic blockade. *Simulation*, 18:197–205, 1972.
- [7] R.C. Croston, J.A. Rummel, and F.J. Kay. Computer model of cardiovascular control system response to exercise. *Journal of Dynamic Systems, Measurement, and Control*, pages 301–307, 1973.
- [8] R.W. DeBoer, J.M. Karemaker, and J. Stracke. Hemodynamic fluctuations and baroreflex sensitivity in human: a beat-to-beat model. *Journal of Applied Physiology*, 253(3 Pt. 2):680–689, 1987.
- [9] J.B. Madwed, P. Albrecht, R.G. Mark, and R.J. Cohen. Low-frequency oscillations in arterial pressure and hear rate: a simple computer model. *Journal of Applied Physiology*, 256(6 Pt 2):H1573–H1579, 1989.

- [10] R.J. White, D.G. Fitzjerrell, and R.C. Croston. Cardiovascular modelling: Simulating the human response to exercise, lower body negative pressure, zero gravity and clinical conditions. In *Advances in Cardiovascular Physics*, volume 5 (Part I), pages 195–229. Karger, Basel, 1983.
- [11] T.L. Davis. *Teaching Physiology Through Interactive Simulation of Hemodynamics*. Master's thesis, Department of Electrical Engineering and Computer Science, Massachusetts Institute of Technology, Cambridge, MA, February 1991.
- [12] T. Heldt, E.B. Shim, R.D. Kamm, and R.G. Mark. Computational modeling of cardiovascular response to orthostatic stress. *Journal of Applied Physiology*, 92(3):1239–1254, 2002.
- [13] M. Ursino. Interaction between carotid baroregulation and the pulsating heart: a mathematical model. *Journal of Applied Physiology*, 275(5 Pt. 2):H1733–H1747, 1998.
- [14] R.J. White, D.G. Fitzjerrell, and R.C. Croston. Fundamentals of lumped compartmental modelling of the cardiovascular system. In *Advances in Cardiovascular Physics*, volume 5 (Part I), pages 162–184. Karger, Basel, 1983.
- [15] A.C. Guyton, T.C. Coleman, and H.J. Granger. Circulation: Overall regulation. *Annual Review of Physiology*, 34:13–46, 1972.
- [16] R.C. Croston and D.G. Fitzjerrell. Cardiovascular model for the simulation of exercise, lower body negative pressure, and tilt table experiments. In *Proceedings of the Fifth Annual Pittsburgh Conference on Modeling and Simulation*, pages 471–476, 1974.
- [17] J.F. Green and N.C. Miller. A model describing the response of the circulatory system to acceleration stress. *Annals of Biomedical Engineering*, 1(4):455–467, 1973.
- [18] J.I. Leonard, C.S. Leach, and J.A. Rummel. Computer simulations of postural change, water immersion, and bedrest: An integrative approach for understanding the spaceflight response. *Physiologist*, 22(6):S31–S32, 1979.
- [19] D. Jaron, T.W. Moore, and C.-L.C. Chu. A cardiovascular model for studying impairment of cerebral function during +Gz stress. *Aviation, Space, and Environmental Medicine*, 55(1):24–31, 1984.
- [20] D. Jaron, T.W. Moore, and J. Bai. Cardiovascular response to acceleration stress: a computer simulation. *Proceedings of the IEEE*, 76(6):700–707, 1988.
- [21] F.M. Melchior, R.S. Srinivasan, and J.M. Clère. Mathematical modeling of the human response to LBNP. *Physiologist*, 35(1 Suppl.):S204–S205, 1992.

- [22] F.M. Melchior, R.S. Srinivasan, P.H. Thullier, and J.M. Clère. Simulation of cardiovascular response to lower body negative pressure from 0 to -40 mmHg. *Journal of Applied Physiology*, 77(2):630–640, 1994.
- [23] K.E. Simanonok, R.S. Srinivasan, and J.B. Charles. A computer simulation study of preadaptation of the circulation by removal of different blood volumes to counteract fluid shifts. *Physiologist*, 35(1 Suppl.):S111–S112, 1992.
- [24] K.E. Simanonok, E.E. Srinivasan, R.S. Myrick, A.L. Blomkalns, and J.B. Charles. A comprehensive guyton model analysis of physiologic responses to preadapting the blood volume as a countermeasure to fluid shifts. *Journal of Clinical Pharmacology*, 34(5):440–453, 1994.
- [25] M.F. Snyder and V.C. Rideout. Computer simulation studies of the venous circulation. *IEEE Transactions on Biomedical Engineering*, BME-16(4):325–334, 1969.
- [26] R.S. Srinivasan, K.E. Simanonok, and J.B. Charles. Computer simulation analysis of the effects of countermeasures for reentry orthostatic intolerance. *Physiologist*, 35(1 Suppl.):S165–S168, 1992.
- [27] R.J. White, J.I. Leonard, R.S. Srinivasan, and J.B. Charles. Mathematical modeling of acute and chronic cardiovascular changes during extended duration orbiter (EDO) flights. *Acta Astronautica*, 23:41–51, 1991.
- [28] R.J. White and C.G. Blomqvist. Central venous pressure and cardiac function during spaceflight. *Journal of Applied Physiology*, 85(2):738–746, 1998.
- [29] Consensus Committee of the American Autonomic Society and the American Academy of Neurology. Consensus statement on the definition of orthostatic hypotension, pure autonomic failure and multiple system atrophy. *Clinical Autonomic Research*, 6:125–126, 1996.
- [30] J.V. Meck, C.J. Reyes, S.A. Perez, A.L. Goldberger, and M.G. Ziegler. Marked exacerbation of orthostatic intolerance after long- vs. short-duration spaceflight in veteran astronauts. *Psychosomatic Medicine*, 63(6):865–873, 2001.
- [31] T.L. Davis and R.G. Mark. Teaching physiology through simulation of hemodynamics. *Computers in Cardiology*, 17:649–652, 1990.
- [32] J.L. Chang. Cycle-averaged models of cardiovascular dynamics. Master’s thesis, Department of Electrical Engineering and Computer Science, Massachusetts Institute of Technology, Cambridge, MA, June 2002.
- [33] J.J.S. Chen. Analytical solution to a simplified circulatory model using piecewise linear elastance function. Master’s thesis, Department of Electrical Engineering and Computer Science, Massachusetts Institute of Technology, Cambridge, MA, July 2003.

- [34] J.J.S. Chen, T. Heldt, G.C. Verghese, and R.G. Mark. Analytical solution to simplified circulatory model using piecewise linear elastance. *Computers in Cardiology*, 30:45–48, 2003.
- [35] T. Heldt, J.L. Chang, G.C. Verghese, and R.G. Mark. Cycle-averaged models of cardiovascular dynamics. In D.D. Feng and E.R. Carson, editors, *Modelling and Control in Biomedical Systems 2003*, pages 387–391, Oxford, UK, 2003. International Federation of Automatic Control, Pergamon.
- [36] G. Jacob, A.C. Ertl, J.R. Shannon, R. Furlan, R.M. Robertson, and D. Robertson. Effect of standing on neurohumoral responses and plasma volume in healthy subjects. *Journal of Applied Physiology*, 84(3):914–921, 1998.
- [37] Critical Path Control Panel. Critical Path Roadmap (CPR) Baseline Document. <<http://criticalpath.jsc.nasa.gov>>, 2000. Website accessed on July 08, 2003.
- [38] J.M. Fritsch-Yelle, J.B. Charles, M.M. Jones, L.A. Beightol, and D.L. Eckberg. Spaceflight alters autonomic regulation of arterial pressure in humans. *Journal of Applied Physiology*, 77(4):1776–1783, 1994.
- [39] C.M. Lathers and J.B. Charles. Orthostatic hypotension in patients, bedrest subjects, and astronauts. *Journal of Clinical Pharmacology*, 28(10 Suppl.):S29–S32, 1994.
- [40] J.V. Tyberg and D.R. Hamilton. Orthostatic hypotension and the role of changes in venous capacitance. *Medicine and Science in Sports and Exercise*, 28(10 Suppl.):S29–S31, 1996.
- [41] B.D. Levine, J.H. Zuckerman, and J.A. Pawelczyk. Cardiac atrophy after bedrest deconditioning: A nonneural mechanism for orthostatic intolerance. *Circulation*, 96(2):517–525, 1997.
- [42] M.A. Perhonen, F. Franco, L.D. Lane, J.C. Buckey, C.G. Blomqvist, J.E. Zerkwekh, R.M. Peshock, P.T. Weatherall, and B.D. Levine. Cardiac atrophy after bed rest and spaceflight. *Journal of Applied Physiology*, 91(2):645–653, 2001.
- [43] M.A. Perhonen, J.H. Zuckerman, and B.D. Levine. Deterioration of left ventricular chamber performance after bed rest: "cardiovascular deconditioning" or hypovolemia? *Circulation*, 103(14):1851–1857, 2001.
- [44] D.S. Martin, D.A. South, M.L. Wood, M.W. Bungo, and J.V. Meck. Comparison of echocardiographic changes after short- and long-duration spaceflight. *Aviation, Space, and Environmental Medicine*, 73(6):532–536, 2002.
- [45] J.C. Buckey, L.D. Lane, G. Plath, F.A. Gaffney, F. Baisch, and C.G. Blomqvist. Effects of head-down tilt for 10 days on the compliance of the leg. *Acta Physiologica Scandinavica*, 144(S604):53–60, 1992.

- [46] D. Robertson, V.A. Convertino, and J. Vernikos. The sympathetic nervous system and the physiologic consequences of spaceflight: a hypothesis. *The American Journal of the Medical Sciences*, 308(2):126–132, 1994.
- [47] B.J. Yates and I.A. Kerman. Post-spaceflight orthostatic intolerance: Possible relationship to microgravity induced plasticity in the vestibular system. *Brain Research Reviews*, 28(1–2):73–82, 1998.
- [48] C.G. Blomqvist, J.C. Buckey, F.A. Gaffney, L.D. Lane, J.D. Levine, and D.E. Watenpaugh. Mechanisms of post-flight orthostatic intolerance. *Journal of Gravitational Physiology*, 1(1):P122–P124, 1994.
- [49] C.G. Blomqvist. Regulation of the systemic circulation at microgravity and during readaptation to 1 G. *Medicine and Science in Sports and Exercise*, 28(10 Suppl.):S9–S13, 1996.
- [50] S.L. Mulvagh, J.B. Charles, J.M. Riddle, T.L. Rehbein, and M.W. Bungo. Echocardiographic evaluation of the cardiovascular effects of short-duration spaceflight. *Journal of Clinical Pharmacology*, 31(10):1024–1026, 1991.
- [51] P.A. Whitson, J.B. Charles, W.J. Williams, and N.M. Cintrón. Changes in sympathoadrenal response to standing in humans after spaceflight. *Journal of Applied Physiology*, 79(2):428–433, 1995.
- [52] J.M. Fritsch-Yelle, J.B. Charles, M.M. Jones, and M.L. Wood. Microgravity decreases heart rate and arterial pressure in humans. *Journal of Applied Physiology*, 80(3):910–914, 1996.
- [53] J.C. Buckey, L.D. Lane, J.D. Levine, D.E. Watenpaugh, S.J. Wright, W.E. Moore, F.A. Gaffney, and C.G. Blomqvist. Orthostatic intolerance after spaceflight. *Journal of Applied Physiology*, 81(1):7–18, 1996.
- [54] L.F. Zhang. Vascular adaptation to microgravity: What have we learned? *Journal of Applied Physiology*, 91(6):2415–2430, 2001.
- [55] J.G. Defares, J.J. Osborn, and H.H. Hara. Theoretical synthesis of the cardiovascular system. Study I: The controlled system. *Acta physiologica et pharmacologica Neerlandica*, 12:189–265, 1963.
- [56] R.W. Leggett and L.R. Williams. A proposed blood circulation model for reference man. *Health Physics*, 69(2):187–201, 1995.
- [57] J.G. Gibson, 2nd and W.A. Evans, Jr. Clinical studies of the blood volume. II The relation of plasma and total blood volume to venous pressure, blood velocity rate, physical measurements, age and sex in ninety normal humans. *Journal of Clinical Investigation*, 16:317–328, 1937.

- [58] A. Cournand, R.L. Riley, E.S. Breed, E. deF. Baldwin, and D.W. Richards, Jr. Measurement of cardiac output in man using the technique of catheterization of the right auricle or ventricle. *Journal of Clinical Investigation*, 24(1):106–116, 1945.
- [59] J.M. Tanner. The construction of normal standards for cardiac output in man. *Journal of Clinical Investigation*, 28:567–582, 1949.
- [60] B.G. Barratt-Boyes and E.H. Wood. Cardiac output and related measurements and pressure values in the right heart and associated vessels, together with an analysis of the hemodynamic response to the inhalation of high oxygen mixtures in healthy subjects. *The Journal of Laboratory and Clinical Medicine*, 51(1):72–90, 1958.
- [61] Human Systems Information Center. 1988 Anthropometric Survey of the U.S. Army Male/Female Working Data Set. Technical report, U.S. Department of Defense, Wright-Patterson Air Force Base, OH. <[http://iac.dtic.mil/hsiac/Anthro\\_US\\_Military.htm](http://iac.dtic.mil/hsiac/Anthro_US_Military.htm)>; website accessed on 9 April 2004.
- [62] G. de Simone, R.B. Devereux, S.R. Daniels, G. Mureddu, M.J. Roman, T.R. Kimball, R. Greco, S. Witt, and F. Contaldo. Stroke volume and cardiac output in normotensive children and adults. *Circulation*, 95(7):1837–1843, 1997.
- [63] P.L. Williams, editor. *Gray's Anatomy*. Churchill Livingstone, New York, 38 edition, 1995.
- [64] F. Martini. *Human Anatomy*. Prentice Hall, Upper Saddle River, New Jersey, 2nd edition, 1997.
- [65] International Commission on Radiological Protection. *Report of the Task Group on Reference Man*. ICRP publication 23. Pergamon Press, New York, 1975.
- [66] C. Macchi and C. Catini. The use of ultrasonic tomography to measure the calibers of the iliac arteries and veins and the caliber and length of the inferior vena cava and the abdominal aorta. *Italian Journal of Anatomy and Embryology*, 99(3):181–186, 1994.
- [67] P. Bonnichon, F. Gaudard, E. Ouakil, P. Lebozec, C. de Labrouhe, A. Bonnin, C. Aaron, and Y. Chapuis. Biometry of infrarenal inferior vena cava measured by cavography. Clinical applications. *Surgical and Radiologic Anatomy*, 11(2):149–154, 1989.
- [68] United States of America Department of Defense. Anthropometry of U.S. military personnel (metric). Military Handbook DOD-HDBK-743A, United States Department of Defense, 1991. <[http://iac.dtic.mil/hsiac/Std\\_Hdbk.htm](http://iac.dtic.mil/hsiac/Std_Hdbk.htm)>; website accessed on 10 February 2004.



- [69] A.P. Avolio. Multi-branched model of the human arterial system. *Medical & Biological Engineering & Computing*, 18(6):709–718, 1980.
- [70] A. Noordergraaf, P.D. Verdouw, and H.B. Boom. The use of an analog computer in a circulation model. *Progress in Cardiovascular Diseases*, 5(5):419–439, 1963.
- [71] J.W. Remington and W.F. Hamilton. The construction of a theoretical cardiac ejection curve from the contour of the aortic pressure pulse. *American Journal of Physiology*, 144:546–556, 1945.
- [72] P. Hallock and J.C. Benson. Studies on the elastic properties of human isolated aorta. *American Journal of Physiology*, 16:595–602, 1937.
- [73] A.A. Pollack and E.H. Wood. Venous pressure in the saphenous vein at the ankle in man during exercise and changes in posture. *Journal of Applied Physiology*, 1:649–662, 1949.
- [74] D.J. Griffiths. Principles of blood flow through collapsible tubes. In A.M.N. Gardner and R.H. Fox, editors, *The return of blood to the heart: venous pumps in health and disease*, pages 159–170. John Libbey & Company Ltd., London, 1993.
- [75] J.P. Henry. The significance of the loss of blood volume into the limbs during pressure breathing. *Aviation Medicine*, 22(1):13–38, 1951.
- [76] H.W. Ryder, W.E. Molle, and E.B. Ferris, Jr. The influence of the collapsibility of veins on venous pressure, including a new procedure for measuring tissue pressures. *Journal of Clinical Investigation*, 23(3):333–342, 1943.
- [77] R.W. Leggett and L.R. Williams. Suggested reference values for regional blood volumes in humans. *Health Physics*, 60(2):139–154, 1991.
- [78] F. Karim and R. Hainsworth. Responses of abdominal vascular capacitance to stimulation of splanchnic nerves. *American Journal of Physiology*, 231(2):434–440, 1976.
- [79] C.F. Rothe. Venous system: physiology of the capacitance vessels. In T.J. Shepard, F.M. Abboud, and S.R. Geiger, editors, *The cardiovascular system: peripheral circulation and organ blood flow*, volume III of *Handbook of Physiology*, chapter 13, pages 397–452. American Physiological Society, Bethesda, MD, 1983.
- [80] L.B. Rowell. *Human Cardiovascular Control*, chapter 6. Oxford University Press, New York, NY, 1993.
- [81] M.W. Bleeker, P.C.E. De Groot, J.A. Pawelczyk, M.T.E. Hopman, and B.D. Levine. Effects of 18 days of bed rest on leg and arm venous properties. *Journal of Applied Physiology*, 96(3):840–847, 2004.

- [82] C.C. Arnoldi and H. Linderholm. Venous blood pressures in the lower limb at rest and during exercise in patients with idiopathic dysfunction of the venous pump in the calf. *Acta Chirurgica Scandinavica*, 135(7):601–609, 1969.
- [83] M.F. O'Rourke. *Arterial function in health and disease*. Churchill, Edinburgh, 1982.
- [84] H. Suga. Time course of left ventricular pressure-volume relationship under various end-diastolic volumes. *Japanese Heart Journal*, 10(6):509–515, 1969.
- [85] H. Suga. Time course of ventricular pressure-volume relationship under various extends of aortic occlusion. *Japanese Heart Journal*, 11(4):373–378, 1970.
- [86] H. Suga. Left ventricular time-varying pressure/volume ratio in systole as an index of myocardial inotropism. *Japanese Heart Journal*, 12(2):153–160, 1971.
- [87] H. Suga, K. Sagawa, and A.A. Shoukas. Load independence of the instantaneous pressure-volume ratio of the canine left ventricle and effects of epinephrine and heart rate on this ratio. *Circulation Research*, 32(3):314–322, 1973.
- [88] H. Senzaki, C. Chen, and D.A. Kass. Single beat estimation of end-systolic pressure-volume relations in humans. *Circulation*, 94(10):2497–2506, 1996.
- [89] R.G. McKay, J.M. Aroesty, G.V. Heller, H.D. Royal, S.E. Warren, and W. Grossman. Assessment of the end-systolic pressure-volume relationship in human beings with the use of a time-varying elastance model. *Circulation*, 74(1):97–104, 1986.
- [90] W. Grossman, E. Braunwald, T. Mann, L.P. McLaurin, and L.H. Green. Contractile state of the left ventricle in man as evaluated from end-systolic pressure-volume relations. *Circulation*, 56(5):845–852, 1977.
- [91] M.R. Starling, R.A. Walsh, L.J. Dell'Italia, G.B.J. Manchini, J.C. Lasher, and J.L. Lancaster. The relationship of various measures of end-systole to left ventricular maximum time-varying elastance in man. *Circulation*, 76(1):32–43, 1987.
- [92] L.J. Dell'Italia and R.A. Walsh. Application of a time varying elastance model of right ventricular performance in man. *Cardiovascular Research*, 22(12):864–874, 1988.
- [93] J.M. Dernellis, C.I. Stefanadis, A.A. Zacharoulis, and P.K. Toutouzas. Left atrial mechanical adaptation to long-standing hemodynamic loads based on pressure-volume relations. *American Journal of Cardiology*, 81(9):1138–1143, 1998.
- [94] J. Alexander, Jr., K. Sunagawa, N. Chang, and K. Sagawa. Instantaneous pressure-volume relation of the ejecting canine left atrium. *Circulation Research*, 61(2):209–219, 1987.

- [95] F. Schwiep, S.S. Cassidy, M. Ramanathan, and R.L. Johnson, Jr. Rapid in vivo determinations of instantaneous right ventricular pressure and volume in dogs. *American Journal of Physiology*, 254(23):H622–H630, 1988.
- [96] V.-K. Lau, K. Sagawa, and H. Suga. Instantaneous pressure-volume relationship of right atrium during isovolumic contraction in canine heart. *American Journal of Physiology*, 236(5):H672–H679, 1979.
- [97] M.S. Firstenberg, P.M. Vandervoot, N.L. Greenberg, N.G. Smedira, P.M. McCarthy, M.J. Garcia, and J.D. Thomas. Noninvasive estimation of transmitral pressure drop across the normal mitral valve in humans: importance of convective and inertial forces during left ventricular filling. *Journal of the American College of Cardiology*, 36(6):1942–1949, 2000.
- [98] H.C. Bazett. An analysis of the time-relations of electrocardiograms. *Heart*, 7:353–370, 1920.
- [99] K. Sagawa, L. Maughan, H. Suga, and K. Sunegawa. *Cardiac contraction and the pressure-volume relationship*. Oxford University Press, New York, 1988.
- [100] E.T. Ozawa. *A numerical model of the cardiovascular system for clinical assessment of the hemodynamic state*. Doctoral dissertation, Massachusetts Institute of Technology, Cambridge, MA, September 1996.
- [101] L.D. Nguyen and C.L. Leger. Four-dimensional reconstruction of the left ventricle using a fast rotating classical phased array scan head: Preliminary results. *Journal of the American Society of Echocardiography*, 15(6):593–600, 2002.
- [102] F.P. Knowlton and E.H. Starling. The influence of variations in temperature and blood pressure on the performance of the isolated mammalian heart. *Journal of Physiology*, 44(3):206–219, 1912.
- [103] R.W. Brower and A. Noordergraaf. Pressure flow characteristics of collapsible tubes: A reconciliation of seemingly contradictory results. *Annals of Bioengineering*, 1(3):333–335, 1973.
- [104] J.B. West, C.T. Dollery, and A. Naimark. Distribution of blood flow in isolated lung; relation to vascular and alveolar pressure. *Journal of Applied Physiology*, 19(4):713–724, 1964.
- [105] S. Permutt and R.L. Riley. Hemodynamics of collapsible vessels with tone: the vascular waterfall. *Journal of Applied Physiology*, 18(5), 1963.
- [106] A. Shapiro. Steady flow in collapsible tubes. *Journal of Biomechanical Engineering*, 99:126–147, 1977.
- [107] R.D. Kamm. Flow through collapsible tubes. In R. Skalak and S. Chien, editors, *Handbook of Bioengineering*, chapter 23, pages 23.1–23.19. McGraw-Hill, New York, 1987.

- [108] S. Permutt, B. Bromberger-Barnea, and H.N. Bane. Alveolar pressure, pulmonary venous pressure, and the vascular waterfall. *Medicina Thoracalis*, 19:239–260, 1962.
- [109] M.L. Lewis and L.C. Christianson. Behavior of the human pulmonary circulation during head-up tilt. *Journal of Applied Physiology*, 45(2):249–254, 1978.
- [110] L. Dexter, J.W. Dow, F.W. Haynes, J.L. Whittenberger, B.G. Ferris, W.T. Goodale, and H.K. Hellems. Studies of the pulmonary circulation in man at rest. Normal variations and the interrelations between increased pulmonary blood flow, elevated pulmonary arterial pressure, and high pulmonary "capillary" pressures. *Journal of Clinical Investigation*, 29:602–613, 1950.
- [111] R.N. Westcott, N.O. Fowler, R.C. Scott, V.D. Hauenstein, and J. McGuire. Anoxia and human pulmonary vascular resistance. *Journal of Clinical Investigation*, 30(9):957–970, 1951.
- [112] W.R. Milnor, A.D. Jose, and C.J. McGaff. Pulmonary vascular volume, resistance, and compliance in man. *Circulation*, 22:130–137, 1960.
- [113] S.R. Reuben. Compliance of the human pulmonary arterial system in disease. *Circulation Research*, 29(1):40–50, 1971.
- [114] A.C. Guyton and J.E. Hall. *Textbook of Medical Physiology*. W.B. Saunders, Philadelphia, 10th edition, 2000.
- [115] J.E.W. Beneken and B. DeWitt. A physical approach to hemodynamic aspects of the human cardiovascular system. In A.C. Guyton and E.B. Reeve, editors, *Physical bases of circulatory transport: Regulation and exchange*, pages 1–45. W.B. Saunders, Philadelphia, 1967.
- [116] S. Hirakawa. Capacitance of systemic and pulmonary circulatory system during acute venous congestion. *Japanese Circulation Journal*, 37(7):753–760, 1973.
- [117] S. Hirakawa, H. Ito, A. Sakai, and A. Wakabayashi. Estimation of the compliance of the human "venous" system from pulmonary artery wedge pressure tracings. *Japanese Circulation Journal*, 45(1):15–23, 1981.
- [118] T. Tanaka, M. Arakawa, T. Suzuki, M. Gotoh, H. Miyamoto, and S. Hirakawa. Compliance of human pulmonary "venous" system estimated from pulmonary artery wedge pressure tracings. *Japanese Circulation Journal*, 50(2):127–139, 1986.
- [119] R.V. Ebert, C.W. Borden, H.S. Wells, and R.H. Wilson. Studies of the pulmonary circulation. I. The circulation time from the pulmonary artery to the femoral artery and the quantity of blood in the lungs in normal individuals. *Journal of Clinical Investigation*, 28:1134–1137, 1949.

- [120] A.C. Burton. *Physiology and Biophysics of the Circulation*. Chicago Year Book Medical Publishers, 2 edition, 1972.
- [121] W.R. Milnor. Pulmonary hemodynamics. In D.H. Bergel, editor, *Cardiovascular Fluid Dynamics*, pages 299–340. Academic Press, London, 1972.
- [122] W.J. Daly and S. Bondurant. Direct measurement of respiratory pleural pressure changes in normal man. *Journal of Applied Physiology*, 18(3):513–518, 1963.
- [123] J. Mead and E.A. Gaensler. Esophageal and pleural pressures in man, upright and supine. *Journal of Applied Physiology*, 14(1):81–83, 1959.
- [124] B.G. Ferris, Jr., J. Mead, and N.R. Frank. Effect of body position on esophageal pressure and measurement of pulmonary compliance. *Journal of Applied Physiology*, 14(4):521–524, 1959.
- [125] J. Lundvall, P. Bjerkhoel, S. Quittenbaum, and P. Lindgren. Rapid plasma volume decline upon quiet standing reflects large filtration capacity in dependent limbs. *Acta Physiologica Scandinavica*, 158(2):161–167, 1996.
- [126] R.C. Tarazi, H.J. Melsher, H.P. Dustan, and E.D. Frohlich. Plasma volume changes with upright tilt: studies in hypertension and in syncope. *Journal of Applied Physiology*, 28(2):121–126, 1970.
- [127] H. Hinghofer-Szalkay and M. Moser. Fluid and protein shifts after postural changes in humans. *American Journal of Physiology*, 250(19):H68–H75, 1986.
- [128] R.D. Hagan, F.J. Diaz, and S.M. Horvath. Plasma volume changes with movement to the upright position. *Journal of Applied Physiology*, 45(3):414–417, 1978.
- [129] J. Lundvall and P. Bjerkhoel. Failure of hemoconcentration during standing to reveal plasma volume decline induced in the erect posture. *Journal of Applied Physiology*, 77(5):2155–2162, 1994.
- [130] P. Bjerkhoel and J. Lundvall. Rapid and large plasma volume decrease upon short-term quiet standing. *Acta Physiologica Scandinavica*, 150(3):347–348, 1994.
- [131] P. Bjerkhoel and J. Lundvall. Pronounced plasma fluid loss into dependent regions on standing. *Acta Physiologica Scandinavica*, 154(2):275–276, 1995.
- [132] J. Lundvall and P. Bjerkhoel. Pronounced and rapid plasma volume reduction upon quiet standing as revealed by a novel approach to the determination of the intravascular volume change. *Acta Physiologica Scandinavica*, 154(2):131–142, 1995.

- [133] J. Lundvall and P. Lindgren. F-cell shift and protein loss strongly affect validity of PV reductions indicated by Hb/Hct and plasma proteins. *Journal of Applied Physiology*, 84(3):822–829, 1998.
- [134] C.C. Arnoldi. Venous pressures in the leg of healthy human subjects at rest and during muscular exercise in the nearly erect position. *Acta Chirurgica Scandinavica*, 130:570–583, 1965.
- [135] H. Tanaka, B.J. Sjöberg, and O. Thulesius. Cardiac output and blood pressure during active and passive standing. *Clinical Physiology*, 16(2):157–170, 1996.
- [136] R.L.H. Sprangers, K.H. Wesseling, A.L.T. Imholz, B.P.M. Imholz, and W. Wieling. Initial blood pressure fall on stand up and exercise explained by changes in total peripheral resistance. *Journal of Applied Physiology*, 70(2):523–530, 1991.
- [137] J. Lundvall, P. Bjerkhoel, C. Ivarsson, and T. Länne. Dynamics of transcapillary fluid transfer and plasma volume during lower body negative pressure. *Acta Physiologica Scandinavica*, 147(2):163–172, 1993.
- [138] M. Aratow, S.M. Fortney, D.E. Watenpaugh, A.G. Crenshaw, and A.R. Hargens. Transcapillary fluid responses to lower body negative pressure. *Journal of Applied Physiology*, 74(6):2763–2770, 1993.
- [139] W.H. Press, S.A. Teukolsky, W.T. Vetterling, and B.P. Flannery. *Numerical recipes in C: the art of scientific computing*, chapter 16, pages 707–747. Cambridge University Press, New York, NY, 2nd edition, 1992.
- [140] R.W. de Boer. *Beat-to-beat blood-pressure fluctuations and heart-rate variability in man: physiological relationships, analysis techniques and a simple model*. Doctoral dissertation, Department of Physiology, University of Amsterdam, Amsterdam, The Netherlands, December 1985.
- [141] R. Mukkamala. *A Forward Model-Based Analysis of Cardiovascular System Identification Methods*. Doctoral dissertation, Massachusetts Institute of Technology, Cambridge, MA, June 2000.
- [142] G. Mancina and A.L. Mark. Arterial baroreflex in humans. In T.J. Shepard, F.M. Abboud, and S.R. Geiger, editors, *The peripheral circulation*, volume III (Part 2) of *Handbook of Physiology, Section 2: The Cardiovascular System*, chapter 20, pages 755–793. American Physiological Society, Bethesda, MD, 1983.
- [143] R.D. Berger. *Analysis of the Cardiovascular Control System using Broad-Band Stimulation*. Doctoral dissertation, Massachusetts Institute of Technology, Cambridge, MA, June 1987.
- [144] R.D. Berger, J.P. Saul, and R.J. Cohen. Transfer function analysis of autonomic regulation I. Canine atrial rate response. *American Journal of Physiology*, 256(25):H142–H152, 1989.

- [145] C. Borst and J.M. Karemaker. Time delays in the human baroreflex. *Journal of the Autonomic Nervous System*, 9(2–3):399–409, 1983.
- [146] D.L. Eckberg. Nonlinearities of the human carotid baroreceptor-cardiac reflex. *Circulation Research*, 47(2):208–216, 1980.
- [147] R.F. Rea and D.L. Eckberg. Carotid baroreceptor-muscle sympathetic relation in humans. *American Journal of Physiology*, 253(22):R929–R934, 1987.
- [148] C. Keyl, A. Schneider, M. Dambacher, and L. Bernardi. Time delay of vagally mediated cardiac baroreflex response varies with autonomic cardiovascular control. *Journal of Applied Physiology*, 91(1):283–289, 2001.
- [149] M. Rosenbaum and D. Race. Frequency-response characteristics of vascular resistance vessels. *American Journal of Physiology*, 215(6):1397–1402, 1968.
- [150] A.A. Shoukas, C.L. MacAnespie, M.J. Brunner, and L. Watermeier. The importance of the spleen in blood volume shifts of the systemic vascular bed caused by the carotid sinus baroreceptor reflex in the dog. *Circulation Research*, 49(3):759–766, 1981.
- [151] T.J. Mullen, M.L. Appel, R. Mukkamala, J.M. Mathias, and R.J. Cohen. System identification of closed-loop cardiovascular control: effects of posture and autonomic blockade. *American Journal of Physiology*, 272(Heart Circ. Physiol. 41):H448–H461, 1997.
- [152] R. Mukkamala, K. Toska, and R.J. Cohen. Noninvasive identification of the total peripheral resistance baroreflex. *American Journal of Physiology*, 284(3):H947–H959, 2002.
- [153] P.G. Katona and G.O. Barnett. Central origin of asymmetry in the carotid sinus reflex. *Annals of the New York Academy of Sciences*, 156(2):779–786, 1969.
- [154] J.D. Bistow, A.J. Honour, T.G. Pickering, and P. Sleight. Cardiovascular and respiratory changes during sleep in normal and hypertensive subjects. *Cardiovascular Research*, 3:476–485, 1969.
- [155] D.L. Eckberg, M. Drabinsky, and E. Braunwald. Defective cardiac parasympathetic control in patients with heart disease. *New England Journal of Medicine*, 285(16):877–883, 1971.
- [156] T.G. Pickering, B. Gribbin, and P. Sleight. Comparison of the reflex heart rate response to rising and falling arterial pressure in man. *Cardiovascular Research*, 6(2):277–283, 1972.
- [157] T.G. Pickering, B. Gribbin, E. Strange Petersen, D.J.C. Cunningham, and P. Sleight. Effects of autonomic blockade on the baroreflex in man at rest and during exercise. *Circulation Research*, 30:177–185, 1972.

- [158] P.I. Korner, M.J. West, J. Shaw, and J.B. Uther. 'Steady State' properties of the baroreceptor-heart rate reflex in essential hypertension in man. *Clinical and Experimental Pharmacology and Physiology*, 1:65–76, 1974.
- [159] R.W. de Boer, J.M. Karemaker, and J. Stracke. Description of heart rate variability data in accordance with a physiological model of the genesis of heartbeats. *Psychophysiology*, 22(2):147–155, 1985.
- [160] B. Ahn, Y. Skakibara, P. Paulev, A. Masuda, Y. Nishibayashi, W. Nakamura, and Y. Honda. Circulatory and respiratory response to lower body negative pressure in man. *Japanese Journal of Physiology*, 39:919–929, 1989.
- [161] C.M. Brown, M. Dütsch, M.J. Hecht, B. Neundörfer, and M.J. Hilz. Assessment of cerebrovascular and cardiovascular responses to lower body negative pressure as a test of cerebral autoregulation. *Journal of the Neurological Society*, 208(1-2):71–78, 2003.
- [162] A.A. Shoukas and M.C. Brunner. Epinephrine and the carotid sinus reflex: Influence on capacitive and resistive properties of the total systemic vascular bed of the dog. *Circulation Research*, 47(2):249–257, 1980.
- [163] R.M. Berne and M.N. Levy. *Cardiovascular Physiology*. Mosby-Year Book, Inc., St. Louis, MI, 7 edition, 1997.
- [164] A.L. Mark and G. Mancia. Cardiopulmonary baroreflexes in humans. In T.J. Shepard, F.M. Abboud, and S.R. Geiger, editors, *The peripheral circulation*, volume III (Part 2) of *Handbook of Physiology, Section 2: The Cardiovascular System*, chapter 21, pages 795–813. American Physiological Society, Bethesda, MD, 21 edition, 1983.
- [165] J.M. Johnson, L.B. Rowell, M. Niederberger, and M.M. Eisman. Human splanchnic and forearm vasoconstrictor responses to reductions of right atrial and aortic pressure. *Circulation Research*, 34(4):515–524, 1974.
- [166] J.A. Pawelczyk and P.B. Raven. Reductions in central venous pressure improve carotid baroreflex responses in conscious men. *American Journal of Physiology*, 257(Heart Circ. Physiol. 26):H1389–H1395, 1989.
- [167] T.H. Desai, J.C. Collins, M. Snell, and R. Mosqueda-Garcia. Modeling of arterial and cardiopulmonary baroreflex control of heart rate. *American Journal of Physiology*, 1997(Heart Circ. Physiol. 41):H2342–H2352, 1997.
- [168] H.L. Price. Hemodynamic and metabolic effects of hemorrhage in man with particular reference to the splanchnic circulation. *Circulation Research*, 18:469–474, 1966.
- [169] S. Bevegard, J. Castenfros, and L.E. Lindblad. Effects of changes in blood volume distribution on circulatory variables and plasma renin activity. *Acta Physiologica Scandinavica*, 99(2):237–245, 1977.



- [170] W. Giles, D.A. Eisner, and W.J. Lederer. Sinus pacemaker activity in the heart. In David O. Carpenter, editor, *Cellular Pacemakers*, volume 1, chapter 3. John Wiley & Sons, New York, 1982.
- [171] H.H. Hecht. Comparative physiological and morphological aspects of pacemaker tissues. *Annals of the New York Academy of Sciences*, 127:49–83, 1965.
- [172] S. Akselrod, D. Gordon, F.A. Ubel, D.C. Shannon, C. Barger, and R.J. Cohen. Power spectrum analysis of heart rate fluctuation: a quantitative probe of beat-to-beat cardiovascular control. *Science*, 213(4504):220–222, 1981.
- [173] B.W. Hyndman and R.K. Mohn. A model of the cardiac pacemaker and its use in decoding the information content of cardiac intervals. *Automedica*, 1:239–252, 1975.
- [174] R.A. Bloomfield, H.D. Lauson, A. Cournand, E.S. Breed, and D.W. Richards, Jr. Recording of right heart pressures in normal subjects and in patients with chronic pulmonary disease and various types of cardio-circulatory disease. *The Journal of Clinical Investigation*, 25(5):639–664, 1946.
- [175] N.O. Fowler, R.N. Westcott, and R.C. Scott. Normal pressure in the right heart and pulmonary artery. *American Heart Journal*, 46:264–267, 1953.
- [176] E. Braunwald, E.C. Brockenbrough, C.J. Frahm, and J. Ross. Left atrial and left ventricular pressures in subjects without cardiovascular disease: Observations in eighteen patients studied by transeptal left heart catheterization. *Circulation*, 24:267–269, 1961.
- [177] J.W. Kennedy, W.A. Baxley, M.M. Figley, H.T. Dodge, and J.R. Blackmon. Quantitative angiocardigraphy: I. The normal left ventricle. *Circulation*, 34(2):272–278, 1966.
- [178] F. Cucchini, C. Di Mario, A. Iavernaro, R. Zeppellini, A. Barilli, and R. Bolognesi. Peak aortic blood acceleration: a possible indicator of initial left ventricular impairment in patients with coronary artery disease. *European Heart Journal*, 12(8):860–868, 1991.
- [179] W.W. Nichols and M.F. O'Rourke. *McDonald's Blood Flow in Arteries: Theoretical, practical and clinical principles*. Arnold, London, 4 edition, 1998.
- [180] Y.C. Fung. *Biodynamics – Circulation*. Springer-Verlag, New York, 1984.
- [181] C.G. Caro, T.J. Pedley, R.C. Schroter, and W.A. Seed. *The Mechanics of the Circulation*. Oxford Medical Publishers, Oxford University Press, New York, 1978.
- [182] M. Kumada, T. Azuma, and K. Matsuda. The cardiac output-heart rate relationship under different conditions. *The Japanese Journal of Physiology*, 17(5):538–555, 1967.

- [183] J.J. Smith, C.V. Hughes, M.J. Ptacin, J.A. Barney, F.E. Tristani, and T. J. Ebert. The effect of age on hemodynamic response to graded postural stress in normal men. *Journal of Gerontology*, 42(4):406–411, 1987.
- [184] O.H. Gauer and H.L. Thron. Postural changes in the circulation. In W.F. Hamilton, editor, *Handbook of Physiology*, volume 3, chapter 67, pages 2409–2439. American Physiological Society, 1965.
- [185] J. Hisdale, K. Toska, and L. Walløe. Beat-to-beat cardiovascular responses to rapid, low-level LBNP in humans. *American Journal of Physiology*, 281(1):R213–R221, 2001.
- [186] G. Rådegran and B. Saltin. Muscle blood flow at onset of dynamic exercise. *American Journal of Physiology*, 274(1 Pt. 2):H314–H322, 1998.
- [187] J.A. Pawelczyk, B. Hanel, R.A. Pawelczyk, J. Warberg, and N.H. Secher. Leg vasoconstriction during dynamic exercise with reduced cardiac output. *Journal of Applied Physiology*, 73(5):1838–1846, 1992.
- [188] C.A. Williams and A.R. Lind. The influence of straining maneuvers of the pressor response during isometric exercise. *European Journal of Applied Physiology*, 56(2):230–237, 1987.
- [189] E. Asmussen and M. Nielsen. The cardiac output in rest and work determined simultaneously by the acetylene and the dye injection methods. *Acta Physiologica Scandinavica*, 27(2–3):217–230, 1952.
- [190] T. Turányi and H. Rabitz. Local methods. In A. Saltelli, K. Chan, and E.M. Scott, editors, *Sensitivity Analysis*, Wiley Series in Probability and Statistics, chapter 5, pages 81–99. John Wiley & Sons, Chichester, UK, 2000.
- [191] A. Saltelli, K. Chan, and E.M. Scott, editors. *Sensitivity Analysis*. Wiley Series in Probability and Statistics. John Wiley & Sons, Chichester, UK, 2000.
- [192] C.R. Vogel. *Computational methods for inverse problems*. Frontiers in Applied Mathematics. SIAM, Philadelphia, 2002.
- [193] Y. Bard. *Nonlinear Parameter Estimation*. Academic Press, New York, 1974.
- [194] G.H. Golub and C.F. van Loan. *Matrix Computations*. Johns Hopkins University Press, Baltimore, MD, third edition, 1996.
- [195] M. Burth, G.C. Verghese, and M. Vélez-Reyes. Subset selection for improved parameter estimation in on-line identification of a synchronous generator. *IEEE Transactions on Power Systems*, 14(1):218–225, 1999.
- [196] M. Vélez-Reyes. *Decomposed Algorithms for Parameter Estimation*. Doctoral dissertation, Massachusetts Institute of Technology, Cambridge, MA, September 1992.

- [197] G.H. Golub, V. Klema, and G.W. Stewart. Rank degeneracy and least squares problems. Technical Report TR-456, Department of Computer Science, University of Maryland, College Park, MD, 1976.
- [198] J.H. Wilkinson. Householder's method for symmetric matrices. *Numerische Mathematik*, 4:354–361, 1962.
- [199] H. Bowdler, R.S. Martin, C. Reinsch, and J.H. Wilkinson. The QR and QL algorithms for symmetric matrices. *Numerische Mathematik*, 11:293–306, 1968.
- [200] P. Businger and G.H. Golub. Linear least squares solutions by Householder transformations. *Numerische Mathematik*, 7:269–276, 1965.
- [201] G. Bräuer and F. Rossberg. Zum Verhalten der Herzfrequenz des Menschen bei unterschiedlichen Geschwindigkeiten der Übergangs vom Liegen zur Kopfaufwärtsbewegung. *Acta Biologica et Medica Germanica*, 34:1153–1157, 1975.
- [202] F. Rossberg and L. Martinez. Das Übergangsverhalten der Herzfrequenz des Menschen in Abhängigkeit von der Atemphase während des schnellen, passiven Lagewechsels. *European Journal of Applied Physiology*, 50(2):291–300, 1983.
- [203] F. Rossberg and K. Balla. Zur Genese des initialen Herzfrequenzverlaufes bei der Kipptischuntersuchung und dessen Wert für die Beurteilung der autonomen Integrität. *Zeitschrift für die gesamte innere Medizin*, 41(8):221–226, 1986.
- [204] C. Borst, W. Wieling, J.F.M. van Brederode, A. Hond, L.G. de Rijk, and A.J. Dunning. Mechanisms of initial heart rate response to postural change. *American Journal of Physiology*, 243(5):H676–H681, 1982.
- [205] C. Borst, J.F.M. van Brederode, W. Wieling, G.A. van Montfrans, and A.J. Dunning. Mechanisms of initial blood pressure response to postural change. *Clinical Science*, 67(3):321–327, 1984.
- [206] R.L.H. Sprangers, D.P. Veerman, J.M. Karemaker, and W. Wieling. Initial circulatory response to changes in posture: Influence of the angle and speed of tilt. *Clinical Physiology*, 11(3):211–220, 1991.
- [207] R.L.H. Sprangers, J.J. van Lieshout, J.M. Karemaker, K.H. Wesseling, and W. Wieling. Circulatory response to stand up: Discrimination between the effect of respiration, orthostasis and exercise. *Clinical Physiology*, 11(3):221–230, 1991.
- [208] K. Toska and L. Walløe. Dynamic time course of hemodynamic responses after passive head-up tilt and tilt back to the supine position. *Journal of Applied Physiology*, 92(4):1671–1676, 2002.
- [209] G.B. Moody. *WFDB Programmer's Guide*. Harvard-MIT Division of Health Sciences and Technology, Cambridge, MA, 10th edition, April 2003. <<http://www.physionet.org/physiotools/wpg/wpg.htm>>; website accessed on 14 April 2003.

- [210] Wei Zong. *Studies on the ECG feature extraction and the fuzzy logic detection and classification of arrhythmias*. Doctoral dissertation, Xi'an Jiatong University, Xi'an, China, July 1993.
- [211] G.B. Moody. *WFDB Applications Guide*. Harvard-MIT Division of Health Sciences and Technology, Cambridge, MA, 10th edition, April 2003. <<http://www.physionet.org/physiotools/wag/wqrs-1.htm>>; website accessed on 14 April 2003.
- [212] W. Zong, T. Heldt, G.B. Moody, and R.G. Mark. An open-source algorithm to detect onset of arterial blood pressure pulses. *Computers in Cardiology*, 30:259–262, 2003.
- [213] Manned Spacecraft Center (U.S.). Results of the third U.S. manned orbital spaceflight, October 3, 1962. Technical Report NASA SP-12, National Aeronautics and Space Administration, Washington, DC, December 1962.
- [214] Manned Spacecraft Center (U.S.). Mercury project summary, including results from the fourth manned orbital flight. Technical Report NASA SP-45, National Aeronautics and Space Administration, Washington, D.C., October 1963.
- [215] Manned Spacecraft Center. Gemini summary conference. Technical Report NASA SP-138, National Aeronautics and Space Administration, Washington, D.C., 1967.
- [216] R.S. Johnston. Introduction. In Johnston et al. [269], chapter I-1, pages 3–7.
- [217] G.W. Hoffer and R.L. Johnson. Apollo flight crew cardiovascular evaluations. In Johnston et al. [269], chapter III-4, pages 227–264.
- [218] C.S. Leach and W.C. Alexander. Endocrine, electrolyte, and fluid volume changes associated with Apollo missions. In Johnston et al. [269], chapter III-1, pages 163–184.
- [219] S.L. Kimzey, C.L. Fischer, P.C. Hohnson, S.E. Ritzmann, and C.E. Mengel. Hematologic and immunologic studies. In Johnston et al. [269], chapter III-3, pages 197–226.
- [220] L.F. Dietlein. Summary and conclusions. In Johnston et al. [269], chapter IV-1, pages 573–579.
- [221] L.F. Dietlein. Skylab: A beginning. In Johnston and Dietlein [270], chapter 40, pages 408–418. NASA SP-377.
- [222] P.C. Johnson, G.W. Hoffer, A.E. Nicogossian, S.A. Bergman, Jr., and M.M. Jackson. Lower body negative pressure: Third manned skylab mission. In Johnston and Dietlein [270], chapter 29, pages 284–312. NASA SP-377.

- [223] W.L. Henry, S.E. Epstein, J.M. Griffith, R.E. Goldstein, and D.R. Redwood. Effect of prolonged spaceflight on cardiac function and dimensions. In Johnston and Dietlein [270], chapter 35, pages 366–371. NASA SP-377.
- [224] J.B. Charles and M.M. Jones. Cardiovascular orthostatic function of space shuttle astronauts during and after return from orbit. In *43rd Congress of the International Astronautical Federation, Washington, DC*. International Astronautical Federation, 1992. International Astronautical Federation/International Astronautical Association Reprint 92-0262.
- [225] M.M. Jones and J.B. Charles. Human blood pressure and heart rate changes during space shuttle landing and crew egress. *FASEB Journal*, 7:A665, 1993.
- [226] D.L. Harm, R.T. Jennings, J.M. Meck, M.R. Powell, L. Putcha, C.P. Sams, S.M. Schneider, L.C. Shackelford, S.M. Smith, and P.A. Whitson. Gender issues related to spaceflight: a NASA perspective. *Journal of Applied Physiology*, 91(5):2374–2383, 2001.
- [227] W.W. Waters, M.G. Ziegler, and J.V. Meck. Postspaceflight orthostatic hypotension occurs mostly in women and is predicted by low vascular resistance. *Journal of Applied Physiology*, 2(92):596–594, 2002.
- [228] D.S. Martin and J.V. Meck. Presyncopal/non-presyncopal outcomes of post spaceflight stand tests are consistent from flight to flight. *Aviation, Space, and Environmental Medicine*, 75(1):65–67, 2004.
- [229] P.C. Johnson, T.B. Driscoll, and A.D. LeBlanc. Blood volume changes. In Johnston and Dietlein [270], chapter 26, pages 235–241. NASA SP-377.
- [230] C.S. Leach, C.P. Alfrey, W.N. Suki, J.L. Leonard, P.C. Rambaut, L.D. Inners, S.M. Smith, H.W. Lane, and J.M. Krauhs. Regulation of body fluid compartments during short-term spaceflight. *Journal of Applied Physiology*, 81(1):105–116, 1996.
- [231] W.E. Thornton and G.W. Hoffer. Hemodynamic studies of the leg under weightlessness. In Richard S. Johnston and Lawrence F. Dietlein, editors, *Biomedical Results from Skylab*, chapter 31, pages 324–329. NASA, Washington, DC, 1977.
- [232] V.A. Convertino, D.F. Doerr, and S.L. Stein. Changes in size and compliance of the calf after 30 days of simulated microgravity. *Journal of Applied Physiology*, 66(3):1509–1512, 1989.
- [233] C.G. Blomqvist, S.J. Wright, B.D. Levine, J.C. Buckey, R.M. Peshok, P. Weatherall, J. Stray-Gundersen, F.A. Gaffney, D.E. Watenpaugh, P. Arbeille, and F. Baisch. Cardiovascular regulation at microgravity. In *Symposium on Scientific Results of the German Spacelab Mission D-2*, pages 688–690, Köln, Germany, 1994. Wissenschaftliche Projectführung D-2, RWTH Aachen, c/o DLR Köln.

- [234] L.-F. Zhang, Z.-B. Yu, J. Ma, and Q.-W. Mao. Peripheral effector mechanism hypothesis of postflight cardiovascular dysfunction. *Aviation, Space, and Environmental Medicine*, 72(6):567–575, 2001.
- [235] J.M. Fritsch-Yelle, P.A. Whitson, R.L. Bondar, and T.E. Brown. Subnormal norepinephrine release relates to presyncope in astronauts after spaceflight. *Journal of Applied Physiology*, 81(5):2134–2141, 1996.
- [236] J.V. Meck, W.W. Waters, M.G. Ziegler, H.F. deBlock, P.J. Mills, D. Robertson, and P.L. Huang. Mechanisms of post-spaceflight orthostatic hypotension:  $\alpha_1$ -adrenergic receptor responses before flight and central autonomic dysregulation post-flight. *American Journal of Physiology*, 286(4):H1486–H1495, 2004.
- [237] J.D. Levine, J.C. Buckey, J.M. Fritsch, C.W. Yancy, D.E. Watenpaugh, P.G. Snell, L.D. Lane, D.L. Eckberg, and C.G. Blomqvist. Physical fitness and cardiovascular regulation: mechanisms of orthostatic intolerance. *Journal of Applied Physiology*, 70(1):112–120, 1991.
- [238] B.J. Yates, M.J. Holmes, and B.J. Jian. Plastic changes in processing of graviceptive signals during spaceflight potentially contribute to postflight orthostatic intolerance. *Journal of Vestibular Research*, 13(4–6):395–404, 2003.
- [239] C.L. Fischer, P.C. Johnson, and C.A. Berry. Red blood cell mass and plasma volume changes in manned space flight. *The Journal of the American Medical Association*, 200(7):99–103, 1967.
- [240] C.P. Alfrey, M.M. Udden, C. Leach-Huntoon, T. Driscoll, and M.H. Pickett. Control of red blood cell mass in spaceflight. *Journal of Applied Physiology*, 81(1):98–104, 1996.
- [241] D.E. Watenpaugh, J.C. Buckey, L.D. Lane, F.A. Gaffney, W.E. Levine, B.D. Moore, S.J. Wright, and C.G. Blomqvist. Effects of spaceflight on human calf hemodynamics. *Journal of Applied Physiology*, 90(4):1552–1558, 2001.
- [242] J.C. Buckey. Central venous pressure in space. *Journal of Applied Physiology*, 81(1):19–25, 1996.
- [243] F. Louisy, C. Gaudin, J.M. Oppert, A. Güell, and C.Y. Guezennec. Haemodynamics of leg veins during a 30-day-6° head-down bedrest with and without lower body negative pressure. *European Journal of Physiology*, 61(5–6):349–355, 1990.
- [244] L. Beck, F. Baisch, F.A. Gaffney, J.C. Buckey, P. Arbeille, F. Patat, A.D.J. Ten Harkel, A. Hillebrecht, H. Schulz, J.M. Karemaker, M. Meyer, and C.G. Blomqvist. Cardiovascular response to lower body negative pressure before, during, and after ten days of head-down bedrest. *Acta Physiologica Scandinavica*, 144(S602):43–52, 1992.

- [245] F.M. Melchior and S.M. Fortney. Orthostatic intolerance during a 13-day bed rest does not result from increased leg compliance. *Journal of Applied Physiology*, 74(1):286–292, 1993.
- [246] V.A. Convertino. Mechanisms of microgravity induced orthostatic intolerance: implications for effective countermeasures. *Journal of Gravitational Physiology*, 9(2):1–14, 2002.
- [247] M.W. Bungo, D.J. Goldwater, R.L. Popp, and H. Sandler. Echocardiographic evaluation of space shuttle crewmembers. *Journal of Applied Physiology*, 62(1):278–283, 1985.
- [248] O.Y. Atkov, V.S. Bedenko, and G.A. Fomina. Ultrasound techniques in space medicine. *Aviation, Space, and Environmental Medicine*, 58(9 Suppl.):A69–A73, 1987.
- [249] S. Herault, G. Fomina, I. Alferova, A. Kotovskaya, V. Poliakov, and P. Arbeille. Cardiac, arterial and venous adaptation to weightlessness during 6-month mir spaceflights with and without thigh cuffs (bracelets). *European Journal of Applied Physiology*, 81(5):384–390, 2000.
- [250] L.D. Blomqvist, C.G. Lane, S.J. Wright, G.M. Meny, B.D. Levine, J.C. Buckey, R.M. Peshock, P. Weatherall, J. Stray-Gundersen, F.A. Gaffney, D.E. Watenpugh, P. Arbeille, and F. Baisch. Cardiovascular regulation in microgravity. In P.R. Sahm, M.H. Keller, and B. Schiewe, editors, *Scientific Results of the German Spacelab Mission D-2*, pages 688–690, Köln, Germany, 1994. Wissenschaftliche Projektführung D-2 (c/o Deutsches Zentrum für Luft- und Raumfahrt). Proceedings of the Norderney Symposium.
- [251] W. Barańska, P. Skopiński, and A. Kaplański. Morphometrical evaluation of myocardium from rats flown in biosatellite Cosmos-1887. *Materia Medica Polona*, 76(4):255–257, 1990.
- [252] D.E. Philpott, I.A. Popova, K. Kato, K. Stevenson, J. Miquel, and W. Sapp. Morphological and biochemical examination of Cosmos 1887 rat heart tissue: Part I — ultrastructure. *FASEB*, 4(1):73–78, 1990.
- [253] M.A. Goldstein, R.J. Edwards, and J.P. Schroeter. Cardiac morphology after conditions of microgravity during cosmos 2044. *Journal of Applied Physiology*, 73(2 Suppl.):94S–100S, 1992.
- [254] C.A. Ray, M. Vasques, T.A. Miller, M.K. Wilkerson, and M.D. Delp. Effect of short-term microgravity and long-term hindlimb unloading on rat cardiac mass and function. *Journal of Applied Physiology*, 91(3):1207–1231, 2001.
- [255] Q. Fu, A. Arbab-Zadeh, M.A. Perhonen, R. Zhang, J.H. Zuckerman, and B.D. Levine. Hemodynamics of orthostatic intolerance: implications for gender differences. *American Journal of Physiology*, 286(1):H449–H457, 2004.

- [256] J.M. Fritsch, J.B. Charles, B.S. Bennett, M.M. Jones, and D.L. Eckberg. Short-duration spaceflight impairs human carotid baroreceptor-cardiac reflex response. *Journal of Applied Physiology*, 73(2):664–671, 1992.
- [257] B.D. Levine, J.A. Pawelczyk, A.C. Ertl, J.F. Cox, J.H. Zuckerman, A. Diedrich, C.A. Ray, M.L. Smith, S. Iwase, M. Saito, Y. Sugiyama, T. Mano, R. Zhang, K. Iwasaki, L.D. Lane, J.C. Buckey, Jr., W.H. Cooke, F.J. Baisch, D. Robertson, D.L. Eckberg, and C.G. Blomqvist. Human muscle sympathetic neural and haemodynamic responses to tilt following spaceflight. *Journal of Physiology*, 538(1):331–340, 2002.
- [258] T.E. Wilson, M. Shibasaki, J. Cui, B.D. Levine, and C.G. Crandall. Effects of 14 days of head-down tilt bed rest on cutaneous vasoconstrictor responses in humans. *Journal of Applied Physiology*, 94(6):2113–2118, 2003.
- [259] J.B. Charles, J.M. Fritsch-Yelle, P.A. Whitson, M.L. Wood, T.E. Brown, and G.W. Fortner. Cardiovascular deconditioning. In C.F. Sawin, G.R. Taylor, and W.L. Smith, editors, *Extended Duration Orbiter Medical Project*, chapter 1, pages 1–1 – 1–19. National Aeronautics and Space Administration, Houston, TX, 1999.
- [260] J.-S. Shi, D.A. South, and J.V. Meck. Fludrocortisone does not prevent orthostatic hypotension in astronauts after spaceflight. *Aviation, Space, and Environmental Medicine*, 75(3):235–239, 2004.
- [261] National Aeronautics and Space Administration Task Force on Countermeasures. Final report. <[http://peer1.nasaprs.com/peer\\_review/prog/prog.html](http://peer1.nasaprs.com/peer_review/prog/prog.html)>; website accessed on 9 July 2003, 1997.
- [262] S.E. Piwinsky, J. Jankovic, and M.A. McElligott. A comparison of postspaceflight orthostatic intolerance to vasovagal syncope and autonomic failure and the potential use of the alpha agonist midodrine for these conditions. *Journal of Clinical Pharmacology*, 34:466–471, 1994.
- [263] C.D. Ramsdell, T.J. Mullen, G.H. Sundby, S. Rostoft, N. Sheynberg, N. Aljuri, M. Maa, R. Mukkamala, D. Sherman, K. Toska, J. Yelle, D. Bloomfield, G.H. Williams, and R.J. Cohen. Midodrine prevents orthostatic intolerance associated with simulated spaceflight. *Journal of Applied Physiology*, 90(6):2245–2248, 2001.
- [264] S.H. Platts, M.G. Ziegler, W. Waters, B.M. Mitchell, and J.V. Meck. Midodrine prescribed to improve recurrent post-spaceflight orthostatic hypotension. *Aviation, Space, and Environmental Medicine*, 75(6):554–556, 2004.
- [265] C.L. Prosser. *Comparative Animal Physiology*. W.B. Saunders, Philadelphia, PA, 1973.
- [266] M. Kleiber. Body size and metabolism. *Hilgardia*, 6:315–353, 1932.



- [267] T. McMahon. Size and shape in biology. *Science*, 179(79):1201–1204, 1973.
- [268] T.A. McMahon. Scaling physiological time. *Lectures in Mathematics in the Life Sciences*, 13:131–163, 1980.
- [269] R.S. Johnston, L.F. Dietlein, and C.A. Berry, editors. *Biomedical Results of Apollo*. National Aeronautics and Space Administration (U.S. Government Printing Office), Washington, D.C., 1975.
- [270] R.S. Johnston and L.F. Dietlein, editors. *Biomedical Results from Skylab*. National Aeronautics and Space Administration (Scientific and Technical Information Office), Washington, D.C., 1977. NASA SP-377.